annual progress report

2008

VEHICLE TECHNOLOGIES PROGRAM

PROPULSION MATERIALS

U.S. Department of Energy
Energy Efficiency and Renewable Energy
Bringing you a prosperous future where energy is clean, abundant, reliable, and affordable

This document highlights work sponsored by agencies of the U.S. Government. Neither the U.S. Government nor any agency thereof, nor any of their employees, makes any warranty, express or implied, or assumes any legal liability or responsibility for the accuracy, completeness, or usefulness of any information, apparatus, product, or process disclosed, or represents that its use would not infringe privately owned rights. Reference herein to any specific commercial product, process, or service by trade name, trademark, manufacturer, or otherwise does not necessarily constitute or imply its endorsement, recommendation, or favoring by the U.S. Government or any agency thereof. The views and opinions of authors expressed herein do not necessarily state or reflect those of the U.S. Government or any agency thereof.

Printed on recycled paper

U.S. Department of Energy
Office of Vehicle Technologies
1000 Independence Avenue S.W.
Washington, DC 20585-0121

FY 2008

Progress Report for Propulsion Materials

Energy Efficiency and Renewable Energy
Office of Vehicle Technologies
Advanced Materials Technologies

Edward J. Wall **Program Manager, OVT**
Rogelio A. Sullivan **Advanced Materials Technologies Team Leader**
Jerry L. Gibbs **Technology Manager**

January 2009

CONTENTS

INTRODUCTION..... **1**

PROJECT 18516 - MATERIALS FOR ELECTRIC AND HYBRID DRIVE SYSTEMS……. **11**
Agreement 16307 - Modeling/Testing of Environmental Effects on Automotive PE Devices… 11
Agreement 9537 - Graphite Foam for Cooling Power Electronics……. 17
Agreement 16305 - Solder Joint: Materials by Design …….. 25
Agreement 16306 - Power Electronics Materials Compatibility……. 31

PROJECT 18517 – COMBUSION SYSTEM MATERIALS…… **35**
Agreement 11752 - Materials for HCCI Engines…… 35
Agreement 8697 - NO_x Sensor Development …… 41
Agreement 9440 - Fabrication of Micro-orifices for Diesel Fuel Injectors…… 51
Agreement 11754 - Hydrogen Materials Compatibility…… 59

PROJECT 18518 - MATERIALS FOR HIGH EFFICIENCY ENGINES..... 77
Agreement 16304 - High Performance Valve Materials…….……. 77
Agreement 13329 - Mechanical Reliability of Piezoelectric Multilayer Actuators for Fuel Injectors……. 81
Agreement 9010 - Joining of Advanced Materials by Plastic Deformation…… 89
Agreement 13332 - Friction and Wear Reduction in Diesel Engine Valve Trains…… 99
Agreement 9089 - NDE of Diesel Engine Components…….. 103
Agreement 15050 - Materials Testing with ACERT Engine…… 111
Agreement 15054 - Fatigue Enhancement in CIDI/HCCI Engine Components…….. 115
Agreement 15055 - Friction Stir Processing to Tailor Thermal and Mechanical Properties of CIDI Engine Components for Improved Energy Efficiency…….. 121
Agreement 16103 - Concept Feasibility of Bonding Similar and Dissimilar Powertrain Materials Using Reactive NanoFoils…….. 131

PROJECT 18519 – MATERIALS FOR CONTROL OF EXHAUST GASES AND ENERGY RECOVERY SYSTEMS..... ..... **137**
Agreement 9130 - Development of Materials Analysis Tools for Studying NO_x Adsorber Catalysts (CRADA with Cummins, Inc.)…… 137
Agreement 10461 - Durability of Diesel Particulate Filters (CRADA with Cummins, Inc.) 153
Agreement 10635 - Catalysis by First Principles…….. 163

PROJECT 18865 - MATERIALS BY DESIGN..... **175**
Agreement 13723 - Residual Stresses in Thin Films…… 175
Agreement 9105 - Ultra-High Resolution Electron Microscopy for Characterization of Catalyst Microstructures and Deactivation Mechanisms …… 193
Agreement 9110 - Life Prediction of Diesel Engine Components……...… 207
Agreement 14957 - Modeling of Thermoelectrics…….…… 215
Agreement 15529 - Erosion of Materials in Nanofluids…… 221
Agreement 16308 – Science-based Approach to Thermoelectric Materials……. 227
Agreement 16309 - Carbon-based Thermoelectrics……. 231

INTRODUCTION

Propulsion Materials R&D:
Enabling Technologies to Meet Vehicle Technologies Program Goals

The Department of Energy's (DOE's) Office of Vehicle Technologies (OVT) is pleased to introduce the *FY 2008 Annual Progress Report for the Propulsion Materials Research and Development Program*. Together with DOE national laboratories and in partnership with private industry and universities across the United States, the program continues to engage in research and development (R&D) that provides enabling materials technology for fuel-efficient and environmentally friendly commercial and passenger vehicles.

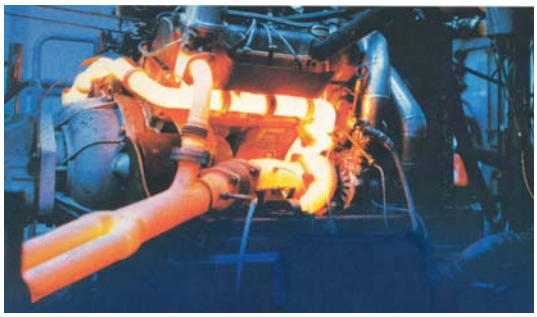

This introduction summarizes the objectives, progress, and highlights of the program in FY 2008. The Propulsion Materials R&D Program has supported the Vehicle Technologies Program since its inception. In research areas where industry views the risks as too high and uncertain, the Vehicle Technologies Program conducts long-term research, development, and demonstration activities that bring the technology to a stage of maturity such that industry can undertake the final commercialization stages. In order to provide more effective support to the program's stakeholders and participants, the former Automotive Propulsion Materials and Heavy Vehicle Propulsion Materials R&D programs were combined in FY 2007 into a single Propulsion Materials R&D program.

The Propulsion Materials program is a partner and supporter of the (OVT) Hybrid and Vehicle Systems, Energy Storage, Power Electronics and Electrical Machines, Advanced Combustion Engines, and Fuels and Lubricants R&D programs. Projects within the Propulsion Materials Program address materials concerns that directly impact the critical technical barriers in each of these programs—barriers such as fuel efficiency, thermal management, emissions reduction, and reduced manufacturing costs. The program engages only the barriers that involve fundamental, high-risk materials issues.

Enabling Technologies

The Propulsion Materials program focuses on enabling and innovative materials technologies that are critical in improving the efficiency of advanced engines. The program provides enabling materials support for combustion, hybrid, and power electronics development, including the following:

- Materials for low-temperature combustion, for example, homogenous-charge compression-ignition
- Materials for hydrogen engine fuel systems
- Materials for 55% thermal efficiency heavy-duty diesel engines
- Materials for waste-heat recovery via thermoelectric modules, with potential 10% increase in fuel efficiency
- Materials for efficient and effective reduction of tailpipe emissions

The program supports these core technology areas by providing materials expertise, testing capabilities, and technical solutions for materials problems. The component development, materials processing, and

characterization that the program provides are enablers of the successful development of efficient and emissions-compliant engines.

Program Organization

The Propulsion Materials Program consists of five R&D projects which support the OVT propulsion technologies. Each project consists of several related R&D agreements.

- Materials for Electric and Hybrid Drive Systems
  - Develop materials appropriate for power electronics and other hybrid system applications

- Combustion System Materials
  - Develop materials for HCCI engines and fuel injection systems

- Materials for High Efficiency Engines
  - Develop materials for efficient engine components, such as valve-train components, fuel injectors, and turbochargers

- Materials for Control of Exhaust Gases and Energy Recovery Systems
  - Develop materials for exhaust aftertreatment and thermoelectric exhaust heat recovery applications
- Materials by Design
  - Adopt a computational materials – atomic-scale characterization protocol to develop advanced materials for NO_x catalysts, lithium-ion batteries, thermoelectric generators

R&D Projects and Agreements are evaluated annually using strategic objectives. Agreements are evaluated on relevance to OVT objectives and supported team's priorities, strength of industrial support for the activity, and perceived value of the R&D activity to the OVT Program. In order to keep the program fresh and up-to-date, over 10% of agreements are retired annually. New projects are selected in accordance with identified Office of Vehicle Technologies needs, for example:

- Advanced Combustion Team
  - Internal combustion engine materials
  - Thermoelectric materials
  - Catalysts and aftertreatment materials
  - Materials for engine sensors

- Hybrid Electric Systems Team
  - Power electronics materials
  - Materials for energy storage

- Fuels Team
  - Alternative fuels materials compatibility

Selected Highlights:

Materials for Electric and Hybrid Drive Systems

The goal of the Automotive Power Electronic and Electric Machines (APEEM) Program is to reduce the size, weight, and volume of the power electronics without increasing the cost or reducing the reliability. Many, if not most, technical barriers are directly linked to the contemporary material limitations of subcomponents found within devices that comprise inverters, converters, and motors. The material limitations include:

- Insufficient temperature capability
- Excessive thermal insulations
- Excessive electrical insulation
- Insufficient power density in permanent magnets
- Insufficient bandgap

Many of these issues are already being addressed in the Vehicle APEEM Program, but there is interest in additional means to overcome some of those materials limitations through the application of advanced materials science and engineering. In 2008 modeling and analysis of a new concept for a direct-cooled power electronics substrate were conducted by R&D staff of the Oak Ridge National Laboratory (ORNL). The concept of the direct-cooled substrate is shown in Figure 1.

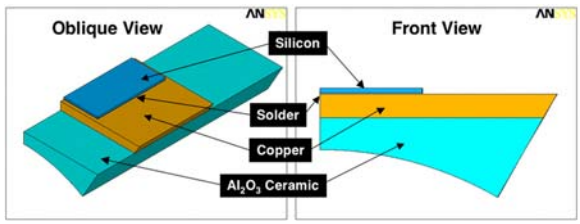

Figure 1. *Model of a direct-cooled ceramic substrate.*

A finite element model of stress and temperature was constructed. Experimental strength data for an alumina ceramic substrate were used with the finite element model and the Cares/Life computer code to predict the probability of survival of the direct-cooled substrate, Figure 2. The probability of survival was predicted to be greater than 99.999%. The direct-cooled ceramic substrate could be of interest for use in hybrid vehicle inverters because it has the potential to substantially reduce both the volume and weight of the inverter. A prototype will be fabricated in FY09.

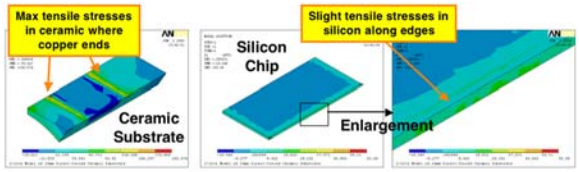

Figure 2. *First Principal stresses in the ceramic substrate and the silicon*

The strength of several candidate substrates and silicon chips were measured for use in probabilistic analyses; biaxial flexure strengths are shown in Table 1.

Table 1. *Comparison of Weibull strength distributions for anticlastically fractured silicon and silicon carbide chips.*

Material	Descriptor	Number of Specimens	Characteristic Equibiaxial Strength* (MPa)	Weibull Modulus
Aluminum Nitride	As Fired	15	665	33.0
Aluminum Nitride	Lapped	10	452	13.0
Aluminum Oxide	AD96	10	595	12.7
Aluminum Oxide	AD995	10	692	16.9
Boron Nitride		15	50	12.8
Silicon Carbide	Sintered Alpha	10	518	4.8
Silicon Nitride	SN460	15	1097	17.7

* Test Fixture: Ball on Ring (15mm Ring, 1/2" WC Ball, XHD=0.5 mm/min)

Combustion System Materials

Increasingly stringent emissions regulations will require the development of advanced gas sensors for a variety of applications. For example, compact, inexpensive sensors are needed for detection of regulated pollutants, including hydrocarbons (HCs), CO, and NO_x, in automotive exhaust. Of particular importance will be a sensor for NO_x to ensure the proper operation of the catalyst system in the next generation of diesel (CIDI) automobiles. Current work at Lawrence Livermore National Laboratory has made significant advances in terms of developing prototype sensors more suitable for commercialization. Also, dynamometer testing has provided real-world sensor performance data that will be useful in approaching potential suppliers to whom the technology for commercialization might be transferred. Figure 3 shows a schematic of a NO_x prototype sensor based on a Pt/YSZ/Au cell and a photograph of a Pt/YSZ/Au prototype built on a heated substrate and packaged into an oxygen sensor housing. Both the incorporation of a heated substrate and an oxygen sensor housing indicates that the impedancemetric NO_x sensor technology can be adapted to a commercial sensor platform.

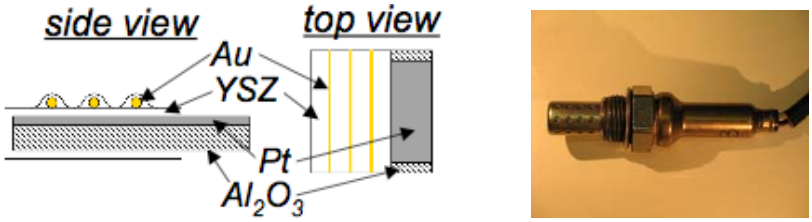

Figure 3. *a, Schematic of a Pt/YSZ/Au cell, b, photograph of the prototype packaged into an oxygen sensor housing*

Hydrogen-fueled internal combustion engines, utilizing direct injection, can be viewed as a high-efficiency, low-emissions technology for bridging the transition to the hydrogen economy that is based on fuel cell technology. It has been estimated that a hydrogen direct injection (DI) engine can be integrated into a hybrid vehicle system to result in fuel consumption (fuel energy utilized per unit distance) that is only about 15% to 20% greater than a hybridized fuel cell vehicle of similar mass. Significantly lower hardware cost (as compared to present fuel cell systems) and the ability to use existing manufacturing facilities for conventional reciprocating engines makes this an attractive consideration. Some engine manufacturers have identified robust fuel injection technology as one of the key enablers for commercialization of advanced hydrogen DI engines.

In collaboration by Pacific Northwest National Laboratory, Ford Motor Company, The Argonne National Laboratory, and the Oak Ridge National Laboratory, the friction and wear characteristics of fuel injector materials were measured in hydrogen environments, including in-situ and ex-situ materials characterization and a design approach to hydrogen injectors based on material behavior and experimental data was developed.

Wear-resistant diamond-like coatings, including those developed by Argonne National Laboratory, were tested for friction and wear in a hydrogen atmosphere. New nanolaminate coatings were evaluated using the sliding-impact testing apparatus at ORNL. A comparison of DLC materials that had been exposed to a 100% hydrogen environment at 300 Bar for 100 hours is shown in Figure 4; the objective was to compare all diamond-like coating materials that had been exposed to a 100% hydrogen environment at 300 Bar for 100 hours.

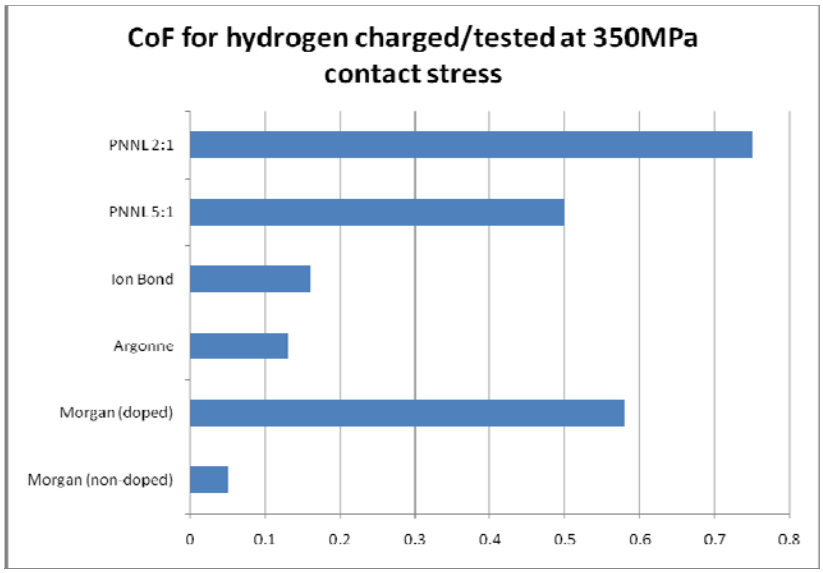

Figure 4. *Coefficient of friction of coatings exposed to300 Bar/100 hour hydrogen, tested to 1000 cycles*

Materials for High Efficiency Engines

In order to enable to enable the improved selection and use of materials, surface treatments, and lubricating strategies for value train components like exhaust valves and seats in energy-efficient diesel engines, researchers at ORNL designed and built a specialized, high-temperature repetitive impact apparatus (Figure 5) to investigate the combined effects of mechanical contact, high temperatures, and oxidizing environments on the durability of high-performance diesel engine valve materials. The testing system is capable of testing actual valves as well as simpler specimens of promising materials not currently available as valves. A set of diesel engine exhaust valves was provided by Caterpillar Corporation to serve as best-practice commercial materials for benchmark testing and to ensure that the apparatus would properly fit commercial valves. Initial experiments used a specimen holder inclined at 45 degrees to mimic the actual seat angle and produce a combination of impact plus slip on the contact surfaces.

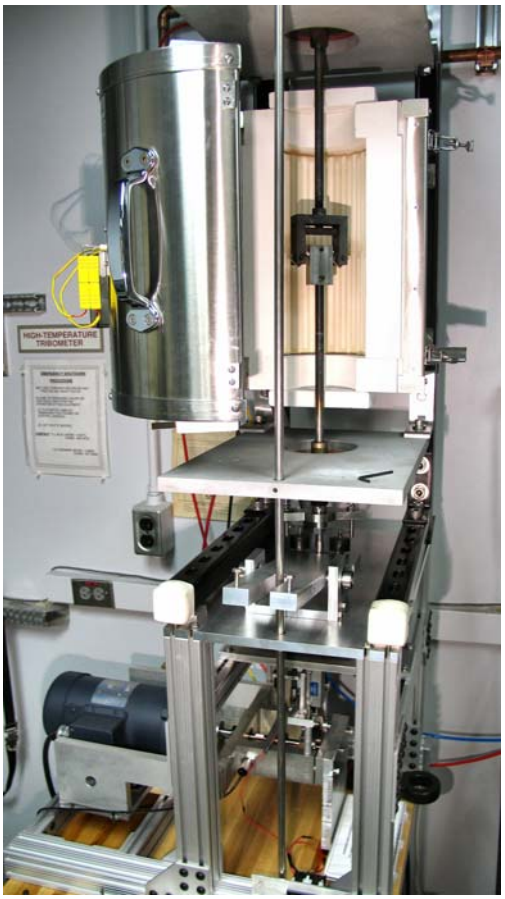

Figure 5. *High-temperature repetitive impact testing machine with the furnace door open to reveal the specimen holders.*

Monitoring gas composition, such as O_2, NO_x, CO, CO_2, in the combustion environment with good accuracy has been of great importance since the advance of combustion heat engines in the last century. NO_x (NO + NO_2) sensing is also considered one of the key elements of next generation internal combustion engines. A reliable and accurate NO_x sensor is needed to monitor NO_x and trigger the regeneration of NO_x adsorption catalysts, or control the injection of reductants for continuous NO_x reduction. A bonding technique developed earlier has been applied by Argonne National Laboratory researchers to produce NO_x sensors that could enable simultaneous measurements of NO_x and O_2 in a combustion environment. A Pd/PdO-containing reference chamber was sealed within a stabilized zirconia superstructure by the high pressure/temperature bonding method. NO_x sensing was conducted in both amperometric and potentiometric modes (Figure 6). Pt-loaded zeolite Y was used to obtain total NO_x capacity and to cover Pt electrodes for detecting oxygen in the presence of NO_x. Both amperometric and potentiometric type sensors shows good NO_x/O_2 signal stability and total NO_x response.

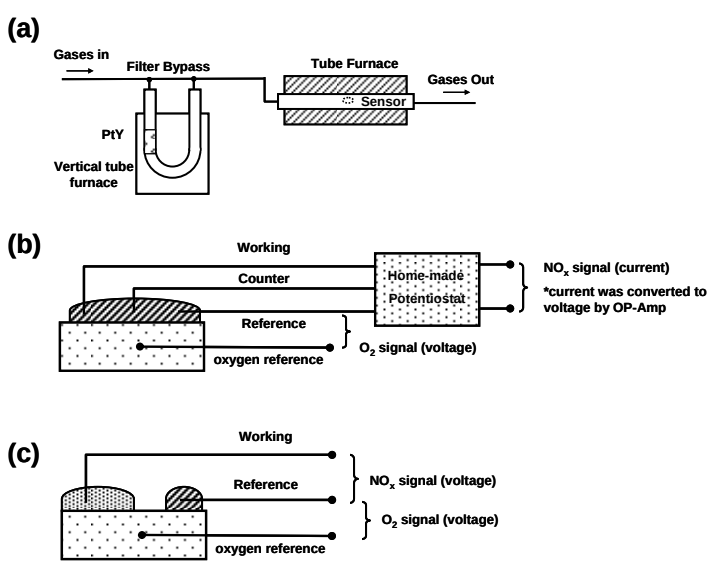

Figure 6. *(a) sensor testing setup (PtY = Pt-zeolite Y); (b) Measurement setup for the amperometric configuration; (c) Measurement setup for the potentiometric configuration.*

Engine manufacturers have recognized several key needs that need to be addressed in order for heavy duty diesel engines to achieve a national efficiency goal of 55% by the year 2012. These include 1) improved structural materials to accommodate higher cylinder pressures and temperatures (associated with advanced combustion methodologies), 2) improved thermal management and waste heat recovery technologies, 3) improved durability, 4) improved transient performance, and 5) better aftertreatment performance. These needs address barriers associated with high parasitic losses, high-efficiency clean combustion and thermal management of the cylinder and exhaust. A cooperative research and development agreement between Caterpillar, Inc. and the Oak Ridge National Laboratory brings together comprehensive expertise in engine design and testing and materials development within both organizations to address these critical barriers. Caterpillar provided ORNL with two 600 hp motoring dynamometers and a C15 ACERT engine for testing of engine components and materials (Figure 7). Caterpillar, working with ORNL will develop and provide prototype components to be evaluated on the engine platform. ORNL engine research staff will evaluate the engine performance with emphasis on combustion diagnostics, optimization and modeling. Materials scientists at ORNL will examine material performance and provide guidance to materials development.

Figure 7. *Photograph showing mounted Caterpillar engine and dynamometer in ORNL engine test cell. The engine will be used for testing advanced component designs and materials.*

The Pacific Northwest National Laboratory and Caterpillar are investigating the application of a new material processing technology, Friction Stir Processing, to improve the thermal and mechanical properties of Compression Ignition Direct Injection engine components. The objective is to produce components with functionally graded surfaces that are optimized for thermal properties and for better in-service performance. The direct goal of the project is to increase the energy efficiency of the engine through better management of thermal conditions, reduced parasitic losses and indirectly through better part durability and wear resistance. Friction stir processing is a new technology that has an opportunity to be used to create compositionally graded surfaces (Figure 8). In recent years, PNNL has worked on developing techniques and tools that allow friction stir processing to be accomplished in steels, cast iron and aluminum. The process for these materials is not yet commercially ready, but it has shown the potential for success if additional investments are made to develop and optimize the technology.

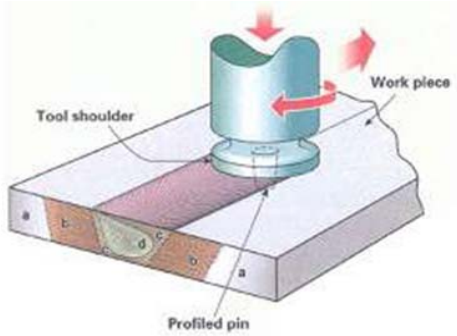

a)

b)

Figure 8. *a) Friction Stir process illustration; b) typical tool used to stir ceramic powders into surface of aluminum substrate (two start scrolled shoulder with a stepped spiral pin for producing a 0.25 in thick processed region.*

Materials for Control of Exhaust Gases and Energy Recovery Systems

The development of new emission-treatment catalytic systems is still largely dominated by trial and error, which is often slow and expensive. A knowledge gap between theory and experiment has been a major contributing factor: traditional computational approaches have been significantly simplified in comparison to real materials, and experimental studies, especially on emission treatment catalysts, have primarily focused on fully formulated systems that can treat engine-out emissions in vehicles. Researchers at the Oak Ridge National Laboratory are developing a protocol that combines the power of theory and experiment for atomistic design of catalytically active sites that can contribute directly to complete catalyst system suitable for technical deployment. The protocol includes theoretical modeling of catalyst systems via density functional theory, synthesis of experimental catalyst systems, exposure of catalysts under simulated operating conditions (including an ex-situ reactor which permits duplication of the reaction conditions in a bench-top reactor and facilitates high-resolution scanning transmission electron microscopy), and characterization of the catalyst performance and changes that occur in the catalysts during operation. In 2008 theoretical and experimental studies of the oxidation and reactivity of CO, NO_x and HC on Pt clusters supported on alumina, which are a common constituent of a variety of emission treatment catalysts, including three-way, NO_x trap, Oxidation, and HC-SCR catalysts, were conducted.

The durability of diesel particulate filters (DPFs) is being evaluated by research staff at the Oak Ridge National Laboratory and Cummins, Inc. via application of probabilistic design tools, nondestructive evaluation, and refinement and use of lifetime-prediction models. Mechanical and thermal shock characterization test procedures developed earlier were employed to rank the relative thermal shock resistance of several candidate DPF substrate materials. The properties utilized to measure the thermal shock resistance included the fracture toughness, elastic modulus and the coefficient of thermal expansion. The porosity of the cordierite substrate was the most important variable that determined the elastic and fracture mechanical properties of the substrate. The effect of porosity on the fracture toughness of cordierite substrates was quantitatively identified. In addition, the effect of catalytic washcoating and soot loading on the high temperature elastic properties of DPF substrates was characterized. A field returned DPF was thoroughly characterized (Figure 9) and its properties compared to that of virgin, uncoated filters. The difference in the properties of field returned filters were explained based on microstructural observations.

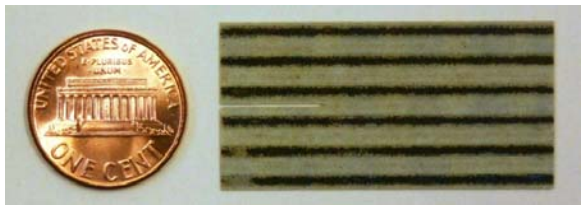

Figure 9. *A double-torsion specimen prepared from a high mileage filter. The alternate dark lines are due to soot loading on the inlet channels of the filter*

Materials by Design

Researchers at the Oak Ridge National Laboratory materials are developing design strategies for thermoelectric materials based on first principles calculations of electronic, vibrational and transport properties to identify potentially low cost, high performance thermoelectric materials suitable for application in vehicles. New insights into thermoelectric materials performance have emerged from density functional calculations in conjunction with transport theory. Promising new potentially low cost thermoelectrics, especially $YCuO_2$ (Figure 10) have been identified, and a mechanism for thermal conductivity reduction in PbTe has been elucidated.

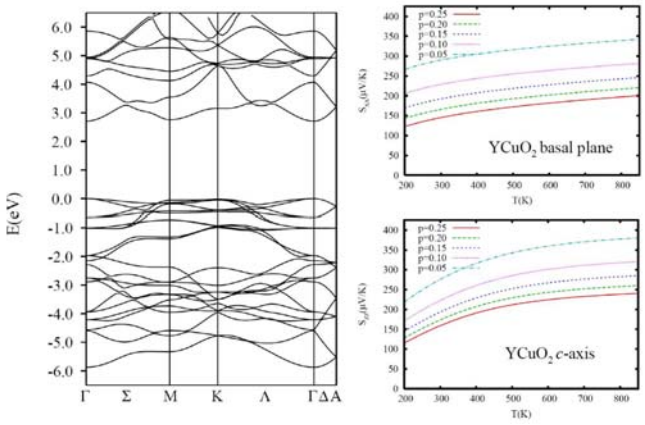

Figure 10: *Calculated band structure (left) and thermopower (right) for delafossite structure $YCuO_2$. Note the very high thermopowers found in the temperature range of relevance for vehicle waste heart recovery. Note also that the basal plane and c-axis thermopowers are both high*

Reducing radiator size may reduce the frontal area of a vehicle and, hence, the aerodynamic drag. However, current radiator designs have already stretched these approaches to their limits. Therefore, an urgent need exists for new and innovative concepts to achieve ultra-high-performance cooling. Nanofluids seem to show enormous potentials as a coolant for radiators and are being investigated at the Argonne National Laboratory. A computational fluid dynamics calculation of a Cummins 500 hp diesel engine using an ideal nanofluid as coolant has shown that the radiator size could be reduced by 5%, reducing weight and size, and hence aerodynamic drag. However, in order for the enhanced thermal conductivity to be utilized it must be shown that liquid erosion of typical cooling system materials will be tolerable. After 750 h of testing no severe erosion damage of aluminum 3003 (used in many automotive radiators) has been observed to date. However, the nanofluids tested thus far were not the extremes. Argonne researchers have designed and are building an apparatus that will allow not only continuation of the well-controlled tests designed to develop the data required to model erosive damage, but will closely replicate “real world” conditions in an automotive water pump.

The remainder of this report communicates the progress achieved during FY 2007 under the Propulsion Materials Program. It consists of annual progress contributions from the several R&D Agreements that make up each of the five overarching R&D Projects that are highlighted above. The R&D contributions provide an overview of the critical work being conducted to develop enabling materials technologies for high-efficiency passenger and commercial vehicles, including goals, barriers, progress to date, and future plans.

Rogelio A. Sullivan
Team Leader, Advanced Materials Technologies
Office of Vehicle Technologies
Energy Efficiency and Renewable Energy

Jerry L. Gibbs
Technology Manager
Office of Vehicle Technologies
Energy Efficiency and Renewable Energy

Project 18516 - Materials for Electric and Hybrid Drive Systems

Agreement 16307 - Modeling/Testing of Environmental Effects on Automotive PE Devices

*A. A. Wereszczak, H. -T. Lin, M. J. Lance, and O. M. Jadaan**
Ceramic Science and Technology Group
Oak Ridge National Laboratory
P.O. Box 2008, MS 6068, Bldg. 4515
Oak Ridge, TN 37831-6068
(865) 576-1169; fax: (865) 574-6098; e-mail: wereszczakaa@ornl.gov
* *University of Wisconsin-Platteville, Platteville, WI*

DOE Technology Manager: Jerry L. Gibbs
(202) 586-1182; fax: (202) 586-1600; e-mail: Jerry.gibbs@ee.doe.gov
ORNL Technical Advisor: D. Ray Johnson
(865) 576-6832; fax: (865) 574-6098; e-mail: johnsondr@ornl.gov

---

Contractor: Oak Ridge National Laboratory, Oak Ridge, Tennessee
Prime Contract No.: DE-AC05-00OR22725

Objectives

- Understand the complex relationship between environment (temperature, humidity, and vibration) and automotive power electronic device (PED) performance through materials characterization and modeling.
- Identify alternative materials and architectures internal to PEDs that will improve reliability and enable higher temperature operation.

Approach

- Evaluate performance of PE devices as a function of temperature, humidity, and vibration.
- Dissect PE devices as part of their postmortem and evaluate failure initiation location.
- Evaluate the thermal management effectiveness of PE devices and seek means to achieve improvements that will enable reliability improvement and higher temperature usage.

Accomplishments

- Modeled thermomechanical stress state in an IGBT module and began considering alternative insulating ceramics for use in them.
- Co-developed a direct-cooled ceramic substrate concept that is applicable to power electronic devices and that can enable reduction of both mass and volume of inverters for hybrid vehicles. Patent applied for.
- Measured strengths of ceramic substrates, and silicon and silicon carbide chips that will be used in modeling.
- Established the candidacy of an electrically insulating polycrystalline silicon carbide as an electronic substrate.

Future Direction

- Compare cooling efficiencies in a hybrid inverter IGBT that contains contemporary and alternative ceramic substrates.
- Establish strength-size-scaling characteristics for {111} silicon and 4HN-silicon-carbide semiconductor chips and refine mechanical test methods that will enable the study of the effects of edge-type strength-limiting flaws.
- Continue to model and interpret thermomechanical stress states of automotive PE devices in support of the APEEM Program and, where applicable, recommend alterative material constituents that will lessen stresses.

- Continue to pursue the development of alternative electrically insulating ceramics having high thermal conductivity and prospects for low-cost production.

Introduction

Research performed under the FreedomCAR and Vehicle Technologies Program's Vehicle Systems subprogram seeks to lessen technical and cost barriers and enable development that will benefit advanced vehicles such hybrid electric vehicles. Weight, volume, and cost targets for the power electronics and electrical machines subsystems of the traction drive system in those vehicles must be attained to achieve success. Research areas include more powerful novel traction motor designs, more efficient and higher temperature-capable inverter technologies, reduced footprint and weight of converters, more effective thermal control and packaging technologies, and motor/inverter concepts.

Many, if not most, technical barriers are directly linked to the contemporary material limitations of subcomponents found within devices that comprise inverters, converters, and motors. For automotive power electronic devices (PEDs), contemporary material limitations include insufficient temperature capability, excessive thermal insulation, and excessive electrical insulation (i.e., generates excessive heat).

This project's objectives are to understand the complex relationship between environment (temperature, humidity, and vibration) and automotive power electronic PED performance through materials characterization and modeling, and identify alternative material constituents and architectures that will improve their reliability and enable their operation at higher temperatures without compromise to electronic function.

Results

The description of this year's progress is divided into modeling and experimental sections. The modeling describes thermomechanical analysis of an insulated gate bipolar transistor (IGBT) module and a direct-cooled ceramic substrate. The experimental section describes mechanical evaluation of contemporary electronic ceramic substrates, semiconductor chips, and electrical evaluation of a new candidate electronic substrate material.

Modeling

A 100A-1200V IGBT module was dissected, and the dimensions and material constituents of its interior were determined. This was done to enable the eventual substitution of alternative ceramics and architectures to improve reliability or enable high temperature capability. The dimensions and identified materials were used to create a finite element analysis (FEA) model of its interior (Fig. 1), and that was used to estimate thermomechanical stresses caused by a typical operational thermal gradient (Fig.2). The boundary conditions, constituents, and the used properties are shown in Fig. 1. The resulting stresses in the ceramic substrate and silicon components are shown in Figs. 3-4, respectively. The First Principal tensile stresses in portions of the ceramic exceeded 100 MPa, and were on the order of tens of MPa for the silicon. Probabilities of survival can be determined with appropriate combination of strength data.

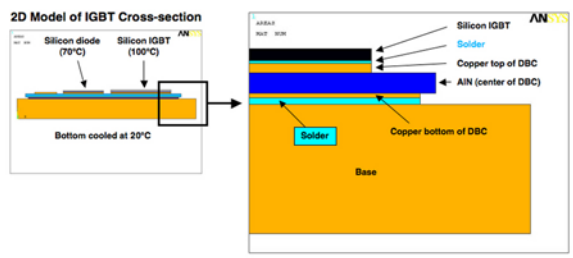

Material / Property	E (GPa)	ν	CTE (ppm/°C)	TC (W/mK)	S_{yld} (MPa)
Silicon	130	0.28	4.1	150	∞ (Elastic)
Copper	135	0.34	17	400	∞ and 138 (Plastic)
AlN ceramic	300	0.24	4.5	150	∞
Solder	12.5	0.36	26	15	∞ and 22

Figure 1. *Model, boundary conditions, constituents, and their material properties.*

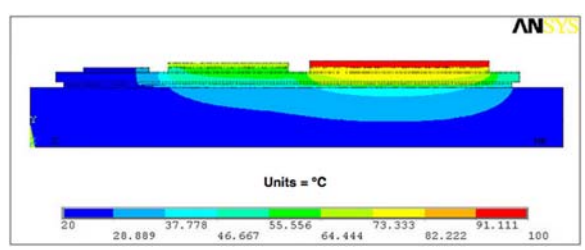

Figure 2. *Resulting temperature profile caused by the conditions shown in Fig. 1.*

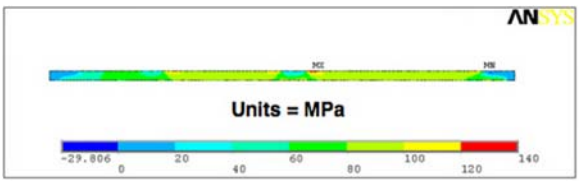

Figure 3. *First Principal stresses caused by the conditions shown in Figs. 1-2. Maximum is approximately 140 MPa.*

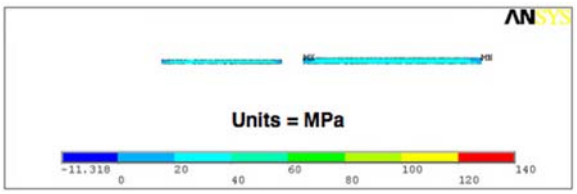

Figure 4. *First Principal stresses in the silicon diode and IGBT caused by the conditions outlined in Figs. 1-2. Maximum is approximately 40 MPa.*

An FEA model was constructed for a direct-cooled ceramic substrate (DCCS) concept. This analysis supported the APEEM program. The model is shown in Fig. 5, and one that is several generations beyond it has been filed for patent publication. The resulting thermal profile for the DCCS is shown in Fig. 6, and the resulting stress profiles are shown in Fig. 7. The stress profiles shown in Fig. 7 were combined with strength data for alumina and CARES/Life analysis, and the probability of survival was found to be greater than 99.999%. The DCCS could be of interest for use in hybrid vehicle inverters because it has the potential to substantially reduce both the volume and weight of the inverter. A prototype will be fabricated in FY09.

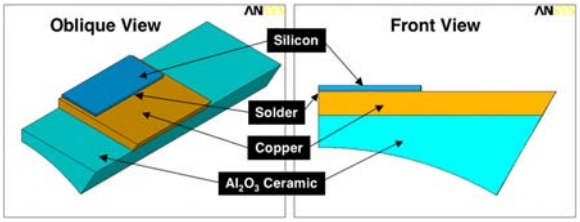

Figure 5. *Model of a direct-cooled ceramic substrate.*

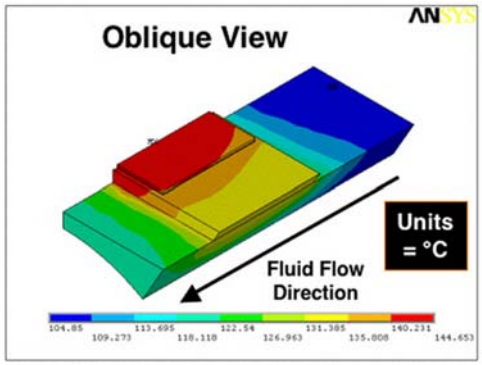

Figure 6. *Thermal profile resulting during service of the direct-cooled ceramic substrate shown in Fig. 5.*

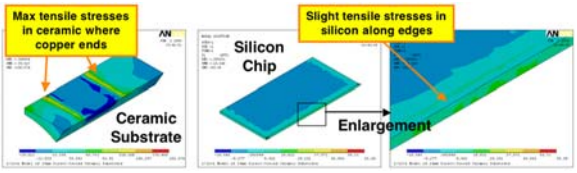

Figure 7. *First Principal stresses in the ceramic substrate and the silicon.*

Experimental

The strength of several candidate electronic ceramic substrates was measured for use in future probabilistic analysis. Aluminum nitride, aluminum oxide, boron nitride, silicon carbide, and silicon nitride substrates were acquired. Their biaxial flexure strength was measured using ball-on-ring testing using a 15 mm support ring and a 12.7 mm diameter ball. Specimen thicknesses ranged between 600-700 µm. The results are summarized in Table 8. The strength of the silicon nitride substrates was substantially higher than any of the other ceramics.

The measurement of strength of silicon and silicon carbide chips was initiated during FY08. Three tests types are under pursuit: anticlastic bending, uniaxial flexure, and biaxial flexure. The surfaces of these chips are finely polished so their strength is more dependent on the conditions of these edges. Therefore, these test method, and the fixture geometries that will be used with them, are designed to purposely cause fracture whose initiation is caused by edge-type strength-limiting flaws.

Material	Descriptor	Number of Specimens	Characteristic Equibiaxial Strength* (MPa)	Weibull Modulus
Aluminum Nitride	As Fired	15	665	33.0
Aluminum Nitride	Lapped	10	452	13.0
Aluminum Oxide	AD96	10	595	12.7
Aluminum Oxide	AD995	10	692	16.9
Boron Nitride		15	50	12.8
Silicon Carbide	Sintered Alpha	10	518	4.8
Silicon Nitride	SN460	15	1097	17.7

* Test Fixture: Ball on Ring (15mm Ring, 1/2" WC Ball, XHD=0.5 mm/min)

Figure 8. *Biaxial flexure strength results of candidate electronic ceramic substrates. Testing was conducted using a ball-on-ring fixture.*

Anticlastic bending was the first of the three methods pursued. An example of a semiconductor plate under anticlastic bending is shown in Fig. 9. Its loading initiates a sinusoidal profile of stress on all four of its edges, and examples of that are shown in Fig. 10. Silicon and silicon carbide chips of nominal dimensions of 10x10x0.25mm were tested, and the strength distributions for both are shown in Fig. 11. The characteristic strength of the silicon carbide was significantly higher than the silicon though the Weibull modulus was much smaller (i.e., the silicon carbide exhibited wider scatter). Uniaxial and biaxial flexure testing of these materials is now underway, and the strength-size-scaling of all three will be correlated based on edge-length scaling.

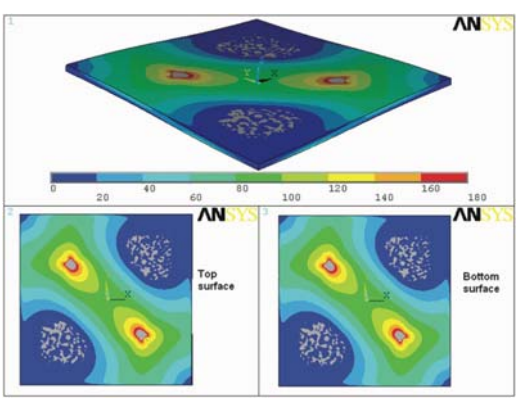

Figure 9. *First Principal stresses in an anticlastic bend specimen. This specimen is under use to measure the strength of semiconductor chips.*

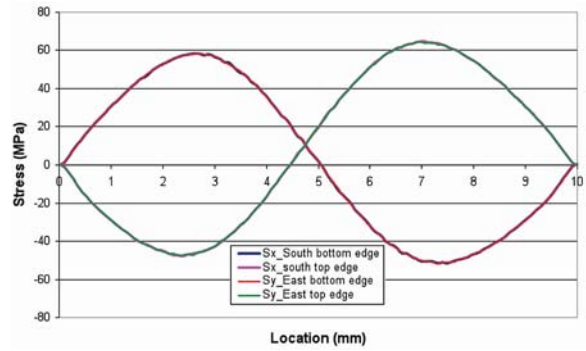

Figure 10. *Stress profiles along the edges of an anticlastic specimen. The tensile stresses cause fracture initiation.*

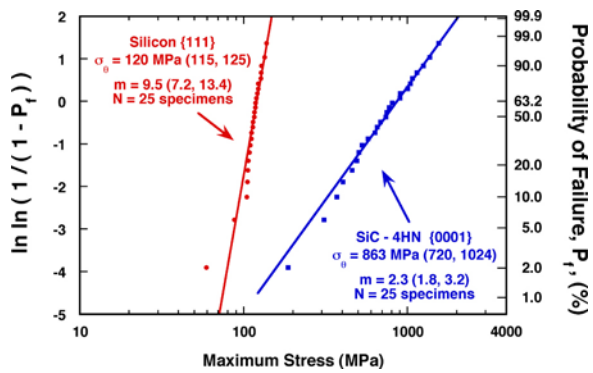

Figure 11. *Comparison of Weibull strength distributions for anticlastically fractured silicon and silicon carbide chips.*

Another effort that was initiated in FY08 was the consideration of high resistivity polycrystalline silicon carbide as an electronic ceramic substrate. Typically, polycrystalline silicon carbide is semi-conductive; however, two compositions developed by Saint-Gobain (Carborundum) back in the 1990s were claimed by the manufacturer to have electrically insulative character. Those two compositions (designated as ER08 and ER11) were acquired, and their electrical resistivity was measured as a function of frequency at room temperature. Those results are shown in Figs. 12-13. The ER11 electrical resistivity is as (desirably) large valued as aluminum nitride and aluminum oxide (two conventional substrate materials). The thermal conductivities and coefficients of thermal expansions (CTE) of the ER08 and ER11 silicon carbides were measured and were approximately 75 W/mK and 3.3 ppm/°C,

respectively. The relatively high thermal conductivity and low CTE make this material attractive as a candidate substrate material. Commercial viability will be explored in FY09.

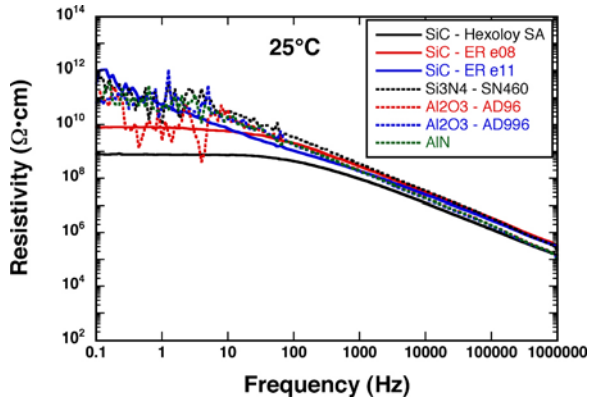

Figure 12. Room temperature *electrical resistivity of several ceramic materials as a function of frequency.*

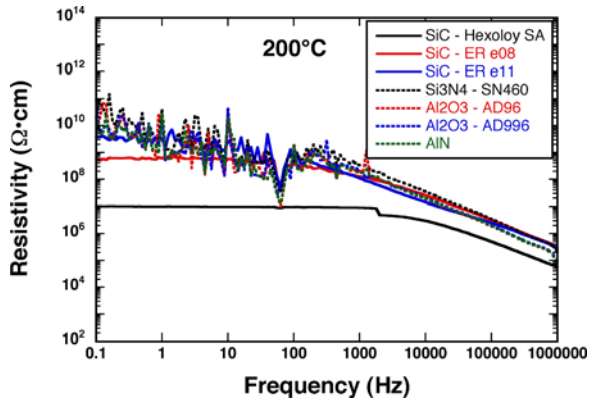

Figure 13. 200°C *electrical resistivity of several ceramic materials as a function of frequency.*

Conclusions

The thermomechanical stress state in an IGBT module was modeled, and the consideration of using alternative insulating ceramics in them started.

A direct-cooled ceramic substrate concept was developed that is applicable to power electronic devices. It will be able to reduce both weight and volume of inverters for hybrid vehicles. A patent for this was applied for.

The strength measurement of ceramic substrates occurred, and that for silicon and silicon carbide chips initiated. Test methods are under development to assess the effects of edge-type flaws on the strength of the silicon and silicon carbide chips.

Electrically insulating polycrystalline silicon carbide is under consideration as an electronic substrate.

Agreement 9537 - Graphite Foam for Cooling Power Electronics

Nidia C. Gallego
Oak Ridge National Laboratory
P.O. Box 2008, MS 6087, Bldg. 4508
Oak Ridge, TN 37831-6087
(865) 241-9459; fax: (865) 576-8424; e-mail: gallegonc@ornl.gov

Brian E. Thompson and Qijun Yu
Foam Application Technologies, Inc.
Mayaguez, Puerto Rico

DOE Technology Manager: Jerry L. Gibbs
(202) 586-1182; fax: (202) 586-1600; e-mail: jerry.gibbs@ee.doe.gov
ORNL Technical Advisor: David P. Stinton
(865) 574-4556; fax: (865) 241-0411; e-mail: stintondp@ornl.gov

---

Contractor: Oak Ridge National Laboratory, Oak Ridge, Tennessee
Prime Contract No.: DE-AC05-00OR22725

Objective

- Collaborate with an automotive partner to develop an optimized heat exchanger/heat sink design that best utilizes the heat transfer properties of graphite foam to significantly reduce the size and weight of the thermal management system.

Approach

- Study fundamental mechanisms of heat transfer in graphite foam and develop an engineering model that can be used to design and/or evaluate optimized thermal management systems using graphite foam.
- In collaboration with Koppers and ThermalCentric, evaluated alternative processing to develop new foams with tailored properties for various applications.

Accomplishments

- Utilized newly develop graphitic foams materials to design simpler, easier to implement, finned heat sinks.
- Demonstrated that finned heat sinks made with new graphitic foams, of same volume, matched the thermal performance of conventional finned heat sinks, but their weight is 10%, 20% or 30% of those made from stainless steel, copper or aluminum, respectively.
- Transferred the technology on graphite foam heat exchangers from ORNL to ThermalCentric, Inc. ThermalCentric, Inc. has formed a joint venture with Koppers (manufacturer of foam) to commercialize graphite foam heat exchangers

Future Direction

- Project was completed at the end of FY 2008.

Introduction

Porous graphite foam developed at Oak Ridge National Laboratory (ORNL)[1,2] is being investigated as a material to improve both single-phase and multiphase heat transfer. Graphite foam has a high effective conductivity (40–160 W/m K) because of the high material conductivity of the graphite material (800–1900 W/m K). In comparison, similar porous aluminum foams have effective conductivities of 2–26 W/m K, resulting from material conductivities of only 140–237 W/m K (for various aluminum alloys).[3] The high effective conductivity of the porous graphite foam combined with the open, interconnected pore structure facilitates high internal heat transfer and the potential for high convective heat transfer enhancement.

Our work in FY 2007 focused on designing, fabricating and testing a proof-of-concept thermal siphon utilizing graphite foam elements and it was carried out in collaboration with Thermal Centric. The experimental results showed that cooling rates of the proof-of-concept graphite foam-based thermal siphon improved by about 20% over conventional thermal siphons. The next phase of the research (during FY 2008) was going to be directed at quantifying the performance of the thermal siphon in an experimental HEV engine. However, after several discussion/planning meetings with personnel from the Power Electronics and Electrical Power Systems Research Center at the NTRC, ThermalCentric disclosed that they have, in partnership with Koppers (manufacturer of carbon foams) developed new foams with significantly different properties that could enable us to design simpler, more conventional-type heat sinks, easier to be incorporated into existing automotive systems. This disclosure from ThermalCentric, made us re-consider the focus of the work for the remainder of the year and redirected it, once again, towards finned heat sinks. Simultaneously, part of the effort was also directed towards understanding the oxidation behavior of graphite foam materials at high temperature in and oxidizing environment.

Background

In early FY 2008, ThermalCentric developed a new form of Graphitized Carbon Material (GCM) with significantly different properties than the ones previously considered. These new GCM's have lower porosity and permeability, ***but*** greater strength and bulk conductivity than previous, high-permeability foams. This new material opened the door to a new style of finned heat sinks.

Early measurements made by ThermalCentric showed that heat sinks and heat exchanger elements made from these new graphitized-carbon materials can match the thermal performance of conventional finned heat sinks made from metals (same volume), ***but*** can weigh 10%, 20% and 30% of those made from stainless steel, copper or aluminum, respectively. Estimates of the performance of finned heat sinks made from highly-conductive GCM have the potential to exceed the thermal performance of metal fins, but this needed to be investigated further.

Feedback from the automakers was that solutions to cooling HEV invertors need to be incorporated into existing systems. The use of evaporative cooling, although adequately effective, would require an addition thermal siphon circuit with motor, evaporator, condenser, and associated piping, and this would add complexity and cost, and decrease reliability of the vehicle. The simpler solution of a high-efficiency liquid-cooled heat sink that could be integrated into the water cooling system can be far more attractive to automakers than the thermal siphon. The combination of automaker feedback and the early results obtained by ThermalCentric resulted in refocusing the present research effort onto the new finned GCM heat sink.

Experimental and Results

Liquid Cooled GCM Heatsink

Figure 1 shows the new style of GCM heatsink with 0.017 inch fins between 0.060 inch gaps with their roots on a 0.039 inch base, along with the geometry of this heat sink. Figure 2 shows this heat sink compared to identical (same volume) heat sinks made from copper and aluminum.

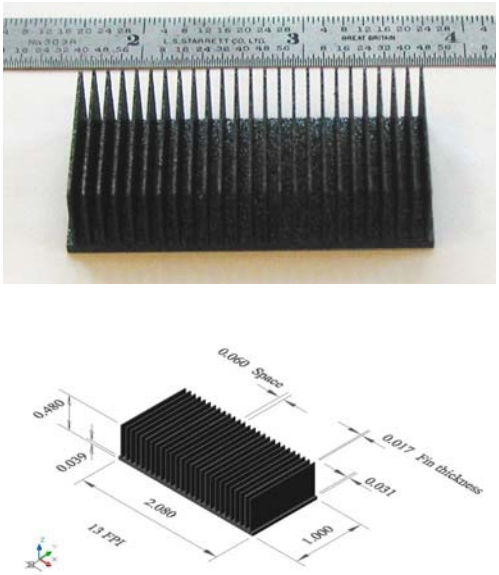

Figure 1. Graphitized Carbon Material (GCM) Heatsink made by ThermalCentric in collaboration with ORNL (dimensions in inches).

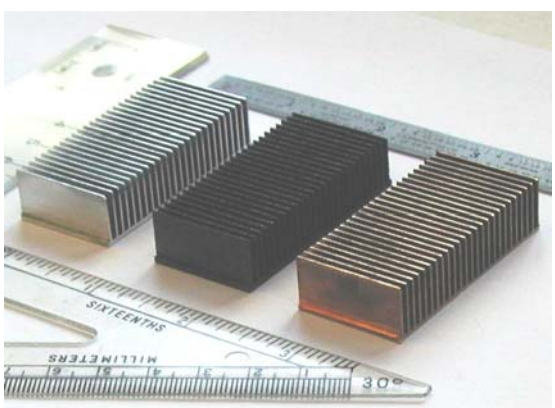

Figure 2. From left to right, aluminum, GCM and copper heat sinks of equivalent dimensions.

Figure 3 shows a schematic of the test section from the experimental set up utilized to study the performance of heat sinks. It consists of a channel made of garolite with a fluid inlet and outlet, a heating element, and fittings for instrumentation attaching on to measure the pressure drop, temperature across the test GCM specimen, and the base temperature of the heating element. The flow channel is 50.8 mm wide by 6 mm high. Test specimens are pressed into the test section of the channel. After assembly, the upper surface of the specimen is pressed firmly against the heating element and the lower surface is adjacent to a phenolic composite (garolite) to minimize heat loss. The whole outside surface of the test section are insulated with 4-in. thickness insulation to avoid heat loss.

The heating element consists of four cartridge heaters inserted into a 50.8 mm x 25.4 mm copper block which is pressed firmly against the test specimens during the experiments. The electrical power input to the heating element is adjusted by changing the power input voltage using a transformer, and the power input level is monitored using a voltmeter and an ammeter. The base plate temperature of the heater is measured using two type-K thermocouples with an accuracy of ± 0.8^{o}F, which are pressed into two holes that are drilled to within 2 mm of the heated surface located at 3 mm from the front and back edges of the heater. The air inlet and outlet temperatures are monitored using two type-K thermocouples with an accuracy of ± 0.8^{o}F, which are placed 20 mm up and downstream of the test specimen.

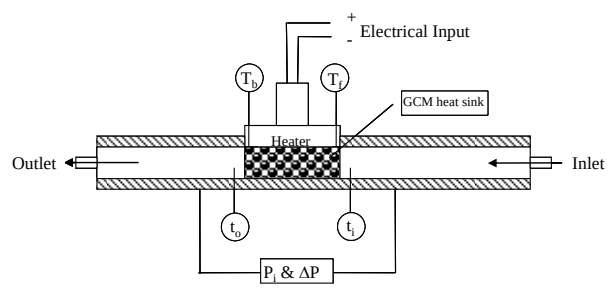

Figure 3. Schematic of experimental test section showing the position and orientation of the GCM element, the fluid inlet and outlet, the heat input, and the measurements.

Figure 4a shows the measured convective heat transfer coefficient versus friction coefficient that is the non-dimensional pressure drop. For this range of Reynolds numbers, all three heat sinks have nearly identical thermal performance however the comparison is a little skewed because GCM heatsinks with the fin efficiency would have fins that are four to five times longer because of the increased conductivity of the solid phase of the foam. Figure 4b shows a comparison of the specific heat transfer that is the heat transfer per unit mass, for the copper,

aluminum and GCM heatsinks shown in Figure 2. GCM heatsinks provide almost an order of magnitude increase in heat transfer per unit weight in this range of Reynolds number.

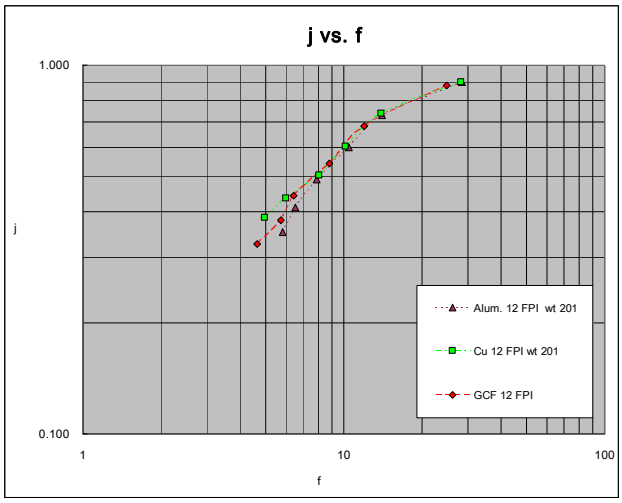

(a)

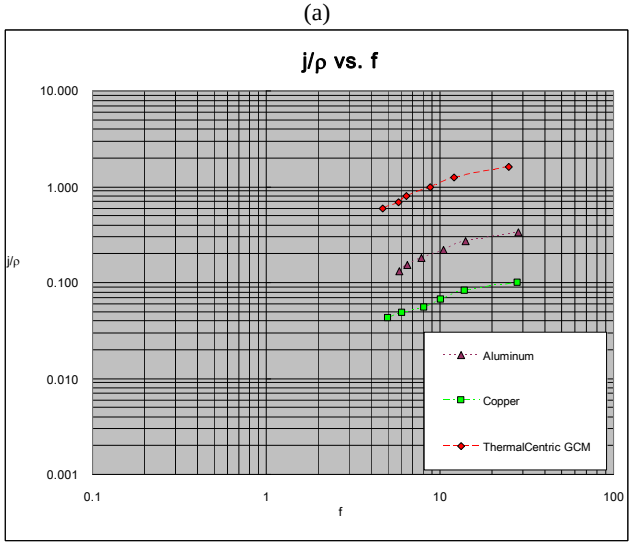

(b)

Figure 4. (a) Heat transfer coefficient, j; and (b) specific heat transfer coefficient, j/ρ versus friction factor (f) for aluminum, copper and GCM heat sinks.

Automotive Inverter Cooler

The goals of the Freedom Car program were used to calculate size and performance of a GCM heatsinks for cooling automotive power electronics. A SEMIKRON INVERTER dissipating 2kW with a surface heat flux of 137 Watts/cm^2 was cooled with 2.5 USGPM of water at 105°C and 35 psia. With a CGM heatsink of the style shown in Figure 1, outlet water inlet temperature was calculated to be 108.5^{o}C and the pressure drop was 13 psig. At the same thermal conditions when the heat surface temperature is 150°C, the heat dissipation will be 4500 W and the water pressure drop will be 13.4 psig. When the heat surface is 175°C the heat dissipation will be 7200 W and the water pressure drop will be 14 psig. Thermal resistance was calculated to be 0.010^{o}C/W which would be slightly better than with a complex jet impingement cooling technique, and about half that of a simple finned aluminum heat sink. This will make finned GCM heatsinks a better choice because of its simple implementation, superior performance, and significantly lighter weight.

OXIDATION STUDIES

Background

Exploring the oxidation behavior of graphitic foams at high temperatures is of importance in order to expand the range of applications of this material. For this study, we evaluated the oxidation behavior of three commercially available graphite foams from Koppers Inc.

Oxidation in air of graphite and manufactured carbon materials is controlled by chemical kinetics at low temperatures, but becomes diffusion-limited at high temperatures.[4,5] In the low temperature limit (regime 1) the oxidation rate depends on the concentration of oxidant in the gas phase and on the intrinsic material's reactivity, which in turn depends on the material's microstructure. As the temperature increases, oxidation rates become more sensitive to surface oxygen concentration (and thus to air flow conditions), and the mechanism shifts to in-pore diffusion control (regime 2). At even higher temperatures oxidation is strictly limited to the surface layer (regime 3) and is controlled by the mass transfer of gas species (O_2, CO, CO_2) through the boundary layer at the solid/gas interface. In this range, oxidation rates are not material-dependent and kinetic measurements were not deemed necessary.[6]

Experimental

Three graphitized foam materials provided by Koppers were characterized for this report, KFOAMS: D-1, L1300 and L1400. The test specimens were machined as right cylinders (1" high, 1" diameter). After machining, the specimens were

sonicated in alcohol in order to remove the dust from machining and were dried at 110°C in air. The size and weight of all specimens were measured and their density before oxidation was calculated, see Table 1 for their average properties.

Table 1: Density of test specimens

	Average Density (g/cm^3)
KFoam D1	0.441
KFoam L1400	0.377
KFoam L1300	0.296

The experimental setup consists of a three-zone vertical tube furnace (90 cm long) and an analytical balance with a weigh-below port feature. An inconel tube (7.30 cm outer diameter, 6.27 cm inner diameter, 150 cm long) placed inside the furnace extends on both ends. The balance (resolution 0.001 g) is placed on top of the vertical furnace, and is thermally shielded such that it operates at constant (room) temperature. The graphite foam specimens machined as cylinders, 2.54 cm diameter and 2.54 cm in height, are placed in a Pt wire basket hanging on a thin Pt wire from the weigh-below port of the balance. The specimens are positioned in the center of the constant temperature zone of the furnace (about 30 cm long). The sample temperature is measured by a K-type thermocouple placed inside the furnace, not touching it, but not more than 5 mm from the graphite sample. Inert gas (dry, oxygen-free nitrogen) or dry air is introduced from the bottom, passing through a 5 cm layer of silica gel beads for additional drying and mixing. The test samples are preheated and weight-stabilized (60 minutes) in a flow of dry nitrogen, after which the flow through the vertical tube is switched to dry air (10 L/min). The weight variations and sample temperature are recorded while maintaining the samples in the air flow at constant furnace temperature. The tests are terminated when the weight loss of the graphite specimens is 15 % of original weight.

Results: Oxidation kinetics

Figure 5 shows weight variations during oxidation of D-1, L-1300 and L-1400 at four different temperatures between 575 and 700°C. These are raw data as measured in the tests. The results were compared to two standard nuclear-grade graphites.

From the comparison, it is apparent that the oxidation rates of KFOAM materials and of nuclear-grade graphite are not very much different, although the density and the open porosity of the two types of materials are very different. KFOAMS have a very open structure, with low density (0.30 – 0.45 g/cm^3) and open porosity of 75-80%. In contrast, the nuclear-grade graphite materials selected for comparison have high density (1.78 – 1.82 g/cm^3) and low porosity (~ 5%). However, comparing the weight loss rates at (for example) 600°C it is seen that the time needed for 15% weight loss is not much different: 50 – 60 hours for KFOAMS and between 40 and 85 hours for the graphite materials selected for comparison.

Figure 6 shows Arrhenius plots (e.g. semi-logarithmic plots of oxidation rates in units of $\%.h^{-1}$ versus the reciprocal of absolute temperature) for the KFOAMS and the two nuclear graphites selected for comparison. At most temperatures, the rates of oxidation of the three KFOAMS materials are intermediate between the oxidation rates of the two high density graphites.

In the temperature range selected, the Arrhenius plots are linear for L-1300 and L-1400. However, the Arrhenius plot for D-1 breaks at 650°C; at higher temperatures the mechanism of oxidation of this material changes from chemical reaction control to in-pore diffusion control. The structure of D-1 foams is probably dominated by narrow or closed pores, which restrict the access of oxygen to the bulk of material. For this foam the oxidation rate increases gradually with the increase of weight loss, as shown by the continuously increasing slope of the weight loss curves in Fig. 5a. A similar effect is very often observed in oxidation of high density graphite, and is attributed to the gradual opening of closed pores in early stages of oxidation. In contrast, the oxidation rates of foams L-1300 and L-1400 materials is independent of the weight loss degree, as shown on the weight loss curves of Figs. 5b and 5c. Based on this observation it is concluded that the structure of L foams consists of open, interconnected pores, where the access of oxygen is fast and not limited by diffusion even at high temperatures.

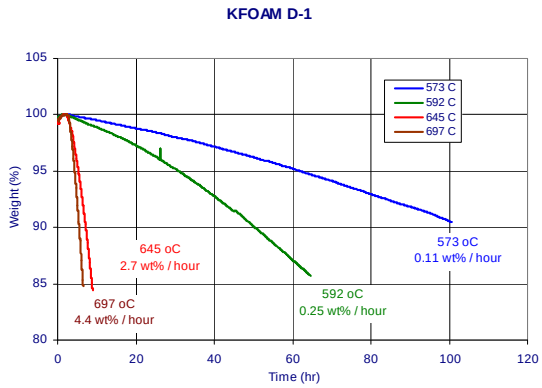

(a)

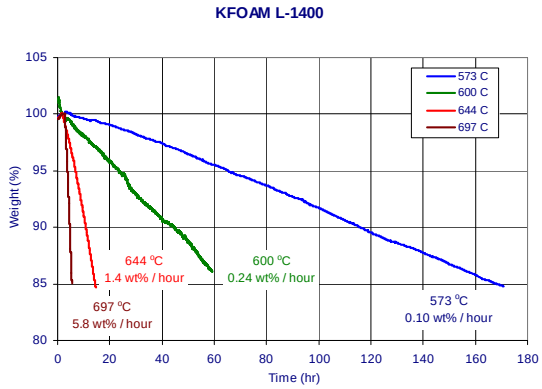

(b)

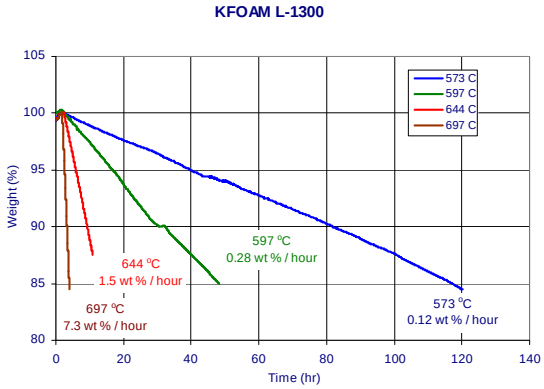

(c)

Figure 5: Weight loss curves on oxidation in air for (a) D1, (b) L1400, and (c) L1300 specimens.

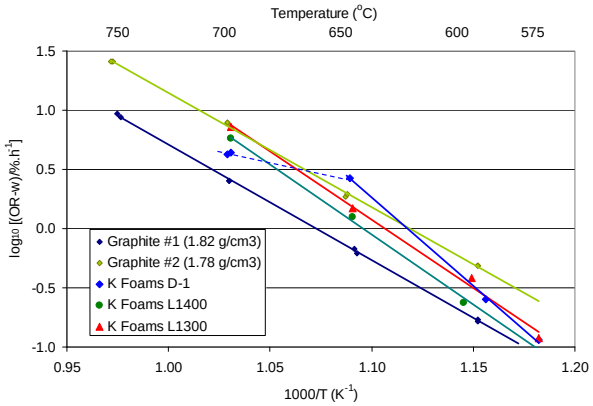

Figure 6: Arrhenius plots of oxidation rates in air of KFOAMS samples and of two high density graphite materials. The oxidation rates were normalized by the initial weight of specimens (units of % /hour).

References

1. W. J. Klett, R. Hardy, E. Romine, C. Walls, T. Burchell, "High-thermal-conductivity, Mesophase-pitch-derived Carbon Foam: Effect of Precursor on Structure and Properties," *Carbon* **38**, 953–973 (2000).
2. N. C. Gallego and W. J. Klett, "Carbon Foams for Thermal Management," *Carbon* **41**, 1461–1466 (2003).
3. W. J. Paek, H. B. Kang, Y. S. Kim, and M. J. Hyum, "Effective Thermal Conductivity and Permeability of Aluminum Foam Materials," *Int. J. of Thermophysics* **21**(2), 453–464 (2000).
4. T. J. Clark, R. E. Woodley, and D. R. de Halas, Gas-Graphite Systems, in "Nuclear Graphite", Ed. R. E. Nightingale, Acad. Press, New York (1962), p. 387
5. W. A. Propp, Graphite oxidation: Thermodynamics / Reactions, DOE/SNF/REP-018, Idaho National Engineering and Environmental Laboratory, September 1988.
6. R. Moormann, H. K. Hinssen, A.K Krussenberg, B. Stauch, and C. H. Wu, Investigation of oxidation resistance of carbon first-wall liner materials of fusion reactors, *J. Nucl. Mater.* **212-215** (1994) 1178-1182.

Publications/Presentations

Publications

K Sultan, CT DeGroot, AG Straatman, NC Gallego, H Hangan, "Thermal Characterization of porous graphitic foam – convection in impinging flow", *International Journal of Heat and Mass Transfer*, submitted.

Agreement 16305 - Solder Joint of High Performance Power Electronics: Materials-by-Design

G. Muralidharan, Jim Kiggans, and Andrew Kercher
Materials Science and Technology Division
(865)574-428; fax: (865) 574-4357; e-mail: muralidhargn@ornl.gov

Larry Seiber, and Burak Ozpineci
Engineering Science and Technology Division
(865) 241-4329; fax: (865) 574-9329; e-mail: ozpinecib@ornl.gov

DOE Technology Manager: Jerry L. Gibbs
(202) 586-1182; fax: (202) 586-1600; e-mail: jerry.gibbs@ee.doe.gov
ORNL Technical Advisor: David P. Stinton
(865) 574-4556; fax: (865) 241-0411; e-mail: stintondp@ornl.gov

---

Contractor: Oak Ridge National Laboratory, Oak Ridge, Tennessee
Prime Contract No.: DE-AC05-00OR22725

Objectives

- Evaluate the reliability of high temperature solders for use in power electronic packages subject to thermal cycling
- Identify material property characteristics that would impact long-term reliability of solder joints to enable materials-by-design approach

Approach

- Evaluate the degradation in solder joint properties due to thermal cycling
- Evaluate the effect of solder joint compositions and hence the mechanical and physical properties on solder joint property degradation.

Accomplishments

- Commercially available power diode module was tested using -65°C to 150°C thermal cycling and electrical properties of commercial power diode modules were found to be degraded after thermal cycling
- X-ray radiography showed a larger incidence of voids in packages whose electrical properties were degraded due to thermal cycling.
- Initial procedures for testing have been developed and a preliminary assessment of lifetime of existing packages exposed to high temperatures has been obtained

Future Direction

- Solder joints representing die attaches in power packages will be fabricated using solder compositions capable of 200°C operation
- Reliability testing of the solder joints will be carried out to understand microstructure and defect evolution

---

Introduction

Development of next generation hybrid and electric propulsion vehicles depend on the availability of high efficiency, lower cost, lower weight and lower volume, power electronic components and subsystems. These future power electronic systems need to operate reliably for 15 years at junction temperatures of 200°C in contrast to current maximum junction temperatures of about 125°C for such packages. Thus, there is a significant need to understand the effect of higher temperatures on power electronic components and subsystems.

Electronic packaging is a multidisciplinary technology which takes additional complications in power electronics due to the advanced thermal management that is required for packaging of such devices. Functions of an electronic package can be classified into a few categories:

1. Electrical interconnection (providing electrical path for power and signals)
2. Thermal interconnections (providing thermal path for the heat dissipated by the parts)
3. Electrical insulation (providing integrity of the electrical signals)
4. Environmental protection (providing protection of the parts and assembly from damage during handling and from the environment, especially moisture)
5. Mechanical support (providing mechanical support, rigidity, and ductility)

Typical packages used for devices consist of multiple elements. In designing a package for electronic devices to operate at high temperatures in harsh environmental conditions, a few important factors have to be considered:

1. Heat dissipation to keep the temperatures at safe operating levels.
2. Materials used must be stable at the higher temperatures and be able to maintain their properties during prolonged exposure to these temperatures and harsh environments
3. Thermal stresses caused by thermal expansion mismatches between the devices and various package elements including the substrate must be mitigated
4. Thermal shock resistance will be needed to withstand thermal cycling during service

Elements of a typical high-temperature package: Figure 1 shows a cross-section of a typical state-of-the-art packaging technology used for packaging SiC devices. Functions of several key elements are outlined below along with the materials requirements.

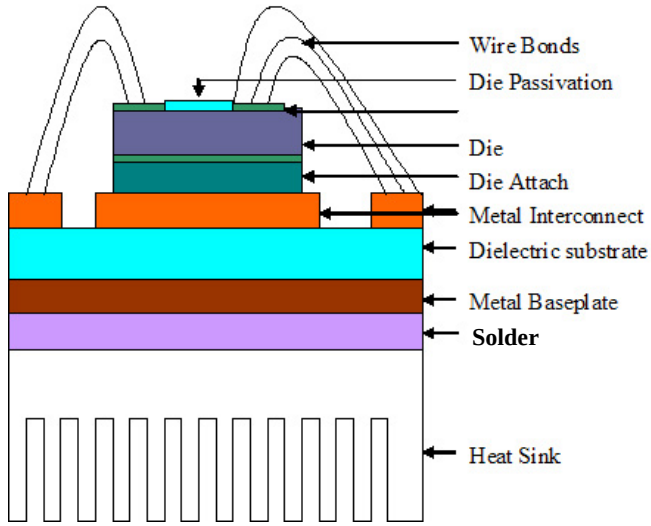

Figure 1. Schematic of a typical high temperature package

***Substrate*:** The key part of the package is the insulating dielectric substrate which has an electrically conductive metallization bonded to it on one surface. The insulating substrate can be either Al_2O_3 or AlN with the metallization layer being copper (as in Direct Bonded Copper (DBC)) or Au. Since SiC devices are designed to operate at high temperatures and high voltages, it is critical that the substrates remain thermally and mechanically stable, while retaining their dielectric properties to desired temperatures.

The metallization layer provides an electrical path between the multiple active and passive devices that may be bonded to the same substrate, and between the packaged devices and the external circuit. It is important that the metallization layer has good bonding with the substrate, retains its good electrical conductivity at high temperatures along with minimum tendency for the formation of intermetallic compounds. In addition, it is desirable that the metallization layer possesses good environmental resistance, and resistance to electromigration. As a rule of thumb, the melting temperature must at least be 1.5 times the operating temperature (in Kelvin) to prevent any diffusion related problems such as creep and electromigration.

Although the substrate is electrically insulating, it is desirable that its thermal conductivity be high to enable efficient dissipation of heat away from the SiC die. Hence AlN which has a higher thermal conductivity than Al_2O_3 is preferred from a thermal management perspective. Another important factor is the difference in the coefficient of thermal expansion between the device and the substrate. Larger differences in the coefficient of thermal expansions cause larger thermal stresses. Both Al_2O_3 and AlN have a thermal expansion coefficient that compares well with that of SiC.

Wire bonds: Electrical path from the device to the package is achieved through the use of one or more wire-bonds. These are typically aluminum wire bonds that are thermo-sonically bonded to the bond-pads on the device and to the metallization layer. Multiple wires are used for high current applications and to reduce stray inductance. It is known that wire-bonds are one of the weakest links within all the packaging elements.

***Die-attach*:** The device or die is mechanically bonded to the metallization layer through the use of a die attach. A die attach material should have the following properties:

1. Good adhesion with both the die and the substrate to that no debonding or delamination occurs
2. Self-resilience to provide good stress relaxation behavior so that the internal stresses are reduced to low levels
3. High thermal conductivity so that the heat dissipated from the power chip and the thermal expansion difference between the die and the substrate can be minimized
4. An appropriate processing temperature and good thermal stability to fit the typical process hierarchy
5. Good corrosion resistance
6. Good reworkability

Although organic materials have been used as die-attaches for packaging Si-based devices, these materials have limited applications in packages designed for temperatures of 200°C. Many different kinds of materials have been explored for potential use in die-attach applications. High melting point solders, such as gold-tin, gold-germanium; gold-indium, as well as Au-Ag-Si transient liquid phase bonding, gold thermo-compression bonding and thick-film materials have been considered in previous work. Thus, the choice of appropriate die-attach materials is critical in achieving desired operating temperatures and performance, including the reliability. Another important issue with the use of increased operating temperature is that devices will have to tolerate deeper thermal cycles. The stresses from mismatched coefficients of thermal expansion (CTE) increase with larger thermal cycles and so the potential for fatigue failure is greater with high-power devices. Since metallic brazes have a relatively large thermal expansion, there is a large expansion mismatch with the SiC device and the substrate (such as AlN, Al_2O_3, or Si_3N_4), thus generating large thermal stresses and hence resulting in premature failure during thermal cycling.

Since solder joints and wire bonds serve as pathways for electrical connection to and from electronic devices used in hybrid and electric vehicles, failure of these solder joints and wire bonds will result in catastrophic failures of critical electronic components and hence systems used in these automobiles. Thus, there is a significant need to study the failures of electronic packages induced by metallurgical changes of solder joints and wire bonds. The focus of this work is to understand factors related to the reliability of a die attach solder joint used in power packages and to help understand factors that affect the selection of the appropriate solder material for reliable high temperature operation.

Task 1. Evaluate the reliability of selected commercially available packages. This task will be accomplished through interactions with industrial partners actively involved in the fabrication of power packages. It should be noted that there are no power packages currently available commercially for use at temperatures of 200°C. Hence this part of the work will be performed on commercially available packages that can operate at the highest temperature currently feasible. The key concept behind this task is to understand the reliability of packages that are currently commercially available for high temperature use. This would establish a baseline to help compare the performance of alternate higher temperature solders in terms of expected lifetime. Since failures are induced in solder joints and other components by combination of temperatures, and stresses it is anticipated that reliability will be evaluated using steady state exposures to high temperatures and thermal cycling between temperature extremes as specified by JEDEC standards. Electrical properties will be measured as a function of thermal cycles to understand the impact of thermal cycling on electrical properties.

Task 2. Evaluate the reliability of joints prepared from selected high temperature solders. In this task, in collaboration with industrial partners, we will identify compositions of solders that have the potential to be used in a package capable of operating at a temperature of 200°C. Single solder joints will be fabricated and will be representative of die attach region in power packages. These joint will be subjected to steady state high temperature exposure and thermal cycling as in Task 1 to understand the evolution of microstructure and defects. The effect of solder melting temperature, and solder physical and mechanical properties on the lifetime observed during thermal cycling will be evaluated. This will eventually result in the identification of solder joint compositions and properties that will result in reliable high temperature packages. It should be noted that current reliability testing of plastic packages using JEDEC standards is limited to a high temperature of about 150°C. Standards to evaluate accelerated testing using thermal cycling representative of exposure to 200°C have not been established at this time. It is anticipated that knowledge gained from this work will assist in the establishment of such standards.

Task 3. Characterize microstructural evolution in solder joints subject to thermal cycling: Microstructural evolution occurs in solder joints during high temperature exposure. Coarsening of solder joint microstructures takes place during high temperature due to accelerated diffusion, and interdiffusion results in the formation of intermetallic compounds. Furthermore, combination of stresses and high temperatures results in creep deformation and combined creep/fatigue of solder joints resulting in the formation of voids. Characterization of microstructure of joints will be carried out using a combination of optical microscopy, x-ray radiography, ultrasonics and other techniques. Emphasis in this task is to understand the effect of high temperature exposure and thermal cycling on the evolution of defects and ultimately the failure of the functionality of the solder joint.

Extensive interaction with industrial partners will occur during all three tasks. Discussion with industrial partners is expected to help in the selection and fabrication of solder joints relevant to the industry. Results obtained in this work on the reliability data can be effectively transferred to industrial partners. It is anticipated that this work will ultimately help in the identification of appropriate solder joint compositions and fabrication of packages with optimum reliability.

Results

Reliability Testing

Based upon discussions with industrial partner, one commercially available power diode module was down-selected and acquired for thermal-cycling testing. Thermal cycling accelerates issues related to thermal expansion coefficient mismatches and shows potential locations of failures.

Figure 2 shows a commercially available 600V/100A diode module that was rated for operation at temperatures up to 150°C.

Figure 2. External image of a commercially available diode module rated for operation at temperatures up to 150°C

Figure 3 shows an internal view of the various components of the module. The diode module tested consists of 8 Silicon diode chips. Wire bonds connect the top of four dies to one terminal, the top sides of the other four dies to another terminal, and all the bottom sides of the dies are connected using solder joints to the third terminal. Solder joints are used to attach the terminal within the package.

One such module was subjected to several sets of thermal cycles between -65°C and 150°C as described in Table 1 below as per JEDEC standards and removed after each set of thermal cycles. The temperatures shown in the table were measured using a thermocouple attached to one of the external terminals of the diode modules to ensure that the temperature measured was that of

the part and not that of the air. Note that the highest temperature in these tests was 150°C, the maximum rated operating temperature of the diode module.

Figure 3. View of the internal construction of the diode module.

Table 1: Conditions of test for one diode module

Condition	Cycles
-65°C to 150°C, 1 min hold	10
-65°C to 150°C, 5 min hold	10
-65°C to 150°C, 5 min hold	10
-65°C to 150°C, 5 min hold	10
-65°C to 150°C, 5 min hold	10
-65°C to 150°C, 5 min hold	10
-65°C to 150°C, 5 min hold	30
-65°C to 150°C, 5 min hold	40
-65°C to 150°C, 5 min hold	40

Electrical Testing

After the conclusion of each set of the thermal cycles, the forward characteristics of the diode were tested to study any degradation in electrical properties. Figure 4 (a) shows an example of the forward characteristics obtained at the beginning of the sequence of the thermal cycles and Figure 4 (b) shows the forward characteristics obtained at the end of all cycles shown in Table 1. Note that the forward resistance of the diode increases as a result of the thermal cycling; this increase in resistance is likely to increase power dissipation and accelerate further degradation in its intended application. Furthermore, it is to be pointed out that the shape of the curve has been affected due to thermal cycling. Instead of a smooth curve, a "knee" has been developed in the curve modifying the diode characteristics. Further experiments are being carried out on other modules using the same testing protocol to understand the failure of other similar modules.

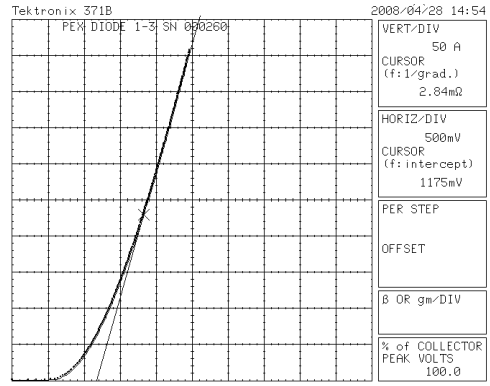

(a)

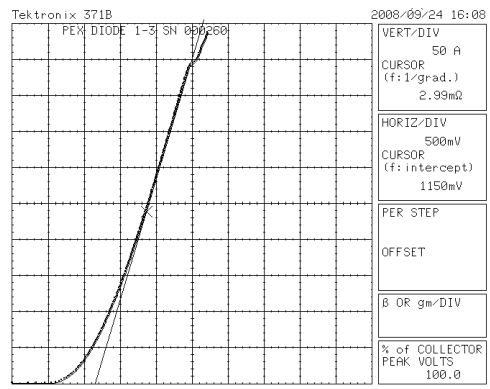

(b)

Figure 4. (a) Forward characteristics of one of the diodes in commercial diode module before thermal cycling and (b) Forward characteristics of the same diode in the commercial diode module after completion of cycling shown in Table 1. Note that the resistance has increased indicating that the properties of the electrical contacts are changing as a function of thermal cycling.

Characterization of Joints

X-ray radiography has been used for a study of the evolution of defects within the solder joints. Figure 5 shows an X-ray radiograph obtained from a decapped package (similar to that shown in Figure 3) to study the defects present in the solder joints in the initial as-received state and to understand the evolution of defects within the package. A larger number of voids are identifiable in the thermally cycled package which points to a potential failure mechanism. From Figure 5, it can be observed that some voids are present in the initial condition. Figure 6 shows an x-ray radiograph from a decapped package that was subject to thermal cycles shown in Table 1. Note the increased presence of voids indicated in the radiograph. These voids seem to be located underneath the silicon die (potentially within the solder joint) since electrical characteristics are affected. Furthermore, it was noted that the soldered connector bonded with a solder joint was very weakly bonded, which could be another location of failures. Further work will isolate the solder joints to observe the effect of thermal cycles.

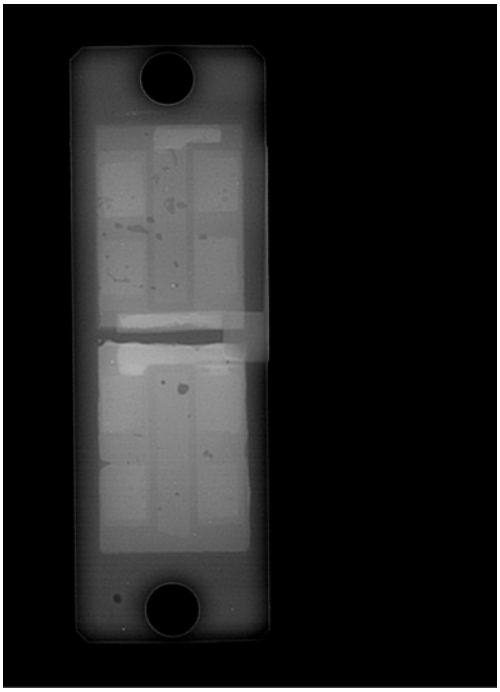

Figure 5. *X-ray image of a typical as-received package (decapped) to show the internals and initial void contents.*

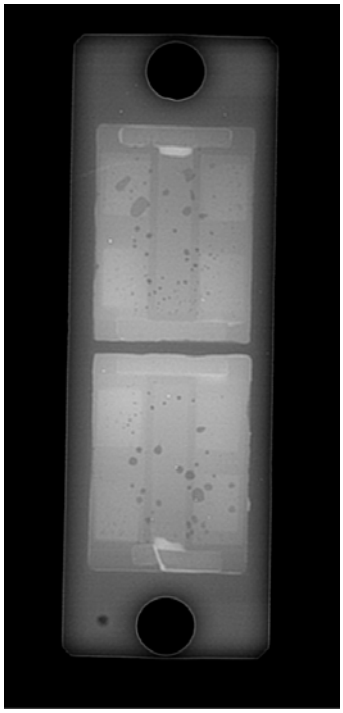

Figure 6. *X-ray image from a thermally cycled package discussed above. Note the increase in voids underneath the die and in other areas.*

Conclusions

- Commercially available power diode module packages were tested using -65°C to 150°C themal cycling
- Electrical properties of commercial power diode modules were found to be degraded after thermal cycling
- X-ray radiography showed a larger incidence of voids in packages whose electrical properties were degraded due to thermal cycling.

Publications/Presentations

None at this time

Agreement 16306 - Power Electronics Materials Compatibility

B.L Armstrong, D.F. Wilson, C.W. Ayers and S.J. Pawel
Oak Ridge National Laboratory
P.O. Box 2008, MS 6063, Bldg. 4515
Oak Ridge, TN 37831-6068
(865)241-5862; fax: (865) 574-4913; e-mail: armstrongbl@orn.gov

DOE Technology Manager: Jerry L. Gibbs
(202) 586-1182; fax: (202) 586-1600; e-mail: Jerry.gibbs@ee.doe.gov
ORNL Technical Advisor: D. Ray Johnson
(865) 576-6832; fax: (865) 574-6098; e-mail: johnsondr@ornl.gov

Contractor: Oak Ridge National Laboratory, Oak Ridge, Tennessee
Prime Contract No.: DE-AC05-00OR22725

Objectives

- Develop the methodology to map the materials compatibility space of power electronic materials in their operating environment.
- Validate the methodology for accelerated evaluation of power electronic devices.
- Populate a materials-coolant performance database.

Approach

- Establish methodology and build a test apparatus based on power pulsing an electronic component while it is immersed in coolant.
- Evaluate degradation mechanisms using analytical tools.

Accomplishments

- Developed accelerated testing methodology
- Built a test apparatus based on power pulsing an electronic component while immersed in coolant.
- Over 540,000 continuous pulse cycles have been completed.

Future Direction

- Refine methodology for accelerated testing.
- Evaluate additional coolant effects and begin development of a database indicating performance boundaries.

Introduction

The use of evaporative cooling for power electronics (PE) has grown significantly in recent years as power levels and related performance criteria have increased. As service temperature and pressure requirements are expanded, there is concern among the Original Equipment Manufacturers (OEMs) that the reliability of electrical devices will decrease due to degradation of the electronic materials that come in contact with the liquid refrigerants. Potential forms of degradation are expected to include corrosion of thin metallic conductors as well as physical/chemical deterioration of thin polymer materials and/or the interface properties at the junction between dissimilar materials in the assembled components.

Barriers to the deployment of new power electronic components in automotive applications include weight, size, reliability and cost. One approach to reduce the weight of the PE system is to use direct cooling from existing air conditioning systems using R134a refrigerant. This would reduce the weight of the power electronics system by eliminating the need for a separate cooling system. However, direct contact 2-phase cooling necessitates the evaluation of the PE compatibility with and reliability in the coolant. This project will develop the laboratory methodology to evaluate the degradation of power electronics materials by evaporative liquids. In addition, a database indicating performance boundaries for standard materials and for several candidate coolants will be established.

Results

Failure Mechanisms

An assessment was made of the possible failure mechanisms for PEs. There are many pathways/mechanisms in which direct contact of a PE with a coolant can cause degradation. General corrosion of the base elements (aluminum, nickel) can occur. The bonds between the aluminum and nickel may lead to galvanic corrosion. The thin polymeric materials in and at the interface of the PE may break down or decompose causing further reactions at PE surfaces. The operational pulsing of the PE will result in local temperature spikes at the metal surface and may cause nucleate boiling, which in turn, may degrade the wires or bonds of the wires to the board. Also, the temperature cycling may result in thermal fatigue. Low levels of impurities or contamination in the coolant may initiate or enhance corrosion. These impurities may be naturally occurring in the coolant or as a result of interaction with the coolant contamination materials (vessel walls, particulates from corrosion up or down stream in the coolant loop). Evaluation of these synergistic effects on the degradation is imperative. As degradation will occur over long time periods and OEMs are reticent to change designs or introduce new materials and coolants, an accelerated testing methodology is desired.

Methodology

A test methodology that involves pulsing of the PE circuit at appropriate power levels and exaggerated cycle times was developed. This approach allows for changes in power-on and power-off times. As such, it facilitates accelerated testing without changes in the failure mode(s) that would be observed in service. Further, the methodology allows for an evaluation of the effect of nucleate boiling on the failure mechanism(s).

Testing

Candidate power electronic components were obtained. For ease of failure mechanism evaluation, simplified circuits were designed and manufactured using commercial methods for this initial evaluation of the proposed methodology. Pre-exposure surface characterization of the circuits was performed. The typical appearance of the circuits is shown in Fig. 1. As shown, each circuit is composed of six wires, which are bonded to the board. The bonds all show uniform contact area and deformation associated with the bonding process.

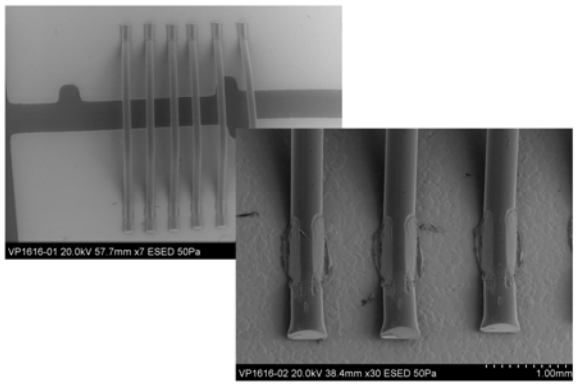

Figure 1. Scanning electron (SE) images of the typical appearance of six-wire test circuit. The bond regions show uniform contact area and deformation associated with the bonding process.

A laboratory test system, shown in Fig. 2, was designed and built. This apparatus allows for high current flow and shaping of the wave form. A square wave of one second on and one second off is driving 10 amperes through 0.4 mm (400 microns) diameter aluminum wire. The apparatus allows for condensation and recycle of the evaporated liquid, data recording and visual observation of the boards during testing. As of the writing of this report, two boards have been running for approximately 150 hours. This equates to about 540,000 cycles.

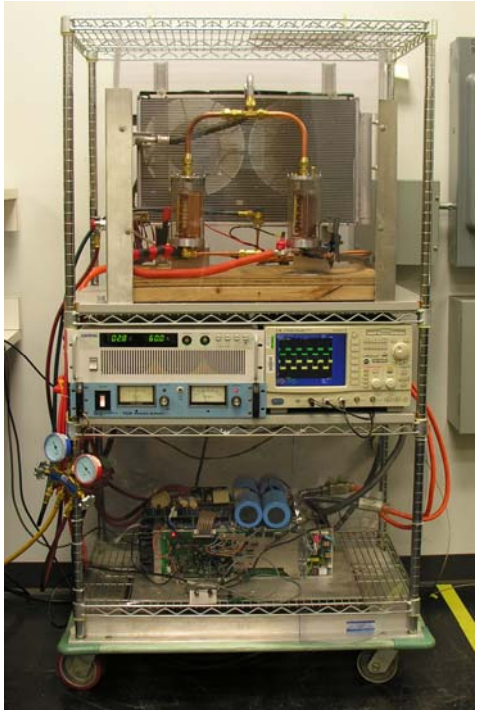

Figure 2. Two circuit boards are shown within their glass enclosures, which are in front of the condensing cooling radiator. Below this is shown the wave form shaping system and the high current power supply.

Conclusions

A testing methodology has been developed and an apparatus for implementing the methodology was designed, constructed, and is currently being operated. As the first testing cycle is on-going, no post-test surface evaluation has yet been performed and hence, no pre- and post test specimen surface comparisons is available. The absence of circuit failures demonstrates that the testing is being performed within the material/environment performance limits. In order to test the boundaries of the available operating space, the testing cycle will be made more aggressive. This will be performed for the second testing period and will involve either increasing the power through the circuits, increasing the power on time, increasing the power off time, or combinations of these approaches. Increasing the power on or power off time should increase the temperature range within which the specimen is being cycled.

Acknowledgements

The authors would like to thank Steven Campbell for all his work assembling the test apparatus.

Project 18517 – Combustion System Materials

Agreement 11752 – Materials for HCCI Engines

G. (Murali) Muralidharan, Rick Battiste, James Bentley, and Edward A. Kenik
Materials Science and Technology Division
(865)574-4281: fax: (865) 574-4357; e-mail: muralidhargn@ornl.gov

Bruce G. Bunting
Engineering Science and Technology Division
(865) 946-1512; fax: (865) 946-354; e-mail: buntingbg@ornl.gov

DOE Technology Manager: Jerry L. Gibbs
(202) 586-1182; fax: (202) 586-1600; e-mail: jerry.gibbs@ee.doe.gov
ORNL Technical Advisor: David P. Stinton
(865) 574-4556; fax: (865) 241-0411; e-mail: stintondp@ornl.gov

---

Contractor: Oak Ridge National Laboratory, Oak Ridge, Tennessee
Prime Contract No.: DE-AC05-00OR22725

Objectives

- Identify and catalog the materials operating conditions in homogeneous charge compression-ignition (HCCI) engines and use computational design concepts to develop advanced materials for such applications.
- Interact with designers of HCCI engines and manufacturers of components in order to identify the components that will be affected by the harsh operating conditions resulting from the HCCI design.

Approach

- Identify engine components, currently used materials, and current operating conditions and compare them with the expected component operating conditions for HCCI engines.
- Demonstrate the feasibility of the "materials-by-design" approach for the highest-priority item. Improve material performance for HCCI applications through computational modeling and experimental validation.

Accomplishments

- Fatigue properties of currently used Ni-based valve alloy material at 870°C were obtained through testing at ORNL and compared with that obtained from several other commercial Ni-based alloys.
- Results of fatigue tests have identified several alloys with fatigue properties better than the currently used alloy at 870°C
- Initial steps to developing improved alloys with appropriate price/performance ratio through modifications of existing alloys were initiated using computational thermodynamic modeling.

Future Direction

- Continue to communicate with automotive companies, valve manufacturers, Diesel Cross-Cut Team, FreedomCAR, and 21st Century Truck on the progress made through computational design.
- Promising new alloy/s with desirable fatigue properties and appropriate price/performance rations will be down-selected for testing in valve applications.

Introduction

There has been an increasing interest in HCCI combustion in recent years because of its potential to increase engine combustion efficiency and reduce emissions. However, the use of HCCI combustion will subject the engine components to significantly

higher temperatures and pressures. The temperatures for diesel engines will reach over 1600°F, and pressure may reach > 2000 psi, which is approximately four times that of the normal combustion engine. Such severe engine operating conditions will require a significant improvement in materials performance in order to take advantage of the HCCI engine concept. This project deals with identifying materials requirements for HCCI engines for automotive and truck applications and the development of advanced, yet cost-effective, materials through computational design.

"Materials-by-design" is an Oak Ridge National Laboratory (ORNL) concept that encompasses a collection of materials-related techniques including modeling, correlation, and materials modification. The premise behind materials-by-design is that mechanical properties are correlated to microstructure and phase chemistry. The phase composition and microstructure can be achieved through thermodynamic equilibrium or through non-equilibrium techniques such as quenching, rapid casting solidification, or mechanical working. These characteristics can then be correlated to desired mechanical properties through equilibrium thermodynamics or through a variety of correlation techniques. The correlations allow untested compositions or treatments to be modeled so that desired trends can be rapidly established. Small heats of targeted materials can then be processed to confirm the modeled properties and to broaden the correlation data base.

Finally, there are several techniques, such as magnetic processing or low-temperature carburizing, that can be applied to allow further modification and optimization of desired properties. Materials-by-design is ideally suited to cast materials and heavily thermally processed materials (e.g., stainless steels, Ni alloys, cast irons, alloy steels, and brazed wrought aluminum alloys), and the concept has been successfully applied in such diverse areas as high-temperature furnace components, exhaust valves, exhaust manifolds, and tube fittings. Figure 1 and Table 1 provide an outline of the materials-by-design approach and a summary of the techniques that can be applied.

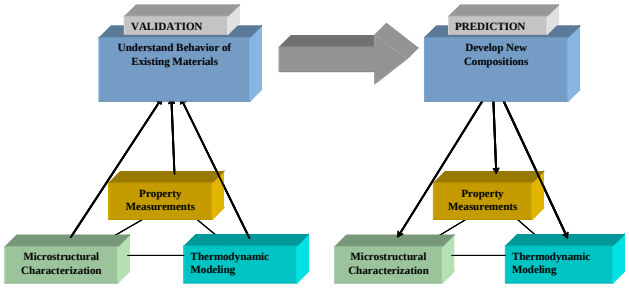

Figure 1. Overall approach for materials-by-design.

In our approach, we examined critical heavy-duty diesel engine materials and identified means to reduce their cost for acceptance in HCCI applications. This was accomplished through the following tasks:

Task 1. Identify critical material requirements for HCCI engines based on their operating conditions. This task will be accomplished through interactions with advanced engine and component designers. The interactions will include personal visits to six companies: Caterpillar, Cummins Engine, Deer, International Truck, Eaton Corp., and General Motors. Visits will be supplemented by a literature search, a review of advanced engine design studies, and follow-up discussions afterward. The key outcomes from this task will include (1) identifying operating conditions for advanced engine concepts, with a focus on the HCCI concept; (2) identifying components most affected by these operating conditions; (3) identifying currently used materials, new requirements, and performance targets; and (4) ranking the highest-priority items for study by the materials by design approach.

Task 2. Demonstrate the feasibility of materials-by-design approach for the highest-priority item. In this task, we will identify the details of the currently used material for the highest-priority item. Specifically, we will examine material compositions, processing methods, mechanical properties, corrosion properties, and cost.

Based on the available mechanical properties data, microstructural analysis, and thermodynamic phase stability calculations, we will identify the underlying mechanism that delivers the current properties.

Table 1. ORNL materials-by-design toolbox

Modeling	Experimentation	Characterization
Thermodynamic modeling of material properties vs alloy composition	Ultra-high-gauss magnetic stabilization of alloy steels	Advanced microscopy techniques
Neural-network modeling of diverse, nonlinear materials properties and process variations	Low-temperature gas carburization of finished components	X- ray and neutron scattering
Detailed microstructure based empirical modeling	Ability to produce small quantities of materials and fabricate them into test bars for property measurements and production of prototype components by a variety of methods, including sand and die casting, extrusion, forging and rolling	Surface and bulk property measuring techniques
Non-equilibrium modeling of solidified structures		
Extrapolation of properties from simple alloy systems to complex systems using interaction parameters		

Task 3. Improve materials performance for HCCI application through computational modeling and experimental validation. In this task, we will use computational modeling (key basis for the material-by-design concept) to identify compositions that will deliver the desired phases for two purposes: (1) improving property performance and (2) finding alternatives to reduce cost for both current and improved performance. The outcome of the analysis will be validated through experimentation. The validation will be carried out in the following steps:

1. Prepare compositions identified based on computational design in 1-lb heats for microstructural analysis and very limited property determination; compare the results with output based on computational analysis for validation.
2. Scale up the validated composition into 20-lb to 100-lb heats and cast them into ingots for processing trials. In most cases, the material is expected to be used in the wrought condition. However, if it is to be used in the cast condition, we will save part of the ingots for analysis of as-cast properties.
3. Subject cast ingots to processing steps that are currently used by industry. Develop optimum processing and heat-treatment conditions to obtain the desired microstructure.
4. Carry out microstructural analysis and mechanical properties analysis on the material processed and heat-treated with optimum conditions.
5. Prepare prototype components for HCCI engine tests.

Extensive interaction with industrial partners will occur during all three tasks. This collaboration is expected to result in the rapid transfer of materials improvement from this project to industry for use in HCCI and other advanced engine concepts.

Results

Materials Development through Computational Design

Ni-based alloys have been identified as potential candidates for improved valve materials. There is particular interest in increasing the operating temperature of exhaust valves to about 1600°F (870°C). High temperature fatigue strength has been identified as a critical factor in determining the performance of these alloys in the valve application. An evaluation of the microstructure of various Ni-based alloys and correlation with limited information on the fatigue properties that are available show that the volume fraction of the γ' phase is likely to be a dominant factor in determining the performance of these alloys at high temperatures. Since the size of the

strengthening precipitates is also critical, it is anticipated that the kinetics of coarsening this phase would also be influential in the long-term performance of the alloys in this application. Based upon discussions with various users and suppliers, a range of Ni-based alloys with potentially varying weight fractions (or volume fractions) of γ' have been identified in efforts to correlate the fatigue properties with the microstructure of the alloys. Table 2 shows a summary of these alloys and the compositions of specific heats procured for this study. IN 751 is the alloy currently used, and it has been added to the matrix as a reference.

To obtain initial information on the microstructures of these alloys at equilibrium, thermodynamic calculations have been carried out using JMatPro V4 for all the alloys shown in Table 2. Comparison of the results of the calculations shows that all alloys have a matrix of γ with the major strengthening phase as γ'. One or more carbide phases such as $M_{23}C_6$, MC, and M_7C_3 may also be present in different alloys. The primary difference between the microstructures of the various alloys is in the weight percent of the γ' phase at a given temperature and the highest temperature at which the γ' phase is stable in the different alloys. Figure 2 shows a summary of the amount of γ' and carbide phases present in the down-selected alloys.

Mechanical Property Measurement

In order to develop relationships between the microstructures of the alloys and their mechanical properties, high-temperature fatigue property data is being obtained on all down-selected alloys as a part of the project. Table 3 shows a summary of aging treatments used for the alloys being tested. Load-controlled, fully reversed fatigue tests are being conducted *in-situ* at a temperature of 870°C. Stresses of 21.8 (150) Ksi (MPa), 29 (200 MPa), 39.9 (275 MPa), 43.5(300 MPa), 50.8(350 MPa), and 54.4(375 MPa) have been used to investigate the fatigue performance of the alloys. Figure 3 compares the typical Stress vs Number of Cycles to failure curve (S-N) curve of IN751 and Waspaloy obtained during testing at 870°C. Note that Waspaloy has greater fatigue life at a given stress level than IN751. It should be recalled that thermodynamic calculations show a larger volume fraction of γ' to be present in Waspaloy when compared to that in IN751(see figure 2).

Microstructural Characterization

Microstructural characterization to evaluate the volume fraction of γ' present in the alloys and to study the average size of strenghtening precipitates present in the alloys is on-going. Scanning Electron Microscopy (SEM) is being used to evaluate the volume fraction of γ' present in the alloys using quantitative analyses, while Transmission Electron Microscopy (TEM) is used to study the sizes of precipitates present in the specimens. Both SEM and TEM work is being carried out on material obtained from fatigue specimens subjected to exposure at 870°C. Figure 4 shows a typical TEM image from a Nimonic 90 specimen tested at 870°C with failure occurring after a total time of exposure of 226 hours. Image analysis was performed on the micrograph to obtain average dimensions of the precipitates. Results from this image reveal an average size of about 142 nm (0.142 μm). Similar analyses is being performed on other alloys to understand the coarsening occurring during fatigue testing of the alloys.

Table 2. Compositions of various alloys selected for studying the correlation between microstructure and mechanical properties

Alloy	C	Si	Mn	Al	Co	Cr	Cu	Fe	Mo	Nb	Ni	Ta	Ti	W	Zr
X750	0.03	0.09	0.08	0.68	0.04	15.7	0.08	8.03	–	0.86	Bal	0.01	2.56	–	–
Nimonic 80A	0.08	0.1	0.06	1.44	0.05	19.6	0.03	0.53	–	–	Bal	–	2.53	–	–
IN 751	0.03	0.09	0.08	1.2	0.04	15.7	0.08	8.03	–	0.86	Bal	0.01	2.56	–	–
Nimonic 90	0.07	0.18	0.07	1.4	16.1	19.4	0.04	0.51	0.09	0.02	Bal	–	2.4	–	0.07
Waspaloy	0.03	0.03	0.03	1.28	12.5	19.3	0.02	1.56	4.2	–	Bal	–	2.97	–	0.05
Rene 41	0.06	0.01	0.01	1.6	10.6	18.4	0.01	0.2	9.9	–	Bal	–	3.2	–	–
Udimet 520	0.04	0.05	0.01	2.0	11.7	18.6	0.01	0.59	6.35	–	Bal	–	3.0		
Udimet 720	0.01	0.01	0.01	2.5	14.8	15.9	0.01	0.12	3.0	0.01	Bal	–	5.14	1.23	0.03

Table 3. Summary of alloys and heat-treatment conditions used in the study	
Alloy	**Heat-treatment**
X750	2100°F/ 2 h/ Air Cool, 1550°F/ 24 h/ Air Cool, 1300°F/ 20 h/Air cool
Nimonic 80A	1292°F/16 h/ Air cool
Inconel 751	1600°F/4 h/Air cool, 1350°F/4 h/Air Cool.
Nimonic 90	1292°F/16 h/Air cool
Waspaloy	1544°F/4 h/Air Cool, 1400°F/16 h/Air Cool
Udimet 41	1400°F/16 h/ Air cool
Udimet 520	2050°F/ 4 h/Air cool, 1550°F/ 24 h/Air cool, 1400°F/16 h/Air cool 1500°F/8 h/ Air cool
Udimet 720	2012°F/4 h/Furnace cool, 1202°F/4 h/Air cool, 1400°F/16 h/Air cool (As-received)

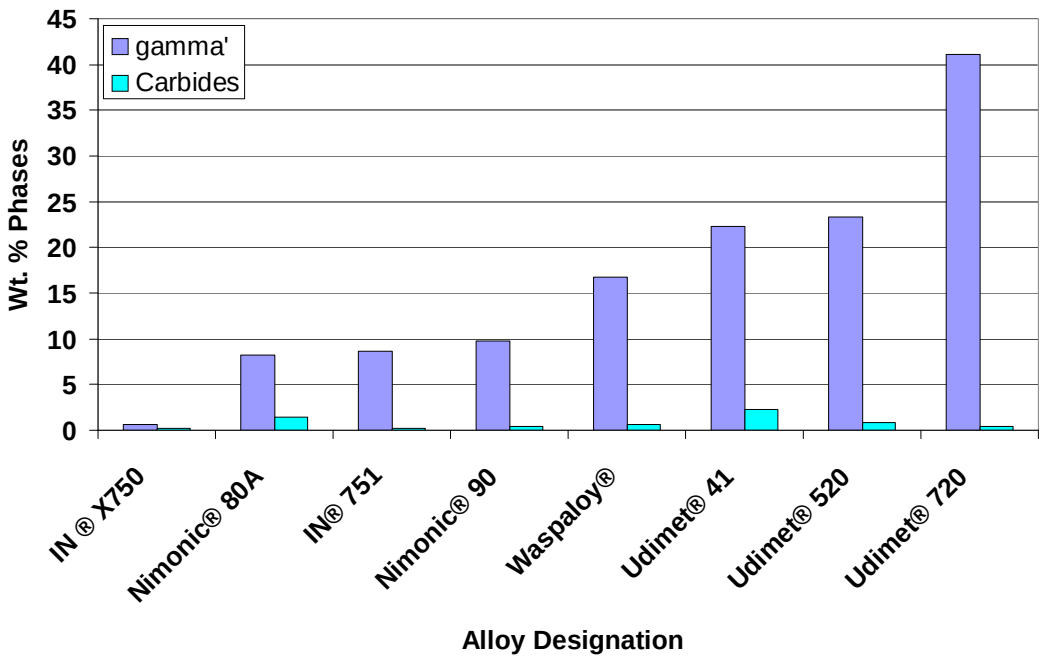

Figure 2. *Variation in wt. % of γ' and carbides at 870°C in the various alloys used in the study.*

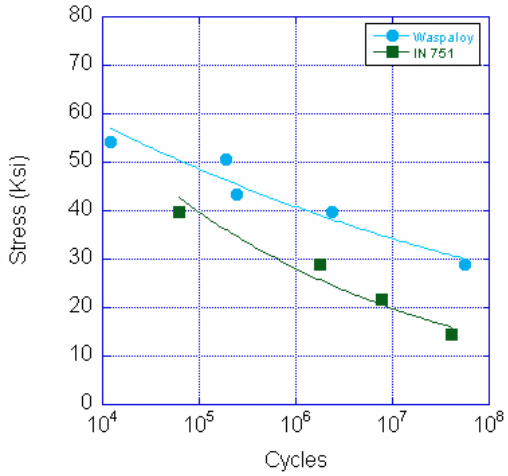

Figure 3. *Typical Stress vs. Number of Cycles to Failure (S-N) curve for Waspaloy and IN751 obtained at 870°C.*

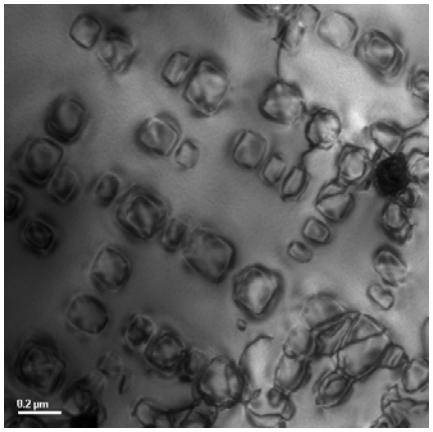

Figure 4. *Transmission Electron Microscope Image Obtained from Nimonic 90 Specimen after226 hours of Exposure at 870°C. Particle Size Analysis Showed an Average Particle Width of 0.142 µm.*

Development of Improved Alloys through Computational Modeling

Based upon the fatigue properties measured in the down-selected alloys, several alloys with desired fatigue properties have been identified whose compositions can be used to guide the development of improved alloys. Computational thermodynamics is now being used to identify other alloys with compositions that will result in similar amount of strengthening phases. Alternate alloy/s with the potential for use in valves will be down-selected for further component scale testing

Conclusions

- Detailed fatigue property obtained from several Ni-based alloys has helped identify compositions with fatigue properties better than currently used alloys
- SEM and TEM work has been used to quantify the volume fraction and size of strengthening phases in existing alloys
- Computational thermodynamics models are being used to seek alternate compositions of advanced alloys using existing alloys with desired properties as an initial guide to development

Publications/Presentations

S. K. Eswaramoorthy, James M. Howe, and G. Muralidharan, "Determining the Nanoscale Chemistry and Behavior of Solid-Liquid Systems," **Science**, 2007, Vol. 318, p.1437.

Agreement 8697 - NO_x Sensor Development

Leta Y. Woo, and Robert S. Glass
Lawrence Livermore National Laboratory
P.O. Box 808, L-367
Livermore, CA 94551-9900
(925) 423-7140; fax: (925) (422-5844); e-mail: glass3@llnl.gov

DOE Technology Manager: Jerry L. Gibbs
(202) 586-1182; fax: (202) 586-1600; e-mail: jerry.gibbs@ee.doe.gov

---

Contractor: Lawrence Livermore National Laboratory, Livermore, California
Prime Contract No.: W-7405-Eng-48

Objectives

- Develop an inexpensive, rapid-response, high-sensitivity and selective electrochemical sensor for oxides of nitrogen for compression-ignition, direct-injection (CIDI) exhaust gas monitoring
- Explore and characterize novel, effective sensing methodologies based on impedance measurements
- Explore designs and manufacturing methods that could be compatible with mass fabrication
- Effectively collaborate with industry so that the technology can (ultimately) be transferred to a supplier and commercialized

Approach

- Use an ionic (O^{2-}) conducting ceramic as a solid electrolyte and metal or metal-oxide electrodes
- Correlate NO_x concentration with changes in impedance by measuring the cell response to an ac signal
- Evaluate sensing mechanisms using electrochemical techniques
- Characterize aging mechanisms and the effects on long-term performance of candidate sensor materials
- Understand and develop methodology to eliminate interferences
- Collaborate with the Ford Research Center to optimize sensor materials, operating parameters, and performance and perform dynamometer on-vehicle testing

Accomplishments

- Characterized sensing mechanisms responsible for impedancemetric NO_x sensing
- Improved sensor design by incorporating an alumina heated substrate which then allowed the development of an advanced prototype sensor that was packaged into a commercial oxygen sensor housing
- Successfully performed engine dynamometer testing on prototype sensors at Ford facilities demonstrating comparable performance with the only commercially-available NO_x sensor (but that does not meet cost, sensitivity, response time, and system architecture goals)
- Published two journal articles, presented a talk at the 32nd International Conference & Exposition on Advanced Ceramics and Composites, and gave an oral presentation to USCAR during their visit to LLNL in April

Future Direction

- Develop advanced prototypes using processes suitable for cost-effective, mass manufacturing
- Evaluate performance of prototypes, including long-term stability and cross-sensitivity, in laboratory, dynamometer, and on-vehicle tests
- Initiate the technology transfer process to a commercial entity

Introduction

Increasingly stringent emissions regulations will require the development of advanced gas sensors for a variety of applications. For example, compact, inexpensive sensors are needed for detection of regulated pollutants, including hydrocarbons (HCs), CO, and NO_x, in automotive exhaust. Of particular importance will be a sensor for NO_x to ensure the proper operation of the catalyst system in the next generation of diesel (CIDI) automobiles.

Because many emerging applications, particularly monitoring of automotive exhaust, involve operation in harsh, high-temperature environments, robust ceramic-oxide-based electrochemical sensors are a promising technology. Sensors using yttria-stabilized zirconia (YSZ) as an oxygen-ion-conducting electrolyte have been widely reported for both amperometric and potentiometric modes of operation.[1,2] These include the well-known exhaust gas oxygen (EGO) sensor.

More recently, ac impedance-based (i.e., impedancemetric) sensing techniques using YSZ have been reported for sensing water vapor, hydrocarbons, CO, and NO_x.[3-6] Typically small-amplitude alternating signal is applied, and the sensor response is measured at a specified frequency. Most impedancemetric techniques have used the modulus (or magnitude) at low frequencies (< 1 Hz) as the sensing signal and attribute the measured response to interfacial phenomena.[3-5] Work by our group has also investigated using phase angle as the sensing signal at somewhat higher frequencies (10 Hz).[6,7] The higher frequency measurements would potentially allow for reduced sampling times during sensor operation.

Another potential advantage of impedancemetric NO_x sensing is the similarity in response to NO and NO_2 (i.e., total-NO_x sensing).[3,4,6,7] Potentiometric NO_x sensors typically show higher sensitivity to NO_2 than NO, and responses that are opposite in sign. However, NO is more stable than NO_2 at temperatures > 600°C, and thermodynamic calculations predict ~90% NO, balance NO_2.[8] Since automotive exhaust sensors will probably be required to operate at temperatures > 600°C, NO is the dominant component in thermodynamic equilibrium and the target NO_x species. Also, the use of upstream catalysts could further promote the conversion of NO_x species to NO. Therefore, the focus of current work is to investigate the response to NO. Nevertheless, minimizing the sensitivity to a variety of competing species is important in order to obtain the accuracy necessary for achieving the emission limits.

Mitigating the effect of interfering gases (e.g., O_2, water vapor, HCs, etc.) is an area of current study. For impedancemetric NO_x sensors, our previous work has demonstrated that the cross-sensitivity to O_2 may be accounted for by comparing measurements at multiple frequencies.[6] Other strategies for compensation are also being explored, including calibration using data from existing sensors located nearby.

Our current work has made significant advances in terms of developing prototype sensors more suitable for commercialization. Also, dynamometer testing has provided real-world sensor performance data that will be useful in approaching potential suppliers to whom we can transfer the technology for commercialization. The advances are a direct result of understanding the sensing mechanisms responsible for impedance-based NO_x sensing and the effect of materials choice and sensor design/geometry.

Background

Previously, we reported the impedance response of a symmetric Au/YSZ/Au cell to O_2 and NO_x.[7] Both electrodes were exposed to the same gaseous environment (i.e., no reference gas) and constant spring-loaded pressure was used to maintain contact between cell components. For real-world sensor applications, spring-loaded devices are obviously

not practical. Nevertheless, the early prototypes were used to initially explore the impedancemetric sensing mechanisms, which resulted in improvements to the sensor design and a platform that did not require spring-loaded pressure.

Impedance-based sensing requires that at least one of the two electrodes act as the "sensing" electrode and provides flexibility in sensor design, which can be either symmetric or asymmetric. Both the electrode composition and microstructure were shown to alter sensitivity, and general criteria for appropriate electrode materials were developed.[9]

Since sensitivity was found to rely on parallel contributions from the NO_x and O_2 reactions occurring at the electrode/electrolyte interface, the rate-determining step for the O_2 reaction needs to be controlled to yield the desired sensitivity to NO_x. In this regard, we have found that the parameters we have under our control are composition and microstructure .[9] NO_x sensitivity relies on electrodes with low catalytic activity towards oxygen, which can be obtained by creating a dense microstructure and choosing compositions that have limited interaction with oxygen.

Figure 1 illustrates the impedancemetric NO_x sensing mechanisms using simplified steps for the electrochemical redox reactions. The actual redox reactions likely involve a much more complex series of steps (e.g., adsorption of gas species, transport along surfaces, electron transfer, diffusion of products away from reaction sites, etc.). Nevertheless, the illustration provides a summary of the important mechanisms involved.

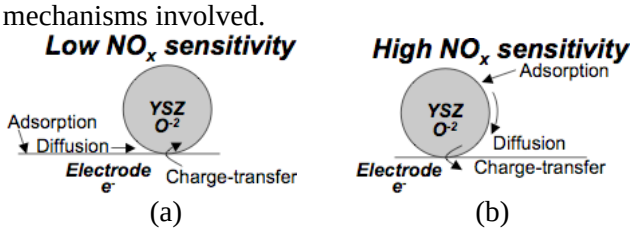

(a) (b)

Figure 1. Illustration of simplified steps involved in impedancemetric NO_x sensing for (a) low NO_x sensitivity and (b) high NO_x sensitivity.

In the case of low NO_x sensitivity (Fig. 1a), processes proceed on electrodes with better oxygen catalytic activity so that the oxygen reaction rate dominates and controls the response; changes associated with variations in much lower concentration levels of NO_x are unable to be resolved. For high NO_x sensitivity (Fig. 1b), due to the poor oxygen catalytic activity of the electrode, processes can proceed on the electrolyte so that the NO_x reactions are able to compete with those of oxygen, and variation in ppm levels of NO_x can be resolved.

A number of materials potentially meet the sensing criteria, including gold and electronically conducting oxides. The current work builds on the previous findings by focusing on two different material systems and incorporating sensor designs more suitable for commercialization.

Experimental

Two different sensor prototypes were investigated. The first prototype was built on a dense alumina substrate (10 mm × 10 mm × 0.5 mm). Platinum paste was applied to the substrate and fired at 1200°C. Yttria-stabilized zirconia (YSZ) slurry was then applied on top of the fired Pt. Gold wire was tightly wrapped around the prototype and additional YSZ slurry was applied on top of the wires

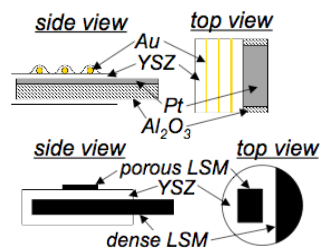

(a) (b)

Figure 2. Schematic of NO_x prototype sensors based on (a) Pt/YSZ/Au cell and (b) LSM_{dense}/YSZ/LSM_{porous} cell.

and fired at 1000°C. Figure 2a shows a schematic of the Pt/YSZ/Au cell prototype.

The second prototype was built using a dense electronically conducting oxide substrate, strontium-doped lanthanum manganite (LSM). A dense pellet was prepared with commercial (Praxair) nominal $(La_{0.85}Sr_{0.15})_{0.98}Mn$ oxide powder by pressing in a uniaxial die and sintering at 1250°C. YSZ slurry was applied on top of the dense LSM, followed by LSM slurry, and fired at 1000°C. Fig. 2b shows a schematic of the LSM_{dense}/YSZ/LSM_{porous} cell prototype.

Gas sensing experiments were performed in a quartz tube placed inside a tube furnace with both electrodes exposed to the same environment. Gas composition was controlled in laboratory testing by mixing air, N_2, and a 1000 ppm NO/NO_2 feed using a standard gas handling system equipped with thermal mass flow controllers. Electrochemical measurements were performed using a Solartron 1260

Impedance Analyzer with a Solartron 1287 Electrochemical Interface.

Dynamometer testing of actual diesel exhaust was performed at Ford Research Center using an engine test cell fitted with a urea-based selective catalytic reduction (SCR) system for reducing NO_x emissions. Data were obtained using a constant engine speed, and the exhaust gas composition was altered using variations in the frequency of urea injection in the SCR system and the percent throttle. The exhaust gas composition, including CH_4, NO, NO_2, NH_3, CO, CO_2, and H_2O, was determined using Fourier Transform Infrared (FTIR) spectroscopy, and O_2 concentration was determined using a paramagnetic oxygen analyzer. The test setup also included a commercially available NO_x sensor located downstream of the prototype. Electrochemical measurements were performed using a stand-alone Solartron 1260 Impedance Analyzer.

Results and Discussion

Sensing Behavior of Prototypes

The Pt/YSZ/Au prototype is a significant improvement over previous sensor platforms by incorporating an alumina substrate. A commercializable sensor platform will need to include a heated substrate, which typically consists of an alumina substrate with Pt resistive heating elements. Figure 3 shows the impedancemetric sensing behavior for the Pt/YSZ/Au prototype at 650°C in laboratory testing. The sensing signal is the phase angle response of the cell to a 25 mV ac signal at 10 Hz.

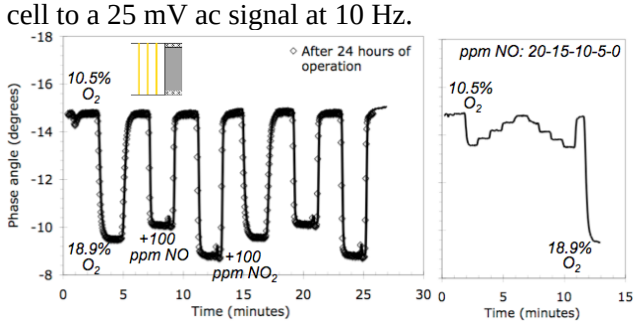

(a) (b)

Figure 3. Sensing behavior of Pt/YSZ/Au prototype at 650°C with changes in oxygen concentration and (a) 100 ppm additions of either NO or NO_2 or (b) response to step changes of 5 ppm NO up to 20 ppm. The sensing signal shown is the phase angle response of the cell to a 25 mV ac signal at 10 Hz.

In Fig. 3a, the background oxygen concentration was initially 10.5%, was then stepped to 18.9%, and the sensor response then recorded upon introduction of alternating concentrations of 100 ppm of NO and NO_2. For all changes in gas concentration, the sensor responds quickly and recovers quickly to the original baseline value (< 10 sec). Furthermore, introducing 100 ppm NO or NO_2 produces a similar type response to changing the oxygen concentration by 8.4%, which demonstrates that the sensor is much more sensitive to NO_x than oxygen. Also, in Fig. 3a the open data points represent data taken after 24 hours of operation, which agree well with the original data (shown as the solid line) and demonstrate sensor stability.

In impedancemetric sensing, NO and NO_2 have similar directional responses, which is an advantage over typical potentiometric sensors where NO and NO_2 have opposite signals that cancel. For the prototype shown in Fig. 3, the response to NO_2 is slightly larger than the response to NO, and will be discussed in further detail below. Also, in Fig. 3b, the Pt/YSZ/Au prototype response is shown for 5 ppm changes up to 20 ppm. The high-sensitivity prototype sensor clearly resolves 5 ppm changes in NO (that is, the sensitivity of the sensor is in the ppm range).

The LSM_{dense}/YSZ/LSM_{porous} prototype is also an improvement over previous sensor designs because it demonstrated impedancemetric NO_x sensing using only high-temperature, potentially more stable materials. For a commercializable sensor platform, a single high-temperature co-firing process is desirable to minimize manufacturing costs. Furthermore, a platform that only utilizes high-temperature ceramics with similar thermal expansion coefficients should improve long-term thermal stability and resist degradation by thermal cycling.

Figure 4 shows the impedancemetric sensing behavior for the LSM_{dense}/YSZ/LSM_{porous} prototype at 575°C in laboratory testing, using the same testing protocol shown in Fig. 3 and discussed above for the Pt/YSZ/Au prototype. The LSM prototype operated at 575°C has similar NO_x sensitivity to the Pt/YSZ/Au prototype operated at 650°C, as shown in Figs. 4a and 4b, and a lower sensitivity to oxygen.

The similarity in NO_x response for the two prototypes using different materials emphasizes that impedancemetric NO_x sensing is not restricted to a specific electrode material. Therefore, we can consider a variety of materials; however, microstructures, aging effects, sensor designs, and other considerations are still important.

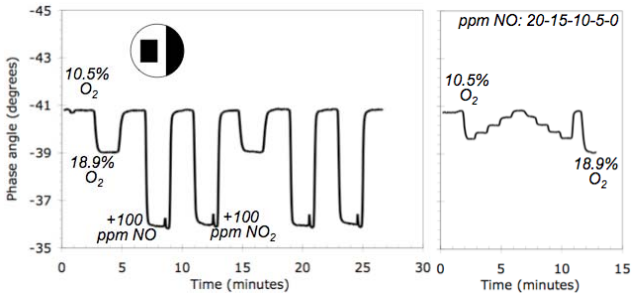

(a) (b)

Figure 4. Sensing behavior of $LSM_{dense}/YSZ/LSM_{porous}$ prototype at 650°C with changes in oxygen concentration and (a) 100 ppm additions of either NO or NO_2 or (b) response to step changes of 5 ppm NO up to 20 ppm.

Temperature-dependent NO_x sensitivity

Based on previous work investigating impedancemetric NO_x sensing mechanisms, the difference in operating temperatures to produce similar NO_x sensitivities for the two prototypes discussed above can be explained by the differing catalytic activities of the sensing electrode materials, Au vs. LSM.

For gas concentrations containing both O_2 and NO_x, the following redox reactions may occur at the electrode/electrolyte interface:

$$\frac{1}{2}O_2 + 2e^- \leftrightarrow O^{2-}$$
$$NO_2 + 2e^- \leftrightarrow NO + O^{2-} \qquad (1)$$

For parallel contributions from the O_2 and NO_x reactions to the measured impedance, the relative rate constants for the two reactions would then determine the relative sensitivities to these gases. Sensing electrodes with low catalytic activity towards the oxygen reaction, and therefore higher rate constants for the NO_x reaction relative to the oxygen reaction, result in improved NO_x sensitivity.

In addition to an appropriate composition, previous work demonstrated that dense electrode microstructures were necessary to limit the oxygen reaction and obtain NO_x sensitivity.[9] For both of the asymmetric prototype sensors in our investigation, only one of the electrode/electrolyte interfaces dominates the measured sensitivity to NO_x. For the Pt/YSZ/Au prototype, the Au/YSZ interface provides the NO_x sensitivity, with Au serving as the sensing electrode; for the LSM prototype, only the dense LSM/YSZ interface influences NO_x sensing, with dense LSM serving as the sensing electrode.

At 650°C, the LSM prototype has very low NO_x sensitivity compared to the Pt/YSZ/Au prototype at the same temperature because LSM is more active towards oxygen catalysis than Au. However, reducing the operating temperature of the LSM prototype to 575°C lowers the catalytic activity and increases the NO_x sensitivity (relative reaction rate) of the dense LSM/YSZ interface.

NO vs. NO_2 Sensing Behavior

In addition to differences in operating temperature, the LSM prototype has identical responses to 100 ppm additions of either NO or NO_2. In comparison, the Pt/YSZ/Au prototype had a slightly larger response to NO_2. Gas phase equilibrium effects are proposed to explain the difference.

The following equation describes the relationship between oxygen, NO, and NO_2:

$$2NO_2(gas) \leftrightarrow 2NO(gas) + O_2(gas) \qquad (2)$$

and can be used to calculate equilibrium values for NO and NO_2 using thermodynamic data for 10.5% O_2. At 575°C and 650°C, the equilibrium NO_x gas mixture has 87% and 93% NO, respectively.

For the LSM prototype, both NO and NO_2 have identical responses. The identical responses could indicate that the equilibrium NO_x concentration is presented to the sensing electrode. For the LSM prototype sensor design, the gas interacts with the porous LSM electrode before reaching the dense LSM/YSZ sensing interface. The porous LSM electrode likely provides enough catalytic activity for complete equilibrium of NO_x so that identical gas concentrations reach the sensing interface, regardless of whether the starting composition is NO or NO_2.

For the Pt/YSZ/Au prototype, NO_2 has a slightly larger response than NO indicating that the equilibrium NO_x concentration does not occur at the sensing electrode. For the Pt/YSZ/Au prototype sensor design, the gas only interacts with a thin layer of porous YSZ before reaching the Au/YSZ sensing interface. The porous YSZ does not provide the same catalysis as the porous LSM. Without a sufficient catalyst, additions of either NO or NO_2 will not result in identical equilibrium concentrations reaching the sensing interface.

Furthermore, in confirmation of this hypothesis, it was found that changing the thickness of the porous YSZ layer on the Pt/YSZ/Au sensor surface altered the response to either NO and NO_2. Figure 5a shows the impedance behavior for a Pt/YSZ/Au prototype with a single layer of porous YSZ on the sensor surface of approximately 50 to 100 μm thickness. The impedance behavior is shown on a Nyquist plot, which is a complex-plane plot with real impedance, Re(Z) plotted versus the negative imaginary impedance,-Im(Z).

In the Nyquist plot, each data point is taken at a different frequency, which increases from right to left; the darkened points and numbers correspond to log of frequency in Hertz. Features in the Nyquist plot, in particular the semicircular arcs, can be used to determine the contributions from interfacial and bulk phenomena to the overall impedance due to their appearance over a specific range of frequencies. The diameter of the individual arcs corresponds to real impedance (resistance) values.

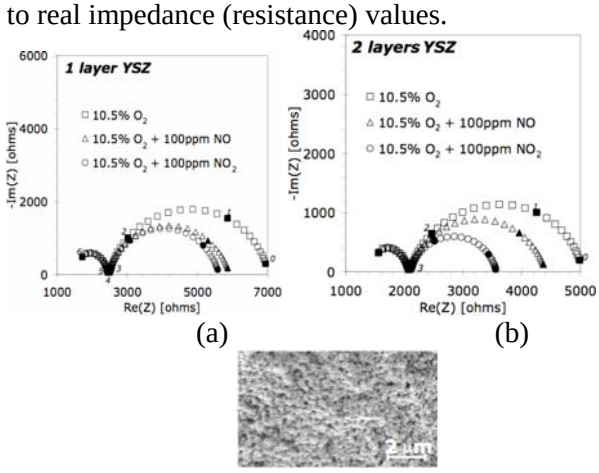

(a) (b)

(c)

Figure 5. Nyquist plot of Pt/YSZ/Au prototype with (a) one layer and (b) two layers of YSZ slurry on the sensor surface at 650°C. (c) SEM picture of porous YSZ slurry.

In Fig. 5a, additions of either 100 ppm NO or NO_2 lead to similar changes in the impedance behavior. However, as the YSZ thickness is increased, as seen in Fig. 5b, additions of NO_2 cause a much larger decrease in impedance, as indicated by the larger decrease in the arc diameter, than additions of NO. Further increases in YSZ thickness with three and four layers (each layer was approximately 50 to 100 μm) did not cause any additional changes in the NO_2 vs. NO response; the overall electrode impedance continued to decrease.

The results from varying the thickness of the porous YSZ on the sensor surface indicate that the porous YSZ provides a more favorable pathway for NO_2, compared to NO, to the sensing interface. Figure 5c shows an SEM picture of the porous YSZ layer. For very thin layers of YSZ, there is limited interaction between the NO_x and the porous YSZ; all the gas introduced reaches the sensing interface without any changes in composition. Additions of NO and NO_2 respond similarly since for impedance-based sensing both the forward and reverse reactions are important.

As the porous YSZ thickness increases, the NO_x interacts with the porous YSZ surface before reaching the sensing interface. Our hypothesis is that the NO_2 has a faster diffusion pathway on the porous YSZ than in the gas phase; NO does not have a faster diffusion pathway on the porous YSZ. The effect of the faster surface diffusion for NO_2 only occurs within a limited distance from the sensing interface, and additional increases in thickness no longer produce additional increases in the NO_2 response relative to the NO response.

Previous results support our observation that NO_2 may have a faster diffusion path on the porous YSZ. For early prototypes using spring-loaded pressure, Au metal contacts were pressed against porous YSZ, a geometry that minimized interaction between NO_x and the porous YSZ. There would be minimal surface diffusion pathways on the YSZ available to NO_x before reaching the sensing interface, and a gas phase diffusion pathway would dominate. This early prototype, with minimal surface diffusion pathways on the YSZ, had almost identical responses to NO and NO_2.[7]

Additional investigation is necessary to fully understand the mechanisms responsible for the difference in behavior of NO and NO_2 in the Pt/YSZ/Au prototype. Nevertheless, we have demonstrated that controlling the thickness of the porous YSZ on the sensor surface can be used to create a total-NO_x sensor with similar responses to NO and NO_2.

Initial Long-term Stability Testing

Results from preliminary aging experiments indicate promising stability for meeting the accuracy and durability requirements, which are currently ±1 ppm and 10 yr/150k miles, respectively. The improved stability associated with impedance-based sensing compared with potentiometric or

amperometric sensing could be due to the low-amplitude signals used, typically around 25 mV, which minimize any electrically driven changes. Furthermore, the use of alternating signals, as opposed to a constant dc signal, may prevent preferential aging effects at the interface associated with specific directional (i.e., cathodic or anodic) electrode reactions.

Figure 6a shows the sensing behavior for long-term aging of the Pt/YSZ/Au prototype at 650°C from 144 to 624 hours and indicates good reproducibility and minimal drift in the baseline and the response.

Figure 6b shows the sensing behavior for an LSM prototype similar to the one previously discussed, but the porous LSM electrode was replaced with Pt. However, the sensing interface (dense LSM/YSZ) is identical for both prototypes and should be suitable for comparison. The data shown in Fig. 6b were taken at 575°C with a background oxygen concentration of 2% and step changes in the NO concentration up to 20 ppm total.

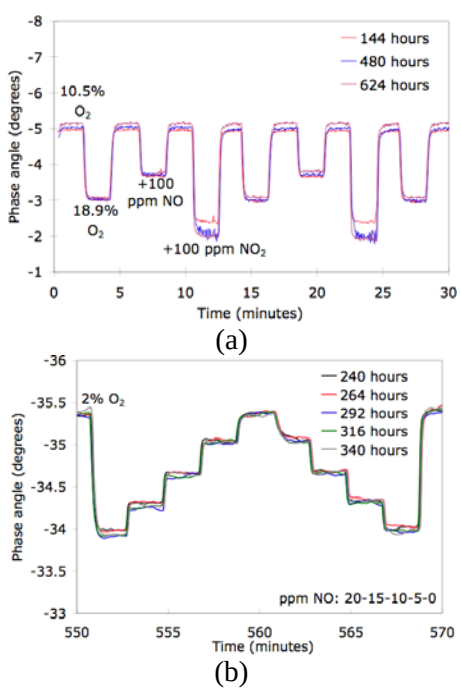

Figure 6. Sensing behavior of (a) Pt/YSZ/Au prototype at 650°C after long-term aging from 144 to 624 hours and (b) LSM_{dense}/YSZ/Pt prototype at 575°C after long-term aging from 240 to 340 hours.

Initially, the LSM/YSZ/Pt prototype at 575°C showed a steady monotonic change in baseline signal before stabilizing after 240 hours of testing. The sensor signal remained stable for an additional 100 hours of testing, as shown in Fig. 6b, before again exhibiting monotonic changes in the baseline signal. The mechanism responsible for the baseline drift is likely microstructural changes in the Pt electrode, which has been shown previous work, and is currently being investigated.

Due to its excellent stability, the Pt/YSZ/Au prototype was selected for dynamometer testing in actual diesel exhaust at the Ford Research Center.

Dynamometer Testing

Engine dynamometer testing was performed on the Pt/YSZ/Au prototype using two different test sequences. The first sequence was designed to minimize changes in cross-interfering species, such as oxygen, while measuring the sensor response to changes in NO_x. Both the engine speed and throttle were held at constant values, 2750 rpm and 30%, respectively. Initially, excess urea was added to react with all the NO_x. The amount of urea was then reduced until all the urea reacted with the NO_x. Finally, the amount of urea was further reduced to produce varying levels of NO_x, as shown in Fig. 7.

In Fig. 7a, the raw sensor data from the prototype agrees reasonably well with data taken with the only currently available commercial NO_x sensor. (which, as previously noted, does not fully meet automobile application requirements). The NO gas concentration measured by Fourier Transform Infrared (FTIR) spectroscopy is also shown for comparison in Figure 7a.

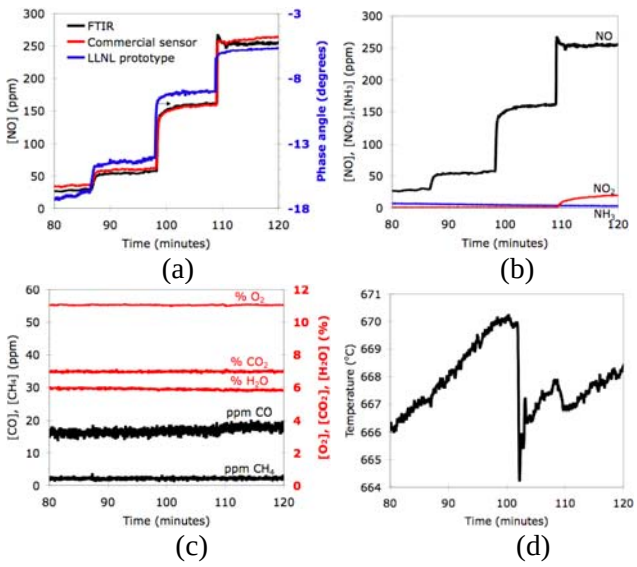

Figure 7. Dynamometer test results comparing (a) raw data from the Pt/YSZ/Au prototype with a commercial sensor and FTIR. (b) FTIR concentrations for NO, NO_2, and NH_3. (c) Constant values for CO, CH_4, CO_2, H_2O, and O_2. (d) Variations in temperature.

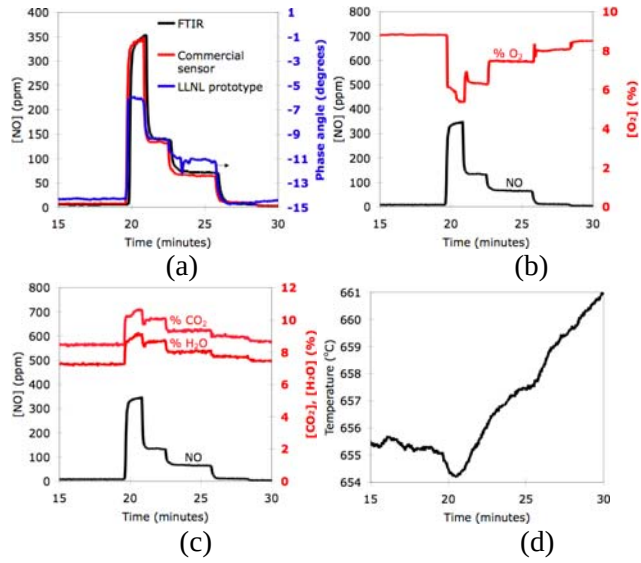

Figure 8. Dynamometer test results comparing (a) raw data from the Pt/YSZ/Au prototype with a commercial sensor and FTIR. Changes in (b) oxygen and (c) CO_2 and H_2O concentrations. (d) Variations in temperature.

Additional data from FTIR and a paramagnetic oxygen analyzer, shown in Figs. 7b and 7c, demonstrate that NO is the primary species changing during the dynamometer test with low levels of NO_2, NH_3, CO, and CH_4. Also, O_2, CO_2, and H_2O remained constant during testing. Temperature measurements near the prototype, as shown in Fig. 7d, indicate fluctuations of around six degrees and do not correlate with trends seen in the prototype. Therefore, the measured changes in the prototype are a direct evaluation of its ability to detect changes in NO concentration in actual diesel exhaust.

The second test sequence was designed to investigate cross-interference from oxygen. The engine speed was held constant at 2750 rpm, with an initial throttle of 30%. Based on the first test sequence, enough urea was then introduced to minimize NO_x concentrations. Finally, the amount of throttle was stepped to 40%, 35%, 32.5%, and 30% to vary gas concentrations, as shown in Fig. 8.

In Fig. 8a, the general trend of the prototype agrees with the commercial sensor. However, the prototype no longer agrees in terms of relative response magnitudes, as measured in the first test sequence when interfering gases were minimized.

The second sequence also exhibited low levels of NO_2, NH_3, CO, and CH_4. However, O_2, CO_2, and H_2O no longer remained constant during testing when the percent throttle changed. Figure 8b shows a decrease in the oxygen concentration as throttle initially increased.

From laboratory testing, changes in oxygen concentration have a similar directional effect on the sensor signal as changes in NO_x concentration, although with much smaller sensitivities (see Fig. 3). Therefore, since the oxygen concentration is decreasing at the same time that the NO concentration is increasing, the combined effect is measured by the sensor. For the sensor signal, the decrease in oxygen concentration cancels out some of the signal associated with the increase in NO concentration.

The effect of oxygen interference is shown in Fig. 8a, where the prototype signal has a decreased response relative to the actual NO concentration increase (from 0 to 350 ppm) due to the simultaneous decrease in oxygen concentration from 9% to 6%. Changes in H_2O and CO_2 concentration are shown in Fig. 8c, and temperature fluctuations of around seven degrees are shown in Fig. 8d.

Previous work has demonstrated that the cross-sensitivity to oxygen may be accounted for by comparing measurements at multiple frequencies.[6] Other strategies for compensation are also being explored, including calibration using data from existing sensors located nearby. Cross-sensitivity studies are ongoing. The effectiveness of these strategies are currently being evaluated using the dynamometer results and will be published separately.

Commercializable Sensor Designs

The technology from the Pt/YSZ/Au prototype built on the alumina substrate was successfully transferred onto actual heated substrates provided by Ford. Initial sensing experiments for prototypes built on heated substrates agree reasonably well with data taken for the prototypes built on alumina substrates (without heating elements).

Additionally, the heated substrate prototypes were packaged into an oxygen sensor housing by a U.S. supplier, as shown in Fig. 9. Initial sensing experiments for the packaged Pt/YSZ/Au prototypes indicate reasonable sensitivity.

Figure 9. Photograph of Pt/YSZ/Au prototype built on a heated substrate and packaged into an oxygen sensor housing.

Both the incorporation of a heated substrate and an oxygen sensor housing indicates that the impedancemetric NO_x sensor technology can be adapted to a commercial sensor platform. In addition, utilizing these advanced sensor platforms removes the need for a furnace during testing. Additional laboratory and dynamometer testing are ongoing to evaluate the platforms.

Conclusions

Our work focused on two different impedancemetric NO_x sensor prototypes. Both demonstrate NO_x sensitivities to less than 5 ppm and response times of less than 10 seconds. Earlier prototypes have demonstrated response times of a few second (< 5 sec.); however, the prototypes discussed here have not been optimized for response time. The advances in sensor development are a direct result of previous and current work characterizing impedancemetric NO_x sensing mechanisms based on YSZ-electrolyte cells.

The sensing mechanism depends on the porous YSZ/dense electrode interface, where only dense electrodes that are poor O_2 catalysts result in effective sensors. In impedancemetric sensing, either one or both electrodes can serve as the sensing electrode. The technology is not limited to a specific electrode material, and a number of materials potentially meet the sensing criteria, including gold and electronically conducting oxides, both of which were incorporated into prototypes in this study: Pt/YSZ/Au and LSM_{dense}/YSZ/LSM_{porous}.

Dynamometer engine testing in actual diesel exhaust was performed using appropriate test parameters in order to isolate the effect of NO_x. The sensing behavior of the prototype was compared alongside the only commercially-available NO_x sensor and a standard analytical FTIR instrument and demonstrated reasonable agreement.

Furthermore, advances toward a more commercializable sensor platform were achieved by incorporating a heated substrate. The heated substrate was also packaged into an oxygen sensor housing. Preliminary results show reasonable sensitivity from the advanced sensor platforms. Additional tests are ongoing.

References

1. F. Menil, V. Coillard, and C. Lucat, *Sensors and Actuators B* **67**, 1 (2000).
2. W. Göpel, G. Reinhardt and M. Rösch, *Solid State Ionics* **136–137**, 519 (2000).
3. N. Miura, M. Nakatou and S. Zhuiykov, *Ceram. Int.*, **30**, 1135 (2004).
4. N. Miura, M. Nakatou and S. Zhuiykov, *Sensors and Actuators B* **93**, 221 (2003).
5. N. Wu, Z. Chen, J. Xu, M. Chyu and S. X. Mao, *Sensors and Actuators B* **110**, 49 (2005).
6. L. P. Martin, L. Y. Woo, and R. S. Glass, *J. Electrochem. Soc.*, **154**, J97 (2007).
7. L. Y. Woo, L. P. Martin, R. S. Glass, and R. J. Gorte *J. Electrochem. Soc.*, **154**, J129 (2007).
8. J. Yoo, F. M. Van Assche, and E. D. Wachsman, *J. Electrochem. Soc.*, **153**, H115 (2006).
9. L. Y. Woo, L. P. Martin, R. S. Glass, W. Wang, S. Jung, R. J. Gorte, E. P. Murray, R. F. Novak,

and J. H. Visser. *J. Electrochem. Soc.*, **155**, J32 (2008).

Publications/Presentations

"Investigating the stability and accuracy of the phase response for NO_x sensing 5% Mg-modified $LaCrO_3$ electrodes," *ECS Transactions*, **6**(20):43-62 (2007).

"Effect of electrode composition and microstructure on impedancemetric nitric oxide sensors based on YSZ electrolyte," *J. Electrochem. Soc.*, **155**(1):J32-J40 (2008).

Oral presentation made at the 32nd International Conference & Exposition on Advanced Ceramics and Composites, Jan. 27 – Feb. 1, 2008 in Daytona Beach, FL: "Sensing Mechanism of Impedancemetric NO_x Gas Sensors Based on Porous YSZ/Dense Electrode Interfaces."

Oral presentation entitled "NO_x Sensor Development for Monitoring Diesel Emissions" made during a visit by USCAR (United States Council for Automotive Research) to LLNL on April 23, 2008.

Agreement 9440 - Fabrication of Micro-orifices for Diesel Fuel Injectors

George R. Fenske and Nicholaos Demas
Argonne National Laboratory
9700 South Cass Avenue
Argonne, IL 60439
(630)252-5190; fax (630)252-4798; e-mail: gfenske@anl.gov

DOE Technology Manager: Jerry Gibbs
(202) 586-1182; fax: (202) 586-1600; e-mail: jerry.gibbs@ee.doe.gov

Contractor: Argonne National Laboratory, Argonne, Illinois
Prime Contract No.: DE-AC02-06CH11357

Objectives

- Develop a methodology for reducing the diameters of fuel injector orifices to 50 µm by applying material to the internal diameter (ID) of the orifice. Micro-orifices should improve fuel distribution, increase efficiency, and reduce emissions in compression-ignition, direct-injection (CIDI) engines.
- Characterize the spray and combustion properties of the fuel injector system coated with electroless nickel (EN) and other advanced ID coating processes.
- Transfer the developed technology to DOE industrial partners.

Approach

- Evaluate the potential of EN plating for improving the surface finish and reducing deposit formation on injector nozzles.
- Evaluate the potential of vapor deposition processes to form uniform nickel (Ni) coatings.
- Evaluate the potential of laser micro-drilling processes to form uniform orifices in high length-to-diameter configurations.

Accomplishments

- Devised a new approach for preparing test nozzles in concert with the U.S. Environmental Protection Agency–National Vehicle and Fuel Emissions Laboratory (EPA-NVFEL). Also initiated collaboration with a major fuel injector manufacturer for further engine testing of plated nozzles for deposit mitigation.
- In concert with Imagineering, Inc. (a commercial plating company), developed a method for improving the surface finish of commercial-scale plated nozzles.
- Developed an X-ray phase contrast imaging technique for nondestructive examination of thin EN coatings applied to the interiors of diesel injectors.
- In collaboration with the U.S. EPA, characterized the spray characteristics of EN-coated commercial nozzles.
- Examined the microstructure and micro-hardness of commercial nozzles.
- Characterized EN-coated commercial nozzles from Imagineering; the thickness of the coatings was between 43 and 48 µm.

Future Direction

- Evaluate coating integrity by examining the variation of coating thickness as a function of depth.
- Characterize spray properties of EN-coated nozzles using advanced x-ray analytical techniques.
- Provide coated injector tips to EPA-NVFEL personnel for spray characterization and combustion tests.
- Explore establishing a consortium with industrial partners to integrate EN process into a production setting.

Introduction

In 2007, EPA regulations mandated reduction in diesel engine emissions to 0.01 grams of particulate matter (PM) per engine horsepower per hour and 0.2 grams of nitrogen oxide (NO_x) per engine horsepower per hour. Further reductions are expected for 2010. To achieve these levels, CIDI engines are being redesigned to reduce in-cylinder soot production. One design change under consideration is the reduction of the diameter for the fuel injector orifice.

Pickett and coworkers[1,2] demonstrated significant reductions of soot in a test cylinder using experimental injectors with orifice diameters of 50 μm, even with high levels of exhaust gas recirculation and concomitant reduction in NO_x emissions. NVFEL researchers have observed reduced PM emissions from a light-duty diesel engine equipped with 75-μm-diam injector orifices. These reductions arise from increases in fuel atomization efficiency, leading to more complete combustion.[3] Although it is currently possible to economically mass-produce injectors with 100-μm-diam orifices by using electrodischarge machining, further reductions in hole size are accompanied by unacceptable fabrication error rates.

Reducing the orifice diameter (e.g., from 150 to 50 μm) carries with it a number of penalties, however. It will reduce the amount of fuel that can be delivered to the combustion chamber without increasing the number of spray holes, the injection pressure, and/or the discharge coefficient. The potential impact of coking on smaller orifices is also much greater, as smaller holes will be more readily blocked by coking deposits on the injector tip and in the spray holes themselves. Coking deposits are a particular problem with tapered-orifice nozzles, another technique for increasing fuel atomization and thus reducing PM emissions.

Another issue is alternative fuels. One method to minimize dependence on foreign oil is the increased use of bioderived fuels, such as vegetable oil esters. Because of the presence of carbon-carbon double bonds in the carboxylic acid chain precursors, these fuels readily form coking deposits in the combustion chamber—a major problem in concert with smaller spray holes. Other alternative fuels include alcohols such as methanol or ethanol. These are not typically used neat but are blended with conventional diesel fuel. One emissions reduction strategy is to inject an ethanol/water mixture along with conventional fuel, reducing the combustion temperature and NO_x emissions. However, alcohol partial oxidation products can include corrosive carboxylic acids, which will damage the steel nozzles over time. In concert with more commonly used fabrication techniques, EN plating has been used to prepare fuel injector nozzles with orifice diameters as small as 50 μm. EN plating also promises to mitigate or solve all of the difficulties described above. The plated surface is corrosion-resistant and smoother, and the discharge coefficient of the plated orifices is higher. This method can be used to deposit a wide variety of alloys, offering the possibility of tailoring surface chemistry to reduce or eliminate deposit formation.

Approach

As described in previous progress reports, the diameter of the orifice can be reduced by coating its interior with EN plating. This technique has been used to deposit nickel/phosphorus or nickel/boron alloys onto metallic surfaces from aqueous solutions. It has been successfully used in previous years to reduce the orifice diameter from 200 to 50 μm on a bench scale, and from 180 to 75–80 μm on a commercial scale. Other metal alloys have been deposited by the same technique.

Having demonstrated that EN plating reduces the orifice diameter to the desired size, we next sought to demonstrate the usefulness of EN-plated nozzles for solving the challenges described in the Introduction: improving spray properties and discharge coefficient, reducing deposit formation, and resisting corrosion. To this end, the use of

phase-contrast x-ray imaging at Argonne's Advanced Photon Source (APS) was explored for nondestructive examination of plated nozzles. This technique is capable of measuring coating thicknesses on internal passages and was applied as a quality check on nozzles that were sent to the EPA for engine tests.

In collaborative studies with the EPA, fuel sprays produced with EN-coated commercial nozzles yielded encouraging results, and during FY08, we explored the application of EN plating to produce multi-sized orifices (e.g., 50 µm and 125 µm) on a given nozzle. Research also continued to evaluate the use of EN coatings as an approach to mitigate erosive wear.

Results

Initial research focused on demonstrating the feasibility of coating internal passages with EN. The early laboratory results on single nozzles were very successful. Commercial nozzles with orifices 200 µm in diameter and 1 to 1.55 mm in length were plated with EN, producing an orifice 50 µm in diameter.[4, 5, 6] The coatings were uniform in thickness along the orifice and as smooth as, or smoother than, the original orifice surface. Figure 1 shows a scanning electron micrograph of a coated nozzle that was cross-sectioned to measure the thickness of the coating. The image illustrates the excellent continuity and adhesion of the coating.

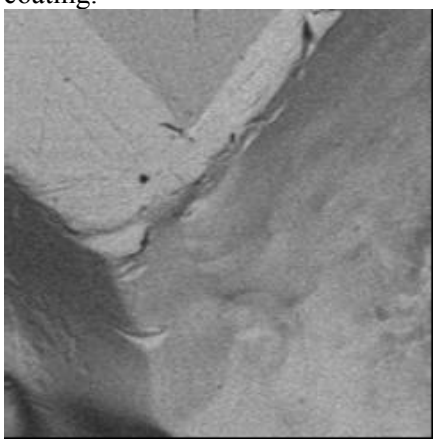

Figure 1: Scanning electron micrograph of EN-plated orifice.

The EN plating concept was transferred to a commercial plating company (Imagineering) specializing in electroless coatings—particularly Ni-phosphorus coatings. Imagineering modified its coating process to eliminate surface blemishes/pits observed on initial coating trials.

Recent tests[7] at the APS indicated that the phase contrast x-ray imaging technique, developed to image the motion of a pintle inside an operating injector, had sufficient resolution to differentiate the Ni coating from the surrounding ferrous body. This technique was applied to validate the thickness of EN coatings applied to a series of light-duty injectors that were sent to EPA-NVFEL for engine and flow visualization studies.[6]

Two nozzles, one with 50-µm orifices, and one with 75-µm orifices, were sent to EPA-NVFEL to investigate the flow characteristics by high-speed laser imaging. The test rig uses a hydraulically intensified fuel system (3,000 psi intensified 11:1) injecting fuel into a 500 psi chamber. The pulse width in all cases was 1 msec. Figure 2 shows snapshots taken 0.6 msec after start of injection for three nozzles[8, 9]: one with coated 50-µm orifices (far left), one with coated 75-µm orifices (center), and one with uncoated 100-µm orifices (far right). Figure 3 shows quantitative data on the fuel penetration as a function of time for each of the cases in Figure 2. Qualitatively, the 100-µm sprays appear denser (as indicated by the color, white vs. green, in Figure 2) than the 50- and 75-µm sprays. Aside from a slightly deeper penetration, the fuel penetration data for the 75-µm orifice do not differ dramatically from those of the uncoated 100-µm nozzle. The 50-µm nozzle, however, shows a dramatic difference in the fuel penetration profile. The penetration is not only shallower than that of the 75- and 100-µm orifices, as expected, but it also is linear with time in contrast to the non-linear dependence observed for the 75- and 100-µm nozzles. Plans are being developed to demonstrate

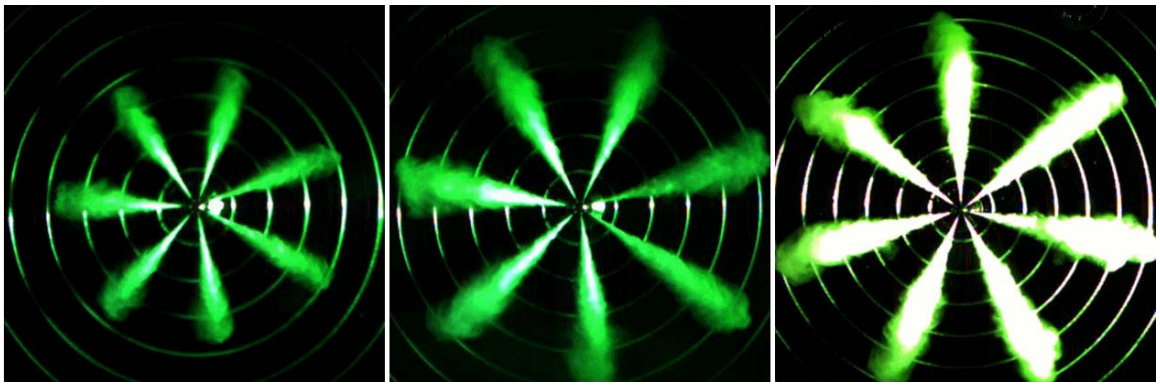

Figure 2: Laser images of fuel sprays from 50-, 75-, and 100-µm orifices.[6, 9]

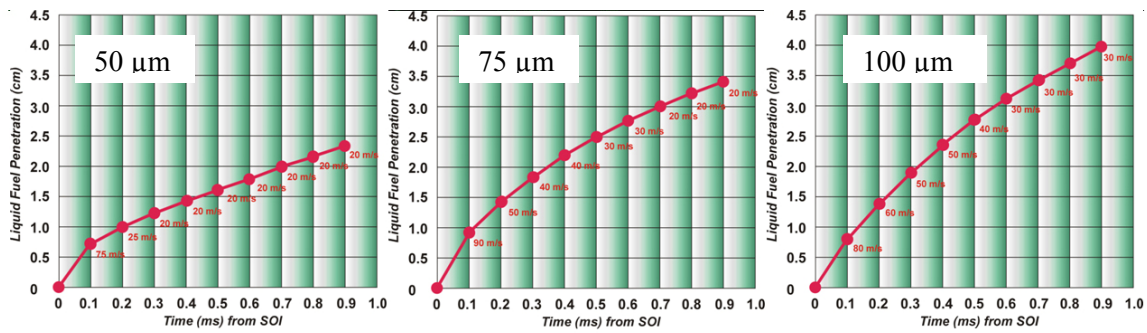

Figure 3: Fuel penetration as a function of time from start of injection (SOI) for 50-, 75-, and 100-µm nozzles.[6,9]

the feasibility of producing multi-sized orifices on experimental nozzles for spray visualization studies and, if successful, for engine emission studies. Argonne is also exploring application of the EN process to provide cavitation-erosion.

In FY08, activities were initiated to develop/demonstrate the ability to fabricate multi-sized orifices (to improve the ability to direct fuel to a broader range of the combustion chamber) as well as to evaluate the potential to use EN platings to mitigate orifice erosion. These activities involved the use of nozzles from multiple partners. It was soon realized that the alloys and heat treatments used by the different vendors were not identical. Information on the alloy composition and heat treatments was not available, and thus it was necessary to characterize the microstructure and composition of the nozzles.

Therefore, four commercial nozzle designs were sectioned and prepared for microstructural analysis. Design A was a six-orifice nozzle (125-µm orifices) selected for use in the multi-sized orifice activity. These nozzles will be plated to produce 50-µm orifices, then reground, then machined using electron discharge to introduce larger orifices (125 µm) with which to produce 50- and 125-µm orifices on the same nozzle. Design B is a standard baseline six-orifice nozzle (approximately 200-µm orifices) that we have used in prior studies. Design C is an eight-orifice, nitrided, high-pressure experimental nozzle, and design D is a seven-orifice, non-nitrided, experimental nozzle.

Figure 4 shows the microstructures of each of the nozzles. Analysis of these microstructures indicated that nozzle A consisted of tempered martensite; B, martensite; C, tempered martensite with nitride precipitates located along prior austenitic grain boundaries; and D, bainite and fine pearlite.

Energy dispersive x-ray analysis was performed for all nozzles to determine their

composition. Nozzle A showed levels of Cr, Mn, and Ni that suggest an alloy comparable to AISI 4340. Nozzle B showed levels of Cr and Fe and lack of significant levels of other elements that suggest an AISI H13 alloy. Nozzle C showed levels of Cr and V that suggest an AISI H11/H13 alloy. Nozzle C also exhibited a nitride-rich surface, consistent with nitriding. Finally, nozzle D showed levels of Cr and Fe that suggest an AISI H11/H13 alloy.

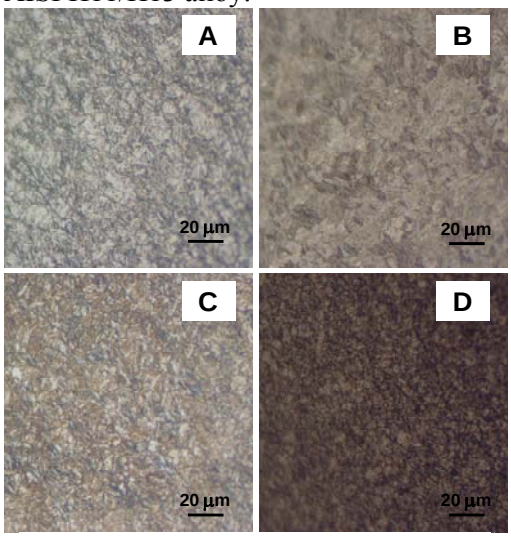

Figure 4: Microstructure of different nozzle designs.

For each nozzle, a series of hardness measurements was performed along the tip and side. Table 1 shows the hardness results for the representative locations shown in Figure 5.

Table 1: Rockwell C hardness measurements of cross-sectioned nozzles.

Location	1	2	3	4	5	6
A	65	56	65	65	52	66
B	50	58	64	66	52	65
C	50	72	74	55	64	72
D	57	57	57	59	57	57

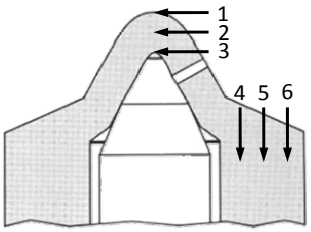

Figure 5: Cross-section schematic of nozzles showing approximate locations of hardness measurements (Table 1).

The four types of nozzles were sent to Imagineering for plating. Figures 6 and 7 show borescope images taken before and after the plating process, respectively. Some pits can be seen on the nozzles after the plating (Figure 7). Early measurements show a decrease in the orifice diameter in comparison with the specifications.

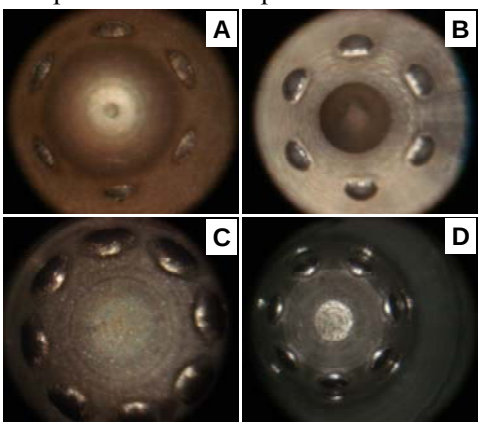

Figure 6: Boroscope images of nozzles A, B, C, and D before EN plating

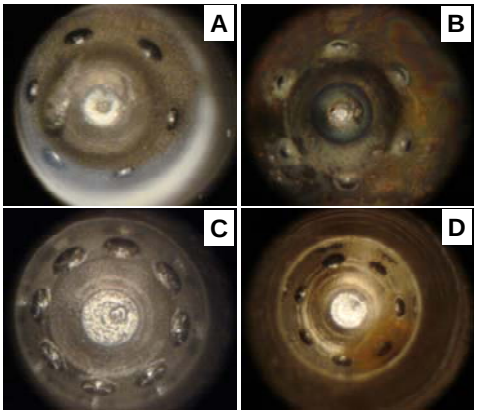

Figure 7: Boroscope images of nozzles A, B, C, and D after EN plating.

Witness pieces were used to monitor the coating thickness during the coating process. Figure 8 shows a micrograph of the cross section of one of the witness pieces. The coating thickness is 48 μm.

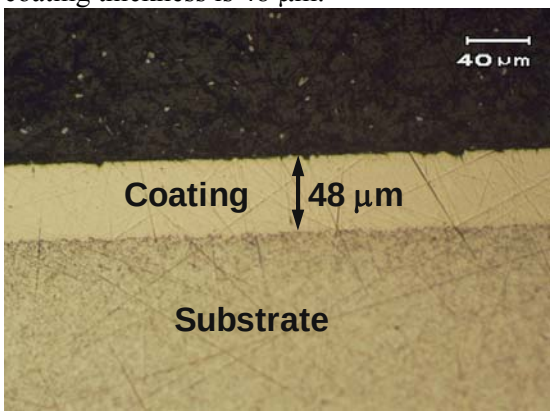

Figure 8: Witness piece showing coating thickness.

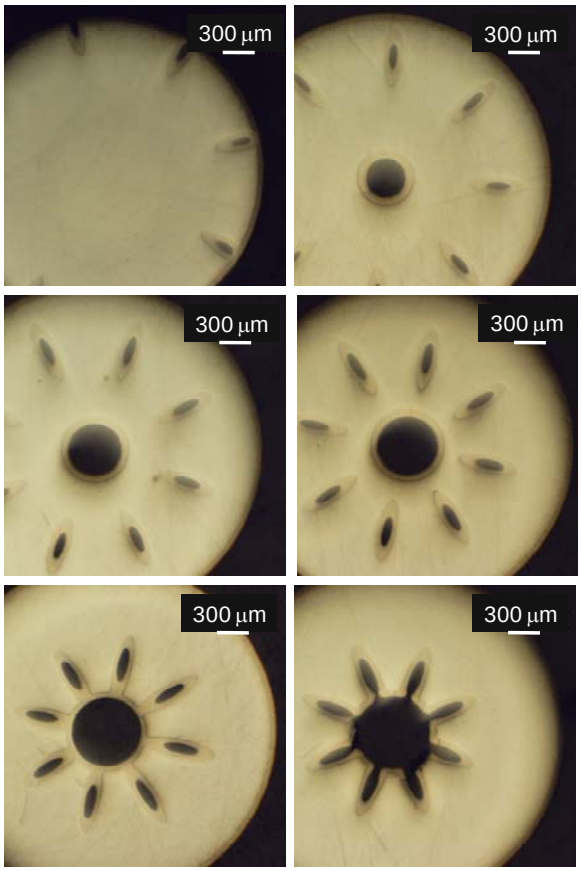

Figure 9: Images of progressive material removal for one of the nozzles.

The coating thickness and orifice diameter of the various nozzles were examined with an optical microscope and measured as a function of depth. Figure 9 shows a series of micrographs as material was progressively removed for one of the nozzles (nozzle C) starting from the tip. Material was removed approximately every 50 μm. Note that the dimension representing the coating thickness and diameter of the orifice is along the minor axis of the elliptical hole. The coating in these images was relatively uniform, with its thickness varying between 43 and 48 μm.

Conclusions

Several candidate methods are being evaluated and developed for fabricating nozzles with small (50-μm diam) micro-orifices. Development of the EN aqueous-based plating process has been advanced to the stage where commercial nozzles were treated and characterized with an advanced phase-contrast x-ray imaging technique that confirmed uniform coating deposition along the orifice. Preparations were initiated to fabricate multi-sized orifices (50 and 125 μm) on a commercial nozzle. Preliminary analysis of the coating uniformity on sibling nozzles confirmed that the coating was uniformly deposited along the orifices. Effort will continue in FY09 to prepare the multi-sized orifices in preparation for flow-spray studies at the EPA.

References

1. Lyle M. Pickett and Dennis L. Siebers, Paper No. 2001-ICE-399, ICE Vol. 37-1, ed. V. W. Wong, *2001 Fall Technical Conference*, American Society of Mechanical Engineers, 2001.
2. L. M. Pickett, D. L. Siebers, A. F. Morales, J. Hachman, and A. K. Sinensky, "An Investigation of Diesel Soot Formation Processes Using High Aspect Ratio Micro-Orifices," presented at HARMST 2003 High-Aspect Ratio Micro-Structure Technology Workshop, Monterey, CA, 2003.
3. John B. Heywood, *Internal Combustion Engine Fundamentals*, McGraw-Hill, New York, 1988.
4. John B. Woodford and George R. Fenske, "Fabrication of Small Fuel

Injector Orifices," *2005 Annual Progress Report, Automotive Propulsion Materials*, U.S. Department of Energy, Washington, D.C., 2005.
5. John B. Woodford and George Fenske, "Fabrication of Micro-orifices for Diesel Fuel Injectors," *2006 Annual Progress Report, Automotive Propulsion Materials,* U.S. Department of Energy, Washington, D.C., 2006.
6. George Fenske, "Fabrication of Micro-orifices for Diesel Fuel Injectors," 2007 *Annual Progress Report, Automotive Propulsion Materials*, U.S. Department of Energy, Washington, D.C., 2007.
7. Kamel Fezzaa, Wah-Keat Lee, Seong-Kyun Cheong, Christopher F. Powell, Jin Wang, and Ming-Chia Lai, "Ultrafast X-ray Phase-Enhanced Microimaging for Visualizing Fuel Injection Process," SAE 2005-24-093, Society of Automotive Engineers, 2005.
8. R. Schaefer, US EPA-NVFEL, private communication, July, 2007.
9. G. Fenske, J. Woodford, J. Wang, and R Schaefer, "Fabrication and Characterization of Micro-orifices for Diesel Fuel Injectors," SAE 2008-01-1595, 2008.

Publications and Presentations

J. Woodford and G. Fenske, "Fabrication of Small Orifice Fuel Injectors," DEER (Diesel Engine Emissions Reduction) Conference, August 2005.

J. B. Woodford and G. R. Fenske, *Fabrication of Small-Orifice Fuel Injectors for Diesel Engines*, Argonne National Laboratory Report, ANL-05/06, March 2005.

J. B. Woodford, G. R. Fenske, and J. M. Perez, "Deposit Formation on Electroless Nickel," submitted to *Energy & Fuels*.

G. Fenske, J. Woodford, J. Wang, and R Schaefer, "Fabrication and Characterization of Micro-orifices for Diesel Fuel Injectors," submitted for presentation at the 2008 SAE International Powertrains, Fuels and Lubricants Congress, June 23-25, 2008, Shanghai, China, SAE paper 2008-01-1595.

G. Fenske, J. Wang, and E. El-Hannouny (ANL), R Schaefer and F. Hamady (NVFEL), "Fabrication of Micro-orifices for Diesel Fuel Injectors," DEER (Diesel Engine Emissions Reduction) Conference, August 2008.

Agreement 11754 - Hydrogen Materials Compatibility

James Holbery, Chuck Henager, Jr., Stan Pitman, Joe Ryan, Kyle Alvine, Ken Johnson
Pacific Northwest National Laboratory
P.O. Box 999
Richland, Washington 99354
(509) 375-3686; fax: (509) 375-2379; e-mail: james.holbery@pnl.gov

Collaborators:
Peter Blau, Jun Qu
Oak Ridge National Laboratory
Oak Ridge, TN 37831
(865)574-5377; fax: (865) 574-6981; e-mail: blaupj@ornl.gov

Ali Erdemir, George Fenske
Argonne National Laboratory
Argonne, IL 60439
(630) 252-6571; erdimer@anl.gov

DOE Technology Manager: Jerry L. Gibbs
(202) 586-1182; fax: (202) 586-1600; e-mail: jerry.gibbs@ee.doe.gov

---

Contractor: Pacific Northwest National Laboratory, Richland, Washington
Prime Contract No.: DE AC06 76RLO 1830

Objectives

- Measure the friction and wear characteristics of injector materials in hydrogen environments, including in-situ and ex-situ materials characterization.
- Measure the performance of piezoelectric actuators and actuator materials in hydrogen environments.
- Develop a design approach to hydrogen injectors based on material behavior and performance in hydrogen based on experimental data.

Approach

- Develop quantifiable performance test data on piezo materials in high-pressure 100% hydrogen.
- Conduct failure analysis of actuator piezo materials and epoxy layers.
- Develop diffusion models to predict hydrogen diffusion effect on metallic, polymer, and piezo materials.
- Develop sliding wear data on injector materials, coatings in hydrogen environment.

Accomplishments

- Collaborated with three manufacturers of diamond-like carbon coatings, including Argonne National Laboratory, to procure coatings on two substrate alloys.
- Tested the friction and wear properties of diamond-like carbon coatings in hydrogen. This body of data is thought to be the most thorough analysis of DLC in hydrogen to date.
- Developed new nanolaminate coatings and characterized their friction, wear, and hardness properties.
- Utilized the sliding-impact apparatus at ORNL to test nanolaminate coatings.
- Initiated precision diffusion modeling of hydrogen into several polymer thin films synthesized by spin coating. These films are anticipated to act as diffusion barriers for the piezoelectric injector actuator. This will be the most comprehensive attempt to measure hydrogen diffusion into polymer thin films to date.
- Refined the friction-wear predictive modeling tool.

Future Direction

- Complete the series of wear and friction property measurements on diamond-like carbon and nanolaminate coatings.
- Complete hydrogen diffusion studies on polymer thin films to establish the durability of these coating selections in a high-pressure hydrogen environment.
- Collaborate, with Sandia National Laboratory, to determine the performance degradation of coatings and piezoelectric materials following exposure to hydrogen at pressures up to 20ksi.
- Develop accelerated test methods and durability metrics for materials used in hydrogen injector systems.

Introduction

For the transportation sector, hydrogen internal combustion engines utilizing direct injection can be viewed as a high efficiency / low emission technology for bridging the transition process to the hydrogen economy based upon fuel cell technology. It has been estimated that a hydrogen direct injection (DI) engine can be integrated into a hybrid vehicle system which would demonstrate fuel consumption (fuel energy utilized per unit distance) that is only about 15% to 20% greater than a hybridized fuel cell vehicle of similar mass. Significantly lower hardware cost (as compared to present fuel cell systems) and use of existing manufacturing facilities for conventional reciprocating engines makes this an attractive consideration. Some engine manufacturers have identified robust fuel injection technology as one of the key enablers for commercialization of advanced hydrogen DI engines.

The basic hydrogen injector architecture had been originally designed and developed for earlier direct injection natural gas engine programs. Fundamental issues limiting injector durability were expected and potential engineering solutions have been evaluated by PNNL with their partners Westport Innovations and Ford Motor Company. Overall, the injectors we have used in our research have been useful research tools for developing engine combustion and assessing fuel system technology. If there was eventually a significant level of interest in this type of engine technology, the long range intention is to advance the injector technology to the point where it could enter limited production.

Compared to liquid hydrocarbon fuels, hydrogen is a challenging fluid to use in precision injectors because it has very low viscosity, low density and can alter material properties through atomic diffusion or chemical reduction. The goal of this work was to understand the basic mechanisms that limit injector life and identify promising strategies to provide significant improvements for the next phase of research and development. Operational experience on an experimental hydrogen DI research chamber has provided many hundreds of hours of test experience to help expose weaknesses in design or material selection and to evaluate new materials and processes.

Furthermore, research on a single cylinder hydrogen DI engine at Ford Motor Company (Dearborn, MI) has confirmed significant potential for very low emissions, high efficiency and high power density. The engine testing is significant for the injection system because it is very difficult to replicate or model the entire set of thermal, chemical, and mechanical effects – usually only a few aspects are reproducible on a test rig. Nonetheless, specialized research rigs and tools did provide insight into different degradation mechanisms.

Fundamental data and understanding has started to emerge as a result of extensive single-cylinder engine testing and recent test bench work with a hydrogen autoclave (with 1 to 300 bar, and 20°C to 300°C capability). The autoclave at PNNL (reported in FY07 DOE Office of Vehicle Technology year-end report) has been able to partially reproduce environmental effects seen on injector sub-components after extended operation on an engine.

General Engine/Fuel System Description

For much of the work, the hydrogen direct injection research engine generally uses a centrally mounted injector, with a 4-valve layout much like a modern diesel engine. Direct injection (DI) can eliminate engine tendency to backfire in the intake manifold and minimizes pre-ignition because fuel residence time in-cylinder can be shorter (based on injection timing strategy). With DI, there is no combustible mixture in the intake manifold. And ignition occurs well after the intake valve closes.

Direct injection can greatly increase the opportunity to maximize power density over a port-injected engine (Figure 1). In port injected engines, at stoichiometric air/fuel ratio, an 18% in loss of power (relative to gasoline) occurs because of air displacement by hydrogen. In practice this level of fueling is difficult to achieve without backfiring (unwanted pre-ignition) when the intake valve is open, especially at higher loads. As a result there is a further de-rating of a hydrogen port engine, such that it is only able to demonstrate 65% of the torque (or BMEP) that a similar sized gasoline engine can achieve. Conversely, direct injection hydrogen engines, can exceed the output of a gasoline engine. A properly designed turbocharging system can dramatically raise the potential output of the hydrogen engine further, just as it does for a diesel engine or direct injection gasoline engine.

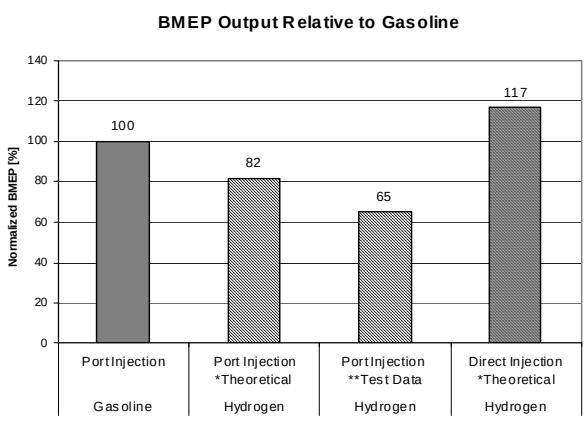

Figure 1: Brake Mean Effective Pressure relative to gasoline.

In current research, hydrogen is typically injected at pressures between 50 bar and 250 bar depending on the engine combustion strategy. Late injection (near TDC), especially on engines with turbocharging will require higher hydrogen injection pressures to overcome higher peak cylinder pressure and maintain sonic fuel flow at the nozzle. A pressure ratio of approximately 2:1 (ratio of injection pressure to chamber pressure) is required throughout the injection phase. Earlier injection results in a more homogeneous fuel/air mixture (longer mixing time). After the fuel mixture is prepared, it is then later ignited with a spark plug. Fuel can also be injected after ignition occurs if the fuel pressure is significantly higher than the cylinder pressure. In this environment, the external surface of the upper injector body which is in contact with the engine oil (under the valve cover) and cooling jackets of the cylinder head, runs at temperatures on the order of the engine coolant (i.e. 90ºC) when the engine is fully warmed up. Table 1 summarizes the environmental conditions to which the injector is exposed. The tip of the nozzle is exposed to higher temperatures.

Table I: Injector environmental conditions.

Injector Environmental Conditions			
	Minimum	**Nominal**	**Maximum**
Body Surface Temperature	-40ºC	90ºC	12 ºC
Nozzle Tip Temperature	-40ºC	200ºC (est.)	30 ºC (est.)
Fuel Pressure	50 bar	100 bar	250 bar

Injector Design and Function

In an effort to provide high instantaneous flow with hydrogen (about 4 g/sec to 6 g/sec instantaneous flow, with 100 bar supply), a new injector family was derived from a similar natural gas research injector. This injector uses piezoelectric actuation in place of magnetostrictive actuation previously used for natural gas injectors. Mass delivered is controlled with pulse-width.

In simple terms, the injector is composed of 4 main sub-assemblies (Figure 2):

1. **Body & cap** – contains the pressurized fuel
2. **Piezoelectric actuator** – provides opening and closing motion of the moving parts
3. **Hydraulic compensator** – allows passive adjustments for variation in part tolerances during assembly, thermal changes during normal operation, and normal wear over the life of the injector.
4. **Needle and nozzle** – directs and controls the flow of fuel into the combustion chamber.

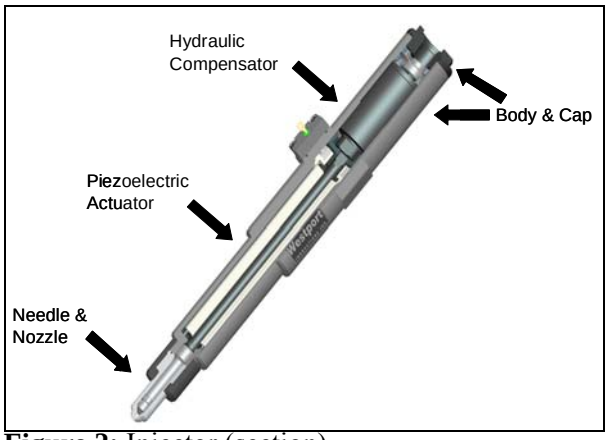

Figure 2: Injector (section)

Both the hydraulic compensator and the needle are pre-loaded with a spring. To open the injector, electrical charge is applied to the piezoelectric actuator in a controlled manner with a special electronic driver. As the piezoelectric element lengthens (either 100 µm or 130 µm, depending on actuator model), it pushes on the hydraulic compensator which in turn lifts the needle. Over the very short injection period, typically 5 msec or less, the relative motion inside the hydraulic compensator is minimal. As the needle lifts, it admits hydrogen through the nozzle, roughly in proportion to the needle lift. At the end of the injection period, the electric charge is drained from the piezoelectric actuator, its length is reduced and the whole assembly returns to the closed position.

It can be seen from Figure 2 that injector is normally closed when de-energized. It is also noteworthy that special circuitry in the injector (bleed resistors) and the electronic driver are used to guarantee closure of the injector for any failure mode involving the main harness or driver circuitry. The electronic driver was developed, like the injector, for engine research in a test cell. A more compact injector driver design would need to be developed for multi-cylinder engines or vehicle demonstration.

Early screening tests examined possible interactions between the piezoelectric ceramic material and the hydrogen fuel, but there were no significant operational issues during very short term exposure (the failure of the epoxy has been detailed, and reaction products at the electrode assembly have been identified, by PNNL per DOE-OVT FY07 Final Report).

Hydrogen Single Cylinder Test Cell Results

Recent engine development work described here has been performed at Ford Motor Company using a single cylinder research engine to determine the benefits of direct injection with hydrogen. The investigation examined the effects of injection strategy on engine efficiency, emissions and power density. Injector performance was closely monitored including flow rate, response and dynamic range over many different rail pressure and engine conditions. Durability related measures such as static leakage versus pressure and operational time were also closely tracked. A picture of the test cell and some specifications are shown in Table II and Figure 3 respectively.

Table II: Test cell and engine specification.

Type	Ford single cylinder design
Bore	80-92 mm, 89 typical
Stroke	80-100 mm
Displacement	0.4 to 0.6L
Compression Ratio	Variable (approx.) 9:1 to 16:1
Rated speed	6000 RPM
Max. speed	7000 RPM
Max. cylinder pressure	120 bar
Number of valves	2 intake, 2 exhaust
Valve Sizes	35mm intake 30mm exhaust
Valvetrain	DOHC, direct acting mechanical bucket, toothed belt, 230 deg duration event
Max. valve lift	9.5 mm / 9.5 mm
Lubrication	Dry sump
Cylinder liner	Wet

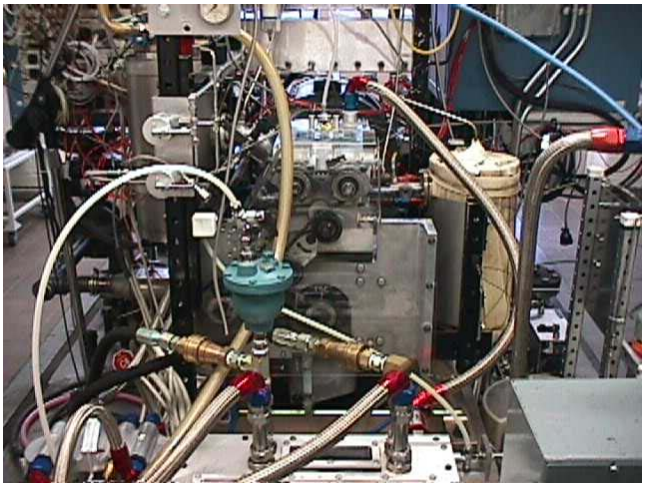

Figure 3: Engine test cell located at Ford Motor Company.

The wide flammability limit of hydrogen affords great freedom to injection strategies with which to improve engine efficiency. Further, gasoline-type fuels generally create high levels of CO and soot if injected as a liquid into the combustion chamber after the spark, but with a carbon-free fuel this, of course, is not a limitation.

As shown in Figure 4, four basic injection strategies are shown in both a low load and high load condition as related to engine bottom dead center (BDC), intake valve closure (IVC), and combustion (TDC) positions. With a sufficiently fast response injector, it is possible to further divide each injection event into multiple injections for additional mixing control to further optimize efficiency and NO_x emissions.

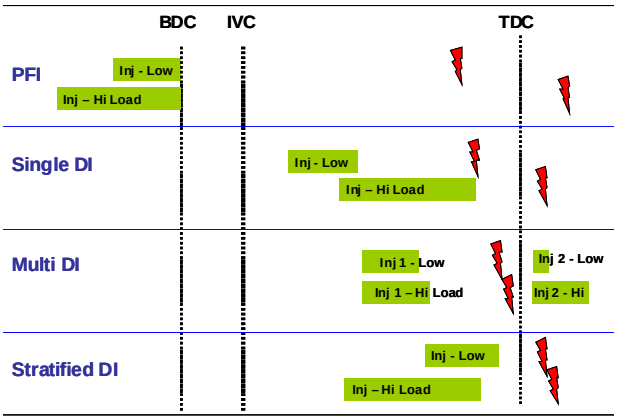

Figure 4: Comparison of injection strategies.

A key focus of Ford's approach to hydrogen engine development is to pursue efficiency improvements. Cycle fuel efficiency directly addresses customer fuel costs on board storage requirements and range. With the goal to exceed typical automotive diesel-cycle efficiency levels, the test program continually developed the single cylinder research engine over the 3 year duration of this program. When applying published friction levels from a production multi-cylinder engine (0.7 bar @ 3000 RPM per FEV, 4.8L), a brake thermal efficiency of 45% is demonstrated, as shown in Figure 5. *One of the 2010 US Department of Energy Office of Vehicle Technology goals for H2ICE's is a* ***peak thermal efficiency of 45%***

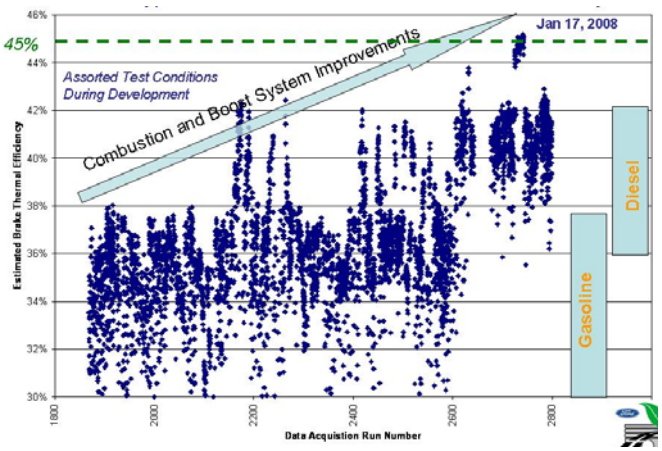

Figure 5: Brake Thermal Efficiency comparison between research hydrogen engine and typical automotive gasoline and diesel peak efficiency

Technical Challenges

Four issues are critical to the success of the hydrogen direct injector technology (Figure 6):

1. Impact related wear at needle/seat interface.
2. Sliding wear between lower needle and nozzle/guide surface.
3. Hydrogen diffusion into dielectric coating or piezoelectric actuator.
4. Integrity of seal in hydraulic compensator.

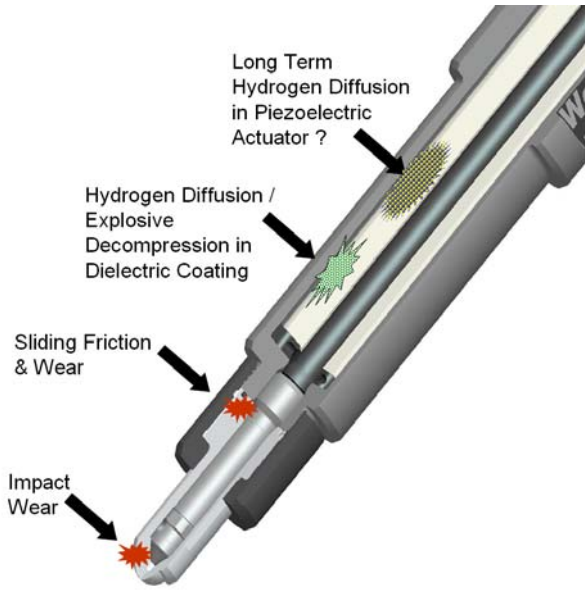

Figure 6: Critical technical challenges of the H-ICE direct injector.

The needle in Figure 6 is very precisely guided by the upper cylindrical surface on the nozzle. Using special honing and matching techniques, the nominal clearance is only 2 μm (radial). The needle and the nozzle use hardened tool steels of different compositions. Furthermore, the needle currently uses a commercial protective coating with very high hardness to protect against galling (cold welding between metals) which was seen earlier in another injector design (solenoid type) where there was sliding. The coating (applied to the outside of the needle) has only a moderately low friction coefficient (μ = 0.1 to 0.2).

The effects of hydrogen exposure on tribological characteristics have been investigated for hydrogen internal combustion engine needle-nozzle material interface combinations. Scuffing-resistance, identified as the critical tribological properties for the needle-nozzle component, was evaluated for candidate needle-nozzle materials with different hydrogen exposure levels. Tests were conducted under pin-on-flat reciprocating sliding in an inert (argon) environment to eliminate the oxidation effects. The onset of scuffing was chosen as a critical parameter in these tests because the onset of scuffing can quickly lead to catastrophic failure due to the tight geometric tolerance between the needle and nozzle.

PNNL, in conjunction with several commercial suppliers, Argonne National Laboratory, and Oak Ridge National Laboratory have explored several advanced coatings for sliding-wear applications in injector needle-nozzle applications. PNNL has developed two dedicated high pressure autoclaves (Figure 7, reported in DOE OVT FY07 report) for performing friction/wear studies with a special reciprocating pin-on-flat test rig in hydrogen. The autoclave is also used to drive hydrogen diffusion issues in various components and materials.

The friction and wear characteristics of metallic materials depend upon several factors, including material conditioning, environment, lubrication, and in the case of many materials, the growth of surface oxide films. Within a hydrogen service environment, which by definition is chemically reducing, the progressive loss of the surface oxide by wear will result in bare surface contact, commonly resulting in increased friction and wear.

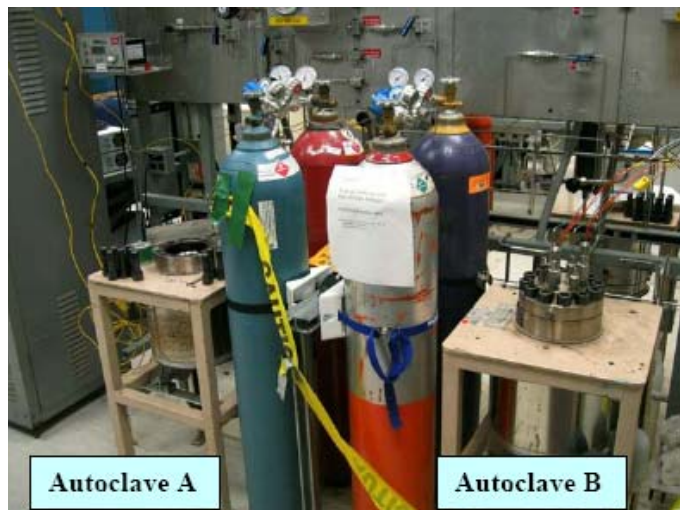

Figure 7: PNNL Autoclave A and B (1 to 300 bar, 20ºC to 300ºC capability). Completed and reported in DOE-OVT Hydrogen Materials Compatibility Final Report, FY07.

Material Selection

The candidate needle and nozzle materials were jointly selected by Ford Motor Company, Westport Innovations, and PNNL. Substrate materials, shown in Table III, included M2 tool steel procured with certification and heat treated to Rc = 60-64 (Metal Samples, Alabama, USA) and J-10 steel (LE Jones, Ohio, USA), a Co-rich steel with Rc = 54. Each was polished with 1μm diamond and a colloidal solution

(Beuhler, USA) to achieve a surface roughness in compliance with ASTM tribological test standards. Each of these surface roughness were achieved prior to coating the samples with either DLC or nanolaminate architectures.

Table III: Specifics of the substrate materials procured and subsequently coated for model needle-nozzle friction and wear.

	M2 (Tool Steel)	J-10 (LE Jones – Triballoy T400)
C	0.87	0.08
Co		Balance
Cr	3.9	7.5-8.5
Fe	81.33	
Mn	0.3	
Mo	4.78	26.5-29.5
Ni		3.0 max(Ni + Fe)
P	0.22	0.03
S	0.001	0.03
Si	0.24	2.2-2.6
V	1.78	
W	6.09	

Diamond-like carbon (DLC) coatings had been found to perform well in hydrogen during the course of this program (refer to FY07 report) and thus, it was determined that this would be a primary pursuit of this research in FY08. Several suppliers of DLC, each with a unique formulation, were contracted to coat 16 samples (10 M2 substrates and 6 J-10 substrates) with their formulation (Figure 8). The DLC suppliers selected were as follows:

A. Morgan Ceramics (Ohio, USA)
B. Ion Bond (New York, USA)
C. Argonne National Laboratory

PNNL, with Westport Innovations, has worked with Dr. Ali Erdemir of ANL to supply nearly-frictionless carbon (NFC) coatings for this program. These coatings are some of the most advanced DLCs in the world and are negotiations are underway to license this technology to the commercial sector. We are very thankful for ANL's participation in this project.

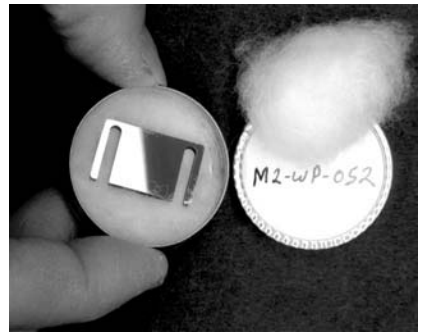

Figure 8: As-received DLC substrate sample from supplier.

Carbon coatings can be characterized and classified by the atomic bonding in each coating. The ternary phase diagram for carbon films is provided in Figure 9 indicating the relationship between hydrogen content, the carbon hybridization, and the type of film produced. Hard DLC has a relatively high sp^3 bond concentration and may exhibit more reactivity to hydrogen, leading to a higher coefficient of friction in a hydrogen atmosphere. Nearly-frictionless carbon has a relatively high concentration of sp^2 hybridized bonds, which are much more passive with regards to hydrogen.

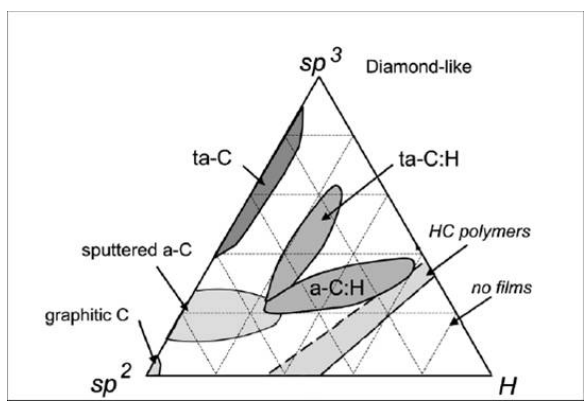

Figure 9: Ternary phase diagram for carbon films: diamond, graphite, and hydrocarbons. ta-C is tetrahedral amorphous carbon.

Raman spectroscopy was conducted to obtain a more complete understanding of the differences in DLC structure between the various suppliers. For carbon and carbon containing films, Raman scattering spectra depend on the following parameters:

a. the presence of sp^2 rings or chains
b. bond type variety or disorder
c. the ratio of sp^2/sp^3 hybridized carbon
d. clustering

Raman spectra of disordered carbon materials typically consist of two overlapping peaks, termed G and D, which reflect the character of the sp^2 hybridized bonding sites. The G peak (~1560) is due to bond stretching of all pairs of sp^2 atoms in both rings and chains. The D peak (~1360) is a reflection of the breathing modes of sp^2 atoms in rings. Evaluating the results of our analysis in Figure 10, the larger D peak for the NFC from ANL suggests a higher percentage of ring structures, indicating a more **graphitic carbon structure.** Contrary, a weaker relative D peak ratio such as that exhibited in the Ion Bond materials is indicative of a more disordered structure or one more closely resembling tetrahedral amorphous carbon. The Raman spectra from the Morgan Ceramic materials fall in the middle of these two extremes.

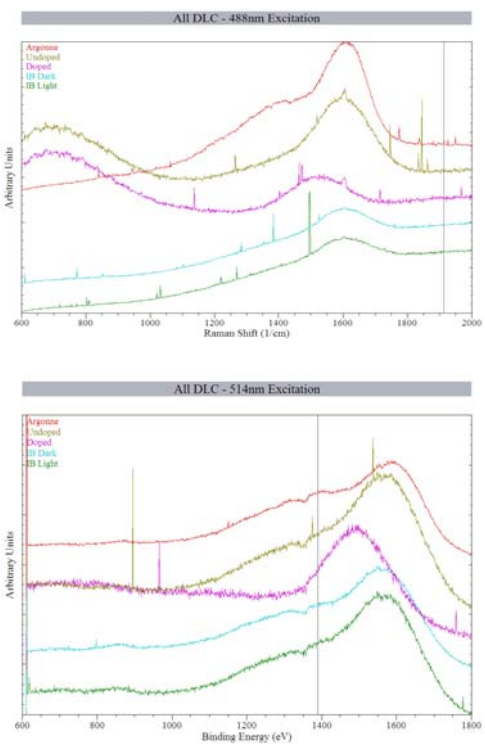

Figure 10: Raman excitation results at 488nm (top) and 514 nm (bottom). The top peak is the ANL DLC, "undoped" and "doped" refer to the Morgan Ceramic materials, and the two bottom spectra reflect Ion Bond materials.

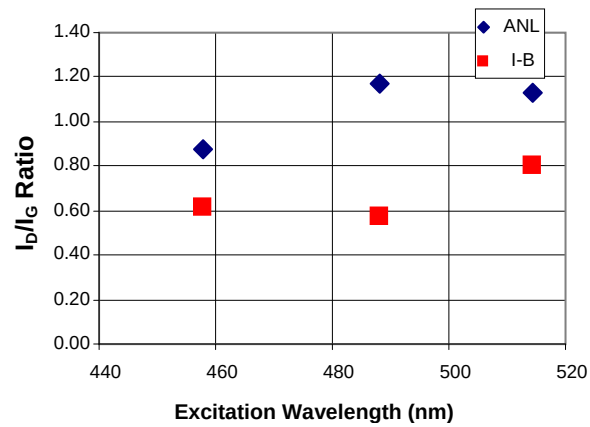

Figure 11: A comparison of the ratio of the D and G peak intensities (I_D/I_G) from Ion Bond and ANL indicating unique differences in the DLC structure of each across multiple excitation wavelengths.

Further analysis of all the data, in this case comparing only the ANL and Ion-Bond materials, accentuates the structural differences in the two DLCs (Figure 11). For example, note that the I_D/I_G (ratio of the D and G peak intensity) is consistent at three different wavelengths measured. There is a clear trend and this indicates the structure of these two advanced materials is quite different, and will have unique performance characteristics.

Received samples were tested using nanoindentation to determine hardness and modulus (Figure 12). Pertinent structural information can be obtained from these plots such as the following:

1. The doping of the Morgan sample appears to have been detrimental both for mechanical properties and wear in hydrogen
2. The Argonne NFC had the lowest observed modulus and hardness values
3. This agrees with suggestion (from Raman) that there is a significant fraction of chain or sheet carbon in the Argonne DLC.

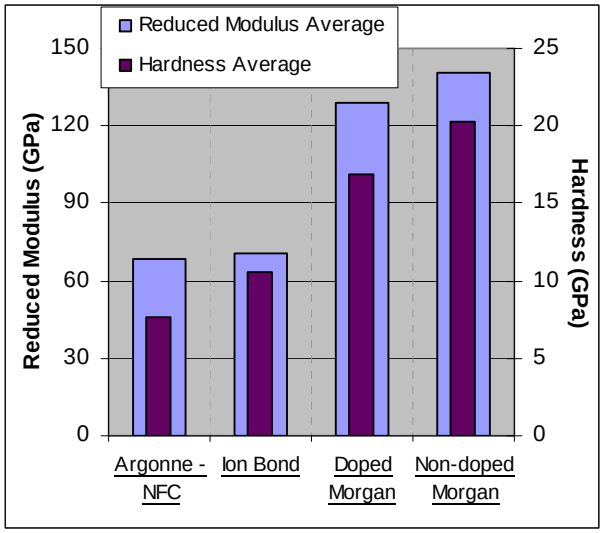

Figure 12: Nanoindentation results of hardness and reduced modulus of the DLC coatings tested. Note the reduced modulus is reported due to unknown Poisson ratio of each material. Furthermore, two samples from Morgan are provided as the company had two varieties of DLC submitted to the program.

Pins were produced from both M2 and J-10 base materials, and these were uncoated during testing. Pin materials were matched with base materials. Sliding tribology testes were performed in both argon and in hydrogen; refer to FY07 report for results indicating that a non-oxidizing environment was found to be preferable for conducting these tests. Samples were also tested after exposure to 4000 psi hydrogen pressurized for 100 and 500 hours. A total of 88 sliding tribology tests were conducted in FY08; the objective was to (1) determine threshold for scuffing for all DLC base materials in pure Ar, and (2) conduct tribology tests after H_2 exposure in Ar and H_2 (10 psi). No high-pressure in-situ hydrogen tests were run as it was determined that the tribo instrument motor will fail after one test in high-pressure hydrogen.

Upon receipt and characterization of the substrates, and preparation of the pins, reciprocating sliding friction-wear tests were conducted to the following protocol:

1. The desired contact stress was determined.
2. The polished pin diameter was determined.
3. The necessary load was determined:
   Insert pin radius
   Conduct Hertzian stress model
4. Adjust load until desired stress is obtained.
5. Secure pin in carriage; secure weight(s) to pin carriage.
6. Ensure that pin aligns with wear plate.
7. Attach pin carriage to tribometer (Figure 13).
8. Run test until scuffing occurs.
   Scuffing – sliding-induced contact damage to a bearing surface, usually associated with asperity-scale plastic deformation.

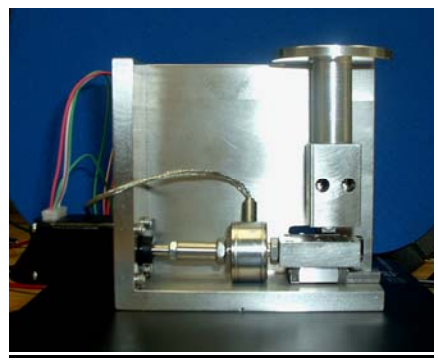

Figure 13: PNNL sliding tribometer.

Each substrate material and DLC supplier coating was initially tested in argon to determine the threshold for scuffing – the contact stress at which a sample could reciprocate and not attain scuffing for at least 600 cycles. Several tests were run for each sample material; Figure 14 provides the results. These results indicate that in tests in the non-oxidizing argon environment on samples in 'As-received' condition, the ANL DLC performs to a much higher contact stress than other materials tested.

As seen in Figure 14, the Argonne National Laboratory DLC material was superior by a significant amount as compared to all other DLC materials tested. It is noted that this is in the 'As-Received' condition with no exposure to hydrogen, tested in an argon non-oxidizing environment.

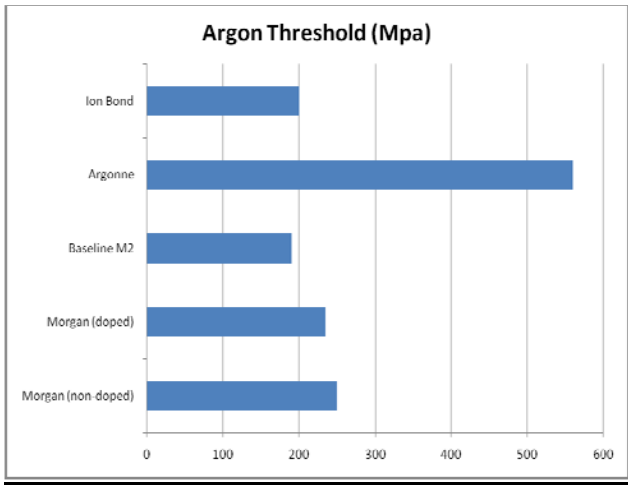

Figure 14: The contact stress (MPa, x-axis) that determines the onset of scuffing for each of the DLC materials tested.

The next set of experiments undertaken was to determine the effect of hydrogen exposure on each of the surfaces. The effect of hydrogen on DLC must be taken into account as the exposure duration and pressure affects the friction and wear properties, and depending upon the coating, perhaps for the better. For example, the M2-Morgan non-doped DLC actually appear to perform longer and at a lower coefficient of friction after exposure to 300 Bar hydrogen for 100 hours.

Table IV indicates results of Morgan non-doped samples and it can be seen that the 'As-received' material reaches scuffing at 250 MPa. After exposure to hydrogen at 300 Bar/100 hours, tested in *either* argon or hydrogen at contact stresses 100 MPa *higher* than 'As-received', each sample ran for 1000 cycles and did not reach a scuff condition all the while running at or below the 'As-received' coefficient of friction. This result was evident to some degree in all of the DLC materials tested.

Table IV: Sample results for M2 substrates coated with Morgan non-doped DLC, tested in various conditions. Note the hydrogen exposed materials had a higher contact stress tolerance.

Environment	Test Stress	CoF
Argon – as received	250 MPa Threshold to scuff	0.05-0.2
H2 charged 300 Bar – 100 hours/Argon	353 MPa	0.04
H2 charged 300 Bar - 100 hours/H2 tested ambient pressure	349.5 MPa	0.07

Subsequent experiments were conducted at a contact stress of 350 MPa to compare all sample materials. The objective was compare all DLC materials that had been exposed to a 100% hydrogen environment at 300 Bar for 100 hours. All tests were run in Argon. Figure 16 indicates the performance of the candidate DLCs, and two PNNL nano-laminates for comparison, with the coefficient of friction reported on the x-axis. From these results, it is clear that the Morgan Ceramic non-doped DLC outperforms all other coatings tested by a significant measure.

Table V provides an overview of selected tests and parameters; these are provided as an example.

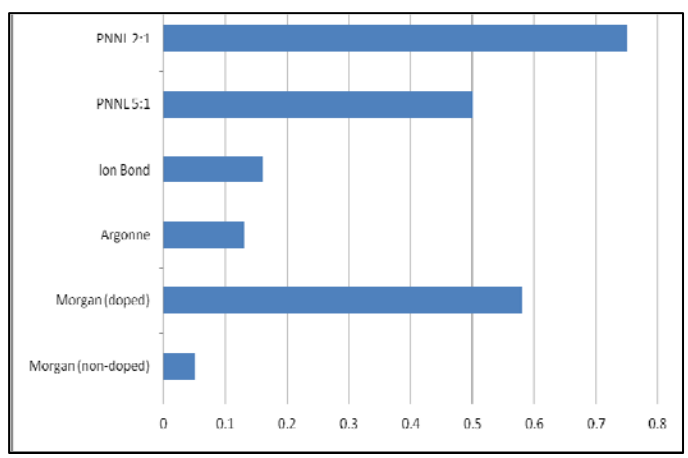

Figure 16: Coefficient of Friction of coatings exposed to 300 Bar/100 Hour Hydrogen, tested to 1000 cycles. Morgan (doped) scuffed at 42 cycles.

Table V: Selected sample test results and parameters. A total of 88 tests have been performed.

Plate	Coating	Pin	ENV.	Max. Tensile Stress (Mpa)	Plate Scuff?	Vickers	Rc	CoF	#Cycles to Scuff	CoF at Scuff End
M2-WP-005	Morgan (D)	M2-P-039	Ar	191	Y	2381		0.65	190	0.7
M2-WP-006	Morgan (D)	M2-P-036	H	349	Y	2167	78.6	0.5	33	0.55
J10-WP-033	Morgan (D)	J10-P-003	Ar	250	Y	2361		0.5	27	0.9
J10-WP-031	Morgan (D)	J10-P-012	H	352	Y	-		0.4	42	0.6
M2-WP-010	Morgan (ND)	M2-P-034	Ar	207	N	1889	79.6	0.05	1000	0.05
M2-WP-009	Morgan (ND)	M2-P-038	H	353	N	2167		0.07	1000	0.07
J10-WP-034	Morgan (ND)	J10-P-009	H	344	N	2385.5		0.05	1000	0.05
M2-WP-025	Ion Bond	M2-P-027	Ar	156	N	1172.8	71.3	0.07-0.17	1000	
M2-WP-053	Ion Bond	M2-P-038	Ar	200	Y	1700	77.5	0.15	200	0.3
M2-WP-024	Ion Bond	M2-P-026	H	349	N	1294.9	72.8	0.16	1000	
J10-WP-043	Ion Bond	J10-P-010	H	352	N			0.19-0.22	1000	
M2-WP-015	ANL	M2-P-029	Ar	250	N	1326	73.1	0.22		
M2-WP-015	ANL	M2-P-040	Ar	453	N	1326	73.1	0.05	1000	
M2-WP-015	ANL	M2-P-036	Ar	560	Y	1326	73.1	0.1	~100	0.5
M2-WP-015	ANL	M2-P-037	H	350	N	1326	73.1	0.13	1000	
M2-WP-013	ANL	M2-P-029	H	561	N	1587.8		0.11	1000	
J10-WP-037	ANL	J10-P-011	H	351	N	2018		0.09	1000	

PNNL Nanolaminate Coatings

PNNL undertook an effort in FY08 to produce a series of nanolaminate coatings to provide harder, more resistant surfaces that are not susceptible to hydrogen diffusion by stacking different materials or phases in the nanometer-scale range. These structures, known as nanolaminates, have been proven to be particularly effective in improving the mechanical strength, hardness, and toughness of the component materials by several mechanisms. The most important of these is through the interruption of crack propagation at the interface of each layer. When a crack reaches an interface, the stress at its tip is dissipated into the stress field created by the lattice mismatch between the two phases. This stress field can also be utilized to create areas of localized compression in some layers which will serve to increase the effective yield strength in that medium. Through the judicious choice of materials systems, a nanolaminate can be designed with alternating layers of a hard material and one with lubricating qualities. This technique is also technically mature, and is ideal for creating application-specific nano-structured materials.

The materials that were explored are as follows:

1. CrN / BN
2. $Cr^{-}_{2}N$ / BN
3. SiC_4 / SiC_xN_y
4. B_4C / BC_xN_y

Magnetron sputtering was used to produce these coatings. In most cases two targets have been used, with the deposition rate of each source individually controlled by applied power. Conditions have been chosen such that the correct stoichiometry is produced with an identical ratio of reactive gas. Substrate rotation speed was adjusted to produce the correct nanolaminate period with the substrate heated to 300°C to ensure production of desired phase.

Boron carbide/boron carbonitride nanolaminates have been one of the nanolaminates explored during the course of this development effort. B4C has been selected because it is second only to SiC in measured modulus. To produce these laminates, these materials have been deposited simultaneously with SiC/SiCN nanolaminate depositions, with the nitrogen replacing the boron structure (as opposed to carbon). In Raman analysis of these coatings, there is no free carbon observed. During the deposition process, the nitrogen atmosphere has been varied to produce different coating structures. Figure 17 indicates the effect of nitrogen atmosphere on the atomic percent of the coating deposition condition. The resultant mechanical property of the coating is altered by this structural change; Figure 18 is a verification of the property variation.

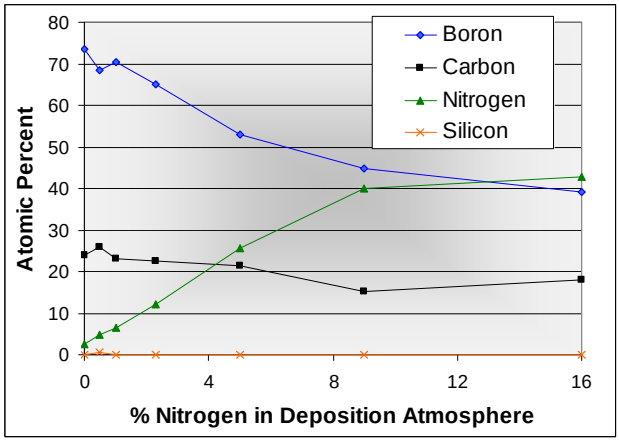

Figure 17: Atomic percent of B, C, N, and Si as a function of percent nitrogen in the deposition chamber.

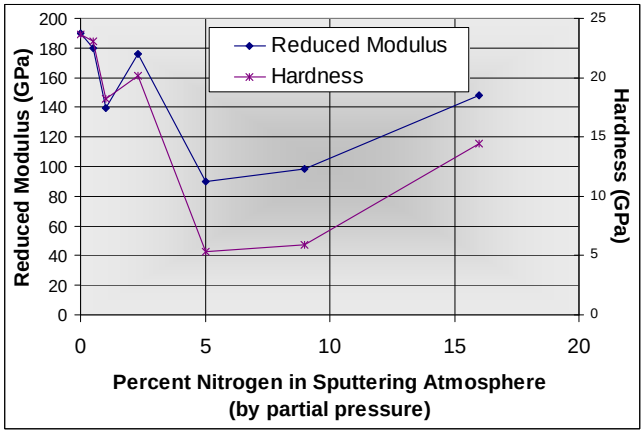

Figure 18: Reduced modulus and hardness change as a function of %N in the sputtering chamber.

Mechanical properties of these coatings have been characterized with nanoindentation; specifically, hardness and reduced modulus have been measured. All coating substrates have been prepared with a Cr adhesion layer, common in sputtered hard coatings. The data is Figure 19 suggests the BN is the hardest coating exhibiting the highest reduced modulus; additionally, from this data it appears one could 'tailor' the coating property to a selected application.

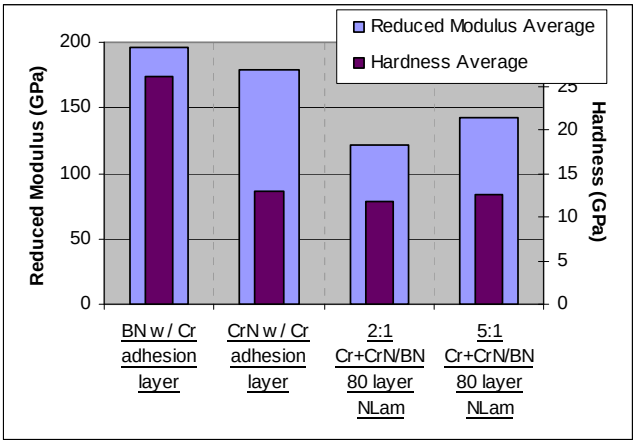

Figure 19: Reduced modulus and hardness of each material combination produced in the PNNL nanolaminate development program.

During this development effort, silicon carbide/silicon carbonitride nanolaminates have been produced by successfully varying the stoichiometry between SiC and SiCN. It was found that increasing the nitrogen content within the deposition chamber creates a nanoheterogenous film (Specifics of the atomic content are presented in Figure 20). Additionally, it can be seen from Figure 21 that the hardness and modulus follow a decreasing trend with an increase in nitrogen content.

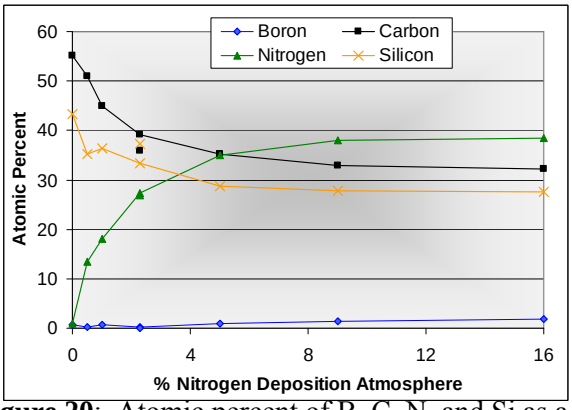

Figure 20: Atomic percent of B, C, N, and Si as a function of percent nitrogen in the deposition chamber.

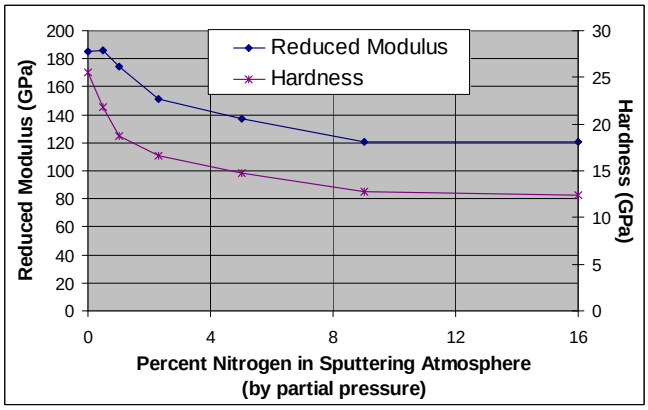

Figure 21: Reduced modulus and hardness as a function of N in the sputter chamber.

A direct comparison of all coating mechanical properties is presented in Figure 22. In general, the reduced modulus and hardness of each PNNL nanolaminate is greater than the DLCs produced by commercial suppliers. The exact application of these materials will be explored in future work; the application to this project is an impact resistant injector needle tip that could withstand the durability challenges that occur with a 10000 hour service life..

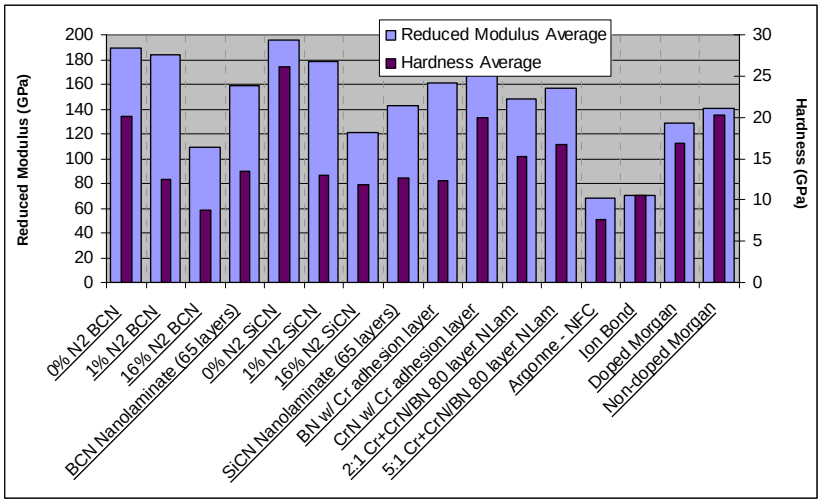

Figure 22: Reduced modulus and hardness of DLC coatings compared directly to PNNL nanolaminates.

Sliding Impact Characterization

PNNL, in conjunction with Dr. Peter Blau, ORNL, conducted a series of sliding-impact tests of several coatings on the new ORNL test apparatus depicted in Figure 23. This apparatus has been designed and built at PNNL by Dr. Blau and his colleagues; the first series of experiments carried out on the instrument have been for this project. This tool has great promise to test injector and other materials up to 300C; there is a need to further develop the technique but eventually this will be a great asset to the DOE Laboratory system.

Samples were prepared by coating the edges of square blocks that were then fit within the apparatus (Figure 24 and 25) coated both at PNNL and at ANL (NFC – DLC). These samples were then run in a series of tests both at room temperature and 300C.

Tests were conducted in a variety of conditions as outlined in Table VI. Images of samples that have been tested are provided in Figures 26 and 27; each figure description indicates the conditions of the test.

One of the challenges with the technique will be to accurately quantify the outcome; as can be seen from the images, the wear pattern is difficult to quantify. This is likely due to difficulties in aligning the sample block to the cylinder. Future work will attempt to solve these test technique challenges.

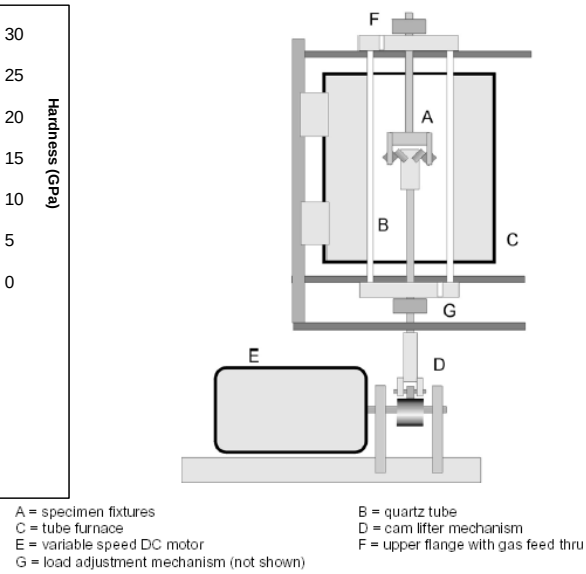

Figure 23: ORNL sliding-impact apparatus (courtesy Dr. Peter Blau, ORNL).

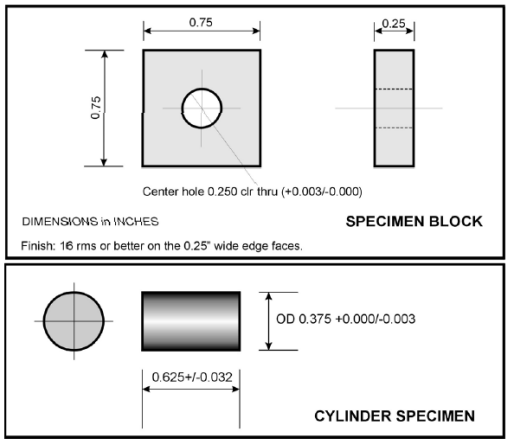

Figure 24: ORNL sliding-impact sample geometry (courtesy Dr. Peter Blau, ORNL).

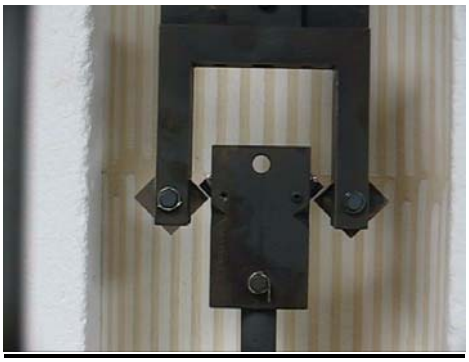

Figure 25: ORNL sliding-impact apparatus with sample blocks installed.

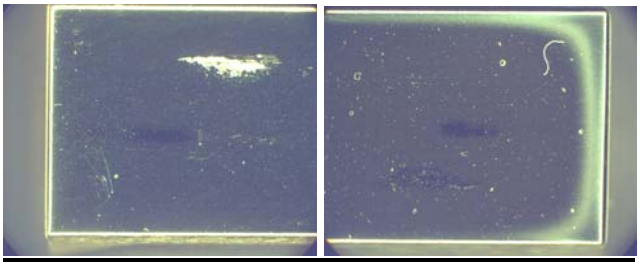

Figure 26: Two different test sample wear tracks shown after 15000 cycles of room temperature wear.

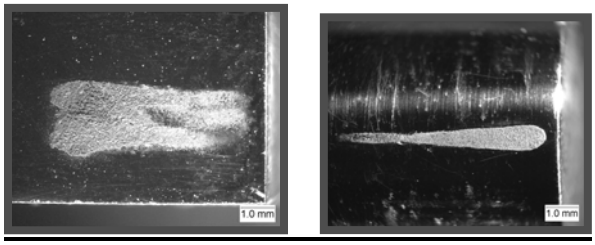

Figure 27: Block specimen pitted and covered with debris (Left) and pin specimen wear zone (right). Room temperature tests of non-coated M2 – 15,000 cycles.

Table VI: A list of all sliding impact samples tested at ORNL, with test conditions.

Left block matl	Right block material	Load (N)	Rate (rpm)	Rate (cyc/s)	Temp (C)	Test length (cyc)
304 B4C/BCN 65 layer lam	**304** SiC/SiCN 65 layer lam	29.6			room	
304 SiC/SiCN 65 layer lam	**304** B4C/BCN 65 layer lam	29.6	115	1.9	room	5117+575
304 B4C/BCN 65 layer lam	**304** SiC/SiCN 65 layer lam	29.6	115	1.9	room	4966
M2 SiC/SiCN 65 layer lam	**M2** B4C/BCN 65 layer lam	29.6	115	1.9	300	5175
M2 B4C/BCN 65 layer lam	**M2** SiC/SiCN 65 layer lam	29.6	253	4.2	300	10484
M2 BCN 16%N2	**M2** SiCN 16%N2	29.6	40 / 152		300	5014
M2 Cr+CrN/BN 2:1 N2/Ar 80 layer lar	**M2** Cr+CrN/BN 5:1 N2/Ar 80 layer la	29.6	180	3.0	room	15125
M2 Cr+CrN/BN 5:1 N2/Ar 80 layer lar	**M2** Cr+CrN/BN 2:1 N2/Ar 80 layer la	29.6	258	4.3	300	15000
M2 Argonne NFC DLC	**M2** Argonne NFC DLC	29.6	258	4.3	room	15000
M2 Argonne NFC DLC	**M2** Argonne NFC DLC	29.6	250	4.2	300	15157
M2 B4C/BCN 65 layer lam	**M2** SiC/SiCN 65 layer lam	29.6	234-218	~ 3.8	300	14968
M2 SiC/SiCN 65 layer lam	**M2** B4C/BCN 65 layer lam	29.6	235	3.9	room	1001
Bare M2	Bare M2	29.6	245	4.1	room	15002
Bare M2	Bare M2	29.6	245	4.1	300	15001

Injector Needle-Nozzle Prediction Tool

PNNL has undertaken the task to refine a predictive engineering tool in FY08 and utilize the tool to model a sliding friction test case performed at PNNL. The objective has been to develop a predictive engineering tool to model the contact stress of the needle-nozzle interface under different sliding-impact conditions to aid in material and coating selection. This fiscal year the tool has been refined to address 2-dimensional axisymmetric cases of a surface coating on a wear surface with an uncoated pin. The model takes into account the contact radius, load, material properties, and in its current state addresses static contact stress. An obvious extension of this model would be to address sliding with friction to address the dynamic case, but the funds are not available in FY08 to extend the model.

When the injector needle opens and then closes, the seat and needle do experience a small amount of wear. Upon close analysis, the needle/seat interaction is actually one of sliding impact as the needle contacts the nozzle. Inevitably some energy is dissipated at the contact points. During break-in it has been observed the contact patch (between the needle face and nozzle seat) will experience some plastic deformation until reaching equilibrium. Typically the contact patch is an annular ring (~6 mm diameter) with has a nominal width of 250 μm.

Figure 28 shows an example of analysis used to understand the effect of impact on the needle which is made of a hardened tool steel. Although, it is only very small region, this example shows that for a peak impact force of approximately 2000 N (based on elastic energy considerations) that the needle sealing surfaces approaches 500 MPa peak compressive stress (which is 15% of the material's yield stress). Apparent wear rate at the needle seat interface with the injector is considered to be low. However, occasionally, leakage has been observed due to slight surface damage after 1 to 20 million cycles.

The PNNL trials have addressed two test cases, both with M2 substrate and pin materials, reconstructed to determine the validity of the model to the test cases. Material properties of the samples are provided in Table VII. Each sample had a different load condition and contact stress, one with a load of 51.8g and the other with a load of 81.8g. While the tip radii were near equivalent, this created a different contact stress and a different sliding friction result (the lower loaded pin did not scuff, the higher loaded pin did scuff in actual experimental work).

Upon constructing the model, several features of the case were developed to aid the designer in making the coating and test condition selection including contact stress, Von Mises equivalent stress, and the specific coating stress. Figures 29-34 illustrate the output of selected trials; the results of each test condition

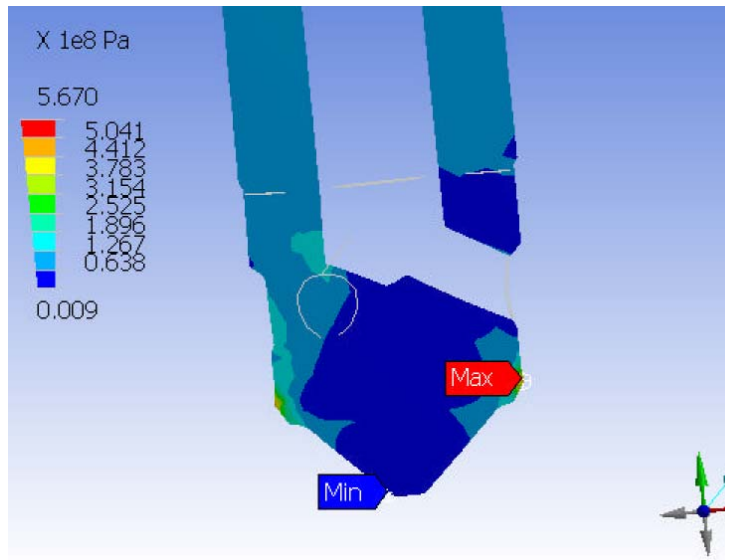

Figure 28: Stress contours in needle tip with 2000 N axial load (compressive stress x 108 Pa). Model constructed by Westport Innovations.

Table VII: Assumed model material properties. M2 Compressive strength is reported to be 2 – 3 GPa.

Material	Elastic Modulus (GPa)	Poisson's Ratio
Pin (uncoated M2)	200	0.3
Plate (coated M2)	200	0.3
Coating	500	0.3

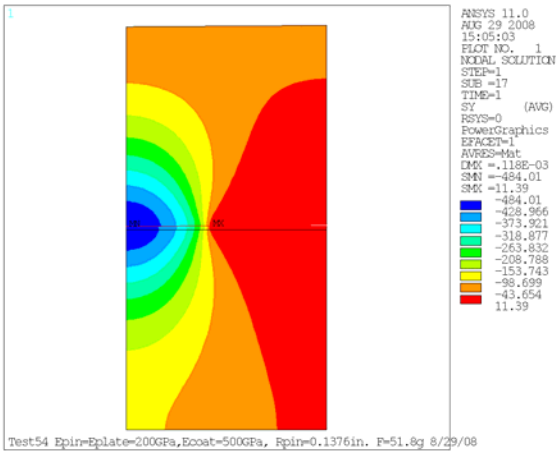

Figure 29: Analytical run with a pin radius = 0.137 in, and F=51.8 g. Contact stress for this case is 484 MPa.

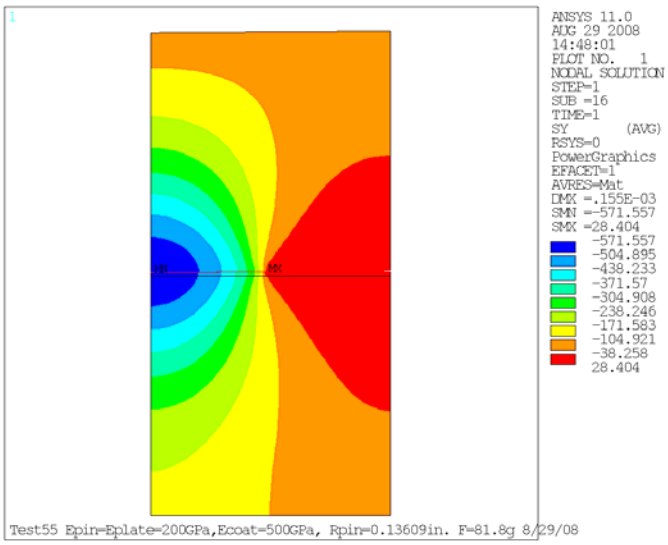

Figure 30: Analytical run with a pin radius = 0.136 in, and F=81.8 g. The equivalent contact stress resulted in 572 MPa.

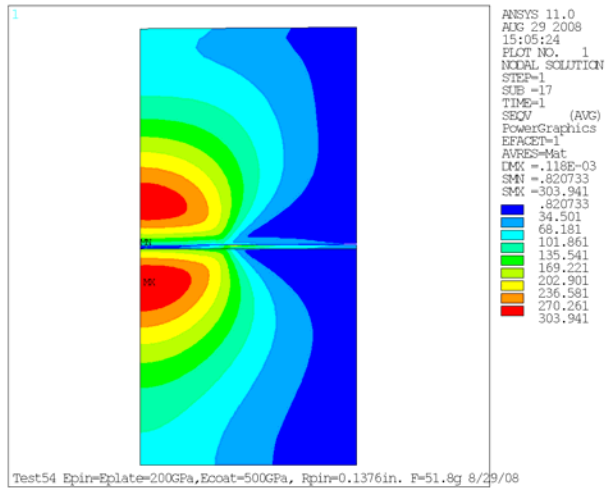

Figure 31: Analytical run with a pin radius = 0.137 in, and F=51.8 g. Von Mises equivalent stress for this case is 304 MPa.

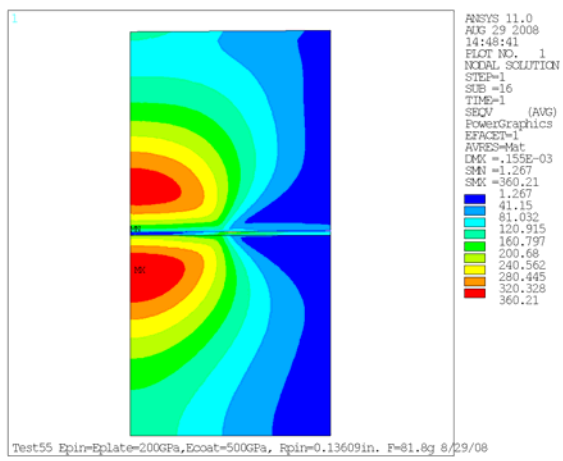

Figure 32: Analytical run with a pin radius = 0.136 in, and F=81.8 g. The von Mises equivalent contact stress resulted in 360 MPa.

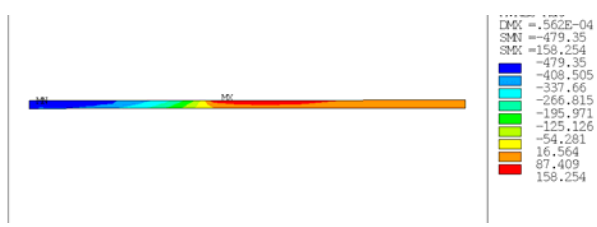

Figure 33: Analytical run with a pin radius = 0.137 in, and F=51.8 g. The coating tensile stress is 158 MPa, insufficient to cause scuff.

Figure 34: Analytical run with a pin radius = 0.136 in, and F=81.8 g. The coating tensile stress increases to 205 MPa, causing scuff.

Conclusions

This project has developed the following conclusions in FY08:

1. DLCs have been thoroughly explored and the following trends have been observed:
   - The hardness of certain tool steel materials appears to be slightly higher than that of the non-exposed samples.
   - Tool steel alloy composition is a significant factor determining the effect of hydrogen.
   - Previous hydrogen exposure does have an effect on frictional behavior. It appears beneficial for steels tested in argon but had mixed influence in air testing due to the oxidizing environment. Different dominant wear modes were observed; oxidized-wear in air and abrasive-wear in argon.
   - DLC coatings have been shown to improve greatly scuffing resistance.
   - ANL and Morgan ND coatings exhibited the highest threshold to scuff.
   - Morgan ND samples exhibited the lowest COF post-H_2 exposure, with ANL 2nd.
2. PNNL has successfully created a suite of nanolaminate coatings that may be tailored to hydrogen applications. These laminates are particularly important where hard, impact resistant surfaces are needed.
3. PNNL has worked with ORNL to further develop the sliding-impact test apparatus at ORNL. The test shows promise but it is felt additional trials are needed before quantitative data is procured.
4. PNNL has further refined the predictive engineering tool that is an aid to mechanical and materials scientists working in the area of friction and wear. The tool must include dynamic friction cases to be fully operational.

Key Words

Hydrogen, internal combustion engine, direct fuel injection, nanolaminate, diamond-like carbon.

Brief Description of Report

List of Acronyms Used

H-ICE – Hydrogen internal combustion engine
ICE – Internal combustion engine
DI – Direct inject
DLC – Diamond-like carbon
NFC – Near frictionless coating

Agreement 16304 – High Performance Valve Materials (HPVM)

P. J. Maziasz, and N. D. Evans
Materials Science and Technology Division
Oak Ridge National Laboratory
P.O. Box 2008, MS-6115
Oak Ridge, TN 37831-6115
(865) 574-5082; fax: (865) 754-7659; e-mail: maziaszpj@ornl.gov

N. S. L. Phillips
Advanced Materials Technology
Caterpillar Technical Center
14009 Old Galena Rd.
Mossville, IL 61552
(309) 578-5788; fax: (309) 578-2953; e-mail: phillips_nate@cat.com

DOE Technology Manager: Jerry L. Gibbs
(202) 586-1182; fax: (202) 586-1600; e-mail: jerry.gibbs@ee.doe.gov
ORNL Technical Advisor: D. Ray Johnson
(865) 576-6832; fax: (865) 574-6098; e-mail: johnsondr@ornl.gov

---

Contractor: Oak Ridge National Laboratory, Oak Ridge, Tennessee
Contract No.: DE-AC05-00OR22725

Objectives

- Characterize current engine exhaust seats and valves to define and understand temperature, performance and durability limitations
- Use understanding of the behavior of current valves and seats to enable advanced designs and/or selection of advanced materials and processing to upgrade temperature capability and performance/durability limitations.

Approach

- Support Caterpillar (CAT) partnership with diesel engine valve and seat suppliers to validate temperature/performance limitations of current technology, and facilitate upgraded seat and valve options that are commercially viable and can be supplied as prototype modified components for testing and evaluation.
- Analyze (at ORNL) the various seat and valve components from simulation-rig or engine testing to provide microanalysis to define the nature and causes of wear/degradation of exhaust valve/seat pairs, and compare to fresh components. Use detailed analysis data to define options for producing and testing components with upgraded performance and capability.

Accomplishments

- ORNL has obtained both fresh and Buettner-Rig wear-tested exhaust seats of standard J3 alloy and Pyromet 31V exhaust valves and completed initial microstructural and microcompositional analysis.
- Based on detailed microanalysis of the seat components, ORNL and Caterpillar were able to suggest processing modifications of the J3 seats that have the potential to mitigate lower temperature wear currently observed. Caterpillar is currently testing modified seats to characterize and evaluate performance upgrades.

Future Direction

- Address degradation mechanisms and evaluate alloy/processing modifications for exhaust valves.
- Obtain appropriate valve alloy precursors (rod-stock) of new alloys for testing and evaluation at ORNL

Introduction

This is a new ORNL CRADA project with Caterpillar, NFE-07-00995 and DOE, OVT Agreement 16304 that began earlier this year, and will last for about 2.5 years. This CRADA project is focused on addressing the wear and failure modes of current on-highway heavy-duty diesel exhaust valves and seats, and then on evaluating changes in valve-seat design and/or advanced alloys that enable higher temperature capability, as well as better performance and durability. The need for such upgraded valve-seat alloys is driven by the demands to meet new emissions and fuel economy goals, which continue to push diesel exhaust component temperature higher. Requests for more detailed information on this project should be directed to Caterpillar, Inc.

Approach

Caterpillar will provide and analyze the baseline wear and mechanical behavior characteristics of engine-exposed valves and seats, and similar exposure of those components to laboratory simulation-rig testing at Caterpillar. ORNL will provide more in-depth characterization and microcharacterization of those valves and seats. Data will provide the basis for selecting and testing valve and seat alloys with upgraded performance. Caterpillar and ORNL will work with Caterpillar's various component or materials suppliers so that potential solutions are commercially viable, and so that prototype components are readily available for Caterpillar's test rig or diesel engine evaluation.

Upgrading various critical exhaust components should enable the increased engine temperatures needed to allow a 3% decrease in fuel consumption for on-highway trucks.

Technical Progress

Caterpillar

Caterpillar provided exhaust valve and seat materials of standard materials that had been wear-tested at various temperatures on the Caterpillar "Buettner" Rig (Fig. 1). Seats are a J3 Co-based superalloy. Exhaust valves are a Pyromet 31V Ni-based superalloy. After ORNL analysis of components, Caterpillar obtained trail seats with modified processing to improve wear-resistance.

Through their major seat-insert supplier, Caterpillar performed wear resistance evaluations, i.e., a "Plint Wear Test", using the conventional seat-insert material in a modified-processing condition with the base valve alloy. Seat insert materials were tested in various different surface conditions and at three different temperatures. Preliminary fractographic examinations of the wear scars between the tested pin and plate specimens were performed. Additionally, Caterpillar conducted a valve seat insert temperature analysis on valves at three nominal operating temperatures. Knoop microhardness measurements were acquired around the seat insert wear surface in 10° increments, at specific depths from the wear surface. Via calibration, hardness measurements were correlated to temperature around the insert wear surface. Caterpillar continued to facilitate dialogue and data exchange between the participants of this project and their major seat-insert supplier. Caterpillar is currently obtaining prototype seats with modified processing for testing and evaluation on the Buettner Rig next year.

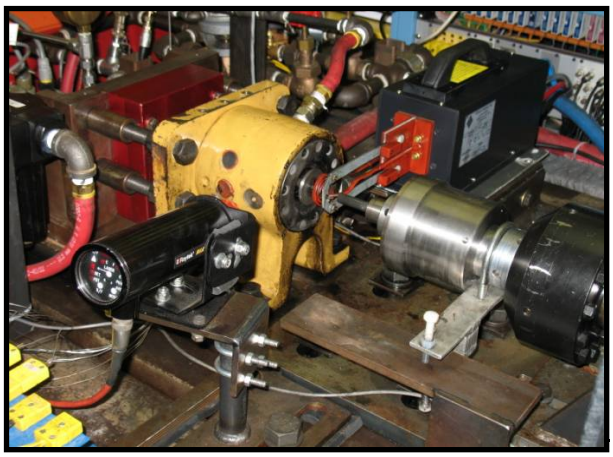

Figure 1. Buettner Rig engine simulation facility for testing high-temperature wear and performance of exhaust valves and seats at the Caterpillar Technical Center.

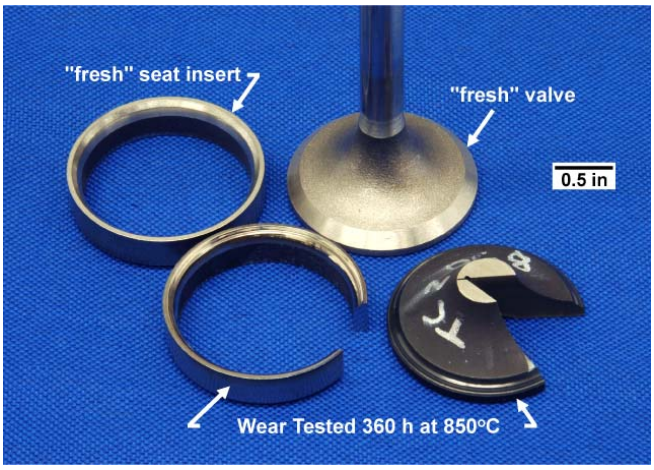

Figure 2. Valve and seat components, fresh and Buettner-Rig tested, received by ORNL from Caterpillar for detailed microcharacterization and analysis.

ORNL

ORNL conducted thorough microstructural and microcompositional characterization studies of the valve and seat components to define the detailed changes occurring at the oxidation-surfaces, and the underlying metal interface and bulk regions (including fresh and aged, non-wear control specimens) (Fig. 2). Combined SEM and XPS studies of surface oxides and sub-surface regions were completed to benchmark microstructures developed during specific aging schedules. Based on detailed analysis of wear-tested seat inserts, processing modifications were suggested that might mitigate some of the wear being experienced between seats and valves at lower temperatures. Caterpillar is in the process of evaluating and testing those changes for seats. ORNL is currently performing such detailed characterization of the exhaust valve components. Analysis of exhaust valve components will continue and be completed next year.

Conclusions

Caterpillar completed testing and characterization on an initial set of exhaust valves and their matching seats previously, and then provided fresh exhaust valves and seats to match with those wear-tested in the lab-test rig to ORNL for further analyses. Based on initial ORNL analysis, Caterpillar defined modified processing options for seats with increased wear-resistance. Caterpillar conducted wear-resistance tests, fractographic examinations of plate and pin wear specimens, and a seat insert temperature analysis. Buettner-Rig testing of seats with modified processing at Caterpillar is planned for next year.

ORNL conducted in-depth microcharacterization studies of non-wear valve seat components. Combined SEM and XPS studies of surface oxides and sub-surface regions were completed to benchmark microstructures developed during specific aging schedules. Preliminary results on seat inserts suggested modified processing to mitigate lower temperature wear. ORNL will continue and complete microanalysis of worn valve surfaces next year.

Publications/Presentations

None

Special Recognitions and Awards/Patents Issued

None

Agreement 13329 - Mechanical Reliability of Piezoelectric Multilayer Actuators for Fuel Injectors

Hua-Tay Lin, Hong Wang, and Andrew A. Wereszczak
Ceramic Science and Technology Group
Oak Ridge National Laboratory
P.O. Box 2008, MS 6068
Oak Ridge, TN 37831-6068
(865) 576-1169; fax: (865) 574-6098; e-mail: wereszczakaa@ornl.gov

DOE Technology Manager: Jerry L. Gibbs
(202) 586-1182; fax: (202) 586-1600; e-mail: Jerry.gibbs@ee.doe.gov
ORNL Technical Advisor: D. Ray Johnson
(865) 576-6832; fax: (865) 574-6098; e-mail: johnsondr@ornl.gov

---

Contractor: Oak Ridge National Laboratory, Oak Ridge, Tennessee
Contract No.: DE-AC05-00OR22725

Objectives

- Apply established structural ceramic probabilistic design and reliability analysis to piezoelectric multilayer actuators (PMLAs).
- Generate required micromechanical property data on lead zirconate titanate (PZT) piezoceramics and macromechanical property data on PMLAs for input into the design and reliability analysis of the latter.
- Identify minimum mechanical performance requirements for fuel injector PMLAs.
- Adapt these strategies to improve reliability of PMLAs under candidacy for use in diesel engine fuel injectors.

Approach

- Evaluate PMLA reliability under representative service conditions.
- Link constituent piezoceramic micro-mechanical and PMLA macro-mechanical responses.

Accomplishments

- A piezodilatometer enabling accelerated fatigue and dielectric breakdown testing for PZT films and stacks has been designed, fabricated, and assembled. The calibration of the unit via the PZT thin film specimen was successfully accomplished.
- Identified ~30-50% strain degradation in commercial PMLAs after about 100 million cycles with significant loss of piezoelectric coefficients under a semi-bipolar electric sine waveform.
- Completed the DOE approval process for ORNL-Cummins CRADA entitled "Design Optimization of Piezoceramic Multilayer Actuators (PMLAs) for Heavy Duty Diesel (HDD) Engine Fuel Injectors

Future Direction

- Develop accelerated tests and database for candidate piezoceramics and PMLAs of Cummins.
- Measure and compare piezoelectric and mechanical reliabilities of tape-cast and pressed PZT piezoceramics.
- Fabricate additional PMLA fatigue test frames.

Introduction

The use of piezoelectric multilayer actuators (PLMAs) as diesel fuel injectors has the potential to reduce injector response time, provide greater precision and control of the fuel injection event, and lessen energy consumption. Compared to conventional solenoid operation of an injector, the alternative use of a PMLA can enable precise rate shaping of the entire injection cycle that accurately controls injection timing and fuel quantity. An example of a fuel injector containing a piezo-actuator is shown in Fig. 1. Piezoelectric multilayer actuators (or piezo-stacks) fuel injectors contain a solid-state ceramic actuator (or "piezostack") that converts electric energy into linear motion precisely controlling the needle's opening and closing. This capability results in an engine with outstanding performance, improved fuel economy, low noise, and low emissions. Their development for the automotive market has progressed and now strong interest exists to adapt their use to heavy vehicle diesel engines.

Figure 1. Piezo-actuated fuel injector used in Ford 6.4L Power Stroke® diesel engine.

Though their use is very attractive for the reasons mentioned above, uncertainty continues to exist over how reliable piezo-actuated fuel injectors will be in the challenging environment of a heavy vehicle diesel engine. Though piezoelectric function is the obvious primary function of lead zirconate titanate (PZT) ceramic PMLAs for fuel injectors, their mechanical reliability can be a performance and life limiter because the PZT ceramic within them is brittle, lacks high strength, and may exhibit fatigue (e.g., electromechanical, slow crack growth) susceptibility. That brittleness and relatively low strength can be overcome with proper probabilistic component design methodology.

This project undertakes the reliability characterization of candidate PMLAs used in these fuel injectors and the piezoceramics used in the PMLAs. During the FY2008 a piezodilatometer facility was designed, fabricated, and assembled to enable the accelerated testing for PZT thin films and stacks. Also, electric fatigue tests were performed on commercially available PMLAs to assess the effect of an applied semi-bipolar sine wave electric field on the response of mechanical strain and piezoelectric coefficients under a mechanical preload.

Approaches

Electric fatigue testing under a mechanical preload of commercially available PMLA was performed using a macromechanical test facility, which enables fatigue testing of PMLAs. Details of the electric and mechanical loading system can be found in Ref. 1. Tested stacks were purchased from Noliac (Denmark). They had an overall size of 5mm x 5mm x 18mm and were composed of 8 active plates (modules) and 2 dead endplates. Individual active plate was actually a multilayer actuator sized with 5mm x 5mm x 2mm and consisted of 30 layers each 67 μm thick. The active plates were coated with a layer of silver approximately 150 to 210 μm thick on 5mm x 2mm surfaces that served as an external electrode, and stacked together on 5mm x 5mm surfaces using bonding. These silver-coated plates were electrically interconnected by a bus wire in a zigzag pattern through soldering. The rated voltage and capacitance of PZT (PZT-5A type) stack were 200 V and 0.76 mF, respectively according to the manufacturer. The grain size of PZT was estimated to be about 2 to 5 μm based on a SEM analysis performed by the authors on the lateral face of a PZT plate. The Curie temperature of PZT-5A is 350°C, which is considered as a good candidate for fuel injection system of heavy-duty diesel engine.

A typical measurement consisted of acquiring signals from six channels. They included one input voltage (from function generator), two capacitance gages, one load cell, and two responses (voltage and current) from the HV amplifier. The raw voltage signals were subsequently processed to determine the electric field (E), applied stress (T), mechanical strain (S) and charge density (D) in cooperation with given parameters of stacks provided by the manufacturer. The peak field-induced response, particularly the mechanic strain S_p, was used to

quantify the response of each tested PZT stack. In addition, Fourier Transformations were used to decompose acquired signals in this study. These decomposed signals served as inputs to determine the frequency response function (FRF) of the actuator being tested. Details of the analytical processes can also be found in Ref. 1.

Results

PMLA Characterization

After 10^8 cycles, both the strain and piezoelectric hysteresis of No. 02 PZA stack were reduced markedly (Fig. 2). A much more reduction was clearly exhibited in these quantities with a semi-bipolar loading than with a unipolar loading. The strain exhibited a monotonic decrease in the measurement with a bipolar mode along with the accumulation of loading cycles whereas that in a unipolar measurement showed a certain amount of restoration around 10^6 cycles. The restoration related to unipolar loading was also observed in fatigue of several other PZT stacks. The variation pattern of piezoelectric hysteresis during the cycling fatigue appeared to be quite similar to that of strain.

Stack No. 05 was also tested under the condition same as that of No. 02. However, it was observed to display a different variation pattern in both the strain and piezoelectric actuation (Fig. 2). A fast drop was exhibited around 10^6 of cycles in both of these quantities, corresponding to a stage when extensive surface discharges emerged on both positive and negative electrode surfaces of the stack. Stack No. 05 showed a higher pre-fatigue level of strain and piezo hysteresis than No. 02, but had a much lower post-fatigue level as a consequence of cycling.

Variation of normalized maximum field-induced strain and piezo hysteresis with cycle number shows more clearly a much more reduction occurred in No. 05 (Fig. 3). A greater than 50% decrease in the strain and piezo hysteresis of No. 05 and an approximately 25% decrease for No. 02 were observed. The amount of variation of these two quantities was quite similar for No. 05 disregarding the electric loading mode (bipolar or unipolar), whilst it was somehow different for No. 02, especially that of piezo hysteresis. Overall, the amount of reduction (24 to 54%) in mechanical strain induced by a semi-bipolar fatigue in these stacks was considerably larger than that caused by a unipolar fatigue (~ 6%) reported previously. That is quite impressive, even though the mechanical preloads and electric field levels as well as frequencies were different in these fatigue tests.

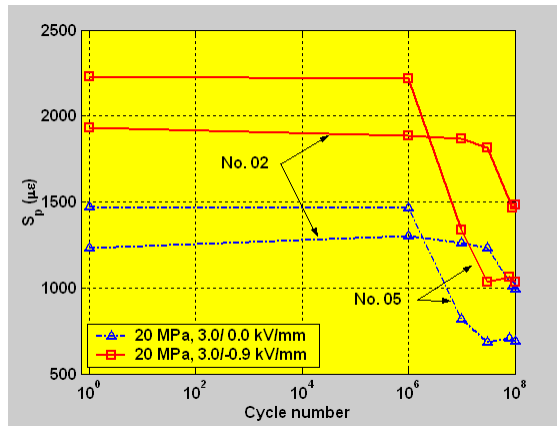

(a)

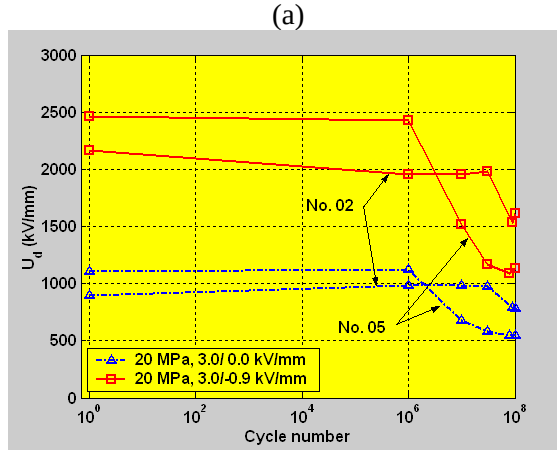

(b)

Figure 2. Variations of peak field-induced strain (a) and piezoelectric hysteresis (b) for stacks No. 2 and No. 5, as a function of cycle number. Mechanical and electric loading conditions in measurement are given in figures.

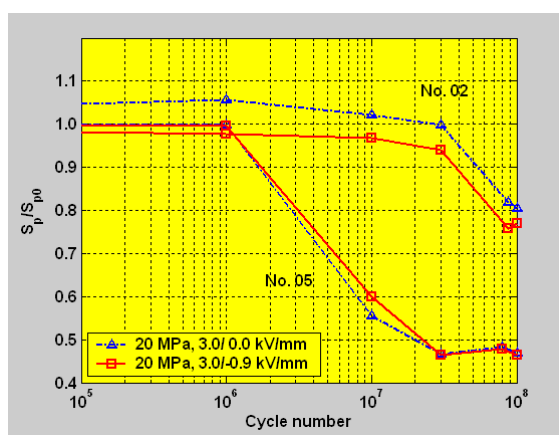

(a)

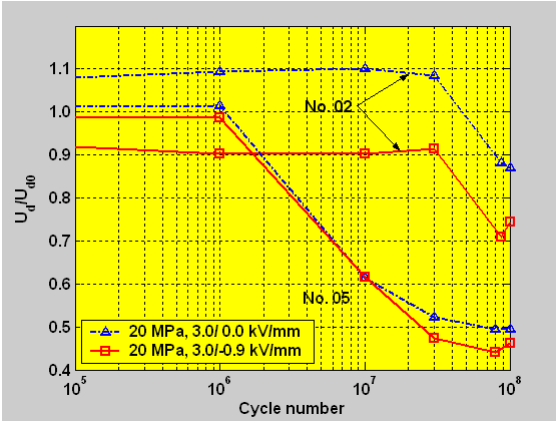

(b)

Figure 3. Variations of normalized peak field-induced strain (a) and normalized piezoelectric hysteresis (b) for stacks No. 2 and No. 5, as a function of cycle number (10^5- 10^8). Mechanical and electric loading conditions in measurement are given in figures.

The value of the first harmonic appeared to be smaller compared with that of the dc component (Fig. 4), showing the piezoelectric coefficient depended on the driving frequency as expected. As far as the case of stabilizing preload (0.7 MPa) is concerned, the pre-fatigue level of piezoelectric coefficient was estimated to be around 450 - 520 pm/V, being quite close to that reported by Andersen *et al.* [2]. The amount of enhancement in piezoelectric coefficient by a negative field depended on the frequency also. A much more increase was observed for the dc component than that for the first harmonic when a semi-bipolar mode was used [Figs. 4(a) and 4(b)]. Overall, the variation pattern of the dc and the first harmonic is similar to that of strain (Figs. 2 and 4). Piezoelectric loss angle exhibited some uncertainty in variation. Under the cycling preload level (20 MPa), an appreciable amount of decrease was exhibited that was followed by a slightly increase with some fluctuation in a semi-bipolar measurement whereas a more monotonic increase was shown in a unipolar measurement over most of the cycling process.

The fast drop in the strain of No. 05 is reflected in its dc and first harmonic components, especially in the latter (Figs. 2 and 4). The increase attributed to the semi-bipolar loading was becoming smaller along with the accumulated cycle number as can be seen from the shrinking distance between the two curves. Although the piezo hysteresis showed a decrease during the later stage of cycling fatigue, the piezo loss tangent exhibited an apparent different trend. A certain amount of fluctuation was observed for the result of semi-bipolar loading whilst an approximately increasing trend was demonstrated for that of unipolar loading.

The normalized dc and first harmonic components [Figs. 5(a) and 5(b)] exhibited similar variation pattern as the strain [Fig. 3(a)] as expected. The shifted piezo loss tangent shows that, while the piezo loss tangent in a semi-bipolar measurement fluctuated and that in a unipolar measurement has a slightly increase, the former was decreased and the latter was increased relative to the respective pre-fatigue level [Fig. 5(c)]. An additional fatigue session of 0.85×10^8 cycles was conducted for No. 05 after 10^8 cycles to explore the tendency of deterioration. No significant variation was observed in the piezoelectric coefficients, but a considerable increase in piezo loss tangent was obtained.

Both stacks exhibited a certain extent of surface damage after more than 10^8 cycles, but No. 5 showed a much greater extent corresponding to larger reductions in mechanical strain and piezoelectric coefficients. The effect of fatigue on the deterioration of stack's surface is more reflected in those of interconnect joints and inter-plate bonds. These areas were becoming increasingly colored or darkened due to the frequent discharges nearby and severely arcing along with the fatigue cycling. Within one module of No. 02, a thin plate-through fracture was also found located near an inter-layer (internal) electrode that was apparently a result of split or delamination occurring on an affected layer/electrode interface.

Optical observations showed that dark areas were observed to reside on five consecutive solder joints as well as plate/plate interfaces on the positive electrode side. Much wider darkened area occurred on both sides of the interface. The enlarged micrograph shows the nearby silver coating was removed to a certain extent (Fig. 6a). An arch opening zone was usually developed around the foot of solder joint where the surface silver coating (~150 μm thick as discussed in the following) eroded and underlying PZT layer was exposed (Fig. 6b). An array of equally-spacing gaps frequently appeared across the opening area. The spacing was estimated to be approximately 134 μm using the image analysis that was exactly 2 times the thickness of a

single PZT layer. Therefore, these linear gaps were identified to be the outcrops of (positive) internal electrode that were developed as a result of deep electrode erosion. In some area, the regular striations attributed to coating process were replaced by a rough or grainy surface covered with residuals from surface discharge that featured bubbles of various size (Fig. 6b) and signified that the heat generated by intensive discharges once boiled the neighboring silver coating.

Development of Piezodilatometer

A prototype of ORNL piezodilatometer has been built and calibrated. The PZT PSI-5A4E material was used in the calibration because it has been extensively studied throughout this project as it has a high Curie temperature (350°C) and is considered as a potential candidate for the fuel injection system in diesel engine. Specimens used in testing were thin plates and had a nominal size of 10mm x 10mm x 0.267mm. The geometric feature of these thin plates was close to that of single-layer elements used in a piezoceramic multilayer actuator.

A 0.1-Hz bipolar sine wave was used to load the specimen. This low frequency wave represents a static loading case. Amplitude of waveform was limited at first to 320 V so that the applied electric field remained within a range less that the coercive strength of material tested (1.2 kV/mm) in both positive and negative directions. A S_{13}-E_3 loop similar to that with a uni-polar waveform was obtained. This was expected because the involved domains were not reversed, and one of results is shown in Fig. 7. It is worthwhile to note that the strain measured in the developed piezodilatometer corresponds to that in the lateral (transverse) direction. The loaded thin plate actually contracts when a positive electric field is applied in the poling direction (E_3) to stretch the plate in the axial (thickness) direction. The correlation between a positive electric (E_3) in the axial direction and a contraction in lateral direction ($-S_{13}$) can be seen quite clearly in Fig. 7. The piezoelectric coefficient was estimated to be -546 pm/V that was much larger than that obtained with a small signal measurement (-190 pm/V) [3], a huge benefit from high field driving.

The amplitude of the sine wave was then increased to 640 V. As the applied electric field was twice the coercive strength of material, the S_{13}-E_3 loop resembled a shape of butterfly as a result of domain switching and domain reverse. Fig. 8 shows the D_3-E_3 and S_{13}-E_3 loops of material in the upper and lowers views, respectively. The tested specimen had a negative remnant polarization. Therefore, the applied positive electric field stretched the plate laterally, and then compressed it when the field level went beyond the coercive fiend strength of material (1.2 kV/mm). The transition at the coercive point was obviously a result of the domain reverse. At the same time, the remnant charge density (0.32 C/m^2) deduced from the upper view of Fig. 8 is close to the remnant polarization of PZT-5A published elsewhere [4].

The same PZT material was used to calibrate the piezodilatometer subsequently in dynamic loading. Fig. 9 presents a one of results when a 20-Hz bipolar sine wave with a peak voltage of 400 V was used. The D_3-E_3 loop drifted, distorted and enlarged when the dielectric breakdown was approached. This is an extreme case in which a combination of applied voltage and frequency drove the specimen to failure in about 20 seconds. The specimen that experienced thermal dielectric breakdown usually had the dielectric strength recovered after being cooled down to the room temperature. However, the specimen usually appeared to be stable to some extent. The self-heating has become a big concern as this soft piezoceramic has a significant hysteresis when it is subjected to cycling loading as can be seen in above figures (Figs. 7 to 9). To address this issue, a K-type thermocouple was mounted onto the center of specimen to monitor the temperature increase during the cyclic loading. The temperature change during the process apparently depended on the driving voltage and driving frequency. Part of results are summarized in Fig. 10 where the temperature rise was measured after a 5-minute cycling with a specific bipolar driving condition and the mark “x” indicates that the cycling was stopped earlier than 5-miunte because of the dielectric breakdown approached. There are no published data available for comparison, but the data obtained in this study revealed that the temperature rise can be significant even for a single layer element in which the thermal dissipation condition is much better than that of those embedded within a multilayer actuator.

Conclusions

Cycling fatigue tests were conducted on commercial PZT-5A stacks using a semi-bipolar

sine wave that had 100 Hz with an equivalent field range of +4.5/-0.9 kV/mm and involved with a 20-MPa preload. Electric cycles were accumulated more than 10^8 in each test and the performance of tested stacks was monitored and evaluated. Results showed that both mechanical strain and piezoelectric coefficient of tested PZT stacks were reduced 24 to 54%. Fatigue response of PZT stacks depended on loading mode and a semi-bipolar load accelerated the fatigue. However, the extent of acceleration on the fatigue remains to be quantified. Optical observations showed that surface discharges and arcing occurred during high field semi-bipolar cycling fatigue that account partially for the reductions observed during cycling fatigue. Pinned domain wall, induced micro-cracks and local volumetric dielectric breakdown complementarily account for rest of the reductions observed.

A prototype of piezodilatometer has been built and calibrated. This work was initiated as an ORNL response to the challenge that is confronting currently the piezoelectric industry as there is neither an effective test facility nor test standard available for characterizing a stand-alone piezoceramic thin-plate element in a loading regime of high field and low frequency. These thin-plate elements are extensively utilized in piezoelectric and electrostrictive actuators that demand an electric driving condition in the above-mentioned regime.

The developed piezodilatometer has been proven to be functioning well as designed under both the static and dynamic loading modes.

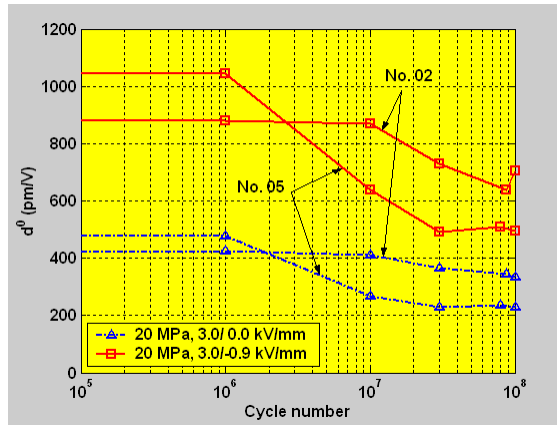

(a)

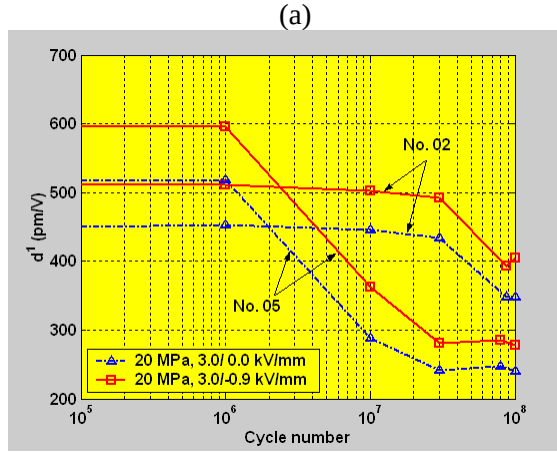

(b)

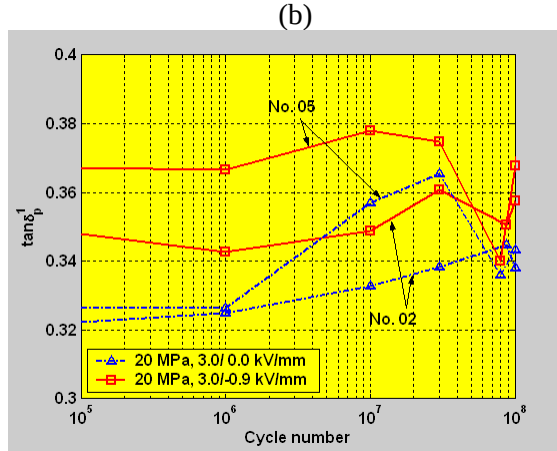

(c)

Figure 4. Variations of (a) the dc and (b) the first harmonic of field-induced strain and (c) piezoelectric loss tangent for stacks No. 2 and No. 5, as a function of cycle number (10^5- 10^8).

References

1. H. Wang, A. A. Wereszczak, and H.-T. Lin, Fatigue response of a PZT multilayer actuator under high-field electric cycling with mechanical preload, J. Appl. Phys., submitted (2008)
2. B. Andersen, E. Ringgarard, T. Bove, A. Albareda, and R. Perez, Performance of piezoelectric ceramic multiplayer components based on hard and soft PZT, Actuator 2000, 7th International Conference on New Actuators, 19-21 June 2000, Bremen, Germany
3. http://www.piezo.com/prodsheet1sq5A.html
4. S. J. Zhang, E. F. Alberta, R. E. Eitel, C. A. Randall, and T. R. Shrout, Elastic, piezoelectric, and dielectric characterization of modified BiScO3-PbTiO3 ceramics, IEEE Trans on Ultrasonic, Ferroelectric and Frequency Control, 52 (11), pp.2131-2139 (2005)

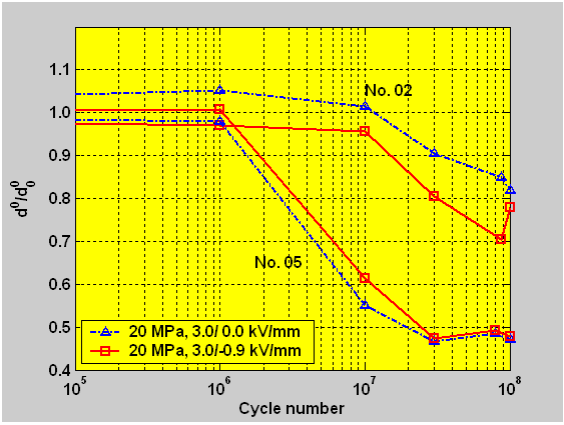

(a)

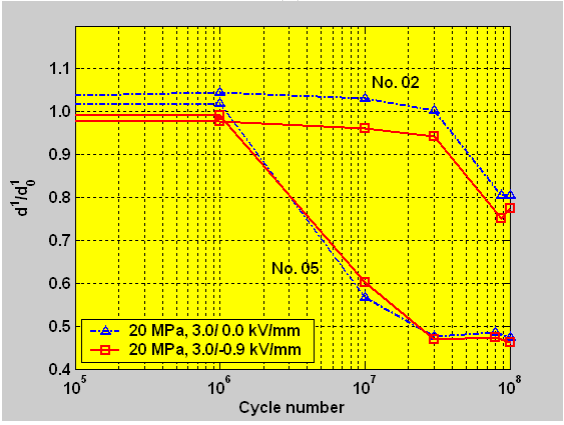

(b)

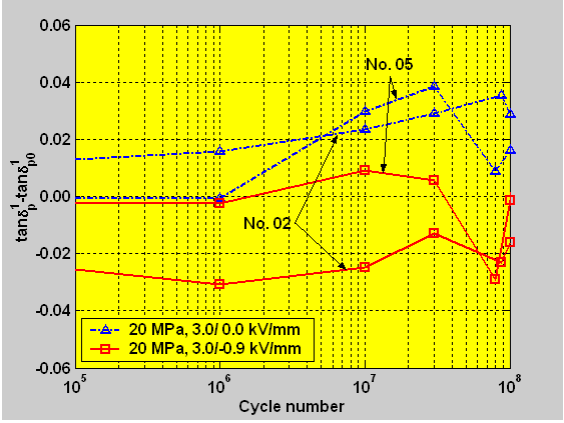

(c)

Figure 5. Variations of (a) the normalized dc and (b) the normalized first harmonic of field-induced strain and (c) shifted piezoelectric loss tangent for stacks No. 2 and No. 5, as a function of cycle number (10^5-10^8). Mechanical and electric loading conditions in measurement are given in figures.

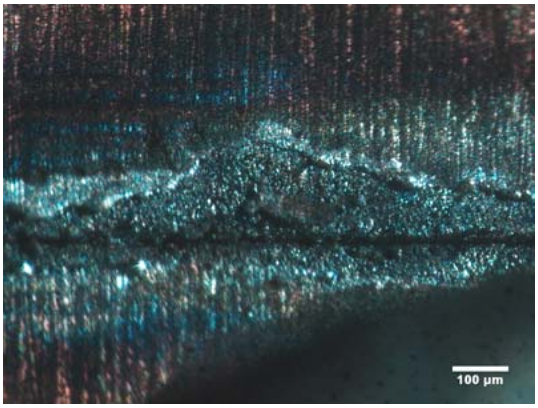

(a)

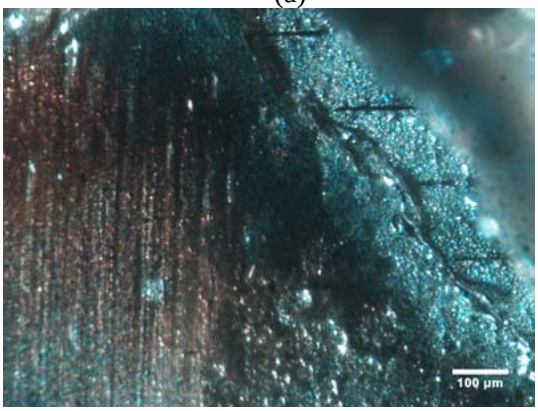

(b)

Figure 6. (a) plate/plate interface segment A. (b) enlarged opening area showing an array of linear gaps identified as outcrops of internal electrodes and a part of local rough surface covered with bubbles of various size

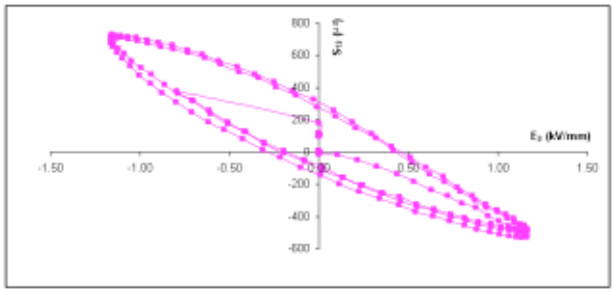

Figure 7. PSI-5A4E-01, 10mm x 10mm x 0.267mm, 0.1-Hz, ±320Vpk sine wave.

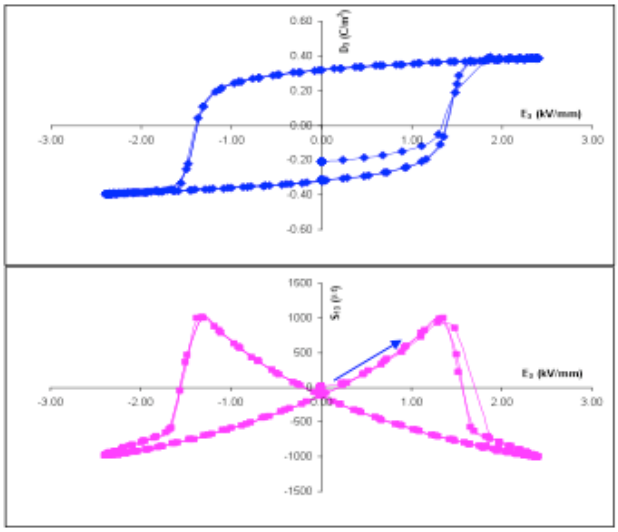

Figure 8. PSI-5A4E-01, 10mm x 10mm x 0.267mm, 0.1-Hz, ±640Vpk sine wave.

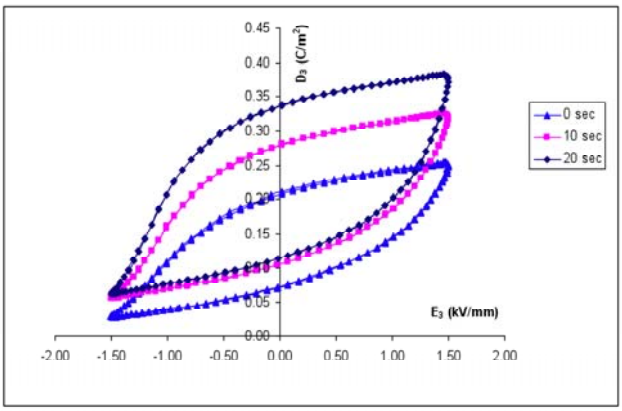

Figure 9. PSI-5A4E-03, 10mm x 10mm x 0.267mm, 20-Hz, ±400Vpk sine wave.

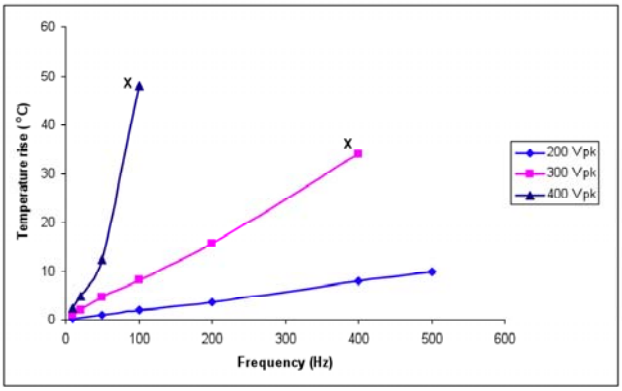

Figure 10. Temperature rise of thin PZT-plate in 5-minute cycling with a bipolar sine-wave. Point with "X" was obtained with < 5 minutes. PSI-5A4E-03, 10mm x 10mm x 0.267mm

Agreement 9010 - Joining of Advanced Materials by Plastic Deformation

Principal Investigator: J. L. Routbort (co-workers: D. Singh, Cinta Lorenzo-Martin)
Argonne National Laboratory
9700 S. Cass Avenue
Argonne, IL 60439-4838
(630) 252-5065; fax: (630) 252-5568; e-mail: routbort@anl.gov

DOE Technology Manager: Jerry L. Gibbs
(202) 586-1182; fax: (202) 586-1600; e-mail: jerry.gibbs@ee.doe.gov

Contractor: UChicago Argonne LLC
Contract No.: DE AC03 06CH11357

Objective

- Join advanced materials such as ceramics, cermets, intermetallics, composites, biomaterials, etc. by plastic deformation, collaborate with industry and universities to produce sensors
- Investigate grain rotation that is assumed to occur during grain–boundary sliding resulting in deformation bonding
- Use joining technique to produce compact oxygen and NO_x sensors with internal reference

Approach

- Apply a modest compressive load to two pieces of similar or dissimilar materials that have had little surface preparation in the temperature region where the materials are known to deform by grain-boundary sliding
- Measure strength of the interface by 4-point bend tests and compare to theory
- Use electron back-scattered diffraction to measure grain rotation as a function of strain
- Perform Advanced Photon Source experiment to measure grain rotation as a function of strain
- Use technique to produce gas sensors with sealed internal references
- Produce gas-tight seals to isolate a metal/metal-oxide powder inside a yittria-stabilized zirconia container to produce oxygen and NO_x sensors

Accomplishments

- Strong, pore-free joints have been made with various ceramics, cermets, intermetallics, composites, and biomaterials, with and without various interlayers, fracture occurs away from interface at the region of maximum residual stress
- Demonstrated that grains in $SrTiO_3$ rotate during deformation
- Published 23 journal papers, 2 patents issued for plastic joining process, patent applications filed for oxygen and NO_x sensor, negotiations for licensing of oxygen sensor started
- R&D 100 Award for oxygen sensor
- Developed initial NO_x sensor

Future Direction

- Program has been transitioned from deformation joining to application of deformation joining to produce sensors, initially concentrating on improvement of NO_x sensors.

Introduction

Monitoring gas composition, like O_2, NO_x, CO, CO_2, in the combustion environment with good accuracy has been of great importance since the advance of combustion heat engines in the last century. For instance, controlling the oxygen level in boilers carefully can maximize energy output and minimize pollutant emissions. It is estimated that yearly savings of $409 million from coal-fired power plants could be saved through combustion optimization. NO_x (NO + NO_2) sensing has also been considered as one of the key elements of next generation internal combustion engines. A reliable and accurate NO_x sensor is needed to monitor NO_x and trigger the regeneration of NO_x adsorption catalysts, or control the injection of reductants for continuous NO_x reduction.

Previously we have demonstrated that it is possible to form pore-free, high-strength joints in yittria-stabilized zirconia (YTZP) by applying a small stress at elevated temperatures ($T/T_m \approx 0.5$, where T_m is the melting temperature in K [1,2]. This technique has been used to produce oxygen sensors by encapsulating a metal/metal oxide powder in a container consisting of a lower YTZP disk, joined to an YTZP cylinder [3]. A metal/metal oxide powder is placed in the cavity that is then sealed by plastic joining to another YTZP disk to which is attached a thin Pt electrode top and bottom side. When placed in a combustion environment, the metal/metal oxide powder decomposes to produce oxygen. The difference between the internal oxygen activity (the reference) and that of the activity of the gas to be measured produces an emf that is proportional to $\ln(a_O/a_{Oref})$ where a_o is the oxygen activity of the gas to be measured and a_{oref} is the activity of the reference gas.

This technique has been applied to produce NO_x sensors that could enable simultaneous measurements of NO_x and O_2 in a combustion environment. The Pd/PdO-containing reference chamber was sealed within the stabilized zirconia superstructure by a high pressure/temperature bonding method that initiated grain boundary sliding between the ceramic components. NO_x sensing was conducted in both amperometric and potentiometric modes. Pt-loaded zeolite Y was used to obtain total NO_x capacity and to cover Pt electrodes for detecting oxygen in the presence of NO_x. Both amperometric and potentiometric type sensors will eventually be tested for signal stability, total NO_x response, and NO_x-O_2 cross interference.

Experimental

Preparation and characterization of sensor materials

As demonstrated in Fig 1, the package superstructure was constructed from five different pieces and placed into a universal testing machine with two spacers. The electrolyte, ring and bottom wafer were cut from densified rods/tubes of 3 mol % yttria-stabilized tetragonal zirconia polycrystals (YTZP, Custom Technical Ceramics). The 8 mol% cubic yttria-stabilized zirconia spacers used as platens were cut from a rod (Custom Technical Ceramics). The YTZP green tapes (Nextech Materials) were laser cut from sheets into rings that matched the YTZP rings cut from tubes. The Pt wire (99.95%, 0.13mm in diameter, Fischer Scientific) to the inner reference electrode was sandwiched between two pieces of YTZP green tape. The devices were constructed by sealing Pd/PdO (Alfa Aesar) into the reference chamber. A small amount of 8 mol % YSZ powder (TZ-8Y, Tosoh) was placed on top of PdO to prevent alloying with the Pt wire of the reference electrode.

Basic platform

Each "sandwich" was compressed in an argon atmosphere at temperatures ranging from 1250°C to 1290°C in a universal testing machine (Instron, Model 1125) at crosshead speeds ranging from 0.01 mm/min to 0.02 mm/min. The initial strain

rate used for all experiments was 4×10^{-5} S^{-1} in order to avoid overstressing the sample and damaging the Pt wire. In the >1250°C temperature domain, this strain rate is expected to yield total stresses on a 1 cm^2 sample of less than 40 MPa [2,3]. Upon reaching the target temperature, the system was left for 30 min to attain thermal equilibrium. Following joining, a glass plug (C153M glass, Asahi) was applied to the region of the sensor package where the Pt wire breached the inner-to-outer environment. C153M is a frit sealing glass composed of SiO2, ZnO, and organic compounds (softens at 800°C, crystallizes at 910°C). The glass powder was mixed with α-terpineol to make a slurry and a small amount was applied to the base of the Pt wire. The sensor was heated to 1200°C for 3 h to densify the glass plug.

Sensor Design

Using the basic sensor package, modifications for NO_x sensing was carried out in Dr. Prabir Dutta's laboratory at the Ohio State University. NO_x sensor was designed to sense in both potentiometric and amphometric modes [4].

Potentiometric

As shown in Fig. 1a, after finishing the sandwich structure, two Pt lead wires were attached to the top of the sandwich structure with a small amount of commercial Pt ink (Englehard, A4731). The end attached to YSZ was shaped into a disc of 2 mm diameter in order to increase the mechanical stability. The Pt ink was cured at 1200°C for two hours to secure bonding between the Pt wire and YSZ. WO_3 powder was mixed with α-terpineol to form a paste, which was then painted on top of the Pt lead wire and YSZ. The WO_3 layer was spread over as much YSZ as possible. After sintering at 700°C in air for 2 h, the WO_3 layer was typically about 200 μm thick. PtY was also mixed with α-terpineol and painted on the top of another Pt lead wire to form the reference electrode. The PtY layer is around 100 μm thick after calcination in air at 600°C for two hours.

Amperometric

Instead of two Pt lead wires on top of the sandwich structure for the potentiometric sensors, three Pt wires (working, counter, and reference) were mounted on the amperometric sensors. At 500°C, the Pt reference electrode on YSZ cannot be a good reversible electrode. A counter electrode is therefore required for accurate potential control. The reference electrode was kept well separated from the working and counter electrode to reduce electrical interference. PtY was mixed with α-terpineol to form a paste and then painted on top of all three electrodes. The sensor was heated in 650°C in air for 2 hour and then cooled back to 500°C for the sensing measurements.

Sensor Testing

The gas sensing experiments were performed at Ohio State University using a quartz tube placed inside a tube furnace (Lindberg Blue, TF55035A). A computer-controlled gas delivery system with calibrated mass flow controllers (MFC) was used to introduce the test gases. Four certified N_2-balanced NO_x cylinders (30 ppm NO, 30 ppm NO_2, 2000 ppm NO, and 2000 ppm NO_2, Praxair) were used as NO_x sources. Sensor tests were carried out with mixtures of dry air, NO_2, and nitrogen with total gas flow rates of 200 cc/min at 500 or 600°C. As schematically shown in Fig. 2a, the gas mixture from MFCs could be introduced into the tube furnace either through or bypassing the PtY filter. The filter is a U-shape quartz tube with 100 mg PtY placed on quartz wool.

Three (or four for the amperometric configuration) Pt wires were used to connect the sensor to external leads. For both configurations (Fig. 2b and 2c), the open circuit potential between the oxygen

reference and the PtY reference (the reference electrode on the top of sensors, covered by PtY) was recorded by a multiplex data acquisition system (HP 34970A). The oxygen reference electrode was connected to the negative terminal of the HP multimeter. For the amperometric configuration (Fig. 2b), a homemade portable potentiostat was used to apply a constant potential on the working electrode. The current (nA range) was converted to voltage (mA range) by a RCA 3140 OP-Amp and was measured also by the HP multimeter; in the potentiometric configuration (Fig. 2c), the open circuit potential between the WO_3 and PtY reference electrode was measured by the HP multimeter with the PtY electrode connected to the negative terminal.

Results

Oxygen sensing behavior

The oxygen sensing behavior was first examined at 500°C and 600°C, the optimal working temperatures for the amperometric and potentiometric NO_x sensing configurations. As shown in Fig. 3, the open circuit potential between the Pd/PdO internal reference and the PtY reference exhibits Nernstian behavior at both temperatures. At 600°C, the calculated internal pO_2 is lower than the theoretical pO_2 created by Pd/PdO probably because the sensor wasn't located in the center of the heating zone.

Total NO_x signal

In Figs. 4 and 5, the NO and NO_2 concentration was changed from 1 ppm to 600 ppm to check the NO_x sensing performance. The amperometric type sensor (Fig. 1b) at 500°C was anodically polarized to 80 mV (versus the PtY reference electrode) and the current in the presence of 1-200 ppm NO_x in 3% O_2 was recorded without gases passing through the PtY filter. PtY filter was only used for potentiometric type sensors in this work. The bias potential of 80 mV was chosen based on the I-V behavior since a measurable current in the presence of NO_x was expected. The calibration plot in Fig. 4a exhibits a linear relationship between current and concentration of NO_x. The similarity of response transits in Fig. 4b and 4c demonstrates that the PtY thick film coated on the sensor surface can equilibrate the NO_x mixture and the sensor produces a total NO_x response.

A potentiometric sensor was tested with the gas mixture passing through the PtY filter heated at 400°C, which was chosen as the optimal filter temperature because maximum NO_x signal was observed without the occurrence of catalytic reductions when CO or NH_3 was also present. As shown in Fig. 5, NO_2 and NO with the same concentration generates almost the same potential on the sensor and the potential displays a logarithmic relation to NO_x concentration. The use of a PtY filter makes it possible to measure total NO_x and reduce the interferences from CO, propane, NH_3, and CO_2. The intense NO_x signal is brought from dissimilarity of catalytic activity of PtY and WO_3. Catalytic activity measurements and temperature programmed desorption indicated that WO_3 was almost inactive toward NO_x equilibration and no chemisorbed NO_x species was released from the WO_3 surface. On the contrary, PtY has much higher activity toward NO_x equilibration. Therefore, on the WO_3 electrode, electrochemical reactions that generate the electric potential compete with weaker heterogeneous catalytic reactions (non-electrochemical reactions) and opposite phenomenon occur on the PtY reference electrode.

Conclusion

Pd/PdO internal oxygen reference was coupled with two electrochemical total NO_x measuring techniques to detect O_2 and NO_x in the combustion environment. High pressure and high temperature bonding

method was used to create an effective physical seal of the Pd/PdO reference chamber, followed by building amperometric and potentiometric NO_x sensing devices outside the chamber. PtY was used to obtain total NO_x capacity and to cover reference electrodes for detecting O_2 in the presence of NO_x. WO_3 was exploited with PtY to create dissimilarity of catalytic activity and generate intense potentiometric signal. Both amperometric and potentiometric type sensors shows good NO_x/O_2 signal stability and total NO_x response.

Future Directions

The first attempt to produce a dual functional sensor must be deemed a success. A patent application was filed in FY08. Research on this project in FY09 will concentrate on simplification of the fabrication process, avoiding the glass seal by using alternatives to Pt electrode materials (an electronically conducting ceramic for which a patent application was filed), establish cross-interference in O_2 and NOx signals, and evaluate long-term drift and stability of the sensors.

Acknowledgements

This work formed part of a Ph.D. thesis, successfully defended by Jiun-Chan Yang at Ohio State University. Dr. Yang's supervisor was Professor Prabir Dutta of the Chemistry Department of OSU.

References

1. F. Gutierrez-Mora, A. Dominguez-Rodriguez, J. L. Routbort, R. Chaim, and F. Guiberteau, "Joining of Yttria-tetragonal Stabilized Zirconia Polycrystals using Nanocrystals," Scripta Mater. **41** 455-60 (1999).
2. F. Gutierrez-Mora, K. C. Goretta, S. Majumdar, J. L. Routbort, M. Grimdisch, and A. Domínguez-Rodriguez, "Influence of Internal Residual Stresses in Superplastic Joining of Zirconia Toughened Alumina," Acta Mater. **50** 3475-3486 (2002).
3. J. V. Spirig, R. Ramamoorthy, S. Akbar, J. L. Routbort, D. Singh, and P. K. Dutta, "High-temperature Zirconia Oxygen Sensor with Sealed Metal/Metal Oxide Internal Reference", Sensors and Actuators B **124**, 192-201 (2007).
4. Jiun-Chan Yang, John V. Spirig, Dale Karweik, J. L. Routbort, Dileep Singh, and P. K. Dutta, "Compact electrochemical bifunctional NO_x/O_2 sensors with metal/metal oxide internal reference for high-temperature applications" Sensors and Actuators, B **131**(2), 448-454 (2008)

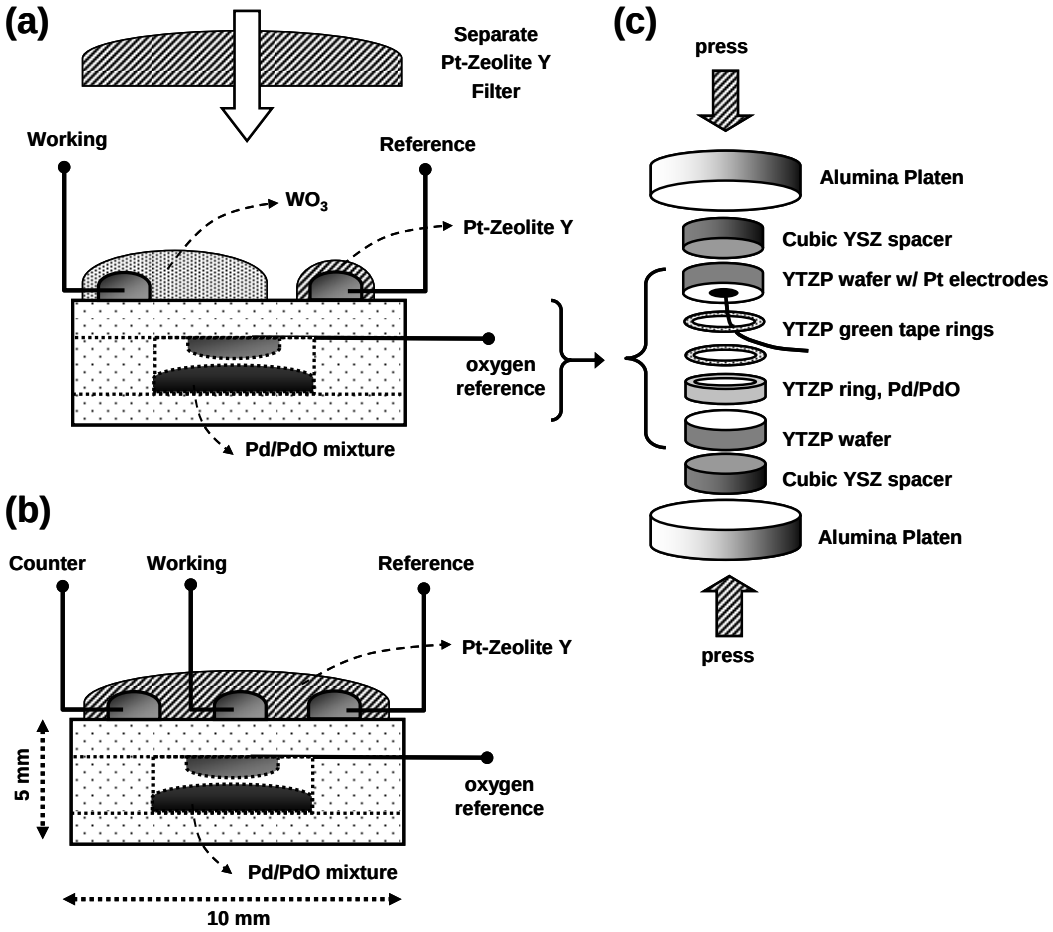

Fig. 1. Cross-sectional view of the sensor assembly: (a) potentiometric configuration with the sensor at 600°C and a separate PtY filter at 400°C; (b) Amperometric configuration working at 500°C; (c) Components of the Pd/PdO chamber package. Cubic YSZ spacers and alumina platens were removed following joining and not part of the package.

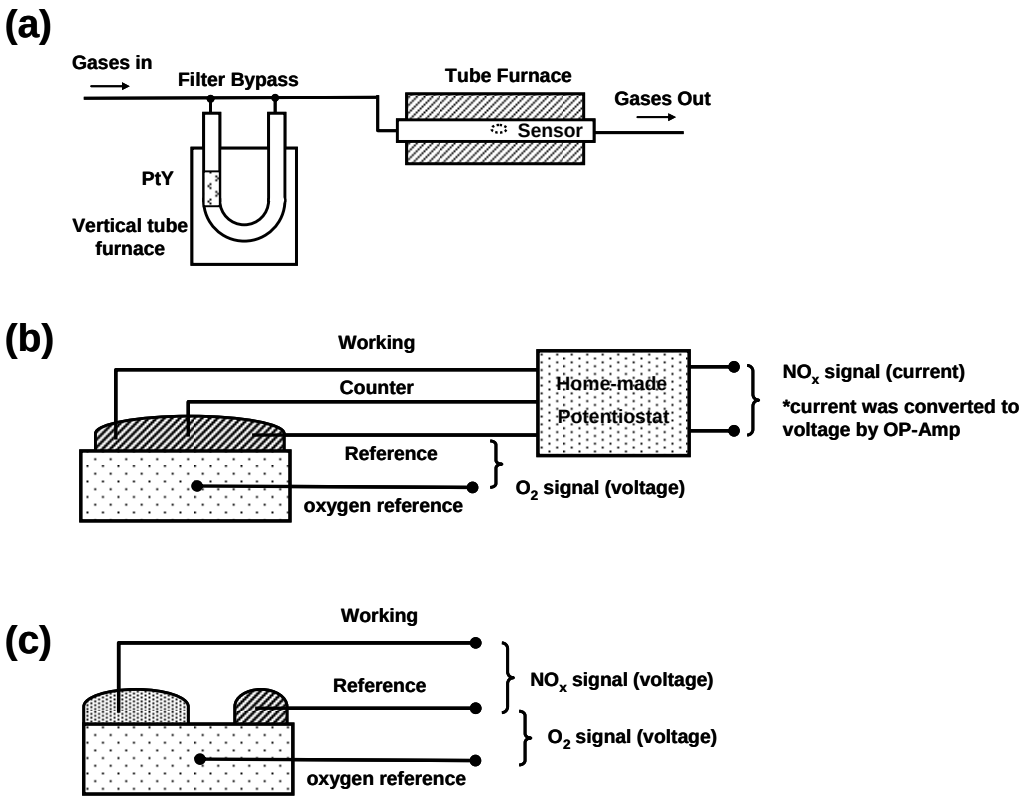

Fig. 2. (a) sensor testing setup (PtY = Pt-zeolite Y); (b) Measurement setup for the amperometric configuration; (c) Measurement setup for the potentiometric configuration.

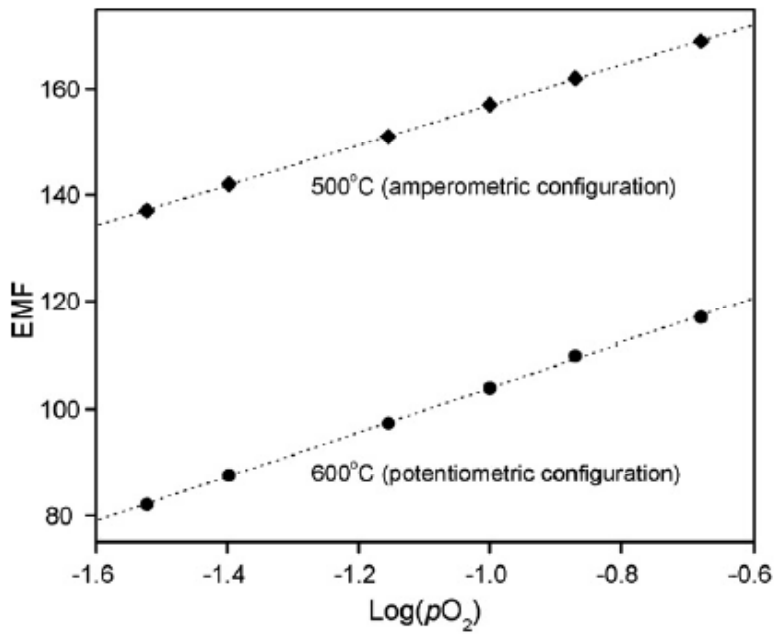

Fig. 3. EMF vs. log [pO_2] plots at 500°C and 600°C

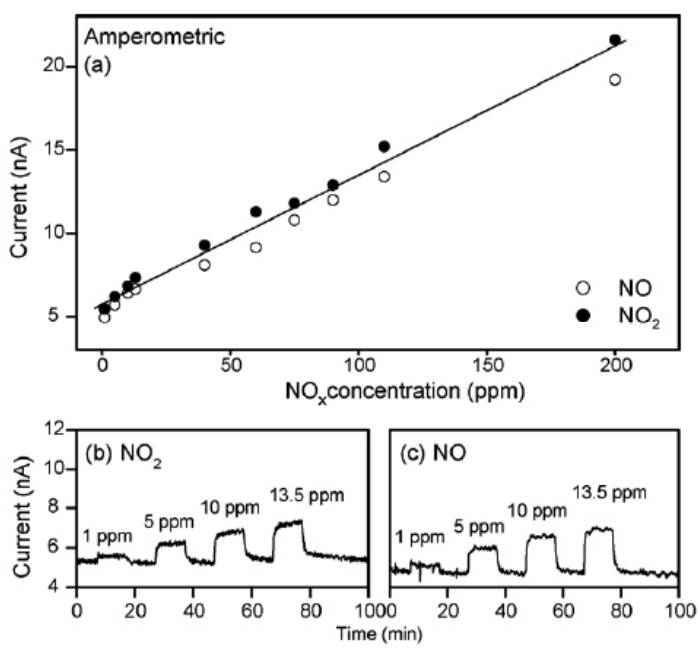

Fig. 4. (a) Current vs. [NO_x] plots for the amperomtric configuration at 500°C in 3% O_2; (b) and (c): Response transients to 1–13.5 ppm NO_2 and NO.

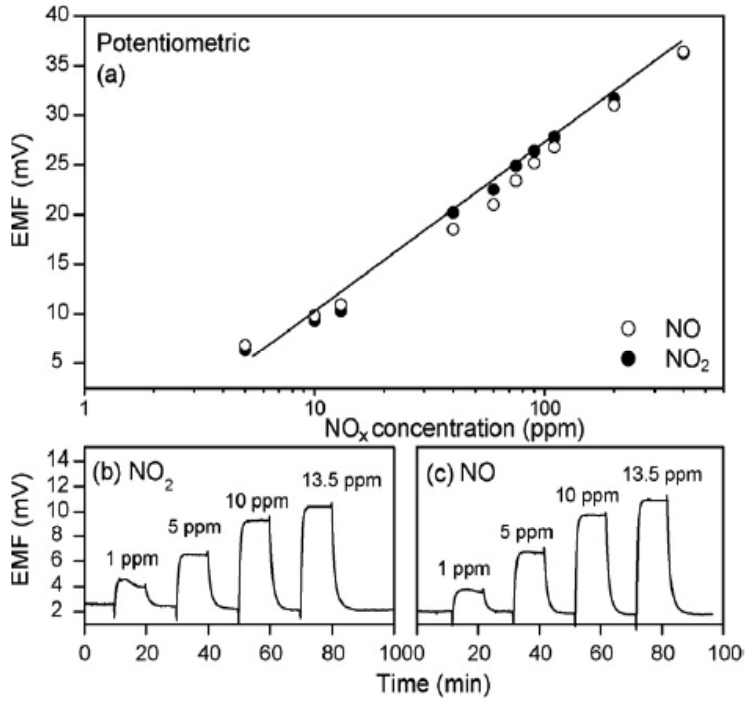

Fig. 5. (a) EMF vs. log [NO_x] plots for the potentiometric configuration at 600°C with gases passing through a PtY filter (400°C). O_2 level is 3%; (b) and (c): Response transients to 1–13.5 ppm NO_2 and NO in the presence of 3% O_2.

Agreement 13332 - Friction and Wear Reduction in Diesel Engine Valve Trains

Peter J. Blau
Oak Ridge National Laboratory, P. O. Box 2008, Mail Stop 6063
Oak Ridge, TN 37831-6063
(865) 574-5377; fax: (865) 574-6918; e-mail: blaupj@ornl.gov

DOE Technology Manager: Jerry L. Gibbs
(202) 586-1182; fax: (202) 586-1600; e-mail: Jerry.gibbs@ee.doe.gov
ORNL Technical Advisor: D. Ray Johnson
(865) 576-6832; fax: (865) 574-6098; e-mail: johnsondr@ornl.gov

---

Contractor: Oak Ridge National Laboratory, Oak Ridge, TN
Prime DOE Contract Number DE-AC05-00OR22725

Objectives

- To enable to enable the improved selection and use of materials, surface treatments, and lubricating strategies for value train components like exhaust valves and seats in energy-efficient diesel engines.

- To design, construct, and use a specialized high-temperature, repetitive impact (HTRI) apparatus to investigate the combined effects of mechanical contact, high temperatures, and oxidizing environments on the durability of high-performance diesel engine valve materials.

- To develop consensus-based friction and wear test standards that enable more realistic bench-scale measurements of diesel engine component durability and energy efficiency.

Approach

- Working with U.S. diesel engine manufacturers, identify exhaust valve operating conditions and failure modes. Then design and build a specialized, high-temperature repetitive impact valve materials testing system to simulate that type of contact damage. The testing system should use be capable of testing actual valves as well as simpler specimens of promising materials that show promise but are not yet available as valves.

- To conduct experiments that investigate the oxidation and re-oxidation of high-performance metallic alloys when subjected to wear and abrasion at temperatures like those to which diesel engine valves and valve seats are exposed.

- Recommend alloys or surface engineering approaches that show the best resistance to the conjoint effects of wear, oxidation, and high temperature resistance.

Accomplishments

- A high-temperature, repetitive impact testing system was designed and built. It is capable of operating from room temperature up to 850°C. Using several different geometric

configurations, the HTRI can be used to test actual diesel engine valves as well as simple test coupons.

- New research results on Fe-, Ni-, and Co-based demonstrated that prior abrasion damage can affect the ability of contact surfaces to form protective or non-protective scales at high temperatures.

- HTRI studies of wear plus oxidation of valve materials are planned for FY 2009

- Plans for FY 2009 are to complete the validation of ASTM standard test method G 181 whose preliminary development was supported by OVT. The standard measures friction of various in-cylinder diesel engine material combinations. An international industry-government team has been assembled under the auspices of ASTM Subcommittee G02.40 on Non-Abrasive Wear, to participate in an inter-laboratory testing program.

Future Directions

- Employ the HTRI apparatus to support the development and selection of more durable exhaust valve materials for advanced, energy-efficient diesel engines.

- Extend the results of the current research to other high-temperature, wear-critical diesel engine components like turbochargers.

Introduction

Heavy truck diesel engine manufacturers face two important challenges: (a) to improve fuel efficiency, and (b) to meet increasingly strict emissions regulations. These challenges are being addressed by introducing new concepts like homogeneous charge compression ignition, designing advanced engine control systems, and using various exhaust gas after-treatments. Such approaches affect the mechanical, thermal and chemical environments to which engine materials are exposed. Current materials and surface treatments may fall short of meeting those needs.

The objective of this effort is to enable the selection and use of durable moving parts in diesel engine components, specifically exhaust valves. The approach draws on metallurgical studies, wear-corrosion experiments, and the systematic evaluation of material options under simulated high-temperature operating conditions.

In prior years, the focus of this effort was on wastegate bushings for exhaust gas recirculation (EGR) systems and fuel injector plungers that must operate in low sulfur fuels. During FY 2006-2007 the effort was redirected to address the selection and use of materials for the demanding environment of diesel engine exhaust valves, where temperatures can reach over 850° C. Consequently, a new apparatus was designed and built. This new system can investigate candidate valve materials, surface treatments, and coatings. In FY 2008, construction of the apparatus was completed and preliminary tests were run to test the specimen alignment and temperature capabilities.

In companion studies during FY 2008, an investigation was conducted to probe the redistribution of near-surface alloying elements in regions that were abraded under controlled conditions. Two journal articles and a presentation describing that work in detail were produced.

Approach

Design and construction of a high-temperature test system. During FY 2007-8 construction was completed on a high-temperature, repetitive impact (HTRI) testing system. The concept for the system was reported in the FY 2007 annual report. The actual system is shown in Figure 1. It consists of a variable-speed drive motor with a roller-follower that raises and lowers the inner specimen(s) onto opposing counterface specimens. Water-cooled mechanical feed-throughs surround a clam-shell furnace that can produce temperatures in excess of 850° C, if required.

A set of diesel engine exhaust valves was provided by Caterpillar Corporation to serve as best-practice commercial materials for bench-mark testing and to ensure that the HTRI would properly fit commercial valves. Initial experiments used a specimen holder inclined at 45 degrees to mimic the actual seat angle and produce a combination of impact plus slip on the contact surfaces. Tests using this geometry will continue in FY 2009.

Effects of prior contact damage on high-temperature oxidation. Systematic experiments were performed to investigate whether high-temperature oxides that form on mechanically-damaged surfaces of alloys differ from those that form on the same surface in the absence of mechanical damage. Three high-performance alloys were used: (1) Custom 465, a martensitic Fe-base, age-hardenable alloy; (2) Pyromet 80A, a Ni-based, oxidation-resistant alloy; and (3) Stellite 6B, a Co-based, superalloy used for both corrosion-resistance and wear-resistance. Coupons of each alloy were prepared and oxidized at 850° C for two hours. Then their surfaces were scratched by a diamond stylus, and the damaged surfaces were re-oxidized for and additional four hours. Experiments were conducted to compare statically oxidized surfaces to those with abrasion damage as described.

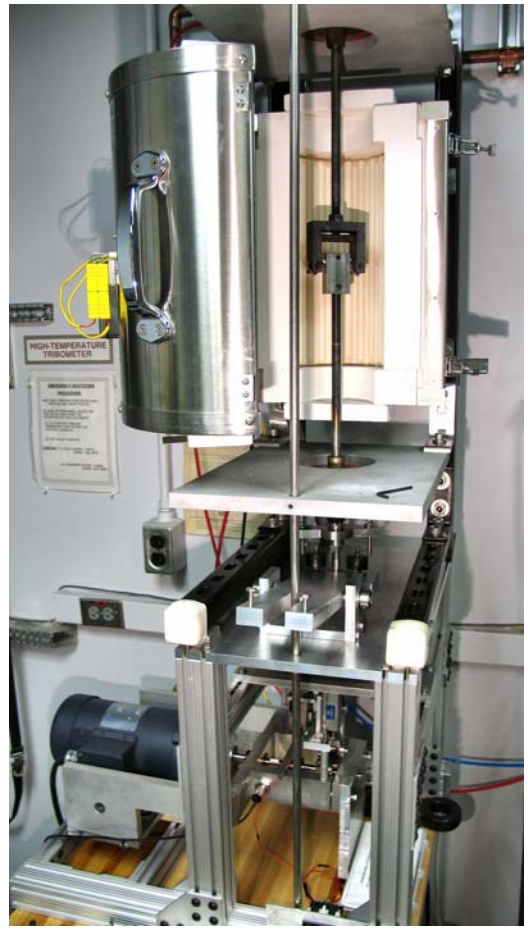

Figure 1. HTRI with the furnace door open to reveal the specimen holders.

Using a micro-gravimetric (weight gain) technique, Bruce Pint, of the Corrosion Science and Technology Group, investigated the static oxidation of the three alloys. The oxide growth rates of the Stellite 6B and the Pyromet 80A were similar, but the Custom 465 experienced a significant increase in the oxidation rate after an incubation period of about an hour. These different growth characteristics were confirmed by examining metallographically polished cross-sections of the oxide layers.

Energy dispersive x-ray analysis was used to map the elemental distribution both on and off the damaged areas of the specimens that had been pre-oxidized, scratched, and re-oxidized. For example, Figures 2 and 3 illustrate that the oxide layer

composition on the abrasion grooves was different than that of the scales that formed on non-damaged areas on both sides. A method called 'taper polishing' allowed the scratch depth to be pseudo-magnified in the vertical direction (note the difference in horizontal and vertical scale bar lengths in Figure 2).

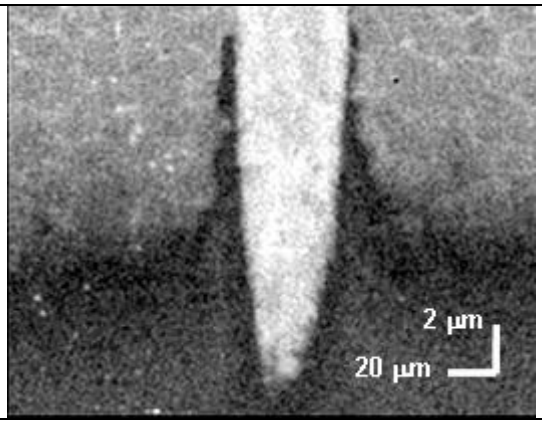

Figure 2. Distribution of chromium on and off a scratch on Ni-based alloy Pyromet 80A™. (Kα x-ray map).

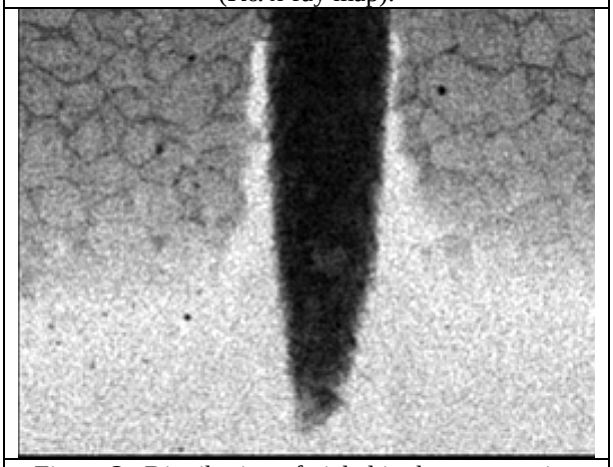

Figure 3. Distribution of nickel in the same region shown in Figure 2. (Kα x-ray map, same magnification)

Wear Test Methods and Standardization. Participation continues with ASTM Committee G2 on Wear and Erosion to advance the development of standards for friction testing of engine materials. This work has led to the provisional approval of ASTM G 181, a method for measuring the friction of piston ring and cylinder liner materials in used oil environments. Work will continue in FY 2009 to coordinate an inter-laboratory wear tests with diesel engine makers, oil companies, and two tribology testing machine manufacturers to establish the repeatability of the new test.

Summary and Conclusions

- A repetitive-impact diesel engine valve material testing system that operates at temperatures in excess of 800° C has been constructed and tested.
- A paper on the effects of prior mechanical damage on the re-oxidation of Fe-, Ni-, and Co-based alloys has been accepted for publication. Results indicated that the oxidation of pre-damaged surfaces produces scales that are compositionally different from those subjected to the same conditions, but without mechanical damage.
- Work continues to providing the diesel engine industry with a new ASTM standard for measuring the friction of candidate materials for piston rings and cylinder liners.

Publications/Presentations

1) P. J. Blau, "The Many Faces of Scuffing: Mechanisms, Measurements, and Control," invited paper, Annual Meeting of the Society of Tribologists and Lubrication Engineers (STLE), May 8, 2008.

2) P. J. Blau and T. M. Brummett, "High-Temperature Oxide Regrowth on Mechanically-Damaged Surfaces," accepted and published on-line by *Tribology Letters*.

3) P. J. Blau, T. M. Brummett, and B.A. Pint, "Effects of prior surface damage on high-temperature oxidation of Fe-, Ni-, and Co-based alloys," accepted for the 2009 International Conference on Wear of Materials, April 19-22; and for publication in the journal *Wear*.

Agreement 9089 - NDE of Diesel Engine Components

Jiangang Sun
Argonne National Laboratory
9700 South Cass Avenue
Argonne, IL 60439
630-252-5169; fax: 630-252-2785; e-mail: sun@anl.gov

DOE Technology Manager: Jerry L. Gibbs
(202) 586-1182; fax: (202) 586-1600; e-mail: Jerry.gibbs@ee.doe.gov
ORNL Technical Advisor: D. Ray Johnson
(865) 576-6832; fax: (865) 574-6098; e-mail: johnsondr@ornl.gov

Contractor: Oak Ridge National Laboratory, Oak Ridge, Tennessee
Contract No.: DE-AC05-00OR22725
Subcontractor: Argonne National Laboratory, Argonne, Illinois

Objectives

- Develop laser-scattering and other nondestructive evaluation (NDE) technologies for detection and characterization of defect and damage in diesel-engine valve-train components made from advanced materials such as ceramics and intermetallics.
- Develop quantitative NDE analysis methods to identify strength-limiting flaws, evaluate damage evolution/growth, and predict mechanical properties for advanced materials.

Approach

- Develop fast and reliable automated laser-scattering NDE systems for surface/subsurface inspection of Si_3N_4 ceramic and TiAl intermetallic engine valves.
- Analyze NDE image data to determine the level of machining damage and accumulated damages in engine valves from bench and engine tests.
- Correlate NDE data with microstructure and strength of advanced materials to establish NDE capability for predicting failure initiation defects and mechanical properties.

Accomplishments

- Completed NDE evaluation for subsurface damage in engine-tested ceramic and TiAl valves.
- In collaboration with Caterpillar and ORNL, correlated NDE data with mechanical properties determined from destructive tests of engine-tested ceramic valves.

Future Direction

- Develop/evaluate x-ray and ultrasonic imaging NDE technologies for inspection of jointed components for diesel engine.
- Develop optical and thermal imaging NDE technologies for evaluation of ceramic coatings for diesel engine components.

Introduction

Advanced ceramics and intermetallics are leading candidates for high-temperature engine applications that offer improved fuel efficiency and reduced emissions. Among them, silicon nitrides (Si_3N_4) and titanium aluminide (TiAl) are being evaluated as valve-train materials for diesel and natural gas engines because of their lighter weight, high strength and corrosion resistance at elevated temperatures. However, these brittle materials are susceptible to microscopic defect/damage within a thin subsurface, which may significantly degrade their mechanical properties. Material damage in the subsurface may be induced by machining or from service due to impact, wear, and corrosion. For silicon nitrides, material strength may also be limited by inherent defects such as voids and porosities within subsurface. To detect and characterize these defects, Argonne National Laboratory (ANL) has developed several laser-based NDE methods for these materials. The objective of this research is to demonstrate that these methods can be used to assess/evaluate the cost-effectiveness and reliability of valve-train components manufactured from advanced ceramic and intermetallic materials for diesel engines. The primary effort in FY 2008 was to utilize a fast NDE valve-scan system to evaluate SN235P Si_3N_4 valves at the end of an engine duration test, and to establish correlation between NDE data and mechanical property of the valve material after destructive tests conducted by ORNL. Another effort was directed on development and evaluation of x-ray and thermal imaging technologies for characterization of diesel engine components made from advanced materials for high-efficiency engines. This research is collaborated with Caterpillar and ORNL.

Approach

The critical region for brittle ceramic and intermetallic components in structural applications is near surface. The common types of defects in this region are mechanical, such as cracks, spalls, inclusions, and voids. The size of the defects that limits the component strength is generally small, say ~100 µm. To detect these defects, ANL developed an optical NDE method based on cross-polarization detection of optical scattering originated from surface and subsurface discontinuities (i.e., defects). Because ceramics are partially translucent to light, optical penetration can reach the subsurface to directly interact with the subsurface defects. For metallic or intermetallic materials, optical penetration is not possible. However, cross-polarization detection eliminates optical reflection from smooth surface and extracts only optical scattering from rough or cracked surface features. By scanning the entire surface (flat or curved) of a component and constructing a two-dimensional (2D) scatter image, surface/subsurface defects can be readily identified as they exhibit excessive scattering over the background, and their type and severity may be analyzed. To apply this technology for NDE of engine valves, ANL has developed an automated laser-scatter system for scanning the entire valve surface with high spatial resolutions (10 or 5 µm). The resulting 2D scattering image data are used to identify the location, size, and relative severity of subsurface defects/damages.

NDE development may also lead to quantitative prediction of mechanical properties for advanced materials and components. For advanced ceramics, although many parameters (e.g., residual stress[1]) are known to affect material strength, the most important parameters are likely the characteristics of individual flaws that cause the initial failure. These characteristics, such as flaw size and depth, can be determined from 3D NDE imaging methods such as confocal microscopy and OCT. For metallic materials, other NDE methods such as thermography and ultrasonic and x-ray imaging may be used to determine these characteristics. By combining NDE data with life-prediction analysis tools, quantitative prediction of the strength and lifetime of diesel engine components may become realistic.

Results

NDE Characterization of Ceramic Valve Surfaces at End of Engine Duration Test

Ten Si_3N_4 and four TiAl valves had been successfully tested for 500-hr in a Caterpillar G3406 generator set at NTRC in 2006, and were installed for the final phase of 500-hr engine test. However, on June 20, 2007 after 55 hours at full load operation, a Si_3N_4 intake valve located in Cylinder 6 (#22) failed, causing the rest of the valves in that cylinder been destroyed[2]. The ceramic debris was also sucked into other cylinders, damaging all other ceramic and TiAl valves. The failure was later identified to be due to a worn metal valve-groove

keeper that allowed the ceramic valve to be dropped inside the cylinder and crashed with the piston. As a result, the engine test was ended. The 10 engine-tested Si_3N_4 valves were analyzed by NDE at ANL in FY2008 before being destructively tested at ORNL. Figure 1 shows a photograph of these valves; note that the damaged valve head for all ceramic valves in Cylinder 6 had been removed prior to the NDE examination.

Figure 1. Photograph of Si_3N_4 engine valves at end of engine duration test.

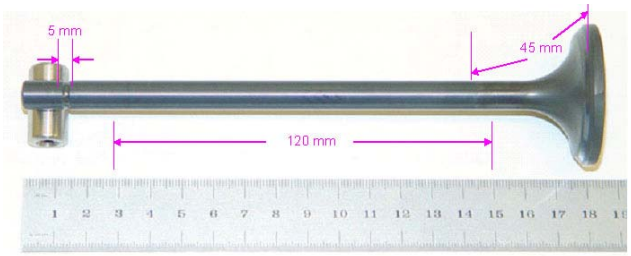

Figure 2. Laser-scatter scanned regions for each Si_3N_4 engine valve.

Laser-scatter NDE scans were performed at three surface regions for each Si_3N_4 engine valve, as illustrated in Fig. 2. The NDE tests for the 120-mm stem regions of the valves were conducted in FY2007[3]. NDE scans for the valve-head and keeper-notch sections were completed in this year. Typical results are presented and discussed below.

Figure 3 shows the laser-scatter image of the valve-head surface of intake valve I#12 that was installed in Cylinder 3. A large chip has spalled off, seen in the inserted valve photograph, likely due to an impact on the valve face surface by large debris. The scatter image shows that the fracture edges are clean, without cracks emanating from the broken region. Within and around the contact surface that matches the seat-insert surface, a few damages were detected. Figure 4 shows detailed NDE images and photomicrographs of two prominent damages within the contact surface. They are up to 1-mm long and have different optical-scatter intensities. These damages were apparently come from scratches or impacts by smaller debris. It is interesting to note that, near the second damage feature shown in the right column in Fig. 4, another apparent scratch (at the top region in the bottom-right micrograph) did not induce detectable signal in the NDE image. In addition, the NDE image in Fig. 3 also indicates many other damage features (circled) on the fillet and nearby stem surfaces. However, the presence of surface contamination and the difficulty to visually examine the curved (fillet) surfaces prevented a visual confirmation of those features.

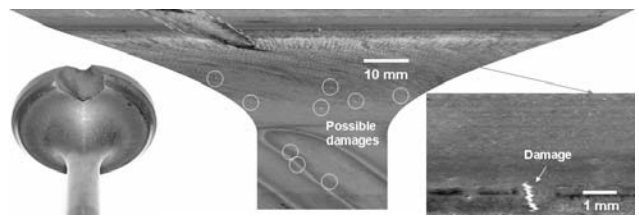

Figure 3. Laser-scatter scan image of intake valve I#12 at end of engine test.

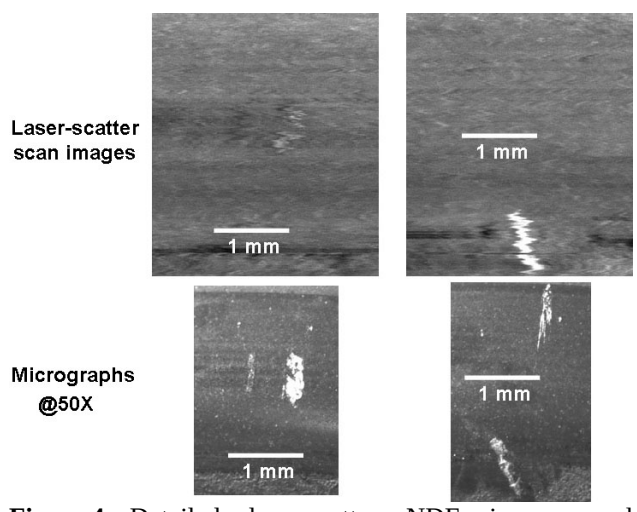

Figure 4. Detailed laser-scatter NDE images and photomicrographs of two prominent damages within the contact surface of intake valve I#12.

The keeper-notch region of all Si_3N_4 valves was scanned for a 5-mm axial length including the notch (see Fig. 2). Figure 5 shows the laser-scatter scan image for the notch surface of exhaust valve E#5 which was installed in Cylinder 2. In the image, the darker horizontal stripes were surface contamination

(possibly embedded fine metal particles) due to contact with the metal keeper. A prominent damage was detected at the bottom edge (towards the valve head side). From the enlarged NDE image and the corresponding photomicrograph shown in Fig. 6, it is apparent that this damage is a crack of ~1-mm long with a few small dents along its length. This damage was probably generated during the engine-test failure process. For other Si_3N_4 valves, only smaller material defects and machining damages were detected. One larger material defect, ~70µm in size (likely a porous pore), is shown in Fig. 7.

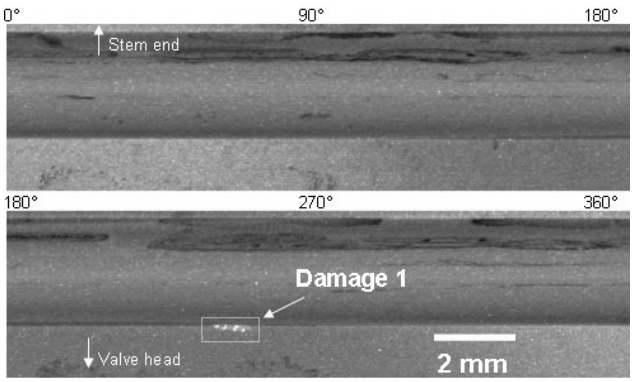

Figure 5. Laser-scatter image in keeper notch region of exhaust valve E#5.

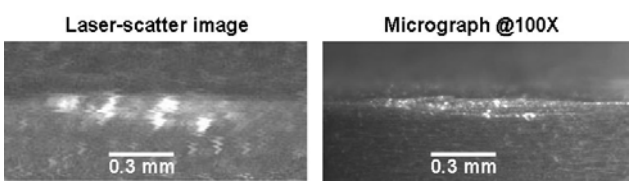

Figure 6. Detailed NDE image and micrograph of damage at notch edge of exhaust valve E#5.

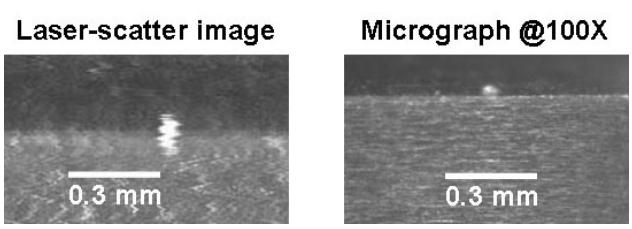

Figure 7. Detailed NDE image and micrograph of a defect at notch edge of an intake valve.

Correction for Valve-Scan Images through Image Processing

In order to achieve high-speed operation in scanning valves, the data acquisition rate is synchronized with the motion of the valve surface that is at a constant-speed rotation. While the data acquisition rate is accurately maintained by an electronic I/O board, the speed of the valve rotation typically varies depending on the friction condition within a lathe support (bearing) that couples the rotation-stage shaft to the valve chuck. Friction is a function of many parameters, including load, room temperature, speed, out-of-use duration, etc. and is difficult to control. As a result, the number of total pixels acquired for each valve revolution may not exactly match the length of the surface circumference. This causes the final laser-scatter image to be skewed, as seen in Fig. 3. In this case, the skew is from top-left to bottom-right, which corresponds to a reduced speed of the rotation stage (due to higher friction in the lathe support bearing). The skew does not affect determination of the size and shape of detected subsurface flaws, but may alter the relative positions of the flaws on the valve surface.

To accurately determine both dimensions and positions of surface/subsurface flaws from NDE scan images, the skewed image must be corrected. One way to achieve this is to implement a skew correction scheme in the image processing codes that derive the final laser-scatter image from the raw scan data. Because each scan for a valve revolution starts from a random beginning point, the alignment of consecutive scan lines is obtained by a cross-correlation matching operation. The following skew-correction scheme was then designed into this operation to optimize the matching. If the scanned length is shorter than the valve circumference, dummy pixels are added to fill the remaining length. The added dummy pixels will not affect the image quality and data accuracy because they are located in random positions in the final image (due to the random start of each scan line) and the width of each scan line is thin, typically <10 µm. On the other hand, excess pixels may be removed from the acquired data if the scan-line length is longer than the valve circumference. This skew-correction scheme has been implemented in the image processing code to reprocess the laser-scatter images for all engine valve surfaces. Figure 8 shows the reprocessed image of valve head I#12. Compared with the un-corrected image in Fig. 3, the corrected image in Fig. 8 shows a perfect alignment of scan lines along the axial direction over the entire valve-head surface. Another example is shown in Fig. 9, the laser-scatter images for the stem surface of

exhaust valve E#21 at before and after the correction. In general, dummy pixels accounting to ~1% of the total number of pixels was appended to each scan line for these images.

Figure 8. Corrected laser-scatter scan image of intake valve I#12 at end of engine test.

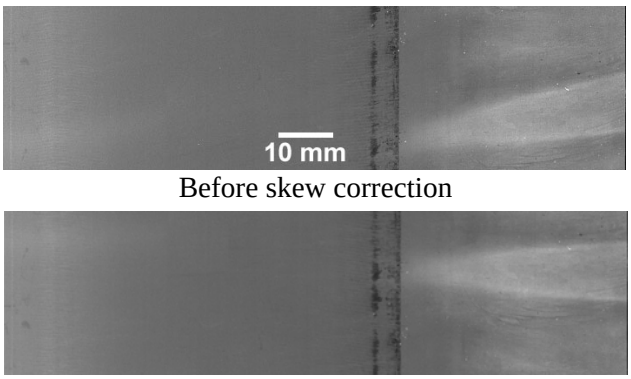

Before skew correction

After skew correction

Figure 9. Laser-scatter scan images of stem surface of exhaust valve E#21.

Correlation of NDE Data with Destructive Test Results and Identification of Fracture Initiation Flaws for Ceramic Valve Stems

The stems of 9 engine-tested Si_3N_4 engine valves (see Fig. 1, excluding E#23) were machined into half-cylinder specimens and then fracture tested at ORNL during this year. The availability of destructive test results (strength) and NDE data for these specimens presented a unique opportunity for correlation between them. Figure 10 shows a photograph of a set of fractured specimens from the stem of exhaust valve E#21. The valve stem has produced 4 fracture-test specimens, each fractured at one or two locations from the destructive test. The laser-scatter NDE image for this stem is shown in Fig. 9, acquired in FY2007. The scanning pixel size was 5 µm by 10 µm in circumferential by axial directions, respectively, which is sufficient to detect material inherent defects and damages due to machining or indent/scratch. The fractured specimens were examined first under optical microscope to determine the location of fracture initiation defect/damage, which is typically near surface and therefore has been detected by the NDE test. By comparing the optical and NDE images, the fracture initiation defect/damage can be identified in the NDE image and its type, size, and geometry are then determined. The NDE data may therefore help to understand the fracture mechanism and to establish correlation between material's mechanical property and strength-limiting flaw parameter.

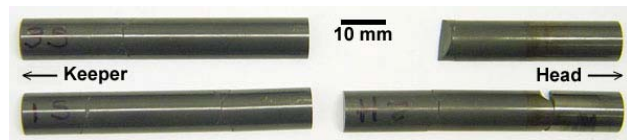

Figure 10. Photograph of fractured specimens from the stem of Si_3N_4 exhaust valve E#21.

All half-cylindrical fracture-test specimens near the valve-head side (the two specimens on the right side of Fig. 10) from the 9 stems were examined. There were 18 specimens with a total number of 25 fractures (note the bottom-right specimen in Fig. 10 has two fractures). The maximum load to fracture these specimens was ~1900N, and the minimum load was ~1300N. The fracture initiation flaws for all specimens were identified. In the following, the results for four specimens with lowest strengths are presented and discussed.

Figure 11 shows optical micrographs of the fracture (left) and tensile surface (middle) and the laser-scatter scan image of corresponding tensile surface area (right) for a specimen from the stem of exhaust valve E#21 (the upper-right one in Fig. 10). This specimen was fractured at a low load of 1303N. From the fracture surface (left image), the fracture-initiation flaw can be easily identified; it is located within the center of the half-circular fracture mirror. The position of the fracture origin was then determined in the tensile surface (middle), which is then mapped in the NDE image to find the flaw that located at the exact position (right image). From detailed examination of the NDE data, the flaw was identified to be a porous pore with a size of ~50µm. However, a linear feature, likely a machining damage, exists, which extends from the pore towards the left along the fracture line. The combined flaw feature has a larger effective size (>130µm), which was responsible for the significant reduction of the material strength.

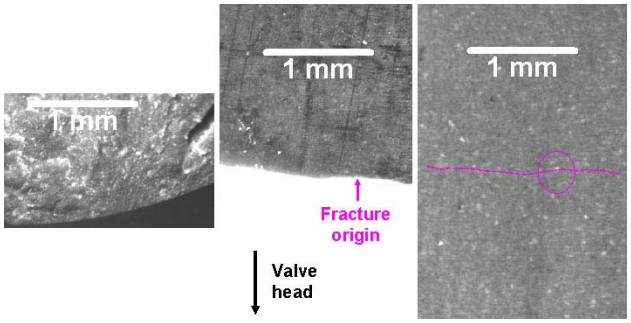

Fracture surface Tensile surface NDE image

Figure 11. Optical and NDE images for fracture specimen from stem of exhaust valve E#21.

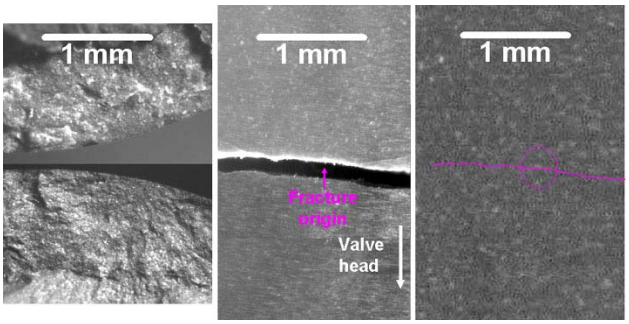

Fracture surface Tensile surface NDE image

Figure 12. Optical and NDE images for fracture specimen from stem of intake valve I#10.

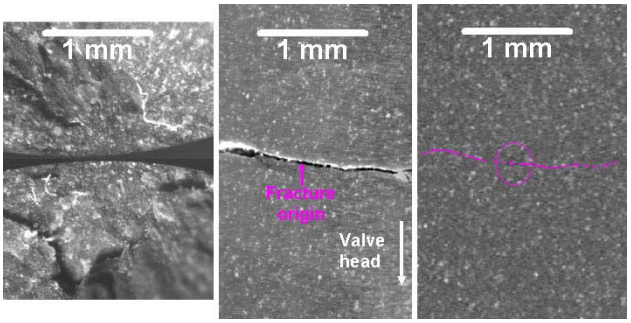

Fracture surface Tensile surface NDE image

Figure 13. Optical and NDE images for fracture specimen from stem of intake valve I#24.

Figures 12-13 show the correlation results for the other two specimens with lowest strength. For the specimen from intake valve I#10 that was fractured at 1300N load (Fig. 12), NDE data indicate that the fracture initiation flaw was a large (porous) feature of ~150µm in size. For the specimen from intake valve I#24 that was fractured at 1395N load (Fig. 13), the fracture initiation flaw appears to be a large inclusion of size ~150µm.

Finally, Fig. 14 shows the correlation for a specimen from intake valve I#22 that was fractured at 1563N load. This specimen appeared to be the only one fractured from impact damage. A closure examination of the data seems to suggest that the impact damage was coincident with a porous pore, resulting in a larger effective flaw.

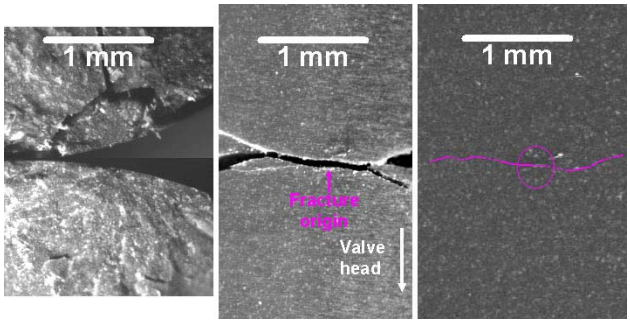

Fracture surface Tensile surface NDE image

Figure 14. Optical and NDE images for fracture specimen from stem of intake valve I#22.

NDE Development for Engine Components Made from Advanced Materials

Several NDE technologies developed at ANL were evaluated for applications for high-efficiency diesel engine materials and components. These include x-ray radiography and computed tomography (CT) for joint inspection and thermal imaging for quantitative measurement of thermal properties for ceramic thermal protection coatings.

ANL has developed advanced x-ray imaging systems and software for CT reconstruction. The x-ray systems include high-power x-ray sources at 320 and 420 kVp and digital x-ray detectors in 2D arrays of 40x40-cm area and 200-µm pixel size and linear array of 90-cm long and 83-µm pixel size. These systems have been used for digital radiography and CT imaging of ceramic components to detect density variation and material flaws such as cracks and voids, and to measure component dimension variation. They can be applied for NDE of large engine components made by metals. One such application is imaging of joints made from friction welding. Friction welding has been used for joining turbocharger wheels made from advanced light-weight materials such as TiAl. To ensure the joining quality and facilitate the process development, NDE is necessary to detect and characterize flaws that may present in the joint. In addition to ultrasonic methods, x-ray imaging may become essential to determine the 3D configuration of joint flaws (cracks). For such applications, however, system

modification and optimization is necessary to account for the high x-ray attenuations by metals.

Infrared thermal imaging has become increasingly widely used for NDE of advanced ceramic materials such as composites and coatings. ANL has established state-of-the-art thermal imaging technologies. A major effort has been on developing new data-processing methods based on pulsed thermal imaging technology. These methods may measure thermal properties (conductivity and diffusivity) of single and multilayer (e.g., coatings) materials, detect vertical and lateral cracks (e.g., cracks in joint; debond in multilayer structure), and determine the depth of flaws under surface. In FY2008 a thermal tomography method was developed and patented which for the first time is capable to construct 3D images (similar to 3D CT data) of material's thermal effusivity in an entire specimen volume. These thermal imaging methods can be utilized to characterize ceramic coatings that are being developed for thermal protection of high-temperature diesel engine components to improve engine efficiency.

Conclusions

Ten Si_3N_4 (6 inlet and 4 exhaust) engine valves that were tested in a Caterpillar natural-gas G3406 generator set at NTRC were examined using ANL's laser-scatter NDE system. These valves were damaged due to the failure of a metal valve keeper during the engine test. The NDE data were analyzed and compared with optical micrographs to identify the extent of damage. In general, impact and scratch marks were observed on valve-head surface as well as on stem surface. NDE data were used to determine the size and shape of these damages. After the valves were destructively tested at ORNL, the NDE data were used to identify fracture initiation flaws to correlate with material strength. The analyses showed that significant reduction of material strength was due to the presence of large flaws near ceramic subsurface, including inherent material defects (pore and inclusion) and damage induced by machining and impact.

Other NDE technologies were evaluated for application to high-efficiency diesel engine materials and components. In particular, x-ray radiography and CT is being evaluated for joint inspection and thermal imaging methods for quantitative measurement of thermal properties for ceramic coatings.

References

1. N. S. L. Phillips, "Lightweight Valve Train Materials," *Quarterly Report for Jan.-Mar. 2007, Heavy Vehicle Propulsion Materials Program*.

2. M. D. Kass, et al., "Report on the G3406 Engine Failure Investigation: Heavy-Duty Natural Gas Lightweight Valve Project," *ORNL Report*, August 7, 2007.

3. J. G. Sun, "NDE of Diesel Engine Components," *Annual Report for FY 2007, Heavy Vehicle Propulsion Materials Program*.

Presentations and Publications

J. G. Sun, J. S. Trethewey, N. Phillips, N. N. Vanderspiegel, and J. A. Jensen, "Nondestructive Evaluation of Silicon-Nitride Ceramic Valves from Engine Duration Test," in *Ceramic Eng. Sci. Proc.*, eds. J. Salem and D. Zhu, Vol.28, no. 2, pp. 371-377, 2007.

J. G. Sun, Z. P. Liu, Z. J. Pei, N. S. L. Phillips, and J. A. Jensen, "Optical Methods for Nondestructive Evaluation of Subsurface Flaws in Silicon Nitride Ceramics" paper to be published in Proc. 32nd Int. Conference & Exposition on Advanced Ceramics and Composites held in Jan. 27-Feb. 1, 2008 in Daytona Beach, FL.

J. G. Sun, J. M. Zhang, M. J. Andrews, J. S. Trethewey, N. S. L. Phillips, and J. A. Jensen, "Evaluation of Silicon-Nitride Ceramic Valves," Int. J. Appl. Ceram. Technol., Vol. 5, pp. 164-180, 2008.

J.G. Sun, "Method for Thermal Tomography of Thermal Effusivity from Pulsed Thermal Imaging," U.S. Patent No. 7,365,330, issued April 29, 2008.

Agreement 15050 – MaterialsTesting with ACERT Engine (CRADA with Caterpillar)

M. D. Kass, T. J. Theiss, R. Wagner, and N. Domingo
Fuels, Engines and Emissions Group
Oak Ridge National Laboratory
NTRC Building
2360 Cherahala Blvd.
Knoxville, TN 37932
(865) 946-1241; fax: (865) 946-1354; e-mail: kassmd@ornl.gov

H. T. Lin
Ceramic Science and Technology Group
Oak Ridge National Laboratory
P.O. Box 2008, MS 6068, Bldg. 4515
Oak Ridge, TN 37831-6068

DOE Technology Manager: Jerry L. Gibbs
(202) 586-1182; fax: (202) 586-1600; e-mail: Jerry.gibbs@ee.doe.gov
ORNL Technical Advisor: D. Ray Johnson
(865) 576-6832; fax: (865) 574-6098; e-mail: johnsondr@ornl.gov

---

Contractor: Oak Ridge National Laboratory, Oak Ridge, Tennessee
Prime Contract No.: DE-AC05-00OR22725

Objectives

- Improved diesel engine performance, efficiency, and emissions through the applications of materials enabled technologies.
- Evaluate material/component performance on a heavy-duty diesel engine platform.

Approach

- Install 2004 Caterpillar C-15 ACERT instrumented for thermal and combustion analysis and modified for dynamometer experimentation.

Accomplishments

- Modified existing lab space to support a heavy-duty engine research cell. Cell infrastructure has been completed.
- Signed CRADA with Caterpillar to work towards materials-enabled high-efficiency diesel engines.

Future Direction

- Perform engine baseline experimentation to confirm operating parameters with Caterpillar.
- Evaluate component/material performance and durability for at least one critical component.

Introduction

The purpose of this Cooperative Research and Development Agreement between UT-Battelle, Inc. and Caterpillar, Inc. is to improve diesel engine performance, efficiency, and emissions through the application of materials-enabled technologies. The demands of meeting new emissions and fuel economy goals are continuing to push heavy-duty diesel engine components to higher temperatures and pressures and improved durability. Engine manufacturers have recognized several key needs that need to be addressed in order for heavy duty diesel engines to achieve an national efficiency goal of 55% by the year 2012. These include 1) improved structural materials to accommodate higher cylinder pressures and temperatures (associated with advanced combustion methodologies), 2). improved thermal management and waste heat recovery technologies, 3) improved durability, 4) improved transient performance, and 5) better aftertreatment performance. These needs address barriers associated with high parasitic losses, high-efficiency clean combustion and thermal management of the cylinder and exhaust.

This CRADA brings together expertise and facilities from the ORNL Materials Science & Technology and Engineering & Transportation Science Divisions. Similarly, materials and engine research staff at Caterpillar are also working together. In anticipation of this CRADA, Caterpillar provided ORNL with two 600 hp motoring dynamometers and C15 ACERT engine. Caterpillar (working with ORNL) will develop and provide components to be evaluated on the engine platform. ORNL engine research staff will evaluate the engine performance with emphasis on combustion diagnostics, optimization and modeling. Materials scientists at ORNL will examine material performance and provide guidance to materials development.

Results

The original Cell 7 infrastructure was removed and modification commenced immediately afterwards. A control room to was installed to separate the operators from the operating machinery. Cooling water and room ventilation capable of handling large heavy duty diesel engines was installed along with the bedplates. The dynamometer was placed on the bedplates and the wiring to the control panel was completed. At the completion of the research cell infrastructure, the engine was mounted and aligned with the dynamometer as shown in Figure 1.

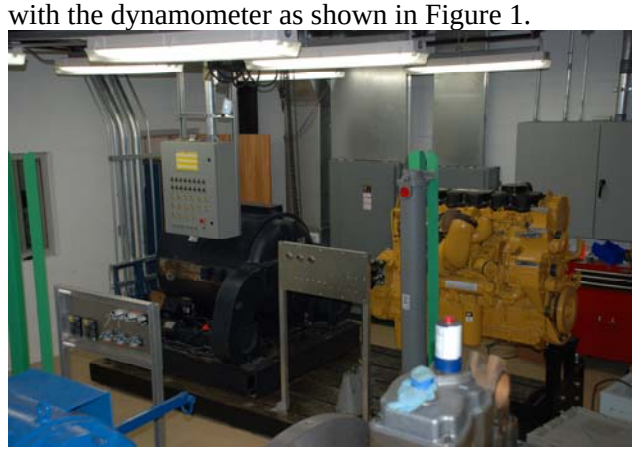

Figure 1. *Photograph showing mounted engine and dynamometer. The control room is on the other side of the wall on the left of th photograph and behind the dynamometer.*

Caterpillar provided a communication adapter and a dynamometer-baed wiring harness to enable baseline operation. The coupling shaft has been ordered along with the flywheel adapter. The cell is currently awaiting completion of the wiring of the control panels and data acquisition system before baseline experiments can be undertaken.

The calibration gas rack and accompanying plumbing were completed and two fuel tanks have been setup outdoors as shown in Figure 2.

Figure 2. Photograph showing fuel tanks (left) and the calibration gas racks (right) used for engine and cell operation.

Conclusions

The installation of the experimental infrastructure has been completed and the engine electronic package to enable dyno operation has been received. At the completion of the installation of the dynamometer controller and data acquisition systems the cell will be operational and baseline experiments will begin.

Agreement 15054 - Fatigue Enhancement in CIDI/HCCI Engine Components

Curt A. Lavender, Elizabeth Stephens
Energy Materials & Manufacturing Group
Pacific Northwest National Laboratory
P.O. Box 9998, MS K2-44
Richland, WA 99352
(509) 372-6770; fax: (509) 375-2186; e-mail: curt.lavender@pnl.gov
(509) 375-6836; fax: (509) 375-4448; e-mail: elizabeth.stephens@pnl.gov

DOE Technology Manager: Jerry L. Gibbs
(202) 586-1182; fax: (202) 586-1600; e-mail: jerry.gibbs@ee.doe.gov

---

Contractor: *Pacific Northwest National Laboratory*
Prime DOE Contract Number: DE-AC05-76RL0 1830

Objective

- Evaluate the fatigue performance impact offered by surface treatments such as laser shock peening (LSP), water jet peening (WJP) and friction stir processing (FSP) to induce compressive residual stresses and modify microstructure in the surface of aluminum, steel and cast iron engine components.
- Compare fatigue performance and thermal stability of these novel surface treatment approaches to traditional shot peening methods.

Approach

- Apply surface treatments to induce subsurface compressive residual stresses in test specimens and evaluate the stress profile vs. depth as well as the surface roughness after treatments.
- Evaluate mechanical properties of surface treated bar specimens using rolling contact fatigue and rotating beam fatigue tests methods.

Accomplishments

- A Cooperative Research and Development Agreement **(**CRADA) project kick-off meeting was held on November 29, 2007 at Cummins Technical Center.
- Cummins manufactured, heat-treated and machined specimen sets for fatigue enhancement treatments and fatigue testing.
- Selected and procured fatigue surface treatment services from selected vendors, including shot peening, LSP and WJP process services.
- Completed LSP surface treatments and residual stress measurements of A354-T6 aluminum specimens.
- Completed shot peening and LSP surface treatments, surface finishes and residual stress measurements of 52100 steel specimens.
- Increased rotating beam fatigue testing capability at PNNL by purchasing a second fatigue test unit.

- Began rotating beam fatigue tests of the as-LSP A354-T6 specimens (no surface finish applied) and the as-shot peened (no surface finish applied), shot peened, LSP and control baseline 52100 steel specimens.
- Initiated investigation of a hybrid cast iron surface treatment/joining development technique via FSP utilizing PNNL friction stir weld machine.

Future Direction

- Complete mechanical testing evaluations of specimens with novel surface treatment techniques to establish fatigue enhancement capability.
- Continue development of surface treatment techniques of cast iron material via FSP.
- Utilize component modeling tools to determine over-stressed regions of engine components that would benefit from residual compressive stress and determine magnitude of stress state needed to improve fatigue performance.
- Develop a non-destructive evaluation tool for estimating part failure by acoustic wave propagation, strain quantification and stress modeling.

Introduction

The primary objective of this project is focused on evaluating laser shock peening (LSP), water jet peening (WJP), and friction stir processing (FSP) on the fatigue performance of aluminum, cast iron and steels. Fatigue performance is an important factor in propulsion materials, especially for fuel system components, cylinder heads and blocks and the like. With the advent of faster injector response and higher pressures for better control of combustion events, cam stresses are significantly increased, leading to reduced contact and flexural fatigue life. Cyclic fatigue improvements of forming dies made from tool steels have been shown by selectively applying compressive residual stresses at the surface. Methods to apply these stresses vary, but among them, LSP has been used successfully, which not only induces compressive residual stresses at the surface (improving cyclic fatigue life more than five times) but has also been shown to decrease the susceptibility of steels to stress corrosion cracking. However, there are some uncertainties with the application of the LSP process for engine components: (1) knowing exactly where to apply the process optimally based on part starting condition and ultimate performance requirements, and (2) the parameters required to improve performance effectively based on failure modes encountered.

For softer metals like aluminum, a lower-energy option that operates similarly to LSP is high-pressure WJP. This process is still in its infancy, but it has shown promise for improving fatigue performance in aluminum castings and wrought products with better control of residual stress distribution. Like the LSP of high strength steels, the fatigue life enhancement mechanisms of WJP and optimum processing parameters are not yet well defined. In addition, further understanding of LSP effects on aluminum alloys is needed.

A cost and energy efficient way of localized metals processing to improve fatigue life and wear resistance is by FSP. This process is known to increase fatigue life by refining grain structure and homogenizing the microstructure of the metal, eliminating any defects in the processed area. Porosity is inherent to a cast metal, and the strength is always lower than a forged metal. By performing FSP in the area of interest, forged properties can be attained in a cast component and by designing in the process, low cost high strength castings can be produced. This process is ideal for applications like cylinder heads and blocks, where high strength and wear properties are desired in localized areas such as the combustion chamber, bolt hole bosses, etc. This process is capable of delivering high strength in aluminum, cast iron and steel. Significant challenges exist in understanding the effect of process parameters on mechanical properties of high temperature materials like steel and cast iron.

This project is anticipated to be a three-year development and demonstration effort and will include active participation by Cummins, Inc. In this program year, a formal CRADA agreement with Cummins was established. PNNL will perform the material characterization, selected mechanical properties tests, modeling and non-destructive evaluation development. This year, much emphasis was placed on specimen preparation and fabrication, including the application of surface treatments for each respective material population investigated.

Experimental Characterization of A354-T6 Cast Aluminum

Laser Shock Peening Evaluation

During this reporting period, A354 cast aluminum rotating beam fatigue specimens were fabricated for evaluation. The specimens were 4 in total length with a 1.5 in gage length and a 0.25 in diameter. All specimens were laser shock peened according to the vendor's recommended process parameters. The specimens were fatigue tested in the as-laser shock peened condition. No final surface finish condition was applied. Figure 1 compares the surface finishes of a laser peened A354 specimen with a control A354 specimen. A low stress ground finish was applied to the control specimen. Surface roughness measurements indicate the R_a surface roughness of the laser peened specimen is approximately 2.4 times rougher than the control specimen (19 µin vs. 8 µin, respectively).

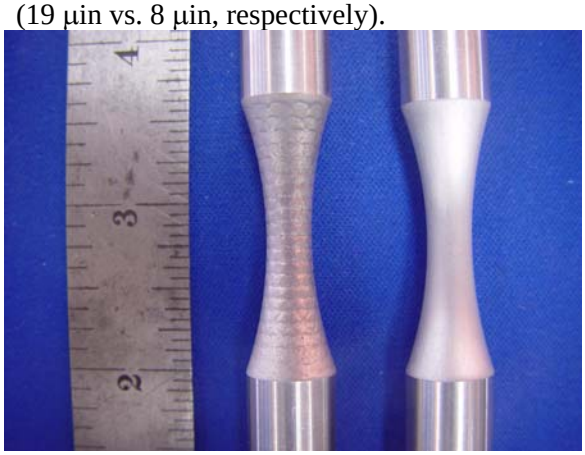

Figure 1. Representative image comparing the surface finish of an A354 cast Al laser peened specimen (left) versus a control specimen.

Preliminary fatigue test results are shown in Figure 2. Despite the rough surface finish, a slight improvement in fatigue life was observed when comparing the as-peened specimens with the control specimens. Residual stress measurements (Figure 3) indicated deep stresses at nearly 70% of the compressive and tensile yield strength of A354. At depths of 0.020 in, greater than 20,000 psi compressive residual stress was observed. This 0.020 in depth would allow for polishing or machining of the surface while retaining the residual stress to help increase the fatigue life of the LSP A354 cast aluminum. Both improvement of the surface finish and optimization of LSP to achieve an even greater residual stress may enhance the fatigue life of LSP A354.

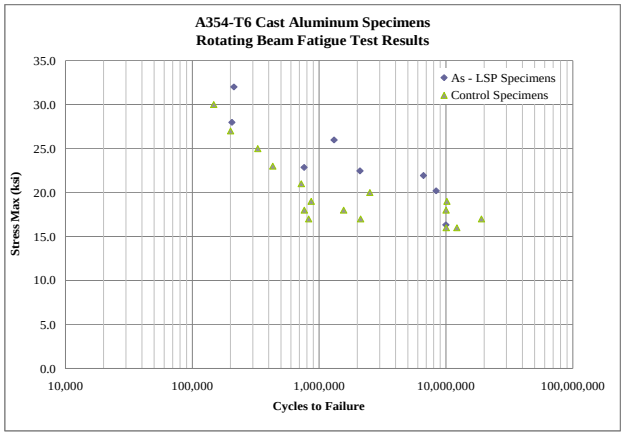

Figure 2. Preliminary fatigue test results of the as-peened and control aluminum specimens.

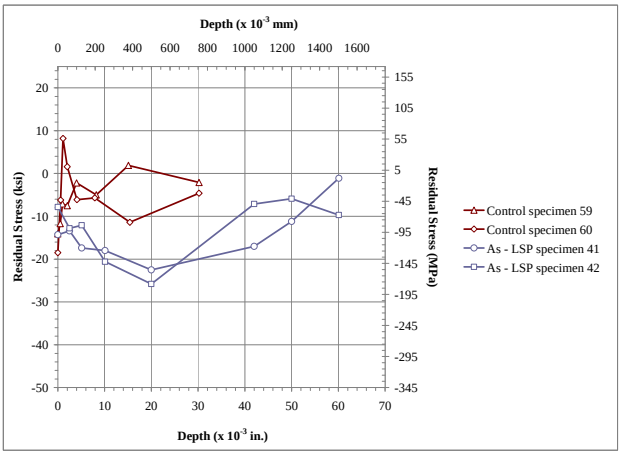

Figure 3. Comparison of the longitudinal residual stress distributions of A354 cast aluminum as-laser shock peened and as-polished specimens.

In addition, pitting was observed in the LSP specimens during evaluation of the fracture surfaces, which may be attributed to LSP processing. These pits may impact fatigue initiation, however, and may be mitigated with further LSP process development.

Further work will include adding a surface finish condition to laser shock peened aluminum specimens and investigating the fatigue crack growth rates of the LSP specimens.

Water Jet Peening Evaluation

The tasks for WJP development were defined this reporting period. The approach focuses on the use of water jet technology for peening the A354 cast alloy to enhance its fatigue life. In Task 1, a screening of water jet methods will be performed to determine the best method to produce a set of samples for evaluation. In Task 2, a parametric study will be performed to determine the optimum processing parameters from the most promising methodology determined in Task 1. For Task 3, a set of rotating beam fatigue specimens will be fabricated and processed with the parameters determined from Task 2.

The methodologies to be evaluated consist of the regular round water jet, the fan water jet (where air is spread into a flat sheet of high speed water) and the "fuzzy" water jet (where air is entrained into the water jet stream). Process parameters that will be determined include pressure, stand-off distance (the distance between work piece and nozzle) and speed/feed rate per unit area.

Experimental Characterization of 52100 Steel

Four populations of 52100 steel rotating beam fatigue specimens were fabricated for evaluation. The specimens were 3 in total length with a 1 in gage length and a 0.30 in diameter. The populations consisted of specimens from the baseline control, laser shock peened, shot peened and shot peened evaluated in the as-peened condition. A stress free/low stress ground surface finish (with an 8μin R_a value) was applied to specimens of the control, LSP and shot-peened. No surface finish was applied to the as-shot peened specimens. Figure 4 compares the surface finishes between a low stress ground finish and an as-shot peened surface finish. All varying surface treatments were performed according to the vendor's recommended process parameters.

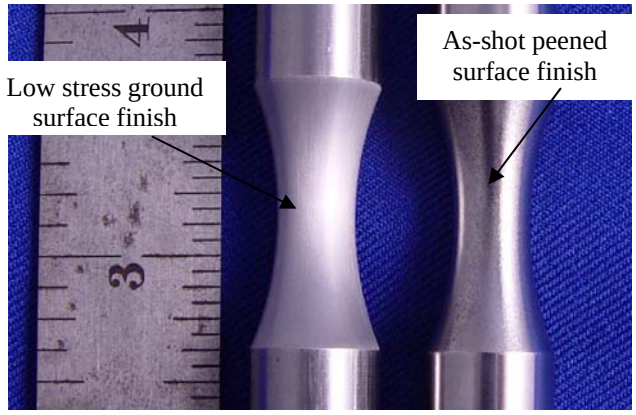

Figure 4. Surface finish comparison of a low stress ground finish and an as-shot peened finish of 52100 steel specimens.

Preliminary rotating beam fatigue test results are shown in Figure 5. The steel LSP specimens show an increase in fatigue life compared with the other three populations. A significant difference is observed particularly at high stresses. Residual stress measurements (Figure 6) indicated that deep stresses (60,000-70,000 psi) remain at 0.020 in of depth after surface grinding the LSP 52100 specimens.

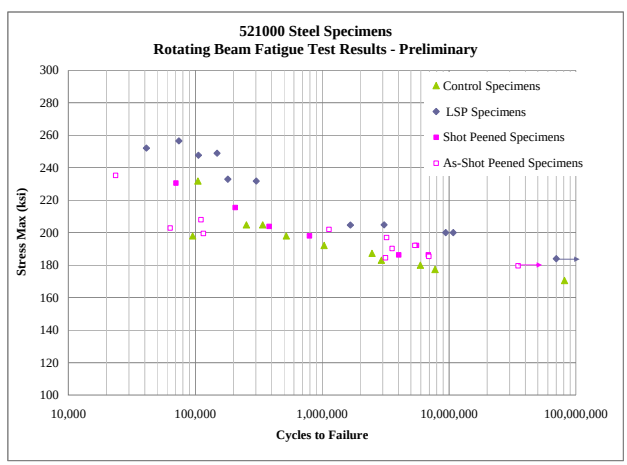

Figure 5. Preliminary fatigue test results of the LSP, shot-peened, as-shot peened and control 52100 steel specimens.

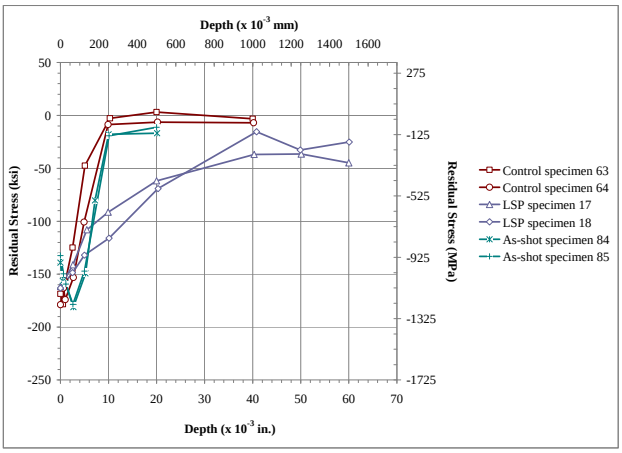

Figure 6. Comparison of longitudinal residual stress distributions of the control, LSP and as-shot peened steel specimens.

Similar fatigue life is observed between the shot-peened and ground specimens and the as-shot peened specimens at lower stresses. At this time, residual stress measurements have not been completed for the shot-peened and ground population to compare with the as-shot peened population.

A statistical analysis of the fatigue test results will be performed among the four steel populations to determine whether the results are significantly different.

Conclusions

During this reporting period, the following conclusions were derived:

- LSP produces a residual stress deep enough for post-peen grinding.
- As-peened fatigue life of aluminum A354 is slightly better than as-polished in spite of relatively rough finish.
- LSP optimization may achieve even higher compressive residual stress in A354.
- In preliminary results, the fatigue life of LSP 52100 steel shows increase over the other populations.
- Similar fatigue life was observed in the shot peened and ground specimens and in the as-shot peened specimens at lower stresses.
- Differences were observed in fatigue life at high stresses among the four 52100 steel populations.

Further investigation of the effect of surface finish and depth of residual stresses on the fatigue life of specimens are underway.

Presentations/Publications/Patents

CRADA Project Kick-Off Meeting, Cummins Technical Center. November 2007.

DOE Vehicle Technologies Program Annual Merit Review. February 2008.

Agreement 15055 - Friction Stir Processing to Tailor Thermal and Mechanical Properties of CIDI Engine Components for Improved Energy Efficiency

Principal Investigator: Glenn J. Grant
Energy Materials and Manufacturing
Pacific Northwest National Laboratory
902 Battelle Blvd.
Richland, WA 99356
(509) 375-6890; fax: (509) 375-4448; e-mail: glenn.grant@pnl.gov

M. Brad Beardsley
Advanced Materials Technology
Caterpillar Inc. Tech Center E/854
P.O. Box 1875
Peoria, IL 61656-1875
(309) 578-8514

DOE Technology Manager: Jerry L. Gibbs
(202) 586-1182; fax: (202) 586-1600; e-mail: jerry.gibbs@ee.doe.gov

---

Contractor: *Pacific Northwest National Laboratory*
Contract No.: DE-AC06-76RLO1830

Objectives

- To develop Friction Stir Processing (FSP) for engine materials (cast iron, alloy steels and aluminum alloys) with the goal of increasing their high temperature performance, durability and thermal properties.
- To deploy Friction Stir Processed components that can enable energy efficient engine design strategies such as HCCI combustion.

Approach

- This project will develop surface modification techniques, modified materials and components that can withstand higher temperatures and pressures without losing appreciable strength, hot hardness or wear resistance and at the same time be much less thermally conductive for increased thermal efficiency.

Accomplishments

- CRADA documents were finalized, and an initial kickoff meeting took place at the end of the first quarter of 2008.
- FSP was used to modify the surface of an aluminum alloy analog to a production piston alloy. Multi-wall nanotubes and several different carbon Nanofiber compositions were introduced to the aluminum surface by FSP.
- Induction pre- and post-heating (in-situ heat treatment) were developed and equipment installed on the friction stir welding machine at PNNL. Induction pre-heating lowers tool loads and increases tool life, and in-situ induction post-heating has been shown in fusion welding to increase weld toughness and ductility. These techniques will be important enablers to FSP work in cast iron and alloy steels beginning in early FY 2009.

Future Direction

- FSP of aluminum alloys will continue in 2009 with the goal of improving high temperature fatigue resistance and modifying thermal conductivity.
- FSP work on steels and cast iron will begin in the first quarter of 2009.

Introduction

The objective of this project is to investigate the application of a new material processing technology, Friction Stir Processing (FSP), to improve the thermal and mechanical properties of Compression Ignition Direct Injection (CIDI) engine components. The objective is to produce components with functionally graded surfaces that are optimized for thermal properties and for better in-service performance. The direct goal of the project is to increase the energy efficiency of the engine through better management of thermal conditions, reduced parasitic losses and indirectly through better part durability and wear resistance. This project has completed the first of a three-year effort and is a CRADA in partnership with Caterpillar, Inc.

Background

Increases in thermal efficiency of internal combustion engines can be gained by decreasing the heat losses from the cylinder during the combustion event. Typical engine efficiencies for CIDI engines are on the order of 35%. The remaining 65% of the fuel heating value goes to approximately 35% energy lost in the exhaust (thermal and chemical) and 30% in other heat losses. These other losses can be further subdivided into engine coolant (~14%), lubricating oil (~7%), ambient (~4%) and internal parasitic friction losses (~5%).[1] The heat transfer associated with these other losses is through the cylinder wall, piston and cylinder head. These components are traditionally made from cast iron, steel and aluminum alloys that conduct heat fairly well. If thermally insulating materials or thermal barriers were employed, heat transfer would be reduced; if taken to the theoretical extreme of no heat loss, engine efficiency would reach the adiabatic limit.

The effective impact of improving thermal efficiency can be expressed by an increase in either fuel economy or engine power output. This improvement can be estimated by how much of the additional heat retained (reduced heat loss) is actually utilized during the expansion stroke when useful work (shaft power) is produced. Heat loss occurs over the entire four-stroke cycle or 720º of crankshaft rotation. However, the expansion stroke accounts for only 25% of the total cycle or 180º. About 35% of the available energy in the fuel is converted to useful work (thermal efficiency) during the expansion stroke. If a 15% decrease in heat loss energy were accomplished, the estimated power output gained or fuel saved would be [(0.15)*(0.35/4)] or 1.3%. A 1% improvement in fuel economy applied to Class 8 line-haul trucks would save approximately $3x10^{13}$ BTU/yr of energy or roughly equivalent to 5.3 million barrels of oil per year.[2]

Most of the remaining reduced heat loss energy (75%) ends up increasing the enthalpy of the exhaust gas. An added benefit is that a portion of this enthalpy increase can recovered by the turbocharger, further increasing the overall engine efficiency. However, these efficiency improvements also result in hotter engine components and an increase burden on materials. Therefore, materials with improved high temperature behavior with lower thermal conductivity are needed. Nickel, titanium, ceramics and similar materials or coatings can potentially be employed. However, these materials are either cost prohibitive or have significant durability problems when used in engine applications.

To achieve improved high temperature behavior with lower thermal conductivity, surface engineering can produce an alternative to monolithic materials. Conventional coating technologies are appropriate in some environments but often suffer durability problems in the high temperature and high stress

conditions seen in the CIDI engine combustion chamber. Compositionally graded structures may be more appropriate, allowing for smoother property gradients while providing enhanced durability or thermal barrier properties in the near surface region.

FSP is a new technology that has an opportunity to be used to create compositionally graded surfaces. In recent years, PNNL has worked on developing techniques and tools that allow FSP to be accomplished in steels, cast iron and aluminum (Figure 1). The process for these materials is far from being commercially ready, but it has shown the potential for success if additional investments are made to develop and optimize the technology.

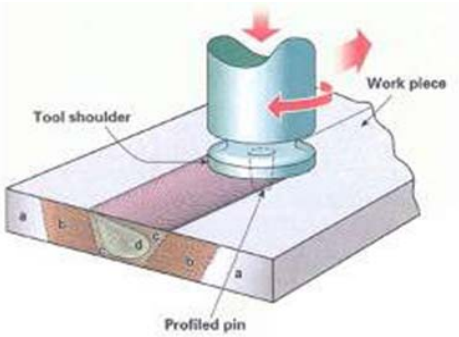

a)

b)

Figure 1. a) Friction Stir process illustration; b) typical tool used to stir ceramic powders into surface of aluminum substrate (two start scrolled shoulder with a stepped spiral pin for producing a 0.25 in thick processed region.

FSP is an outgrowth of friction stir welding (FSW), invented by TWI, Ltd. 17 years ago. It has been recognized that the same techniques and processes used to make a friction stir weld could be used to process a material for enhanced properties. The process can be selectively applied to the surface of a material, and it alters the microstructure by the severe plastic deformation that occurs in the processed zone. FSP can create a robust and graded structure with fundamentally different properties than the underlying surface and has been shown to produce surface regions with improved fatigue life, ductility and strength.

FSP produces a surface modified region that is different from a coating. Commonly, surface treatments designed to enhance wear or thermal performance include various coating methods or fusion-welded hard facings. Most of these processes are liquid state and often involve detrimental temperature effects on the base material. Heat affected zones in the base metal and various deleterious high temperature reactions can create a coated part with less than desirable properties. Also, traditional thin coatings can suffer from issues involving the nature of the interface between the coating and base material (spalling, debonding and cracking on the interface) especially under high stress, gouging wear conditions or under cyclic thermal conditions where CTE mismatch is an issue. Also, failure of a coating under high loading conditions can occur when the substrate below a thin hard coating fails by plastic deformation. Friction Stir Processed regions can show significant robustness over traditional coatings for two reasons (Figure 2). First, FSP produces a modified region that transitions to the base material without a sharp interface. Second, the modified region is generally thicker and the transition region wider than traditional coating because the plasticized region depth is related to the tool geometry, specifically the depth and size of the pin.

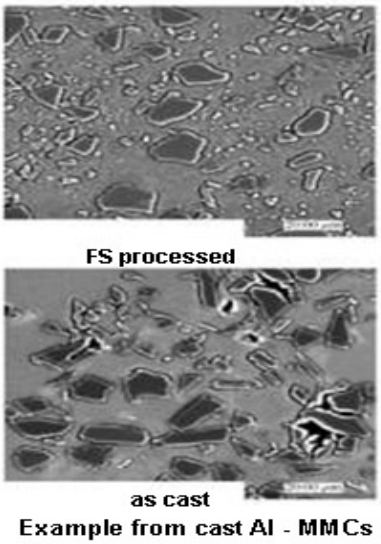

Figure 2. FSP can close porosity in castings and decrease both size and aspect ratio of particles producing better fatigue performance.

It is also possible to use FSP to "stir" insoluble ceramic particles from the surface into the substrate to depths limited only by the FSP tool geometry (Figure 3) in order to create unique surface properties, including increased hardness, wear resistance and thermal characteristics. Figure 3 shows initial trials designed to show the feasibility of stirring ceramic surface coatings into the substrate to modify the thermal conductivity of the base material. To date, the addition of up to 20% ceramic to aluminum has been demonstrated, and approximately 10% addition to steel has been achieved. These trials demonstrated the feasibility, but it is clear that more work is needed to bring the ceramic loading up to the point where it will strongly affect the thermal conductivity.

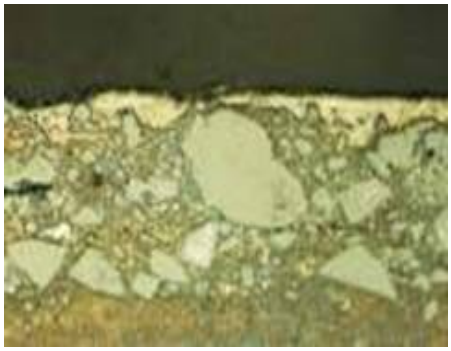

Figure 3. Ceramic particulate can also be stirred into the surface to produce functionally graded surfaces and near surface MMCs.

Approach

This project proposes to develop experimentally the FSP processes and technologies required to engineer the surface of propulsion materials for improved properties. The application focus is to tailor the mechanical properties and thermal conductivity of both ferrous and non-ferrous engine materials by using FSP techniques. This microstructural modification is expected to lead to a set of materials with enhanced surface properties that can handle increased exhaust temperatures and lower heat losses, resulting in improved engine efficiency.

The project scope will involve developing the FSP manufacturing parameters, selecting and evaluating proper tool materials and techniques to produce defect-free FSP regions. In addition, methods to introduce higher volumes of insoluble or elemental powders up to 50% will be developed. Coupon level testing and evaluation of the thermal and mechanical properties will be conducted, focusing on specific performance targets identified by project partners. If performance metrics are met for sample materials enhanced by FSP, then additional research will include developing and demonstrating the appropriate method to apply this process to a 3D geometry. If successfully developed, this class of engineered materials can significantly impact the efficiency and durability of CIDI and potentially address some of the technical barriers to implementing Homogeneous Charge Compression Ignition (HCCI) engines.

Results

During 2008, the project focused primarily on FSP in aluminum materials that are compositional analogs to the typical piston and head alloys seen in small- to mid-sized CIDI engines. Investigations were primarily of two types: FSP of cast hyper-eutectic aluminum (Alloy 356/357) with no introduction of any new component materials and FSP of eutectic Cu-Ni alloys (Alloy 339) by physically "stirring in" various quantities of carbon nanotubes and nanofibers. The two investigations are summarized below.

FSP of Alloy 356

FSP significantly refines microstructure, closes casting porosity and reduces the aspect ratio of the Si particles in hypereutectic cast alloys. These three features produce a dramatic improvement in fatigue life. Figure 4 shows the starting microstructure of the as cast alloy and two graphs illustrating the grain size distribution and aspect ratio of the silicon particles. The average Si particle size is 7.2 µm, and the average aspect ratio is 3.0. In addition, 30-40% particles have size and aspect ratio more than the mean values.

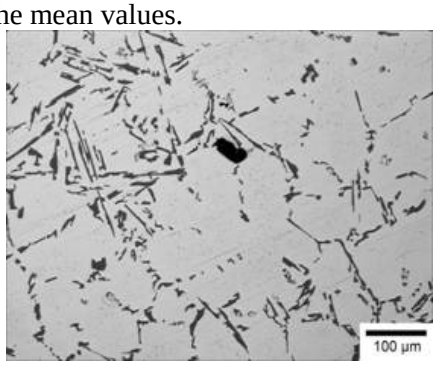

a)

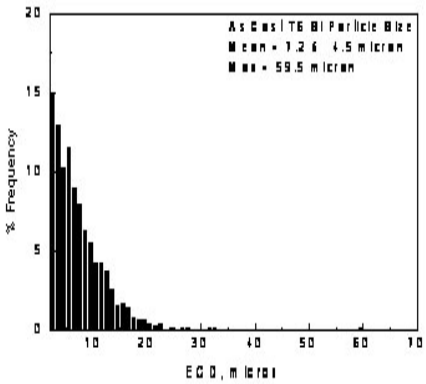

b)

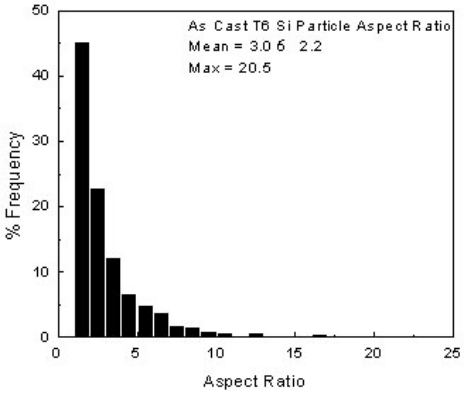

c)

Figure 4. a) Starting microstructure of the as cast 356 alloy; b) Si particle size distribution; c) Si particle aspect ratio.[3]

Figure 5 shows the microstructure and particle distribution and aspect ratio after FSP. The mean particle size is 3.1 µm (reduced from 7.2 µm in the as cast condition), and the mean particle aspect ratio is 1.7 (reduced from 3.0). FSP was able to refine the Si particles by more than 50%.

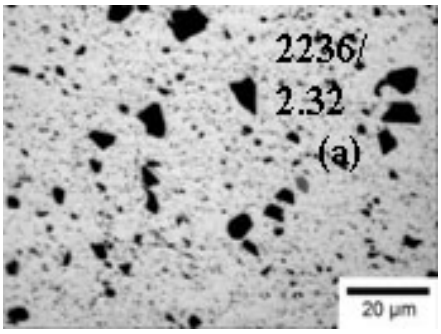

a)

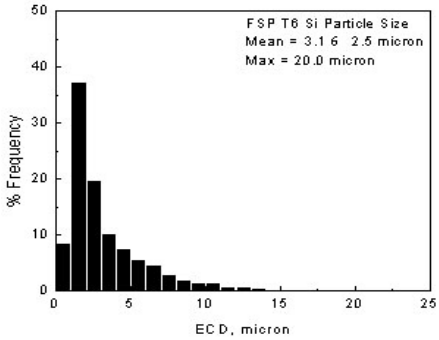

b)

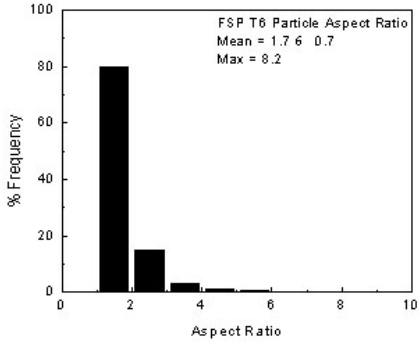

c)

Figure 5. a) Microstructure of the a-FSP processed region; b) Si particle size distribution; c) Si particle aspect ratio.[3]

Also, compared to the as-cast condition, 20-25% of total particles were above mean value after FSP (reduced from 30-40% in the as-cast condition). FSP was instrumental in eliminating comparatively larger particles from the matrix.

The effect of these microstructural modifications is to dramatically improve the fatigue performance of the as-cast materials. Figure 6 shows the S/N curves for both tensile and bending fatigue performance comparing the as cast to the FSP processed material. Improvements in maximum tensile fatigue limits up to 50%, and improvements in bending fatigue lifetime up to an order on magnitude can be shown for this alloy.

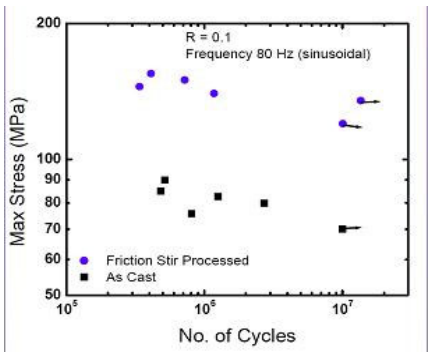

a)

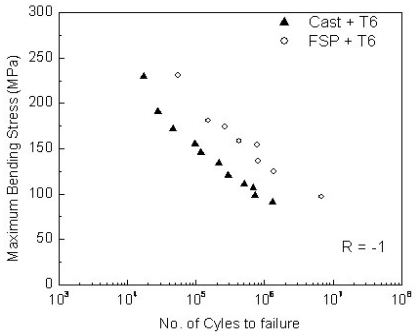

b)

Figure 6. a) SN curve for tensile loading at R=0.1 showing as cast 356 vs. friction stir processed 356; b) SN curve for bending at R=-1 showing as cast 356 vs. friction stir processed 356.[3]

In current applications of these alloys (particularly for pistons and cylinder heads), fatigue and especially thermal fatigue is the primary limiting condition on part life. As CIDI engines go to lean burn and potentially more HCCI like conditions, maximum stress in bowl rim edges, ring landings, bridge areas between valves, etc. will all likely see much higher stress levels than current designs. Improvements offered by selectively friction processing these regions may enable these energy efficient combustion strategies.

FSP of Alloy 339

During the first half of 2008, efforts focused on developing appropriate processing parameters to produce consolidate FSP processed regions in 339 castings (Figure 7).

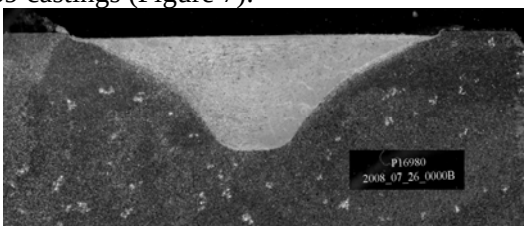

a)

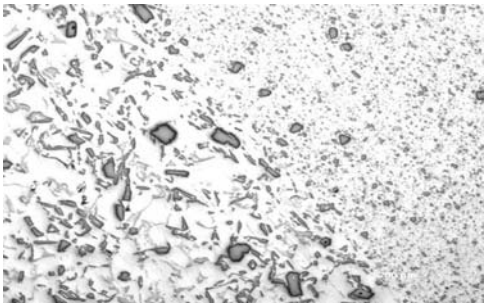

b)

Figure 7. a) Fully consolidated FSP region in cast 339 alloy. Processed region is approximately 0.25 in depth; b) Micrograph showing edge of stirred zone showing particle refinement in processed region.

During the latter half of 2008 efforts focused on improving the fatigue performance of this alloy by FSP. Alloy 339 is close in composition to many diesel piston alloys and as such is representative of a baseline performance. The primary failure in service is fatigue and thermal fatigue at several locations on the piston. New combustion strategies will only make this situation worse. Our goal was to use FSP to improve the mechanical properties that most influence thermal fatigue: CTE, conductivity and to a lesser extent, high temperature strength. The goal is primarily to reduce CTE and increase conductivity. Table 1 shows candidate materials that could be stirred into the base metal to modify mechanical properties potentially and selectively.

Table 1. Potential additions to 339 base material

Material	Modulus	CTE	Conductivity
Aluminum	80 GPa	25 µm/m°C	180 W/m-K
SiC	410 GPa	4.4 µm/m°C	150 W/m-K
Al_2O_3	370 GPa	8.5 µm/m°C	13 W/m-K
Carbon Nanotubes	>600 GPa	Low or Can be negative !	> 1000 W/m-K

Of these, carbon nanotubes and fibers offer the best potential to improve thermal fatigue due to their very low CTE and high conductivity. It should also be noted that other additions that increase wear resistance and decrease conductivity will be investigated later in this project to affect the performance of other high efficiency engine components (skirts, liners, etc.).

Experimental work consisted of cutting 1/8 and 3/16 in wide slots in base plates of aluminum alloy 339. These slots were approximately 1 in long. Mixtures of aluminum and nanotube powders were then packed in square-section aluminum 3003 tubes and press fit into the slots (Figure 8).

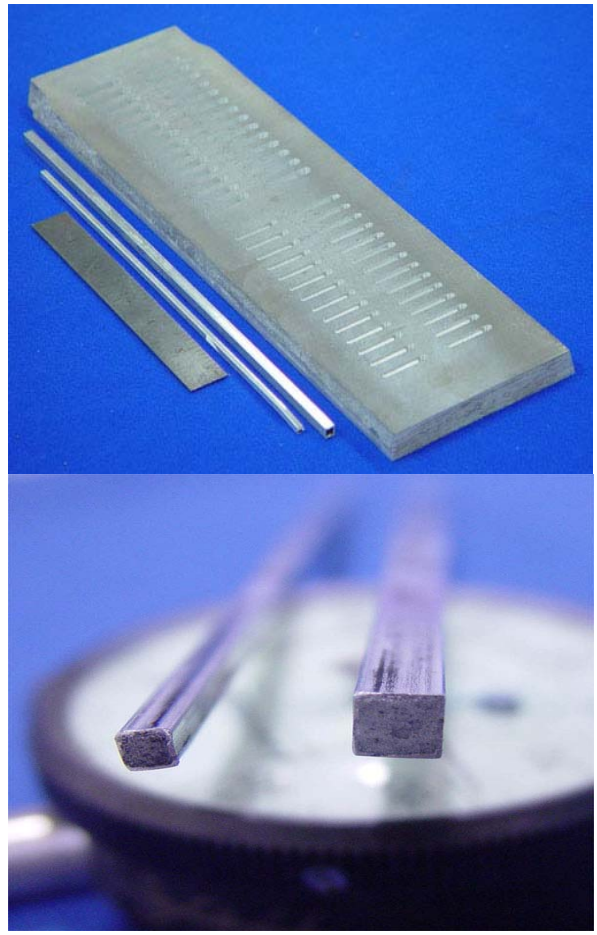

Figure 8. Carbon nanotube/aluminum powders mixtures were loaded into aluminum tubes, cut and press-fit into slots in base metal.

Table 2 shows carbon nanotube and Nanofiber details. We used Showa Denko nanofibers and Bayer "Baytube" multiwall nanotubes in this study in 50/50 and 20/80 wt % ratio mixtures.

Table 2. Carbon nanotube and fiber sources.

Product	ID	Source	OD(nm)	Length(um)	BET(m2/g)
VGCF	VGCF-H	Showa Denko	150	9	13
	VGCF-S	Showa Denko	100	10	
Pyrograf-III	PR-19-HHT	ASI	100-200	30-100	15-25
	PR-24-HHT	ASI	60-150	30-100	
Baytubes	C 150 P	Bayer	13-16	1->10	
	C 150 HP	Bayer	13-16	1->10	

Friction processing trials were recently completed, but mechanical property data were not available by the deadlines for this report. FSP trial results indicate that fully consolidated welds with 1/8 in tubes were obtained at a number of different process conditions, and carbon nanotubes were distributed and intimately mixed with the aluminum substrate (Figure 9). Results of mechanical testing should be available in the first quarter of 2009.

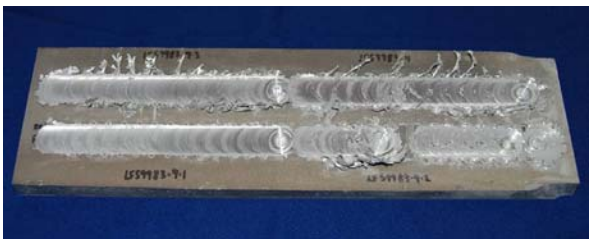

Figure 9. Nanotube and Nanofiber FSP trials on 339 plate.

This project will also investigate FSP in steels and cast iron. Initial trails in steel began during the last quarter of 2008. Much of the efforts involved equipment development for induction pre- (and more importantly post-) heating of the FSP region (Figure 10).

Figure 10. 30 Kva induction heating system showing adjustable heat station mounting frame to vary stand off and trailing heat distance (top) and control unit (bottom).

Steel and cast iron FSP can require additional heat during the plunging phase of the processing run because drastic tool wear can occur when a cold tool is driven into a cold substrate. Induction heating of the plunge zone has been found in earlier work by PNNL and South Dakota School of Mines and Technology to be necessary to preserve the life of the tooling. Induction heating will also be used to accomplish post-processing heating to slow the cooling rates effectively after processing. It has been shown in fusion welding[4] that in-situ or just trailing heating can significantly increase weld region ductility (Figure 11), affect the final microstructure and may be able to affect fatigue performance positively as well using a moving induction heat source behind the stir tool. During the later half of 2008, the project constructed adjustable frames and equipment to investigate this research area.

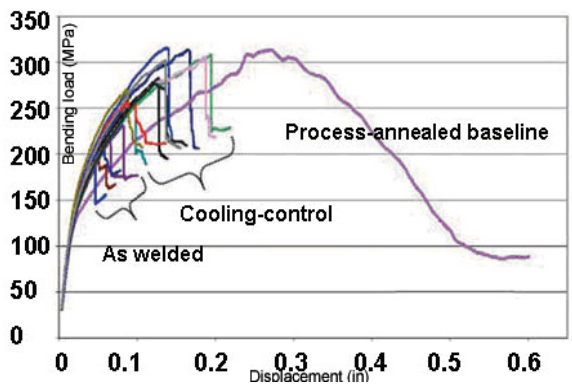

Figure 11. Increase in weld ductility seen if induction heating is used just after welding by installing a moving coil following the weld head.[3]

Conclusions

The goal of this project is to increase the thermal efficiency and durability of CIDI engines through the use of FSP, which produces wide graded structures with increased strength and durability in fatigue over some conventional coating technologies. Surface modification through FSP may have an opportunity to address some emerging material problems seen in very high combustion pressure systems like HCCI engines as well. In addition, the process allows for the incorporation of particulate into the surface, potentially selectively modifying the

properties of materials to enable combustion strategies that can enable increasing thermal efficiency. Experimental work to date on aluminum systems has shown the potential to increase strength and fatigue performance significantly in hypereutectic aluminum alloys using friction processing alone, and on-going work in eutectic, high temperature aluminum alloys has shown the potential to create new mechanically mixed alloys of aluminum, carbon nanotubes and fibers that may provide unique thermal fatigue resistant surface regions to fatigue failure prone CIDI engine components.

References

1. Pulkrabek, WW. 2004. *Engineering Fundamentals for the Internal Combustion Engine*, 2nd Ed.
2. Annual Energy Outlook. 2005. DOE/EIA-0383.
3. Jana, S. 2008. Ph.D. dissertation (in progress). Missouri Institute of Science and Technology.
4. Codd, Daniel S. 2008. Post-weld Induction Heating Provides Controlled Cooling of MSS Welds. In *Heat Treating Progress*, ASM International. September 2008.

Agreement 16103 - Concept Feasibility of Bonding Similar and Dissimilar Powertrain Materials Using Reactive NanoFoils

Principal Investigator: Xin Sun
Computational Science and Mathematics Division
Pacific Northwest National Laboratory
Richland, WA 99352
(509) 372-6489; fax: (509) 372-6099; e-mail: xin.sun@pnl.gov

DOE Technology Manager: Jerry L. Gibbs
(202) 586-1182; fax: (202) 586-1600; e-mail: jerry.gibbs@ee.doe.gov

Contractor: *Pacific Northwest National Laboratory*
Contract No.: DE-AC06-76RL01830

Objective

- Provide an objective bond strength evaluation for NanoFoil® bond in comparison with conventional bonding methods.
- Provide cost and cycle time analyses for using reactive NanoFoil in a mass production environment.

Approach

- Perform bond strength evaluations for both similar and dissimilar metal (advanced high strength steel, aluminum [Al], magnesium [Mg]) as well as metal/non metal (ceramic, polymer) joints.
- Perform economic study considering cost, bond quality and cycle time for the automotive manufacturing environment.

Accomplishments

- Completed bond strength evaluations for both improved aluminum/magnesium and polymer composite/metal bond.

Future Direction

- Perform quantitative economic study considering cost, bond quality and cycle time for automotive manufacturing environment.

Introduction

Advanced joining technology remains to be the key enabler for engine original equipment manufacturers (OEMs) since implementation of advanced combustion technologies will require high fuel pressures, higher peak combustion chamber pressures and better air handling and thermal management. Currently, fusion welding and adhesive bonding are the main joining technologies used in the heavy vehicle production environment. While proven reliable in conventional materials, these methods have drawbacks in joining similar and dissimilar advanced lightweight materials such as advanced high strength steel (AHSS), aluminum (Al) castings and magnesium (Mg). For example, the high heat input of fusion welding tends to destroy the designed AHSS microstructures, rendering less than desirable joint properties.

In this project, we propose to study the performance and cost feasibility of an alternative bonding technology (namely, reactive NanoFoil® bonding) in heavy vehicle powertrain applications, which can include the following: joining of dissimilar metals in lighter weight, high-performance compression ignition engines (e.g., high hardness steel shafting to lighter weight titanium impellers and air handling components), joining metal composite to machinable steel shafting and bearing surfaces, joining metals to ceramic high-wear inserts, and joining corrosion-resistant stainless steels and nickel (Ni)-based alloys for protection of steel and iron substrates for reduced cost and improved performance.

NanoFoil is a multi-layer foil fabricated through the growth of thousands of nanoscale layers of Al and Ni by vapor deposition. Initiated by an energy impulse, the like-like bonds of the atoms of each layer in the foil are exchanged for more stable unlike bonds between atoms from neighboring layers. As the atoms of each layer mix, heat is generated, creating a self-sustaining reaction and localized heat source traveling length of the foil. This type of self-propagating exothermic formation reactions has been observed in a variety of nanostructured multilayer foils, and the reactions are driven by a reduction in atomic bond energy (Ref. 1). The instantaneous release of heat energy by this reaction is controlled by the nanolayer thickness and lay-up such that accurate control of highly localized heat input can be realized, allowing bonding without compromising the properties/integrities of the base materials.

Since this is a new joining technology, the scope of PNNL's feasibility work includes:

- Provide objective bond strength evaluations for NanoFoil bond in comparison with conventional bonding/joining methods
- Provide engine OEMs with cost and cycle time analyses for using reactive NanoFoil in mass production environment.

In order to provide an objective evaluation of bond strength between similar and dissimilar metals bonds, the following material combinations (i.e., joint populations) were examined in FY 2007 (Ref. 2):

- 1.4 mm SAE1008/1.4 mm SAE1008 solder joint
- 2 mm AA5182-O/2 mm AA5182-O solder joint
- 2 mm AA5182-O/2 mm AA5182-O braze joint
- 2 mm AA5182-O/2 mm AZ31 solder joint

For the first three joint populations, it was demonstrated that NanoFoil bonds can achieve similar or higher bond strength compared with those of the structural adhesives. For the Al/Mg population, however, considerably lower bond strength was observed. In FY 2008, we therefore focused our attention on improving the strength of the Al/Mg bond. In addition, we demonstrated the concept feasibility of bonding polymer composite to metal by metalizing the polymer surface with thermal spray process.

Approach

The following technical approach is followed for each joint population:

- Sample surface preparation
- Join each joint population with selected solder material
- Perform C-Scan of bonded areas to ensure bonding
- Examine microstructures of base material and bonded region
- Perform bond strength tests under tensile shear configuration
- Compare tested bond strength with conventional adhesive bonded joints

Results

Improved 2 mm AA5182-O/2 mm AZ31 solder joint

In FY 2007, we pre-applied 96.5Sn-3.5Ag to the Al samples on a hot plate using mechanical agitation. On the Mg side, samples were vapor metalized with Ti/Incusil (Incusil=61.5Ag-23.5Cu-15In) braze, with freestanding Sn-Ag-Cu

(SAC) solder sandwiched between metallization and NanoFoil. Using the above surface preparation, adhesive failure at bond surface was consistently observed for all the samples tested. The measured bond strength is from 2.86-4.9 MPa with a large variation from sample to sample. In addition, the failed samples showed very little bending deformation in them, indicating a brittle joint with a low level of energy absorption.

In order to improve the bond strength and its consistency, an improved surface preparation technique is used for both the Al and Mg. A Sn layer of .015 +/- .002 in thickness was deposited on the Al plate by thermal spray process. On the Mg side, a Ni/Al (95/5 blend) layer of .01 +/- .002 in thickness was first thermally sprayed on the Mg surface. The surface was then top coated by a Sn layer of .015 +/- .002 in thickness also through thermal spray. The two surfaces were then bonded using reactive multilayer foil (NanoFoil) as a heat source. Figure 1 shows the typical scanned image of the solder joint. Good bond quality has been obtained with respect to the percentage of bonded area.

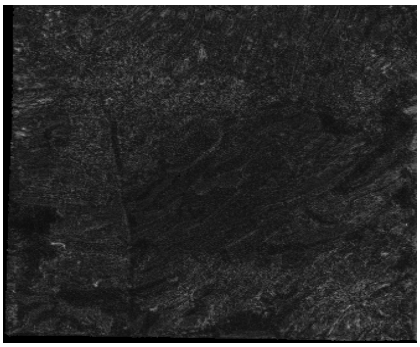

Figure 1. Scan image of the bonded area for improved Al/Mg bond.

Quasi-static bond strength tests were then carried out with a servo-hydraulic load frame. Figures 2(a) and (b) show the typical load versus displacement curve and failure mode for the 2 mm AA5182-O/2 mm AZ31 solder joint. Cohesive failure at bond surface is consistently observed for all the samples tested. With the improved surface preparation, higher strength and more consistent bonds have been achieved. The nominal bond strength is 6.4-7.0MPa. All failed samples show bending deformation, indicating ductile bond failure with good energy absorption capability.

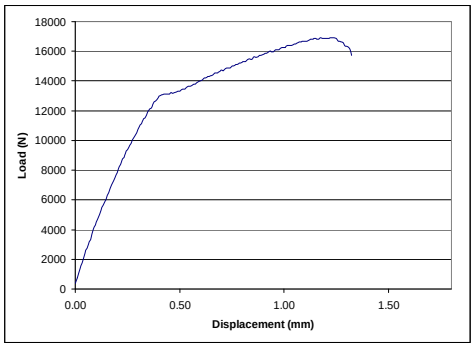

(a)

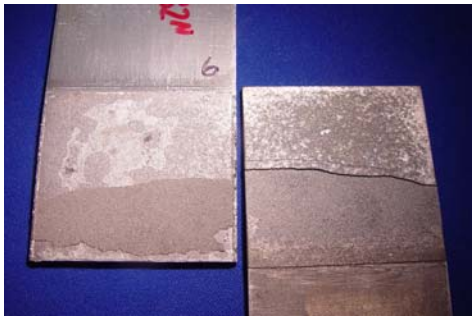

(b)

Figure 2. Typical bond strength test results for the solder joint of 2 mm AA5182-O/2 mm AZ31: (a) load versus displacement curve; (b) failure mode.

With the improved surface preparation, we have demonstrated that the NanoFoil bond strength for Al/Mg can be in par with the strength level of structural adhesive bond between Al/Al (~7.2MPa; Ref. 3).

2 mm AA5182-O/Polymer composite solder joint

In this task, we explore the possibility of bonding Al to polymer composite by metalizing the polymer surface first. For this purpose, a 1/8 in thick fiber-reinforced polymer plate is used to bond with a 2mm AA5182-O sheet. The surface of the polymer was first metalized with a .015 +/- .002 in thick Sn layer with thermal spray process. The process parameter for thermal spray was optimized experimentally such that no surface spallation was observed on the sprayed sample. See Figure 3 for the as-sprayed surface of the composite material prior to bonding. A Sn layer of .015 +/-.002 in thickness was also deposited on the Al plate by thermal spray process prior to bonding.

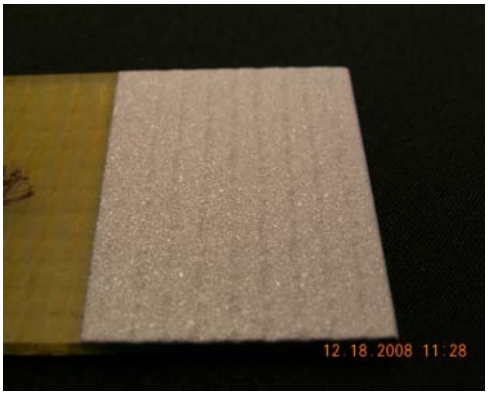

Figure 3. As-sprayed composite surface.

The two surfaces were then bonded together using reactive multilayer foil (NanoFoil) as a heat source. Figure 4 shows the typical scanned image of the solder joint. Good bond quality has been obtained with respect to the percentage of bonded area.

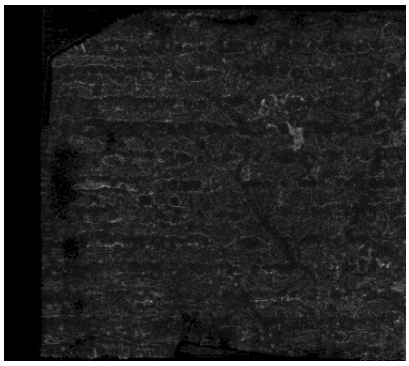

Figure 4. Scan image of the bonded area for Al/ composite bond.

Quasi-static bond strength tests were then carried out with a servo-hydraulic load frame. Figures 5(a) and (b) show the typical load versus displacement curve and failure mode for the 2 mm AA5182-O/polymer composite solder joint.

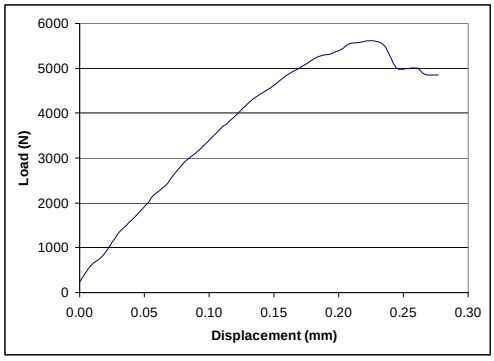

(a)

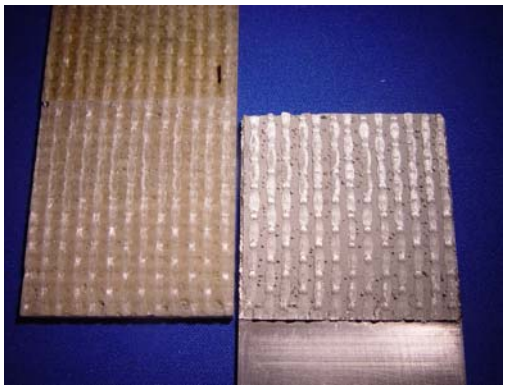

(b)

Figure 5. Typical bond strength test results for the solder joint of 2 mm AA5182-O/metalized polymer composite: (a) load versus displacement curve; (b) failure mode.

Consistent adhesive-type failure at bond surface is observed for all the four bonded samples in this population. It is shown in Figure 5(b) that the thermally sprayed Sn coating is peeled off from the polymer substrate during the strength test with the fiber imprints on the coating surface. The nominal bond strength measured ranges from 1.8-2.2 MPa, much lower than the strength of typical adhesive bonds. All failed samples show very little sample bending, indicating brittle bond failure with poor energy absorption capacity.

It should be mentioned that, due to the adhesive failure mode observed, the measured bond strength is effectively the strength between the thermally sprayed Sn coating to the fiber-reinforced polymer substrate, and that the strength for the solder joint between Sn and Sn achieved by the NanoFoil should be much higher. Our next step in improving the bond strength for this population therefore lies in improving the material/process for the polymer metallization process.

Conclusions

Comparing the bond strength of the two NanoFoil bond populations performed in FY 2008 with those of the populations examined in FY 2007, the following observations/conclusions can be made:

1. Bond strength for the 2 mm AA5182-O/2 mm AZ321 solder population is considerably improved with the new thermal-spray based surface coating method. Average bond strength of 6.7 MPa is achieved for the dissimilar metals joint, very similar to the strength of a typical structural adhesive.
2. Our preliminary study on metal/composite solder joint shows an adhesive type of failure between the Sn coating and the composite substrate with relatively low bond strength. Future work in this area lies in improving the bond strength between the metalized coating and the polymer substrate.

Presentations/Publications/Patents

Sun, X and A Duckham. 2008. "Strength Evaluation of Reactive Nano-Foil Bonded Joints for Automotive Applications." Presented at the XIII Sheet Metal Welding Conference, Detroit, MI. May.

References

1. Wang, J, E Besnoin, A Duckham, SJ Spey, ME Reiss, OM Knio, and TP Weihs. 2004. *J. Appl. Phys.* 95(1): 248-256. January.
2. *Concept Feasibility of Bonding Similar and Dissimilar Powertrain Materials Using Reactive NanoFoils*. Propulsion Materials, FY 2007 Annual Progress Report.
3. *Joining of Dissimilar Metals for Automotive Applications: From Process to Performance*. Automotive Lightweighting Materials, FY 2004 Annual Progress Report.

Key Words

NanoFoil®, bond strength, polymer substrate

Brief Description of Report

This project examines the performance and cost feasibility of NanoFoil®, an alternative bonding technology, in heavy vehicle powertrain applications. The objectives are to provide an objective bond strength evaluation for NanoFoil bond compared with conventional bonding methods and provide cost and cycle time analyses for using reactive NanoFoil in a mass production environment.

Project 18519 - Materials for Control of Exhaust Gases and Energy Recovery Systems

Agreement 9130 - Development of Materials Analysis Tools for Studying NO_x Adsorber Catalysts (CRADA No. ORNL-02-0659 with Cummins Inc.)

Thomas Watkins, Larry Allard, Michael Lance, and Harry Meyer
Oak Ridge National Laboratory
P.O. Box 2008
Oak Ridge, TN 37831-6064
(865) 574-2046; fax: (865) 574-3940; e-mail: watkinstr@ornl.gov

DOE Technology Manager: Jerry L. Gibbs
(202) 586-1182; fax: (202) 586-1600; e-mail: jerry.gibbs@ee.doe.gov
ORNL Technical Advisor: D. Ray Johnson
(865) 576-6832; fax: (865) 574-6098; e-mail: johnsondr@ornl.gov

---

Contractor: Oak Ridge National Laboratory, Oak Ridge, Tennessee
Contract No.: DE-AC05-00OR22725

Objective

- The purpose of this effort is to produce a quantitative understanding of the process/product interdependence leading to catalyst systems with improved final product quality, resulting in diesel emission levels that meet the 2010 emission requirements.

Approach

- Characterize lab-engine tested samples with X-ray diffraction (XRD), spectroscopy, and microscopy. Correlate findings with Cummins data and experience.

Accomplishments

- The evaluation of hydrothermal degradation of a commercial zeolite urea SCR catalyst as a function of operating conditions defined by the end user has been completed.
- Supported continued characterizations of new materials from various stages of the catalyst's life cycle.

Future Direction

- Continue characterization of a commercial zeolite urea SCR catalyst subjected to hydrothermal aging for lifetime prediction model input. Focus on understanding the catalyst degradation mechanisms due to hydrothermal aging using the tools developed under this CRADA.
- Begin ammonia oxidation catalyst characterization.
- Assist Cummins to competitively produce engines which attain the required emission levels for 2010 and beyond while maintaining the advantage of the diesel's inherent energy efficiency.
- Continue to characterize the soot, coke and ash formed on the catalyst from different fuels, including biodiesel.

Introduction

In order to meet the 2010 US Environmental Protection Agency (EPA) emission requirements for diesel exhaust, aftertreatment in diesel engines may be necessary. The technology necessary for 2010 will need to integrate aftertreatment with engine control systems. Currently, no commercial off-the-shelf technologies are available to meet these standards. Consequently, Cummins Inc. is working to understand the basic science necessary to effectively utilize these catalyst systems. ORNL is assisting with the materials characterization effort. This report will focus on the study of materials used in selective catalytic reduction.

Selective catalytic reduction (SCR) is one possible method to reduce NOx emissions. Here, a gaseous or liquid reductant is added to the exhaust gases and adsorbed on to the catalyst, sometimes a zeolite. The reductant reduces NOx to H_2O and N_2.[1] Urea is a typical reducing agent which can operate under lean or oxygen rich conditions as follows:[2] $(NH_2)_2CO + 2NO + 1/2O_2 \Rightarrow 2N_2 + 2H_2O + CO_2$.

A zeolite is classically defined as a crystalline, porous aluminosilicate. More recently, zeolites are defined as porous oxide structures with well-defined pore/channel structures and a high degree of crystallinity. There are an unlimited number of structures possible, making them particularly useful as molecular sieves.[3] There are many chemical interactions with zeolites which center around $Si\text{-}O_4$ and $(Al\text{-}O_4)^{-1}$ tetrahedra and the cations within the pores, supplying charge compensation. Zeolites are often used as ion exchangers in water softeners and shape selective catalysis. The cation with H+ becomes a strong acid, which is catalytically active.

Approach

A commercial Fe zeolite powder is being examined with diagnostic tools developed previously under this CRADA. The crystal structure, morphology, phase distribution, particle size, and surface species of catalytically active materials supplied by Cummins were characterized using transmission electron microscopy (TEM), X-ray diffraction (XRD), X-ray photoelectron spectroscopy (XPS), and Raman Spectroscopy. These materials will come from all stages of the catalyst's life cycle: raw materials, as-calcined, sulfated, regenerated, etc. Both ORNL and Cummins personnel have participated in this work to understand zeolite degradation.

Samples

This year a commercial Fe zeolite powder was hydrothermally aged at 500, 700, or 900°C for 12 hours in a gas composed of 10 H_2O, 72 N_2 and 18 O_2 v% with a space velocity of ~ 42,000 h^{-1} (see Table I).

Results

The above samples were examined with microscopy, XRD and Raman from October 2007 to September 2008, which is summarized below.

Microscopy

Characterization of commercial Fe zeolite materials by electron microscopy techniques was continued. Typical results and observations of samples in Table 1 are reported. It should be noted that electron microscopy of most of the samples in this study was very difficult, as even short exposures of the zeolite material to the electron beam resulted in amorphization and often disintegration of the region of interest.

Powder samples were prepared typically by dry-dipping a TEM grid covered by a holey carbon film into the provided powder, shaking off the excess, and loading the grid into the TEM specimen holder. Samples were examined primarily in the HTML's JEOL 2200FS-AC aberration-corrected electron microscope (ACEM), and one sample in the new Hitachi HF-3300 field-emission TEM with energy-dispersive x-ray spectrometer (EDS) system for elemental analysis. The ACEM provides high-angle annular dark-field (HA-ADF) imaging simultaneously with bright-field (BF) imaging, and allows imaging at the sub-Ångström level (e.g., single atoms of heavy metal species such as Fe can be resolved). The geometry used in the ACEM for recording dark-field and bright field images is shown in Figure 1. The simple concept is that an aberration-corrector element in the illuminating system above the sample allows the formation of an intense electron beam with a diameter of less than one Ångström (0.1nm). Energy-loss electron spectroscopy is actually possible with an energy

filter built into the imaging system below the sample, but was not employed for the work reported here. X-ray spectroscopy was also not conducted on the ACEM, as a new design of detector was not available (coming in December 2008). Both analytical methods will be used for future analyses. The EDS analysis results from the Hitachi HF-3300 will be reported in the next quarterly, along with early results from the new detector on the ACEM.

Prior work on H-Beta-Zeolite (Un-doped) and Fresh Powders [4]

In order to more reliably analyze high-resolution images from the Fe zeolites (specifically to try to locate the Fe species within the framework of the zeolite lattice), we compared the Fe zeolite images with that of a base zeolite material. We had previously determined that our experimental Fe zeolite samples most closely matched the zeolite structure of H-beta zeolite (by XRD analysis). Figures 2a and 2b are a HA-ADF/BF image pair acquired at a magnification suitable to show the zeolite lattice structure in the BF image. This image area represents a reasonably uniform thickness of the sheet-like morphology of zeolite structure. Note that the HA-ADF image shows a smooth, low-contrast structure, in comparison to the open network lattice structure in the corresponding BF image. There is no evidence of bright contrast regions that might correlate to the presence of Fe atoms or clusters in as are seen in all the Fe-doped samples in the following sections.

In order to better understand the imaging of the hydrolyzed Fe ion-exchanged zeolite materials, a sample was prepare which without question had heavy metal species dispersed over the surface. An ion-sputter-deposition system in the HTML was used to sputter a very small amount of chromium species onto a TEM specimen grid onto which had been dispersed aggregates of the blank H-beta zeolite material, supported on holey carbon films. The ability of the ACEM to resolve single atoms of an element lighter in atomic number than iron (24 vs. 26) is shown by the images in Figure 3. These are two images showing both single atoms and small clusters against the low contrast background of the zeolite structure.

Fresh Powder: ACEM Results

For comparison to both the blank H-beta material and the H-beta material with Cr species on the surface, a sample of the fresh Fe zeolite powder (no hydrothermal aging) was imaged, as shown in Figure 4. A typical HA-ADF/bright-field pair of images that were acquired simultaneously is typical of all the images obtained in the Fresh sample. The BF STEM image clearly shows the channels in the zeolite material, while the HA-ADF image shows the Fe-rich phase in the specimen in bright contrast. The Fe-rich phase is seen as a uniform distribution over the image of patches that range between 2-7nm in spatial extent. However, the relatively faint contrast of the Fe-rich phase, and the fact that it is not clearly evident in the associated BF image, suggests that it is distributed in thin layers either over the surface or within the bulk of the zeolite particles. In no instance were individual atomic species or discrete clusters of atoms seen that compared to the observation of the Cr atoms that were indisputably on the surface of the H-beta zeolite.

Hydrothermally Aged Fe Zeolite: ACEM Results

Figures 5 and 6 show the HA-ADF/BF data for the hydrothermally aged samples at 500 and 700°C, respectively. Figures 7-9 show the HA-ADF/BF data for the hydrothermally aged sample at 900°C. Figure 5 shows a pair of images of the 500°C sample. The striking similarity to the Fresh Fe zeolite material is evident in the lattice structure seen in both the ADF and BF images. In no instance were single atoms or discrete clusters of Fe atoms seen, in many such image pairs. This suggests that the hydrothermal aging at 500°C did not cause significant changes in the structure of the catalyst.

Figure 6 shows a similar image pair, typical of the Fe zeolite material hydrothermally aged at 700°C. Again, there is no discernible difference seen between these (or many other such image pairs recorded on the ACEM) and the Fresh Fe zeolite material. It is apparent that even this higher temperature hydrothermal aging treatment did not produce visible changes in the structure of the material.

The sample hydrothermally aged at 900°C, however, showed numerous features different from the lower temperature samples. Figure 7 shows a typical HA-ADF image pair from this sample, at a

lower magnification than the prior images, to show the primary difference: the clear presence of facetted crystallites within the zeolite material. The crystallite shown in the box in Fig. 7a is seen at higher magnification (10Mx direct magnification) in Fig. 8. The maintenance of the lattice structure, seen in both the HA-ADF and BF images, at this magnification indicated an immediate difference in behavior of the 900°C sample relative to the other material. This sample was much more stable in the electron beam than the Fresh and lower temperature treated samples. In no instance with the earlier samples could lattice structure be maintained for a significant time at the beam flux experienced at a magnification of 10Mx or higher. The 900°C sample, however, showed great beam stability, and allowed many images to be recorded at high magnification.

Another graphic example of the retention of structure in the Fe zeolite hydrothermally aged at 900°C is shown in Fig. 9. This HA-ADF and BF image pair was recorded as part of a sequence of images taken at 10Mx direct magnification, and shows an orientation looking nearly down columns of atoms in the ADF image after at least 6 earlier image pairs were recorded. Faint bright patches on the order of 10 nm (smaller than those seen in earlier materials) are evident in the ADF image, and some evidence of differences in intensity of individual atomic columns is also seen. It is not clear from these images, however, that we are directly imaging Fe atoms, as the structure of the crystallite has evidently undergone some damage (a thin amorphous layer is seen around the perimeter, showing a change from the original (not shown) edge of the crystallite. Differences in intensities of atomic columns in any structure with different atom types can result from the presence of different atoms in the column, or from a different number of the same atom type. The ability to make such images is, however, promising for our further studies of the high-temperature hydrothermally aged material, especially utilizing EDS or EELS analysis techniques to better locate the Fe species.

Microscopy Summary:

1. The nominal zeolite structure as determined by XRD was shown to be H-beta zeolite. Images of this material in the ACEM showed only minimum contrast structure in HA-ADF mode.
2. Fresh Fe Zeolite powder shows bright "patches" of Fe 1-5nm in extent, which seem to lack 3-dimensional structure. No such patches are seen in dark-field images of H-beta-zeolite blank material.
3. Fresh Fe zeolite material then hydrothermally aged at 500°C and 700°C showed structure with no discernible difference as compared to the Fresh material.
4. A hydrothermal aging treatment at 900°C showed a significant change in the zeolite structure, with numerous facetted crystallites seen. The structure of the crystallites was much more stable under the electron beam than the extremely beam sensitive Fresh or lower temperature materials.
5. The stability of the higher temperature hydrothermally aged material is promising for further studies using a new capability for elemental analysis by EDS or EELS techniques.

DRIFTS and NMR

Infrared spectroscopy provides information about a materials molecular structure, dynamics and sample environment based on by exciting molecules into higher vibrational states.[5] This information can be used to identify compounds and molecular groups/species, discern couplings of different molecular groups, etc. When the infra-red light impinges on a sample it can be reflected, absorbed or transmitted. Diffuse reflectance is the sum of the surface reflected and bulk re-emitted signal.[6] DRIFTS provides vibrational information from both the sample's surface and bulk.

Figure 10 shows the DRIFTS spectrum for the three hydrothermally aged samples. The spectrum from the 900°C hydrothermally aged sample is different from the other two. In addition to the changed peaks associated with hydrocarbon species, the subtle peaks associated with the Si(OH)-Al and Si-OH bonds are decreasing and increasing, respectively, with increasing hydrothermal aging temperature. Since the peak area is a measure of quantity, the amount or number of Si(OH)-Al and Si-OH bonds are reduced and increased, respectively, suggesting dealumination is occurring within the zeolite.

NMR of Fe zeolite also shows that the lattice is dealuminizing due to hydrothermal aging. NMR relies on the interaction of the nuclear magnetic dipole moment with an external or internal magnetic field.[5] Atomic resonance is obtained when the frequency of the magnetic field is swept or

scanned.[5] In Figure 11, most of the Al atoms are located in one of two different Al tetrahedral sites with a small amount of Al^{3+} and Al_2O_3. Hydrothermal aging has eliminated one tetrahedral site and reduced the other showing that most of the Al is out of the lattice and is probably associated with a Fe center.

XPS

XPS is an analytical technique that is sensitive to the outermost 3-5 nm of the material under examination. XPS analysis gives both elemental and chemical identification of the surface. Low energy resolution survey scans yield the presence and quantity of any element present on the surface. Once identified, high energy resolution scans are made to show the specific chemical bonding of selected species. For this project, Fe-compounds containing known Fe-bonding configurations were analyzed to help identify the Fe-bonding state in the Fe zeolites.

Iron carbonate ($Fe^{2+}CO_3$) and iron oxide ($Fe^{3+}{}_2O_3$) powders were spread on double-sided tape and placed in the XPS analysis chamber. Survey scans showed the presence of Fe, C, and O for both powders. For the iron oxide sample, the presence of C indicated some amount of adsorbed C-containing contamination. This same adsorbed contaminant was also present on the iron carbonate sample and was identified using the high energy resolution scan of the C 1s photoelectron feature. Figure 12 shows the Fe 2p core level for the two iron compounds and highlights the differences between the two valence states of Fe. The main Fe3+ peak and the "satellite" structure are both shifted to higher binding energy. Satellites are common for transition metal compounds and arise due to specific chemical bonding configurations and their presence is often used as a "fingerprint" for such configurations.

Figure 13 shows the Fe 2p spectra for the as received Fe zeolite powders. It is clear the main Fe 2p peak is at a binding energy position similar to a Fe+3 oxidation state. The absence of specific satellite structure is most likely due to the way Fe atoms are bound within the framework of the zeolite structure.

Figure 14 shows the changes that occur when the as-received powders are hydrothermally heat treated at 500, 700, and 900°C. The inset Table gives the compositional analysis. There is an overall decrease in the amount of Fe present at the surface. Additionally, there is a slight increase of both Si and Al at the surface. Detailed scans of the Al 2p indicated that the Al-O bonding within the zeolite framework was being affected as noted by a small increase in the Al 2p binding energy. This increase in the Al binding energy is interpreted as a chemical reduction of the Al atoms, i.e. a loss of Al-O bonding.

Initial XPS analysis of the as-received and hydrothermally aged materials indicates that this technique is able to detect subtle changes in the surface of these Fe zeolites. However, several repetitions are recommended before drawing firm conclusions.

X-ray

X-ray diffraction (XRD) was employed to understand the crystalline nature of the samples. For the unfamiliar, the following analogy can be applied: As a fingerprint identifies a person, so a diffraction pattern identifies a crystalline material.

The XRD patterns for the fresh Fe zeolite powder and the hydrothermally aged powders are shown in Figure 15. Little change is observed in the patterns until 900°C. It is clear (see large arrow ~22°2θ) that the crystallographic structure is changing after the 900°C hydrothermal treatment. Using an analysis from reference 7, the "relative crystallinity" of each powder was determined, based on the assumption that assumes as-received sample is 100% crystalline. This measure of crystallinity also shows a ~25% decrease after the 900°C hydrothermal treatment.

Overall Summary

XRD, TEM, DRIFTS, NMR and XPS all showed the effect of hydrothermal aging after 900°C exposure. XRD indicated that the degree of crystallinity is decreasing. Dealuminization was observed with NMR, DRIFTS and XPS. TEM shows 900°C hydrothermally aged sample is more stable under electron beam relative to as-received sample.

References

[1] Internet: en.wikipedia.org/wiki/Selective_catalytic_reduction
[2] I. Chorkendorff and J. W. Niemantsverdriet, Concepts of Modern Catalysis and Kinetics, Wiley-VCH Verlag GmbH & Co. KGaA, Weinheim, 2003, p. 400.
[3] Internet: www.personal.utulsa.edu/~geoffrey-price/zeolite/zeo_narr.htm.
[4] Propulsion Materials, 2007 Annual Progress Report, Vehicle Technologies Program, US DOE, Energy Efficiency and Renewable Energy, Office of Vehicle Technologies, Advanced Materials Technologies, E. J. Wall, R. A. Sullivan, J. L. Gibbs, Jan. 2008, www.ornl.gov/sci/propulsionmaterials/Reports.html.
[5] ASM Handbook, V10 Materials Characterization, ASM International, 1986, p.112, 277.
[6] Internet: http://www.uksaf.org/tech/ftir.html
[7] Hardenberg et al., Zeolites, 685 (1992); Nicolaides, Applied Catalysis A 211 (1999).

Acronyms

ACEM aberration-corrected electron microscope
BF bright-field
DRIFTS Diffuse reflectance infra-red Fourier transform spectroscopy
EDS Energy dispersive spectroscopy
EPA Environmental Protection Agency
HA-ADF high-angle annular dark-field
NMR Nuclear Magnetic Resonance
NO_x Nitrogen and Oxygen containing compounds
ORNL Oak Ridge National Laboratory
SCR selective catalytic reduction
STEM Scanning Transmission Electron Microscopy
XPS X-ray photoelectron spectroscopy
XRD X-Ray Diffraction

Table I. Samples examined

Sample Designation	Condition	Instrument+Technique
H-beta-Zeolite Undoped w/ & w/o sputtered Cr	No Fe present	ACEM (ADF+BF)
Fe Zeolite, Fresh	As-received	ACEM (ADF+BF)
Cum#H1	Hydrothermally aged at 500°C*	ACEM (ADF+BF)
Cum#H2	Hydrothermally aged at 700°C*	ACEM (ADF+BF)
Cum#H3	Hydrothermally aged at 900°C*	ACEM+HF-3300 TEM w/EDS

* 12 hours in a gas composed of 10 H_2O, 72 N_2 and 18 O_2 v% with a space velocity of ~ 42,000 h^{-1}

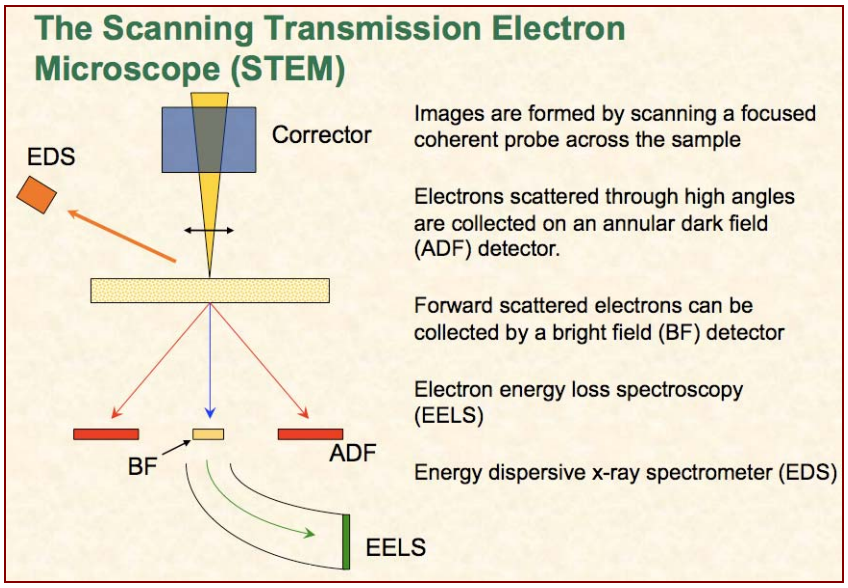

Figure 1. A schematic showing imaging modes for the aberration-corrected electron microscope. Dark-field and bright-field images are acquired simultaneously, providing complementary information. ADF images show heavy elements (e.g., Fe) in bright contrast relative to the light element composition (alumino-silicate) of the zeolite structure.

a. 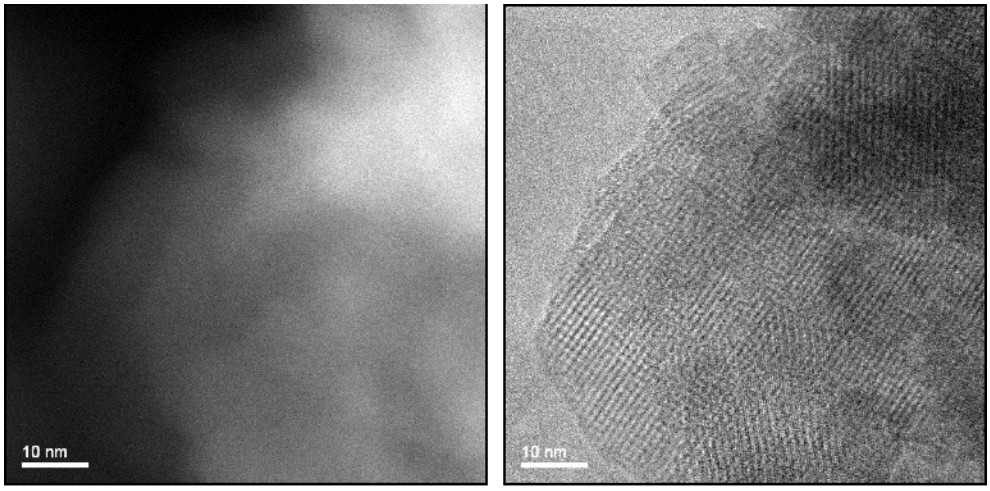

b.

Figure 2. a.) HA-ADF image of H-beta-zeolite blank material, showing uniform contrast with no evidence of heavy element scattering; b.) Corresponding BF image showing crystal lattice that indicates the high resolution of the incident probe.

a. 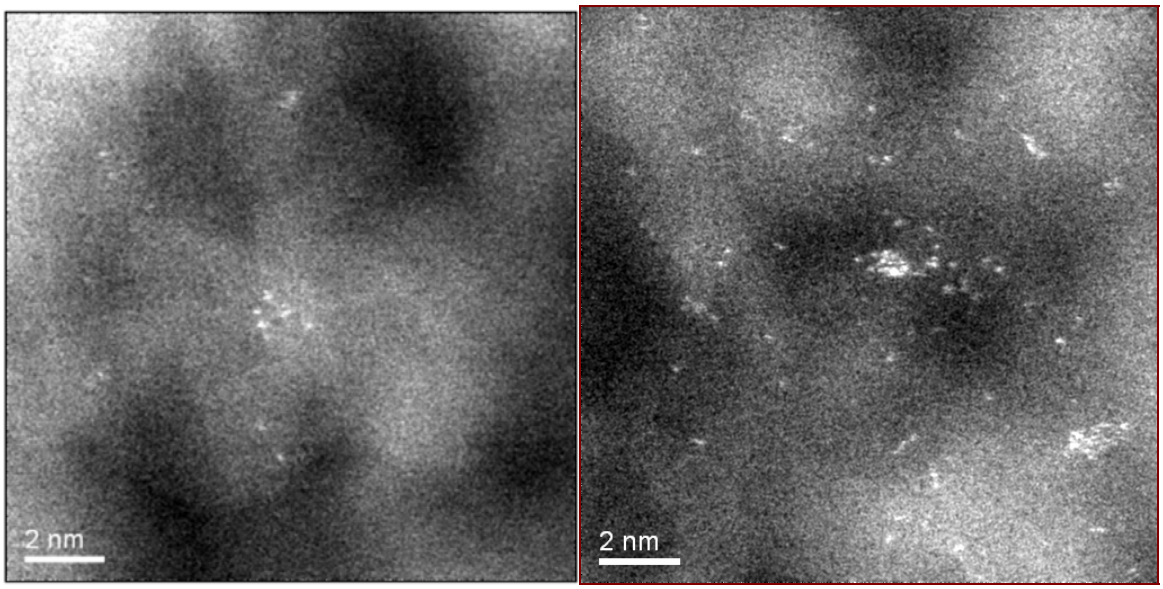

b.

Figure 3. a.) and b.) Both images show Cr clearly in high contrast against the low contrast background of the zeolite structure. Single atoms alone are seen in a., while two very small clusters of a few atoms each, along with mostly single Cr atoms, are seen in b.

a. 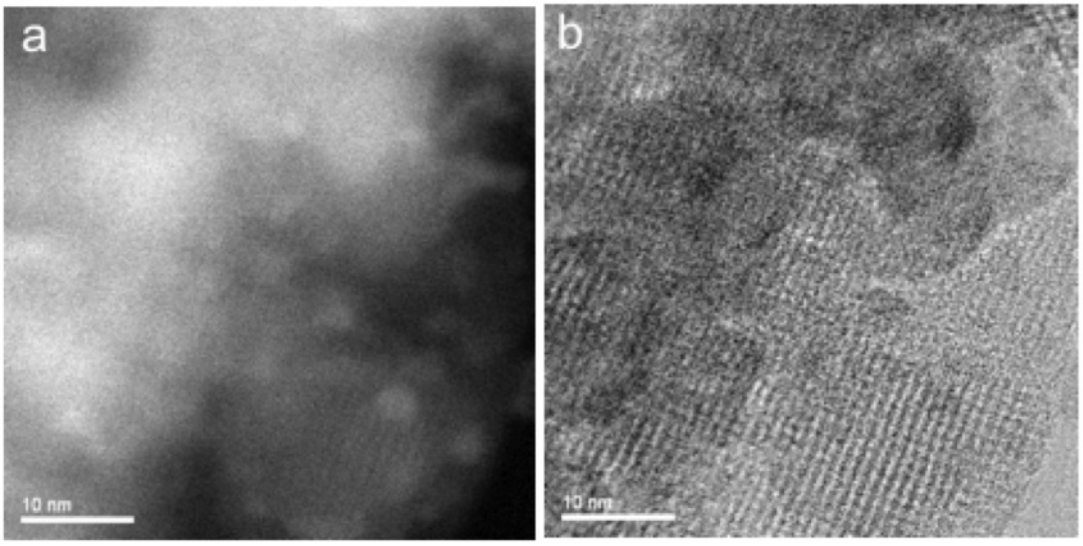

b.

Figure 4. Typical a.) HA-ADF and b.) BF image pair of the Fresh Fe zeolite sample. The BF image shows the lattice structure of the plate-like zeolite material, which can be seen in faint contrast in the ADF image. The 2-5nm bright patches are associated with the Fe species in the lattice or on the surface.

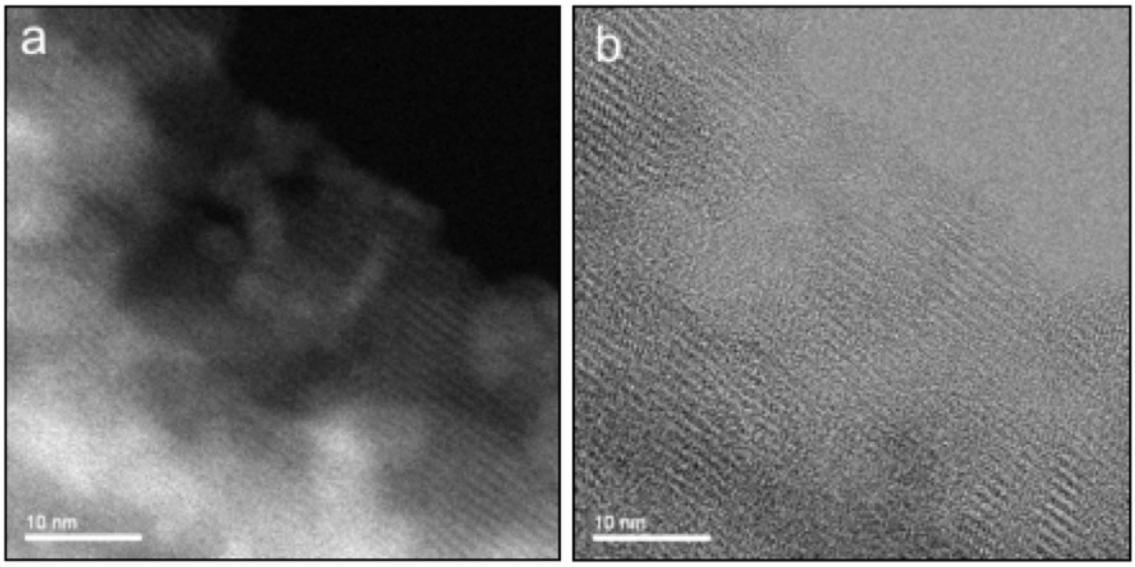

Figure 5. Typical HA-ADF (a) and BF (b) image pair of Fe zeolite material after 500°C hydrothermally aging for 12h. Note that the lattice structure seen in both the ADF and BF, and bright patches in the ADF image very similar to the structure seen in the Fresh Fe zeolite material.

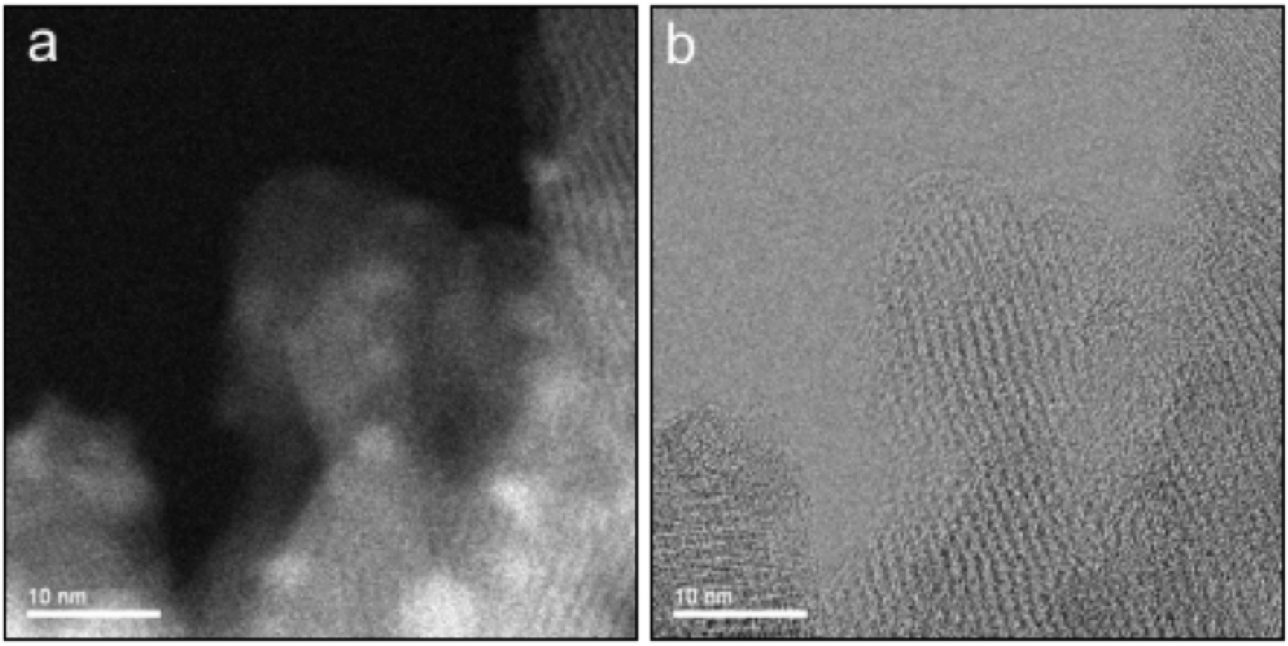

Figure 6. Typical HA-ADF and BF image pair of Fe zeolite material hydrothermally aged at 700°C for 12h. No change in structure is seen relative to the Fresh material, as evident by the lattice structure in both images, and bright patches of Fe species seen in the ADF image similar to the Fresh and 500°C material.

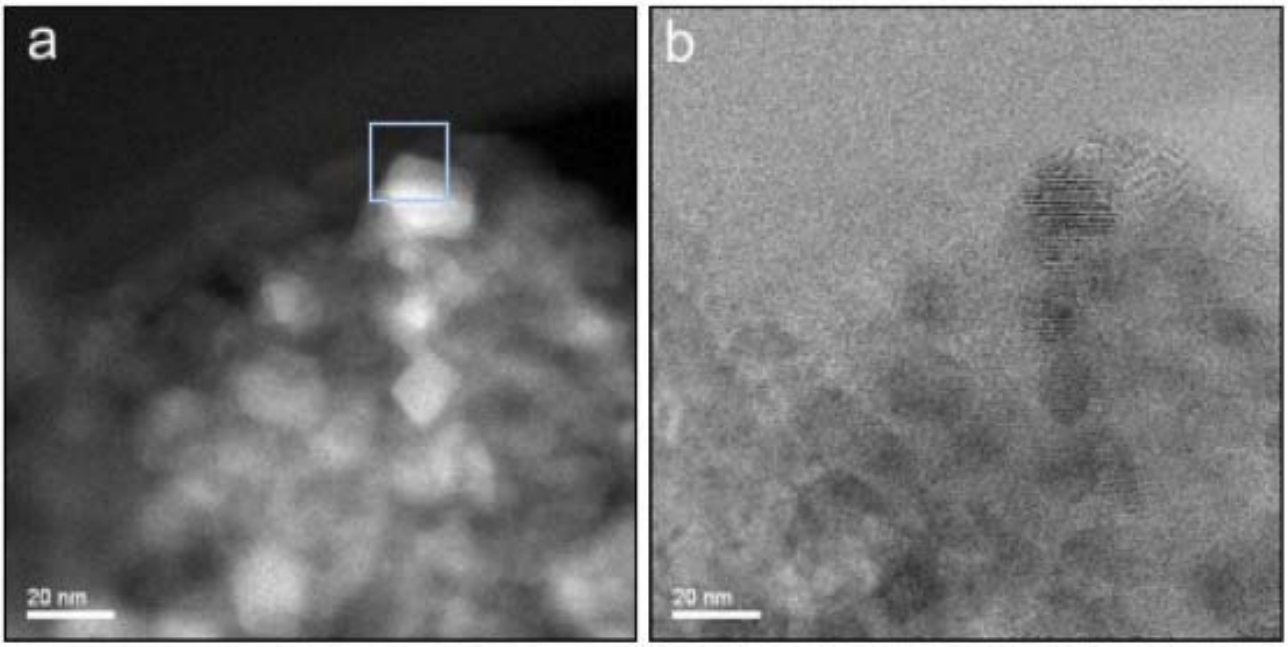

Figure 7. HA-ADF and BF image pair showing facetted crystallites, typical of the microstructure of the sample hydrothermally aged at 900°C. Box inset shows area of Figure 8.

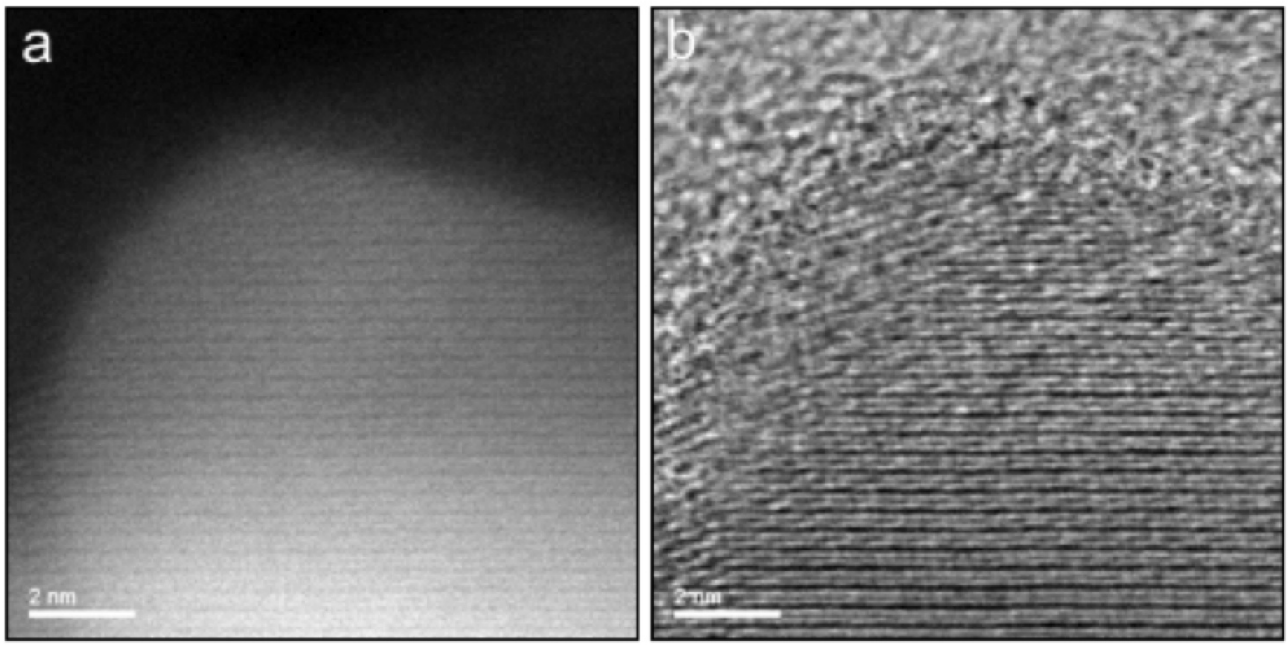

Figure 8. Higher magnification of the crystallite shown in the box in Figure 7. The lattice structure seen in both HA-ADF and BF images was retained after many scans at the direct magnification of 10Mx. Such stability was not seen in any of the earlier samples.

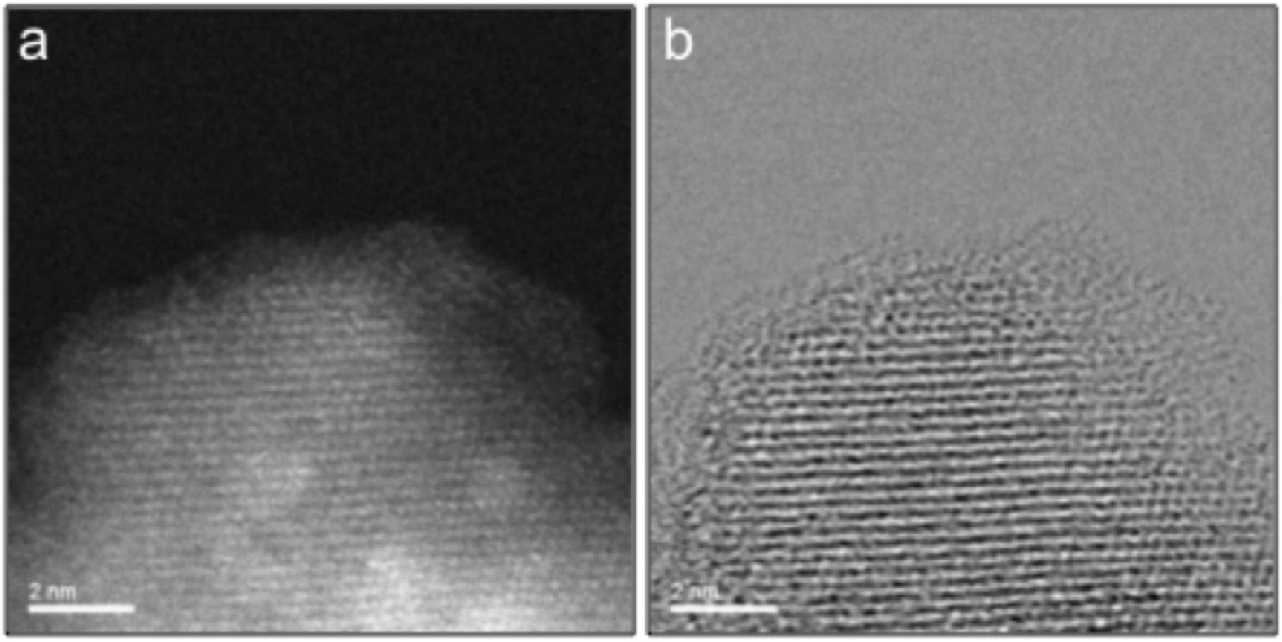

Figure 9. Crystallite image recorded after at least 6 earlier scans, at a direct magnification of 10Mx. The HA-ADF image (a) shows areas looking nearly down atomic columns. Amorphous material at the perimeter resulted from some electron beam damage, but much less than experienced by Fe zeolite samples treated at lower temperatures.

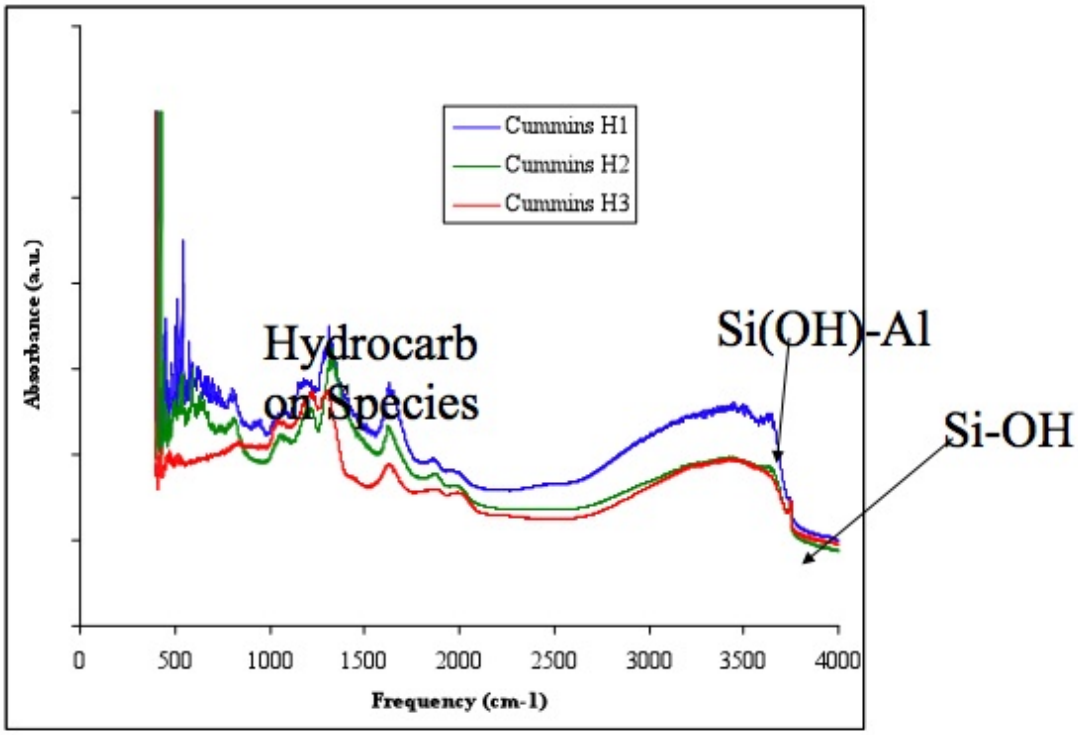

Figure 10. DRIFTS spectra for the Fe zeolite samples hydrothermally aged at different temperatures.

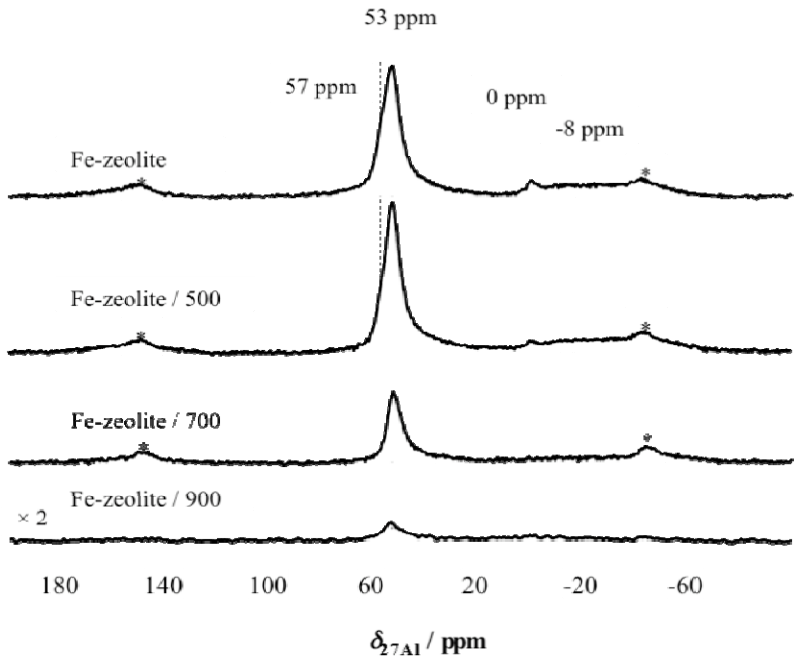

Figure 11. NMR spectra from the Fe zeolite samples hydrothermally aged at different temperatures. The -8 ppm peak is associated with octahedrally-coordinated Al_2O_3, 0 ppm with extra-framework Al^{3+} and the 53 and 57 ppm with tetrahedrally-coordinated Al in the zeolite structure. The asterisked peaks are from the spinning side bands from the main band.

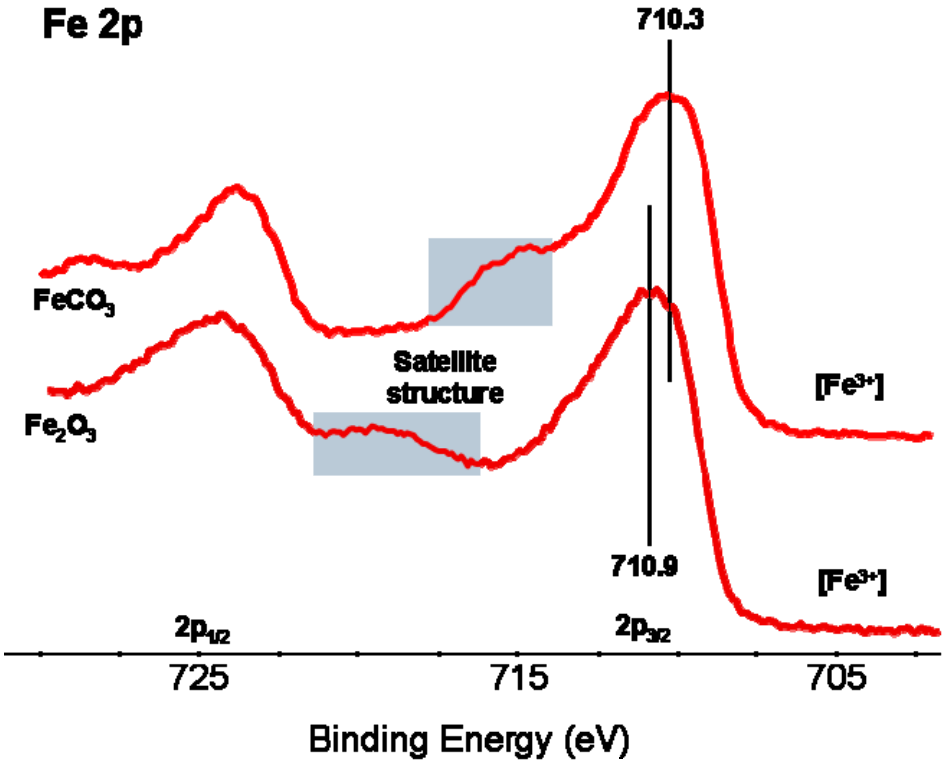

Figure 12. The XPS spectra of $FeCO_3$ and Fe_2O_3 at the Fe 2p core level.

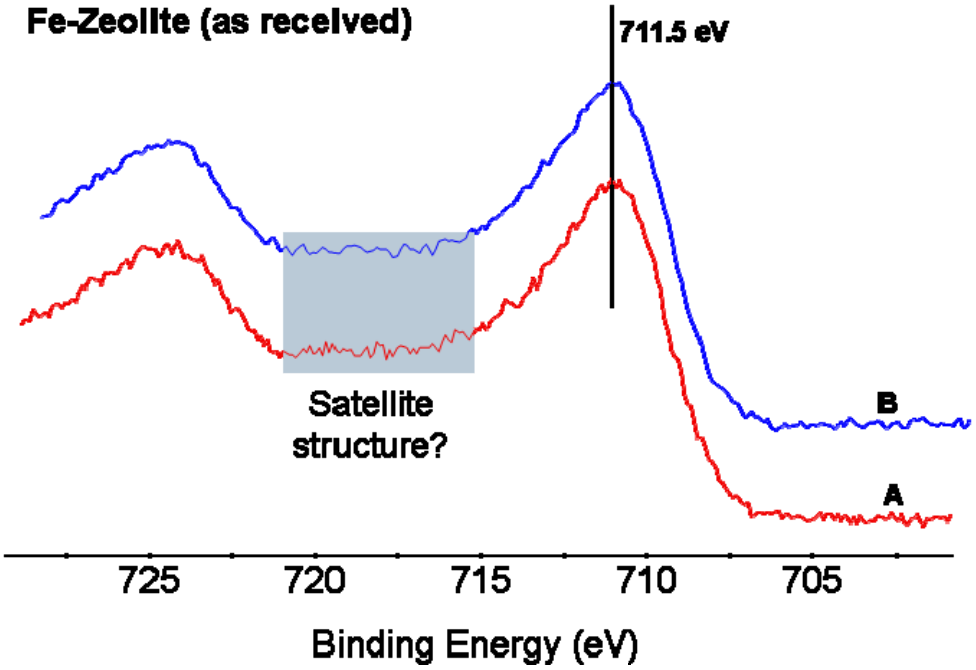

Figure 13. Two XPS spectra of the Fe 2p spectra for the as-received Fe zeolite powder.

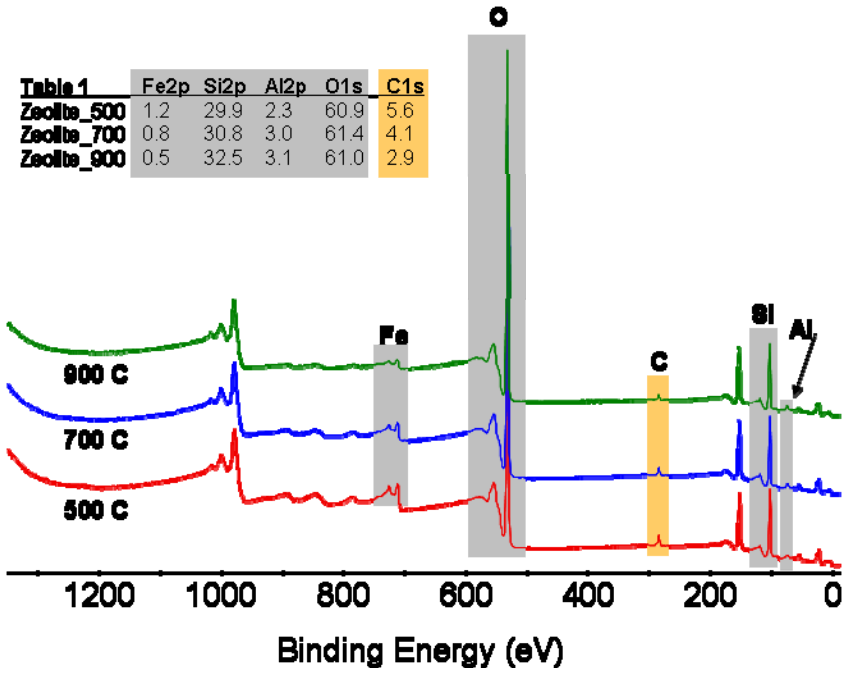

Table 1	Fe2p	Si2p	Al2p	O1s	C1s
Zeolite_500	1.2	29.9	2.3	60.9	5.6
Zeolite_700	0.8	30.8	3.0	61.4	4.1
Zeolite_900	0.5	32.5	3.1	61.0	2.9

Figure 14. The XPS spectra from the Fe zeolite samples hydrothermally aged at different temperatures. The inset Table gives the compositional analysis of each spectrum.

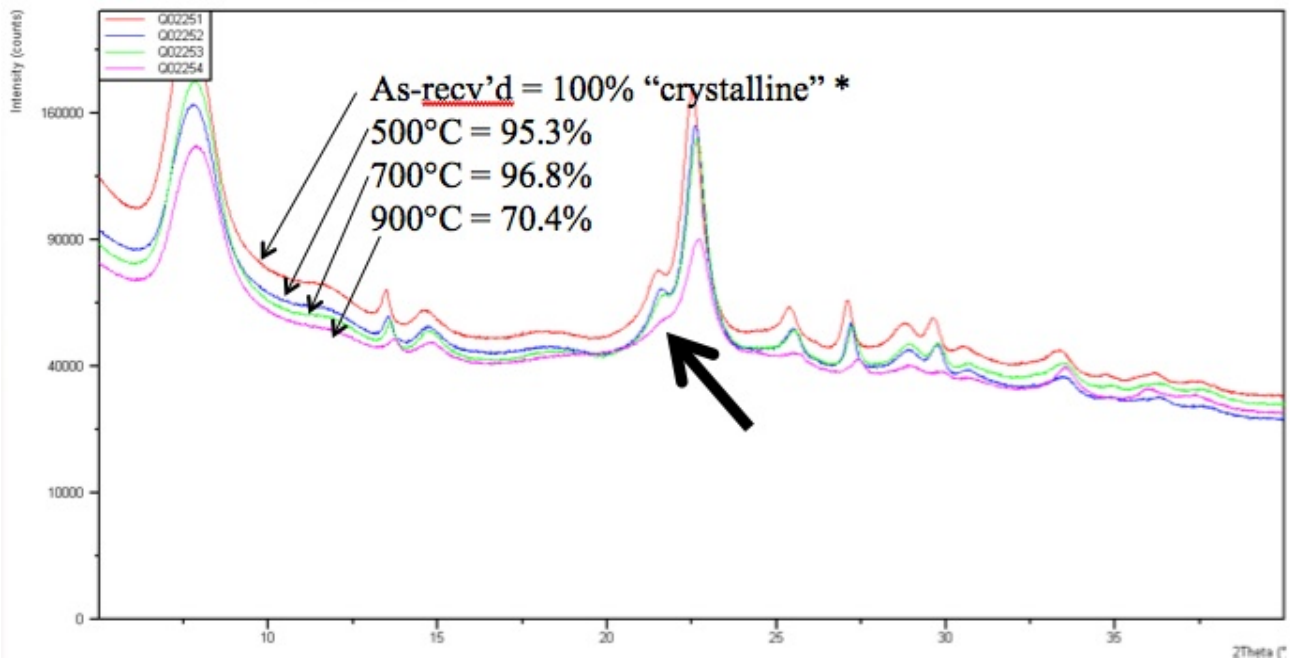

Figure 15. XRD from the Fe zeolite samples hydrothermally aged at different temperatures.

Agreement 10461 - Durability of Diesel Particulate Filters (CRADA with Cummins Inc.)

Amit Shyam, Thomas R. Watkins and Edgar Lara-Curzio
Oak Ridge National Laboratory
P.O. Box 2008, MS-6069
Oak Ridge, TN 37831-6069
(865) 574-2046; fax: (865) 574-4913; e-mail: watkinstr@ornl.gov

DOE Materials Engineer: Jerry Lee Gibbs
(202) 586-1182; fax: (202) 586-1600; e-mail: jerry.gibbs@ee.doe.gov
ORNL Technical Advisor: D. Ray Johnson
(865) 576-6832; fax: (865) 574-6098; e-mail: johnsondr@ornl.gov

Contractor: Oak Ridge National Laboratory, Oak Ridge, Tennessee
Contract No.: DE-AC05-00OR22725

Objective

- Implement test techniques to characterize the physical and mechanical properties of ceramic diesel particulate filters (DPFs) and develop analysis and inspection tools for assessing their reliability and durability.

Approach

- Rank the thermal shock resistance of candidate DPF substrates.
- Application of probabilistic design tools and non-destructive evaluation (NDE) techniques to DPF ceramic substrates.
- Refinement of DPF service lifetime prediction models based on characterization of field returned filters.

Accomplishments

- Carried out physical and mechanical property measurements on several coated and uncoated substrates and ranked their relative thermal shock resistance (continued from FY2007).
- Identified the relationship between porosity and the elastic-fracture properties for diesel particulate filter substrates.
- Characterized field returned diesel particulate filters and compared their properties to virgin filters. This information would be utilized to refine the DPF service lifetime prediction models.

Future Direction

- Detailed examination field returned DPF substrates and other alternate substrates that meet or exceed the mandated Environmental Protection Agency (EPA) 2010 regulations.

Introduction

The EPA regulates the emissions of nitrogen oxides (NO_x) and particulate matter (PM) from diesels engines. Stringent regulation on PM went into effect in 2007. There are many technologies designed to reduce emissions from diesel engines; prominent among the technologies for PM control are DPFs. A DPF is often a ceramic device that collects particulate matter in the exhaust stream. The high temperature of the exhaust heats the ceramic

structure and allows the particles inside to break down (or oxidize). DPFs reduce emissions of PM, hydrocarbons, and CO by 60 to 90%.

Most DPFs consist of a ceramic honeycomb with hundreds of cell passages partitioned by walls (Figure 1). Each cell passage has a square cell opening at one end and is closed at the other end so that the cell passages are alternately closed at each end. The so-called checkerboard plugging structure forces the exhaust gases through the porous, thin ceramic honeycomb walls. When the gases carrying the PM flow through the fine pores of the walls, the PM is filtered out. High porosity values, in the range of 40-70%, heighten filtration efficiency to more than 90% and reduce gas-flow resistance for better engine performance.

The process of diesel PM collection continues while the engine is operating. The particles are collected on the ceramic walls and as a result, the backpressure of the system increases. The back pressure is reduced by oxiding the trapped PM, aided by a catalytic reaction using exhaust gas heat at 400°C or more, into CO_2 and water vapor. This process, called regeneration, results in a cleaner filter. The regeneration process is dependent upon exhaust temperature, oxygen, NO_x content, time, and PM levels.

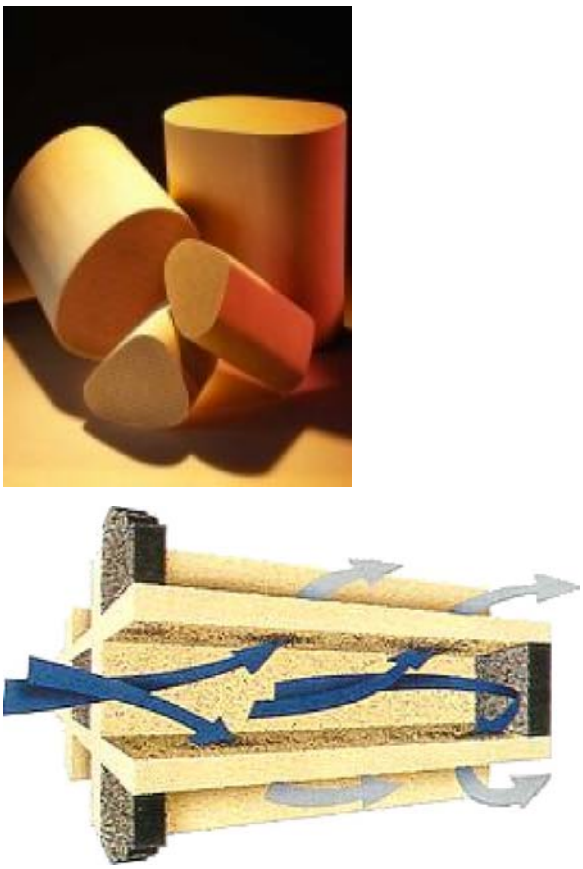

Figure 1. Cordierite-based DPFs.

The key to the successful application of DPFs is to reliably regenerate the filter (e.g., to clean up the PM that the filter continues to trap or collect). Traditionally, combustion of soot is done in an oxygen atmosphere (air). In air, the soot will oxidize at about 500°C. However, this is not a typical operating temperature for diesel engine exhaust. Therefore, to oxidize soot in air, an active system—i.e., one that increases the temperature of the exhaust using some external heat source—is required. But if an active system is not carefully controlled, or if too much PM collects on the filter walls, the filters can experience an "uncontrolled regeneration" where the temperature increases to 600°C or more, resulting in damage to the filter element.

A useful conceptual model for the prediction of reliability is the bathtub curve, which describes reliability-related phenomena of a component over its life cycle.[1] A schematic of the reliability bathtub curve is represented in Figure 2. It consists of three stages: the infant mortality phase is characterized by premature failures due to improper manufacturing or assembly, poor workmanship, or defects introduced during processing. The second stage of the curve corresponds to the useful life of the component and is characterized by a constant failure rate. In this regime, failures are typically associated with random, excessive loads. If sufficiently high safety factors are used during the design process, the magnitude of this failure rate should be negligible. The third stage of the bathtub curve is known as the wear-out phase, wherein the failure rate increases with time as a result of aging phenomena. Aging phenomena include thermal and mechanical fatigue, corrosion, creep deformation and environmentally assisted crack growth. The time at the onset of wear-out is often regarded as the useful life of the component.

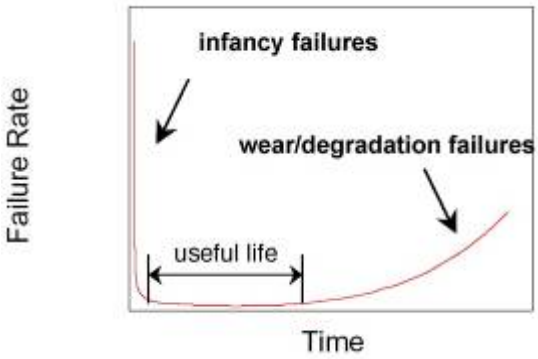

Figure 2. Reliability bathtub curve.

The reliability bathtub curve can be used as a descriptor of how the failure rate of DPFs evolves over time. Infancy failures of DPFs could be related to manufacturing or process defects (large pores, inclusions, cracking) or defects introduced during assembly. Failures of DPFs during their useful life will be dictated by the intersection between the spectrum of thermomechanical loads and the distribution of DPF strengths. Such failures could result from excessive vibration, for example, or unwanted thermal excursions during transients associated with regeneration. Wear-out and degradation failures of DPFs could also be associated with the growth of microcracks by thermal fatigue, and assisted by the chemistry of the environment, and/or by chemical and microstructural changes in the material due to long-term exposure to elevated temperatures in the exhaust environment.

The objective of this project is to implement test techniques to characterize the physical and mechanical properties of ceramic DPF substrates and to develop analysis and inspection tools for assessing the reliability and durability of DPFs. The developed tools and methods would allow the design of more durable and reliable DPFs. An important outcome of the development of the test methods is the ability to rank the relative thermal shock resistance of substrates in different conditions (catalyzed, soot loaded, field returned etc.) and of different candidate substrate materials.

Approach

The design process for making DPFs that are durable and reliable includes a complex materials property optimization and selection process.[2] For example, the porosity of DPFs, which allows them to remove PM from the exhaust gas stream, has a deleterious effect on their mechanical and fracture strength. A higher porosity also decreases the engine backpressure and increases efficiency of the diesel engine. Designing mechanically reliable DPFs is important because these components will experience demanding thermomechanical conditions during service. These include, for example, thermal shock resulting from rapid heating/cooling and thermal stresses that arise from temperature gradients.

Techniques to assess the elastic and fracture properties of virgin or unexposed DPF substrates have been identified, implemented and reported earlier.[3] The test techniques were applied to rank the suitability of common candidate substrates for application in DPFs. The developed test techniques were applied to characterize field returned DPFs. The material properties responsible for the thermal shock resistance and mechanical property degradation in the various stages of the bathtub curve were determined. These properties include thermal expansion, thermal conductivity, heat capacity, density, porosity, elastic properties, strength, fracture toughness, and environmentally assisted crack growth at ambient and elevated temperatures, in air and in relevant environments.

The information generated will be used in turn to implement probabilistic design tools. In particular, the applicability of the Ceramics Analysis and Reliability Evaluation (CARES) code[4] to predict the reliability of DPF ceramic substrates will be investigated. Such probabilistic design methodologies are based on a combination of experimentally determined strength data, stress analyses of the component using a finite-element analysis, and selection of appropriate failure criteria. The durability (service life) of the component can also be predicted using this framework by considering the mechanisms that are responsible for the degradation of material strength, such as slow crack growth or creep. In addition, the service life predictions are refined based on the properties of the field returned filters.

Results

In FY 2007, the comparative mechanical properties and relative thermal shock resistance of several DPF substrates were assessed and reported.[3] This ranking system was populated continuously in FY 2008 by testing several available candidate DPF

substrates. Procedures for characterizing DPF substrates were reported in a journal article[5] and in earlier reports and will not be repeated here. The elastic modulus (E), the fracture toughness (K_{IC}), the coefficient of thermal expansion in directions parallel and perpendicular to the extrusion direction (α) for all DPF substrates are reported in Figures 3-5, respectively.

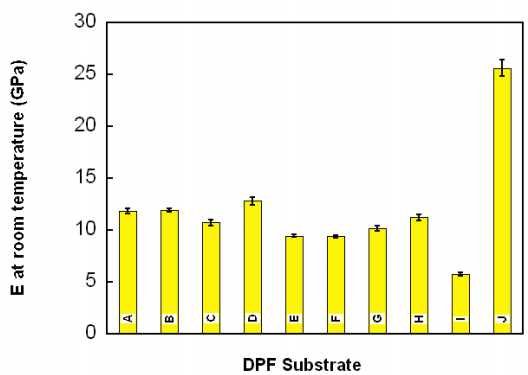

Figure 3. The room temperature elastic modulus of the DPF substrates analyzed. Isotropic elasticity was assumed. The error bars represent the RMS error of the fit for one measurement.

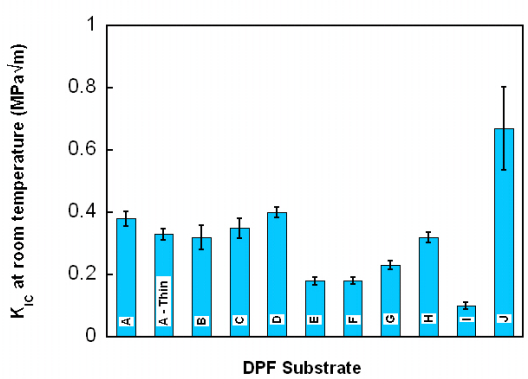

Figure 4. The average room temperature fracture toughness of the DPF substrates analyzed. The mullite substrate (*J*) has a higher fracture toughness compared to the cordierite based substrates. Five tests were carried for all substrates whereas; three tests were conducted for *G* and *J* substrates. The error-bars represent the standard deviation of the values.

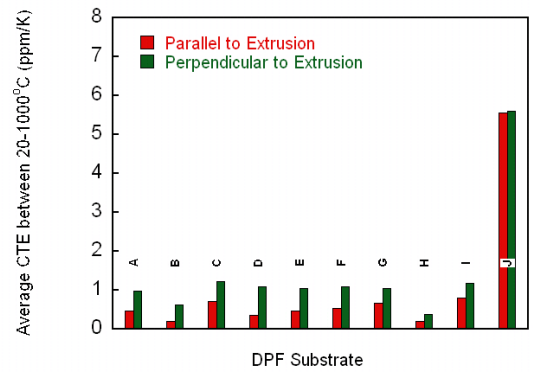

Figure 5. The coefficient of thermal expansion (CTE) of the DPF substrates analyzed. The CTE values reported are the between 20 and 1000 °C and in directions that are parallel and perpendicular to the extrusion direction. One measurement each in the parallel and perpendicular direction.

Table 1: The designations and conditions of the samples examined.

Designation	Material	Coated	Aged	Field Tested
A	Cordierite	No	No	
B	Cordierite	Yes	No	
C	Cordierite	Yes		Yes
D	Cordierite	Yes		Yes
E	Cordierite	No	No	
F	Cordierite	Yes	No	
G	Cordierite	Yes	Yes	
H	Cordierite	Yes	Yes	
I	Cordierite	No	No	
J	Mullite	No	No	

The analyzed substrates in Figures 3-5 are described in Table 1. Five manufacturers are represented by designations *A-D*, *E-G*, *H*, *I* and *J*. The original wall thickness of the *A* filters was around one and a half times the other substrates and therefore, for fracture toughness comparison, some thinner *A* specimens were fabricated and tested as shown in Figure 4. The mean thickness of the *A* specimens for fracture toughness testing and elastic modulus measurement was 0.375 mm, whereas the mean thickness of all the other specimens (including thin specimens of *A*) was 0.275 mm. It was found that the thicker *A* specimens (0.375 mm) had a fracture toughness value of 0.38 $\pm$ 0.02 MPa√m compared to the thinner specimens (0.275 mm) of the same material which had a fracture toughness value of 0.33 $\pm$ 0.02 MPa√m. This behavior was

attributed to a change in the porosity (or equivalently density) of the material with varying thickness.

In order to check this, specimens were ground continuously and the density of the specimens was measured by mass per unit volume calculations. The results are summarized in Figure 6 which clearly shows that the 0.375 mm specimen (called thick in Figure 6) has a higher density than the 0.275 mm specimen (called thin). The surface grinding procedure dislodges the microcracked material and creates a region of higher than average porosity close to the surface. As the thickness of the specimen goes down, the net area fraction of this higher porosity region increases with the porosity of the overall specimen increasing from 50 % to 55 % as thickness of the specimen goes down from 375 μm to 200 μm. This explanation was independently verified by application of image analyses algorithms on cross-sectional images of thick and thin specimens. A higher porosity thin specimen therefore, has a lower fracture toughness compared to a thick specimen of the same material.

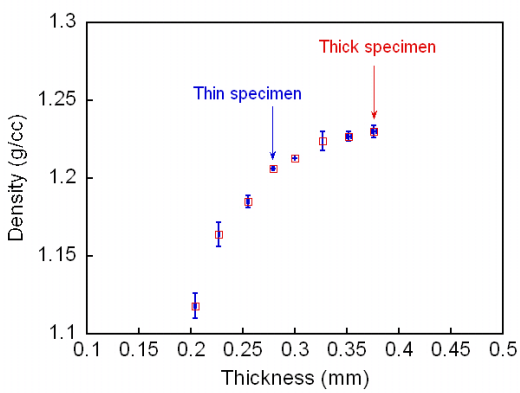

Figure 6. The effect of thickness on the density of prepared rectangular (20 mm x 40 mm) test specimens of porous cordierite (*A* material).

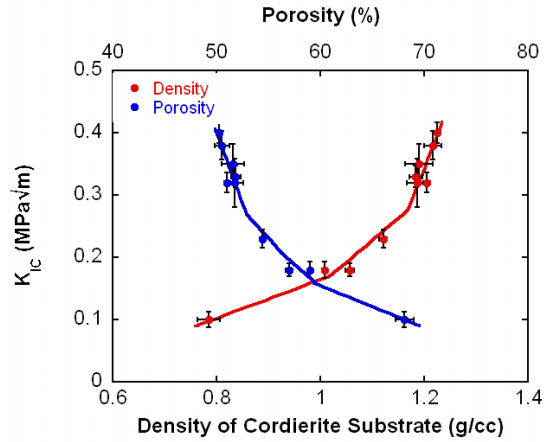

Figure 7. The variation in the fracture toughness of ten different cordierite substrates as a function of density and porosity of the substrate.

Understanding the effects of porosity on fracture toughness of cordierite substrates is relevant because, regardless of other experimental variables, porosity has a decisive influence on fracture toughness. This is illustrated in Figure 7 where the fracture toughness of the various cordierite substrates is plotted with respect to the porosity and density of the substrate. For all the cordierite substrates, the fracture toughness increases with increasing density and conversely the toughness decreases with increasing porosity. This is true for substrates from different manufacturers with or without catalytic washcoating and soot loading and also field returned substrates (*C* and *D* in Figures 3-5). The fracture toughness is highly sensitive to porosity, and an increase in porosity value from 50% to 70% leads to a fourfold decrease in average room temperature fracture toughness. The determination of the porosity dependence of mechanical properties will be utilized in the development of a DPF substrate with optimal porosity where the mechanical robustness requirements balance the filtration efficiency plus engine backpressure requirements.

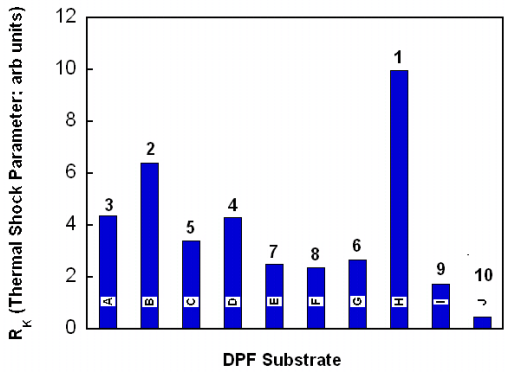

Figure 8. Comparison of the R_K, thermal shock parameter for the examined DPF substrates. The values are based on the average CTE (average of parallel and perpendicular values), room temperature modulus and average fracture toughness values.

The thermal expansion behavior of the substrates is a crucial parameter for determining their thermal shock resistance. The coefficient of thermal expansion for the substrates was measured in directions that were parallel and perpendicular to the extrusion direction. The average coefficient of thermal expansion (CTE) between 20 and 1000 ^{o}C are reported in Figure 5. As was reported previously,[3] the CTE values for the cordierite substrates are higher in the direction perpendicular to the extrusion direction, and the CTE values of the mullite substrate are higher compared to the cordierite substrates. A modified thermal shock parameter called R_K was proposed earlier,[3] where $R_K = (K_{IC}/\alpha E)$. The value of the R_K parameter was calculated for all the substrates (Figure 8). The values used for the calculation are room temperature elastic modulus and fracture toughness and average CTE values between 20 and 1000°C.

The analyzed substrates are ranked according to their thermal shock parameter values in Figure 8. According to this ranking, *H* material will have the highest thermal shock resistance, whereas *J* (mullite) would have the lowest resistance. Among the cordierite based substrates, *I* material with highest levels of porosity has the lowest thermal shock resistance according to the calculations. It is to be cautioned that several simplifying assumptions (such as that the material is homogeneous and isotropic) go in the calculation of the R_K parameter. A real filter has heterogeneities and gradients in properties that a calculation like the one presented above does not take into consideration.

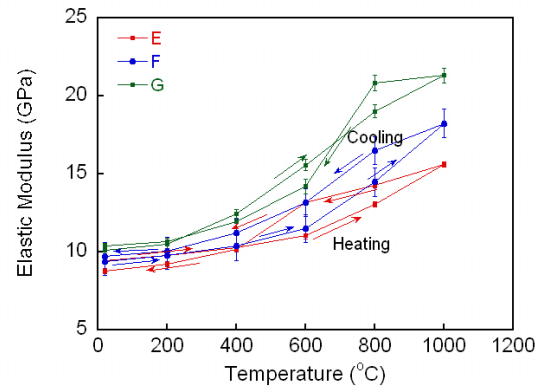

Figure 9. The temperature dependence of the elastic modulus of porous cordierite. The test specimens were subjected to a maximum temperature of 1000 ^{o}C. Error-bars represent root mean square errors of fit.

As detailed above, the thermal shock resistance of DPFs is determined in part by the elastic modulus of the substrate. The calculations above take into account the room temperature elastic modulus values. Procedures for high temperature elastic modulus determination for DPF filter walls by resonant ultrasound spectroscopy (RUS) have been reported earlier.[3] Flat plates of porous cordierite (40 x 20 x 0.275 mm) were prepared by dry grinding methods that have also been reported earlier.[3]

The temperature dependence of the elastic modulus of the plate for three grades of cordierite termed *E*, *F* and *G* is reported in Figure 9. As noted earlier, *E* represents a bare (uncoated) cordierite, *F* represents a *E* type cordierite with a catalytic washcoating and *G* represents a *E* type cordierite with a washcoating and soot loading. It is important to understand the influence of washcoating and soot-loading on the mechanical properties of porous cordierite.

The temperature dependence of elastic modulus for the three grades of cordierite is unusual, in that the modulus values increase with temperature up to 1000°C. Similar behavior for other grades of cordierites was reported in FY 2007.[3] While the room temperature elastic modulus values of *E* and *F* material are similar at 9.5 GPa, the room temperature elastic modulus value of *G* cordierite is slightly higher at 10.2 GPa. The rate of increase of the modulus values with temperature is the highest

for *G* material, followed by *F* and the lowest for *E* material. It is known that the modulus increase with temperature is due to the partial healing or complete closure of microcracks that form during cooling from the processing temperature.

Results presented in Figure 9 suggest that the washcoating and soot particles interact with the microcracks at elevated temperature and change the modulus dependence of temperature. The microcrack closing/healing at elevated temperature and subsequent opening during cooling is a microstructural phenomenon that makes the mechanical properties of the DPF a dynamic property which can change as a result of the operating service history. It is therefore, of interest to characterize the mechanical and thermal shock characteristics of filters that have been returned from field service in order to refine the lifetime prediction procedure for DPFs. Detailed microstructural, mechanical and thermal shock properties of a field returned DPF were characterized in FY 2008 and are reported next.

A high mileage filter was removed from service during a routine upfit of test hardware and obtained for analysis. The filter was fully functional and showed no evidence of abuse or loss of filtration efficiency. The high mileage filter was characterized by Cummins via time-of-flight ultrasound techniques (pulse echo mode). The filter was sectioned in half, and one half was sent to Oak Ridge National Laboratory (ORNL). The ultrasound test results on the ORNL section are shown in Figure 10. The circled numbers or "apparent length" indicate the time a sound pulse took to go through various regions of the filter. This time was converted to apparent length of the filter in inches. The difference in the apparent lengths in Figure 10 indicates the change of the relative properties of the core and the outer regions of the filter. Specimens for mechanical and thermal expansion evaluation were evaluated from the two different regions of the filter with the highest and the lowest time of travel. These regions are labeled *C* and *D* in Figure 10, and the average properties for specimens from these regions are reported in Figures 3-5. The relative co-ordinates of the specimens prepared for thermal expansion and mechanical property evaluation were carefully documented within the filter.

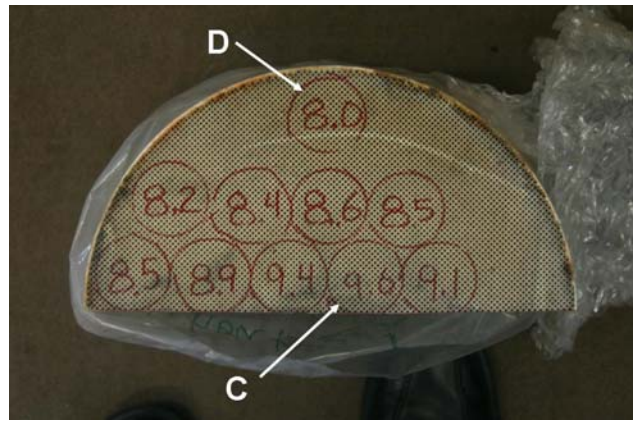

Figure 10. The half-cross section of a high mileage DPF. The numbers indicate the apparent length in inches which are related to the amount of time sound waves took to travel longitudinally though a specific region of the filter.

Table 2: The comparative thermal expansion, elastic modulus and fracture toughness of a virgin DPF and specimens from two regions of a high mileage DPF.

Material	**Average CTE** (ppm/K)	**Elastic Modulus** (GPa)	**K_{IC}** (MPa√m)	**Density** (g/cc)
Virgin (not coated)	0.42	11.91±0.15	0.32±0.04	1.19±0.02
C13 coated	0.97	10.74±0.29	0.35±0.03	1.19±0.03
C19 coated	0.73	12.84±0.37	0.40±0.02	1.23±0.02

The coefficient of thermal expansion (CTE in 20-1000 ^{o}C), fracture toughness and elastic modulus of specimens from the high mileage filter were characterized. Figure 11 is an image of a double-torsion specimen prepared from a high mileage filter. The values of the properties for specimens from the *C* region (core – highest time of flight) and the *D* region (circumference – lowest time of flight) are reported and compared to a similar virgin filter substrate material in Table 2. A single test was performed for elastic measurements by resonant ultrasound spectroscopy and the average thermal expansion value along directions that are parallel and perpendicular to the extrusion direction are reported. Five tests were conducted for fracture toughness measurements by the double-torsion methodology, and the average and standard deviation of the values are reported. The density values of the 0.275 ± 0.005 mm thick double torsion specimens before notching are also reported in Table 2.

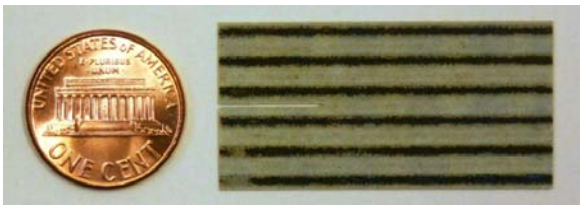

Figure 11. A double-torsion specimen prepared from a high mileage filter. The alternate dark lines are due to soot loading on the inlet channels of the filter.

The elastic modulus of the material in the core region (*C*) is about 20 % lower than the elastic modulus of the outer region (*D*). This is consistent with a 20% higher time of flight for the core region as shown in Figure 10. It is therefore, concluded that the microstructure of the core region changes as a result of the filter service environment with respect to the cooler outer region. The elastic modulus of the virgin filter substrate material which did not have a catalytic coating applied is in between the values for the core and outer regions of the filter.

As shown in Table 2, the fracture toughness of the core region and the outer region of the filter are higher compared to the virgin material by 10 % and 20%, respectively which may be related to the catalytic coating. Thus, as a result of the elevated temperature filter operating environment, the mechanical properties of the outer region of the filter (cooler section of the filter) do not show the same properties as the core region. The changes in the spatial (and perhaps temporal) characteristics of a DPF can be utilized to refine the lifetime prediction calculations. While the filter operating environment leads to slight changes in the mechanical characteristics, as shown earlier in Figure 7, the overall trend is that of the fracture toughness being a strong function of the density (or porosity) of the substrate.

The microstructural aspects of soot loaded filter materials and the relevant microstructure-mechanical properties were also identified in FY 2008. *C* (core) and *D* (periphery) region specimens had a fracture toughness of 0.35 $\pm$ 0.03 and 0.40 $\pm$ 0.02 MPa$\sqrt{m}$, respectively. This is compared to similar virgin (uncoated) specimens that had an average fracture toughness of 0.32 $\pm$ 0.04 MPa$\sqrt{m}$ (Table 1). The increase in fracture toughness due to service conditions can be partially explained by the scanning electron micrographs (SEM) in Figure 12. Figures 12 (a) and (c) are images of the microstructure of *C* (core) region and should be compared with the microstructure of the virgin specimen (*A*) in Figures 12 (b) and (d), respectively. It may be concluded from Figure 12 that the soot particles (bright regions) can have a consolidating effect on the pores and can therefore, help increase the fracture toughness of specimens that have been exposed to service conditions. The elevated temperature service conditions can also lead to permanent healing of microcracks in the microstructure but detailed quantitative microcrack density measurements were not performed.

An SEM image of the microstructure of a specimen from the peripheral region of the filter is shown in Figure 13. Specimens from the outer region have higher levels of soot loading compared to specimens from the core region consistent with higher temperatures in the core region of the filter that can lead to a larger fraction of the soot particles regenerating. The complex interaction between catalytic washcoating, soot and the DPF substrate material would be extensively characterized in FY 2009. This is expected to lead to refinement of the DPF substrate lifetime calculations under service conditions.

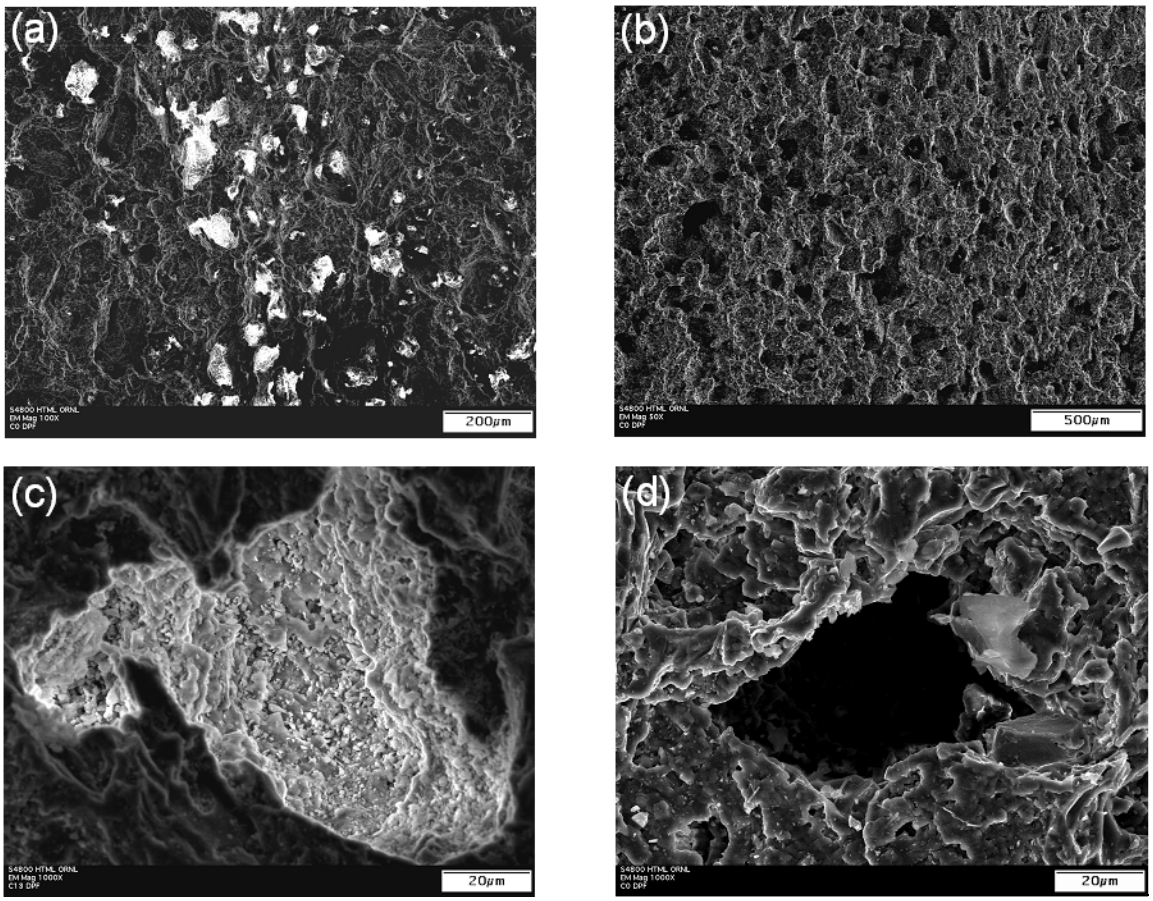

Figure 12: SEM images showing a comparison of the microstructure of the high mileage filter (*C*) with the virgin uncoated material (*A*). (a) and (b) are comparisons at low magnification with the bright regions in (a) representing soot and (c) pore filled with soot (d) pore at the same magnification in the virgin material.

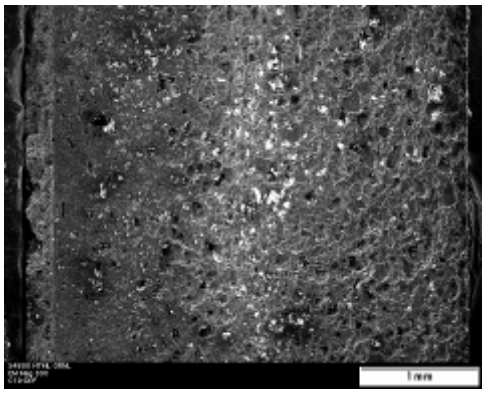

Figure 13: SEM image with microstructure of a specimen from the peripheral region (*D*) of the as-received high mileage filter.

Summary

Mechanical and thermal shock characterization test procedures developed earlier were employed to rank the relative thermal shock resistance of several candidate DPF substrate materials. The properties utilized to measure the thermal shock resistance included the fracture toughness, elastic modulus and the coefficient of thermal expansion. For cordierite substrates, the porosity of the substrate was the most important variable that determined the elastic and fracture mechanical properties of the substrate. The effect of porosity on the fracture toughness of cordierite substrates was quantitatively identified. In addition, the effect of catalytic washcoating and soot loading on the high temperature elastic properties of DPF substrates was characterized. A field returned DPF was thoroughly characterized and its properties were compared to that of virgin, uncoated filters. The difference in the properties of field returned filters were explained based on microstructural observations.

References

1. G. S. Wasserman, *Reliability Verification, Testing and Analysis in Engineering Design*, Marcel Dekker, New York, 2003.

2. J. Adler, "Ceramic Diesel Particulate Filters," International Journal of Applied Ceramic Technology, vol. 2, no. 6, pp. 429-439, 2005.

3. Propulsion Materials, 2007 Annual Progress Report, Vehicle Technologies Program, US DOE, Energy Efficiency and Renewable Energy, Office of Vehicle Technologies, Advanced Materials Technologies, E. J. Wall, R. A. Sullivan, J. L. Gibbs, Jan. 2008, www.ornl.gov/sci/propulsionmaterials/Reports.html.

4. N. N. Nemeth, L. P. Powers, L. A. Janosik, and J. P. Gyekenyesi, "Ceramics Analysis and Reliability Evaluation of Structures Life Prediction Program: Users and Programmers Manual," NASA-GRC, Life Prediction Branch (1993).

5. A. Shyam, E. Lara-Curzio, T.R. Watkins and R. J. Parten, "Mechanical characterization of diesel particulate filter (DPF) substrates" Journal of the American Ceramic Society, vol. 91, no. 6, pp. 1995-2001, 2008.

Presentations, Publications and Patents

T. M. Yonushonis, R. J. Stafford, E. Lara-Curzio and A. Shyam, "Apparatus, system, and method for detecting cracking within an aftertreatment device" *US Patent Application* Filed, March 2007.

A. Shyam, E. Lara-Curzio, T.R. Watkins and R. J. Parten, "Mechanical characterization of diesel particulate filter (DPF) substrates" *Journal of the American Ceramic Society*, vol. 91, no. 6, pp. 1995-2001, 2008.

A. Shyam, E. Lara-Curzio and T.R. Watkins, "Microstructure-property relationships in diesel particulate filter (DPF) substrates", *Materials Science &Technology*, Pittsburgh, October 2008.

A. Shyam, E. Lara-Curzio, T. R. Watkins, R. J. Stafford and T. M. Yonushonis, "The Effect of Porosity on the Mechanical Properties of Cordierite Diesel Particulate Filter Substrates", *33rd International Conference on Advanced Ceramics and Composites*, Daytona Beach, 2009 (abstract submitted).

Agreement 10635 - Catalysis by First Principles

C. K. Narula, L.F. Allard, M. Moses-DeBusk,
Oak Ridge National Laboratory
P.O. Box 2008, MS 6116
(865)574-8445, narulack@ornl.govl

DOE Technology Manager: Jerry L. Gibbs
(202) 586-1182; fax: (202) 586-1600; e-mail: Jerry.gibbs@ee.doe.gov
Field Technical Manager: D. Ray Johnson
(865) 576-6832; fax: (865) 574-6098; e-mail: johnsondr@ornl.gov

---

Contractor: Oak Ridge National Laboratory, Oak Ridge, Tennessee
Contract No.: DE-AC05-00OR22725

Objective

The objective of this work is to search for durable emission treatment catalysts (LNT, TWC, OC) from a protocol based on

- an integrated approach between computational modeling and experimental development,
- design and testing of new catalyst materials to rapidly identify the key physiochemical parameters necessary for improving the catalytic efficiency of these materials.

Approach

- Theoretical Modeling
  - Density functional theory-based first-principles calculations
  - Optimization of Pt clusters supported on alumina
  - Interaction of CO, NO_x, and HC with Pt clusters supported on alumina
- Experimental System
  - Synthesize Pt Nanoclusters on morphologically diverse alumina supports
  - Evaluate systems for CO, NO_x, HC oxidation individually and in combination
  - Understand non-structural changes in catalyst under operating conditions and correlating the changes to performance.

Accomplishments

- We have previously shown by theoretical models that nano-particles of Pt are stable as oxides and metallic particles are poorer catalysts than oxides. We have found experimental evidence to validate theoretical studies.
  - After determining the nano-structure of supported Pt clusters, we evaluated a series of 2%Pt/Al_2O_3 catalysts with different Pt particle sizes and alumina substrate morphologies (1 nm 2%Pt/γ-Al_2O_3; 12 nm 2%Pt/γ-Al_2O_3: 1nm 2%Pt/θ-Al_2O_3) by electron microscopy after testing for CO, NO, and HC oxidation on a bench-top reactor to correlate activity with catalyst's nano-structure.
  - We have established that nano-particles of Pt on alumina support are highly prone to agglomeration and even exposure to CO-oxidation conditions at low temperatures leads to agglomeration. An increase in the average Pt nanoclusters size, as well as the quantity of larger particles/clusters occurs with all of the 2%Pt/Al_2O_3 catalysts. Alumina substrate morphology is not a predictor of the extent of sintering that occurs to 1 nm Pt clusters.
- ORNL ex-situ reactor studies enable us to differentiate between nano-cluster/particle agglomeration and sample-to-sample variation effects. We found that:
  - Pt particle sizes for the 1nm 2%Pt/γ-Al_2O_3 catalyst increase throughout the CO, NO, and HC oxidation process and even under CO oxidation initiation conditions.

- Our results show that large particles formed as result of nano-particles sintering should not be assumed to be metallic particles since we found oxidized ordered particles in as little as 2-3 cycles of quantitative CO oxidation.
- Our *ex-situ* study of the ~12nm 2%Pt/γ-Al_2O_3 catalyst showed that such large Pt particles are more stable than Pt nanoparticles and further sintering, if any, is gradual.

Future Direction

- Understanding of the structures of nano-clusters on support.
  - Theoretical models to understand cluster oxidation state (oxidized, reduced, in equilibrium), dependence on cluster size, and the kinetics of oxidation
  - Experimental studies on the structures of these systems using EXAFS, XANES
- Support interaction with clusters and its impact on the structure and reactivity
  - Cationic or zero-valent metals or both
  - Cationic metals at the metal–support interface
- Reactivity of the clusters
  - Theoretical and experimental studies on structure-reactivity correlation towards NO_x, and HC oxidation studies
  - The impact of cluster size on catalytic activity
- Translate these results into design of durable supported catalysts for lean NO_x catalysts and other systems such as TWC, OC for diesel etc.

Introduction

This research focuses on an integrated approach between computational modeling and experimental development, design and testing of new catalyst materials, that we believe will rapidly identify the key physiochemical parameters necessary for improving the catalytic efficiency of these materials.

The typical solid catalyst consists of nano-particles on porous supports. The development of new catalytic materials is still dominated by trial and error methods, even though the experimental and theoretical bases for their characterization have improved dramatically in recent years. Although it has been successful, the empirical development of catalytic materials is time consuming and expensive and brings no guarantees of success. Part of the difficulty is that most catalytic materials are highly non-uniform and complex, and most characterization methods provide only average structural data. Now, with improved capabilities for synthesis of nearly uniform catalysts, which offer the prospects of high selectivity as well as susceptibility to incisive characterization combined with state-of-the science characterization methods, including those that allow imaging of individual catalytic sites, we have compelling opportunity to markedly accelerate the advancement of the science and technology of catalysis.

Computational approaches, on the other hand, have been limited to examining processes and phenomena using models that had been much simplified in comparison to real materials. This limitation was mainly a consequence of limitations in computer hardware and in the development of sophisticated algorithms that are computationally efficient. In particular, experimental catalysis has not benefited from the recent advances in high performance computing that enables more realistic simulations (empirical and first-principles) of large ensemble atoms including the local environment of a catalyst site in heterogeneous catalysis. These types of simulations, when combined with incisive microscopic and spectroscopic characterization of catalysts, can lead to a much deeper understanding of the reaction chemistry that is difficult to decipher from experimental work alone.

Thus, a protocol to systematically find the optimum catalyst can be developed that

combines the power of theory and experiments for the atomistic design of catalytically active sites and can translate the fundamental insights gained directly to a complete catalyst system that can be technically deployed.

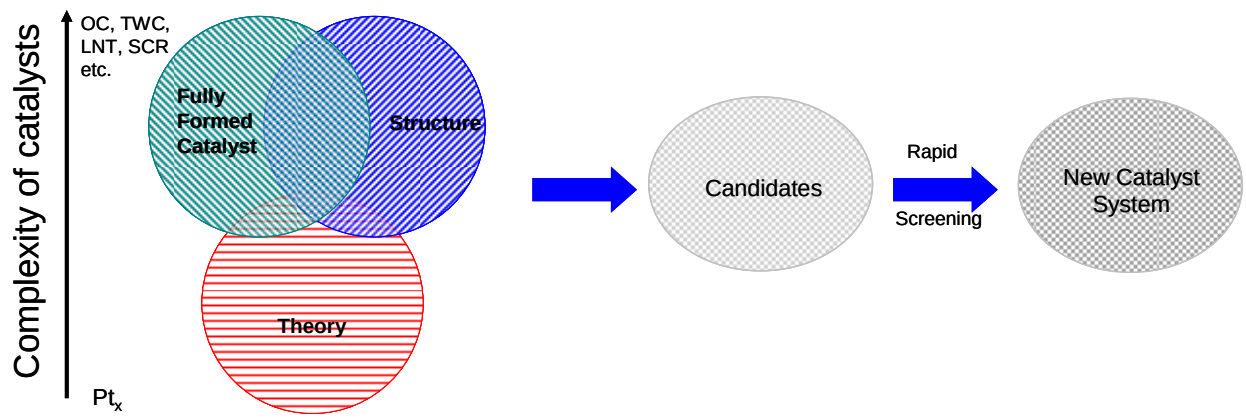

Although it is beyond doubt computationally challenging, the study of surface, nanometer-sized, metal clusters may be accomplished by merging state-of-the-art, density-functional-based, electronic-structure techniques and molecular-dynamic techniques. These techniques provide accurate energetics, force, and electronic information. Theoretical work must be based on electronic-structure methods, as opposed to more empirical-based techniques, so as to provide realistic energetics and direct electronic information.

A computationally complex system, in principle, will be a model of a simple catalyst that can be synthesized and evaluated in the laboratory. It is important to point out that such a system for experimentalist will be an idealized simple model catalyst system that will probably model a "real-world" catalyst.

Thus it is conceivable that "computationally complex but experimentally simple" system can be examined by both theoretical models and experimental work to forecast improvements to obtain optimum catalyst systems.

Approach

The theoretical modeling is based on DFT studies of Pt clusters to understand the relationship between cluster size, structure, composition, and reactivity. This coupled with first-principles thermodynamics provides insights into the effects of oxidizing atmosphere (O_2) – finite (T, p_{O_2}), structure, composition, redox potential on particle size. The results provide guidance for investigations of larger / supported clusters. The next steps of this work will model supported clusters, based on input from experimental results, and their interactions with CO, NO_x, and HC.

Experimentally, we have synthesized a series of Pt clusters/particles of different sizes supported on morphologically different alumina and evaluated the catalysts CO oxidation activity. We monitored the microstructural changes throughout the CO oxidation process to correlate microstructure and activity. We plan to extend the CO oxidation studies to other supports and to broaden our study to the NO_x and HC oxidation processes.

Guided by the theoretical models and experimental results of our study, we will synthesize new set of catalyst materials with higher durability under operating conditions.

Results

Over the last year, we have carried out experimental studies on Pt nanoclusters and nanoparticles to correlate their CO, NO and HC oxidation activity with nanostructural changes.

We employed ORNL *ex-situ* reactor[1] and scanning transmission electron microscopy (STEM) using the HD-2000 to study the nanostructural changes in catalysts upon exposure to CO and NO oxidation condition. It is important to note that the *ex-situ* reactor permits duplication of the oxidation conditions obtained on the bench-top reactor.

The results show the correlation between nanostructural changes and their impact on the catalytic activity and are summarized in the following subsections:

EXPERIMENTAL STUDIES ON Pt/γ-Al_2O_3

CO Oxidation: In previous reports, we have summarized our study on the microstructural effect of the Pt cluster/particle size on the 2%Pt/γ-Al_2O_3 catalysts and demonstrated that fresh 1 nm and smaller Pt clusters agglomerate quickly even under CO oxidation initiation conditions and continue to exhibit sintering through 3 cycles of quantitative CO oxidation. Large particles (based on our tests of supported 12 nm Pt particles), on the other hand, are more stable and do not significantly change after 3 cycles of CO oxidation. These results suggest that the efforts to obtain nanometer and sub-nanometer Pt particles do not offer a significant advantage for CO oxidation.

We also studied the effect of the substrate on the Pt microstructure under CO oxidation conditions employing 1 nm 2%Pt/θ-Al_2O_3. We found that there is no significant difference in activity, and our microstructural studies show there is also no structural differences in Pt particles supported on γ and θ alumina in fresh samples. Furthermore, agglomeration and sintering patterns for both types of samples under various CO oxidation conditions were almost identical.

Impact of Synthetic Routes

While the nanoparticles of precious metals are fairly easy to prepare, the monodisperse particles are extremely difficult to obtain, especially, by tradition wet synthetic routes. In our efforts to narrow the distribution of Pt particles, we employed Platinum-bis(dibenzylideneacetone), $Pt(C_6H_5CH{=}CHCOCH{=}CHC_6H_5)_2$, to deposit Pt on alumina. Experimentally, Platinum(0) bis(dibenzylideneacetone) was dissolved in THF and added to a suspension of commercial γ-Al_2O_3 in THF. After removal of solvent, the catalyst was heated to 400ºC to remove organics.

The STEM images showed that the Pt particles are in the 0.8 to 1.8 nm range with an average size of 1.1 nm. The average size is only slight larger (0.1 nm) and the range falls within the 0.5-1.9 nm range seen for catalyst samples prepared from H_2PtCl_6 impregnation of γ-Al_2O_3. The CO oxidation on the fresh catalyst, derived from $Pt(DBA)_2$, initiates at 150ºC and completes at 180ºC. The third cycle of CO shows activity changes (initiation at 180ºC and completion at 210ºC) suggesting that catalyst has undergone rapid changes.

Interestingly, the synthetic method does not appear to have much impact on the Pt particle size, performance or durability of the catalyst after the first cycle. After 3 cycles of CO oxidations, the catalysts prepared from $Pt(DBA)_2$ and H_2PtCl_6 have very similar activity and Pt particle size distributions (Figure 1).

HC Oxidation: A fresh sample of 1 nm 2%Pt/γ-Al_2O_3 catalyst, prepared from H_2PtCl_6, was exposed to a hydrocarbon mixture of 500 ppm propene and propane in 2:1 ratio, 10% O_2 and balance N_2 at a space velocity of 25k h^{-1} and hydrocarbon conversion was recorded

As expected, hydrocarbon oxidation begins at 180ºC with propene oxidizing first and completes with the complete oxidation of propane (Figure 2). STEM images show significant sintering occurred during the hydrocarbon oxidation study increasing the average Pt particle size to 6.9 nm. The particles size distribution which was shifted to a size range extending from 1.3 to 15.2 nm appears to be bimodal (Figure 3). The location of the larger local maximum is very similar to the distribution seen for fresh larger particles prepared by annealing at 650°C/5h, while the smaller local maximum is located at 4nm. This bimodal distribution clearly shows thermal

effects play a prominent role in the growth of Pt particle under HC oxidation conditions.

NO Oxidation: We exposed 1nm 2%Pt/γ-Al_2O_3 catalyst, prepared by the traditional impregnation method from $H_2PtCl_6 \cdot xH_2O$, to NO oxidation conditions to study the microstructural effects. The fresh material contained monodispersed Pt particles ranging from 0.6 to 1.7 nm in diameter with an average size of 0.9nm.

The catalysts NO oxidation activity was evaluated at a space velocity of 50,000 h^{-1} by monitoring the concentration of NO and NO_2 every 50°C from 100-650°C, see figure 4. NO oxidation is equilibrium limited by the reverse NO_2 reduction at higher temperatures, eq 1.

$$NO + \tfrac{1}{2} O_2 \leftrightharpoons NO_2 \qquad \text{Eq. 1}$$

The temperature was gradually increased to 650°C to determine the temperature at which NO_2 reduction becomes more favored. In the first cycle, NO oxidation initiated at ~250°C and increased through 400°C after which the reverse reduction reaction dominated, and the NO_2 production plummeted. However, during the 2nd NO oxidation cycle, oxidation occurred from 150° to 400°C before reversing. Microstructural changes were studied after the 2nd cycle in order to correlate them to the increase in the NO oxidation activity window seen in the second cycle.

After cycling the 1nm Pt catalyst to 650°C under NO oxidation conditions (10%O_2/ 500ppm NO/ N_2 balance) twice, the particles had sintered to an average size of 10.4nm ranging from 2.8 to 48.9nm. Figure 5 compares the change in particle size distribution from the fresh starting material (fresh 1nm Pt) which highlights the significant sintering that occurred. Also shown for comparison is the distribution of 2%Pt/γ-Al_2O_3 that had been annealed to 650°C/5h (fresh 12 nm Pt). The tested samples distribution is similar to that of the fresh 12nm Pt but shift 2nm lower suggesting the growth pattern observed is temperature related and not an effect of NO oxidation conditions

The reverse NO_2 reduction process as a function of temperature were identical for both cycles, starting at 450°C and progressing comparable to 650°C, suggesting that the reverse reaction is not size limited but temperature limited.

Since the particles growth seen is likely due to the high temperature exposure, both reactor and *ex-situ* studies were performed under NO oxidation conditions at a lower temperature. The catalyst was evaluated for two cycles up to only 450°C, the maximum temperature typically seen by a diesel emission catalyst. The reactor study shows activity ranges identical to the previous higher temperature study for both cycles. However, less of an activity increase was seen in the 2nd cycle when the maximum temperature evaluated was 450°C (Figure 6).

Particle size distributions were obtained for the *ex-situ* study after each cycle from STEM imaging (Figure 7). After the 1st cycle only a slight increase in the average particle size was seen, 1.4 nm, but the size range was extended up to 4.6 nm. The average Pt particle size and distribution range after the 2nd cycle was virtually identical to that seen after the 1st cycle (Figure 8). It was concluded from a second *ex-situ* which only looked at the fresh sample and after 2 cycles of NO oxidation up to 450°C that while the average particles size under these conditions is not effected by the density of Pt particles the degree of particle growth possible is increased, see figures 9 and 10. Since the fresh 1nm 2%Pt/γ-Al_2O_3 catalyst used in the NO oxidation studies has already been calcined at 450°C/5h prior to testing, the sintering observed in the *ex-situ* studies can be primarily contributed to the NO oxidation environment.

Conclusions

Theoretical studies previously reported for this project have shown that O, CO, NO, CO_2, and NO_2 are more strongly adsorbed on Pt nanocluster than bulk Pt. However, the studies indicated that if the Pt nanoclusters were oxidized then the adsorption was weakened. Our experimental CO oxidation studies displayed

greater CO oxidation activity on the smaller nanoclusters than the larger clusters, suggesting that the nanoclusters were Pt-oxides since the CO_2 formation and desorption is exothermic every step along the reaction path regardless if Pt is a nanocluster or bulk material.

On the other hand, DFT studies show that the NO_2 formation and desorption energies on Pt nanocluster is significantly more endothermic compared to bulk Pt(111). Our experimental results reported here show the Pt nanoclusters being less active for NO oxidation than the larger Pt clusters. This result suggest that for NO oxidation the weaker NO and O adsorption strength on the oxidized Pt is not sufficient to over come the increased endothermic reaction path for smaller Pt nanocluster.

References

1. Narula, C.K., Moses, M.J., Allard, L.F. *SAE no. 2006-01-3420*, 2006.
2. Kang, J.H.; Menard, L.D.; Nuzzo, R.G.; Frenkel, A.I. *J. Am. Chem. Soc.,* 128 (2006) 12068.
3. Zhou, C.W., J.; Dhilip Kumar, T.J.; Balakrishnan. N.; Forrey, R.C.; Cheng, H., *J. Phys. Chem. C* 111 (2007) 13786-13793.

Presentations and Publications (FY 08)

1. C.K. Narula, "Catalyst by Design – Bridging the Gap between Theory and Experiments at Nanoscale Level" Encyclopedia of Nanoscience and Nanotechnology, Taylor & Francis, New York, 2008 (invited).

2. C.K. Narula, L.F. Allard, D.A. Blom, M. Moses-DeBusk, "Bridging the Gap between Theory and Experiments – Nano-structural Changes in Supported Catalysts under Operating Conditions" SAE-2008-01-0416.

3. Narula, C.K.; Allard, L.F.; Blom, D.A.; Moses-DeBusk, M.; "Bridging the Gap between Theory and Experiments – Nanostructural Changes in Supported Catalysts under Operating Conditions", Society of Automotive Engineers – international Congress, April 2008.

4. Narula, C.K.; DeBusk, M.M.; Allard, L.F.; Catalyst by Design – Bridging the gap between theory and experiments at nanoscale level, DEER 2008, Detroit, MI.

Figures

Figure 1: Pt particle size distribution of fresh 1nm 2% Pt/γ-Al_2O_3 synthesized by H_2PtCl_6 or $Pt(DBA)_2$ impregnation of γ-Al_2O_3.

Figure 2: Hydrocarbon oxidation on 1 nm 2%Pt/γ-Al_2O_3.

Figure 3: (Left) STEM image of one area of 1nm 2%Pt/γ-Al_2O_3 after 1 cycle of HC oxidation up to 600°C. (Right) Particle size distribution of fresh 1nm 2%Pt/γ-Al_2O_3, after 1 cycle of HC oxidation up to 600°C and fresh 12nm 2%Pt/γ-Al_2O_3 catalyst.

Figure 4: Percentage of NO oxidation as a function of temperature up to 650°C for a 1nm 2%Pt/γ-Al_2O_3 catalyst for 2 cycles and a blank cycle run without a catalyst sample.

Figure 5: Particle size distribution of fresh 1nm 2%Pt/γ-Al_2O_3, after 2 cycles of NO oxidation up to 650°C and fresh 12nm 2%Pt/γ-Al_2O_3 catalyst.

Figure 6: Percentage of NO oxidation as a function of temperature up to 450°C for a 1nm 2%Pt/γ-Al_2O_3 catalyst for 2 cycles and a blank cycle run without a catalyst sample.

Figure 7: *Ex-situ* STEM images of an area of 1nm 2%Pt/γ-Al_2O_3 fresh, after 1 cycle of NO oxidation up to 450°C and after a 2nd cycle of NO oxidation up to 450°C (left to right, respectively). The dark black circle with a white rim near the center of each image is located in the same spot on each image.

Figure 8: Particle size distribution during an *ex-situ* study that monitored the exact same sample areas of fresh 1nm 2%Pt/γ-Al_2O_3 and after a 1st and 2nd cycle of NO oxidation up to 450°C.

Figure 9: *Ex-situ* STEM images of an area of 1nm 2%Pt/γ-Al_2O_3 fresh and the same

area after 2 cycles of NO oxidation up to 450°C (left to right, respectively).

Figure 10. Particle size distribution during an *ex-situ* study that monitored the exact same sample areas of fresh 1nm 2%Pt/γ-Al_2O_3 and after 2 cycles of NO oxidation up to 450°C.

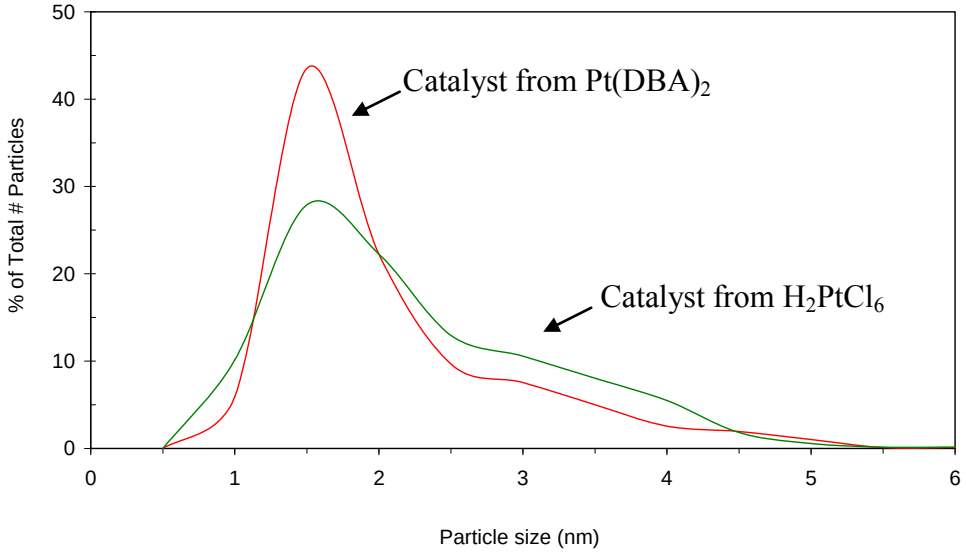

Figure 1: Pt particle size distribution of 1nm 2% Pt/γ-Al_2O_3 synthesized by H_2PtCl_6 or $Pt(DBA)_2$ impregnation of γ-Al_2O_3 after 3 cycles of CO oxidation up to 450°C.

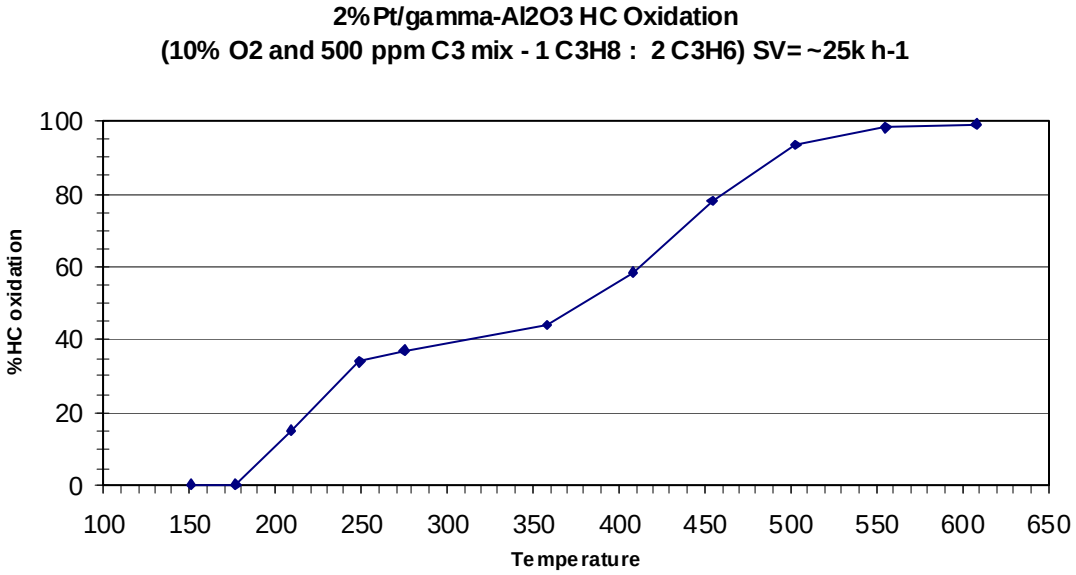

Figure 2: Hydrocarbon oxidation on 1 nm 2%Pt/γ-Al_2O_3.

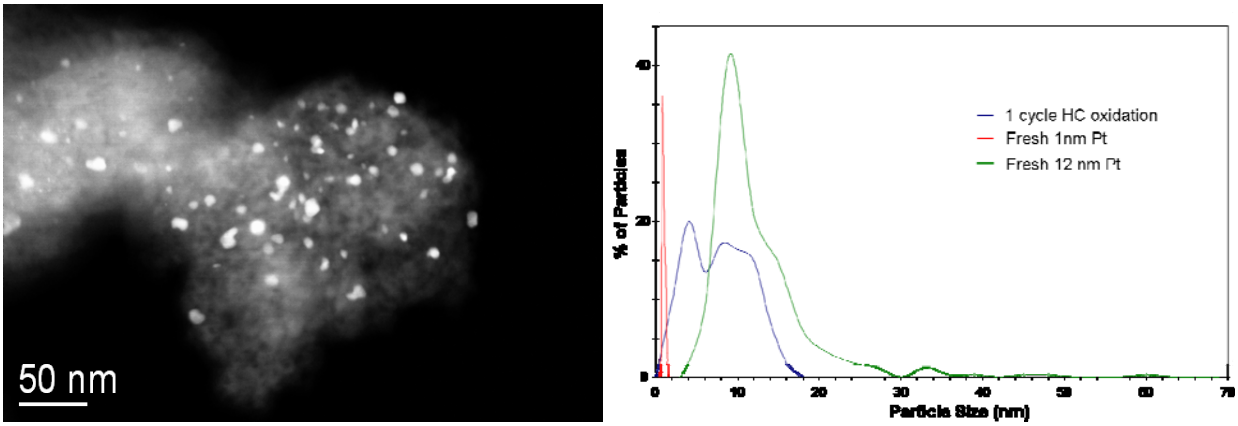

Figure 3: (Left) STEM image of one area of 1nm 2%Pt/γ-Al_2O_3 after 1 cycle of HC oxidation up to 600°C. (Right) Particle size distribution of fresh 1nm 2%Pt/γ-Al_2O_3, after 1 cycle of HC oxidation up to 600°C and fresh 12nm 2%Pt/γ-Al_2O_3 catalyst.

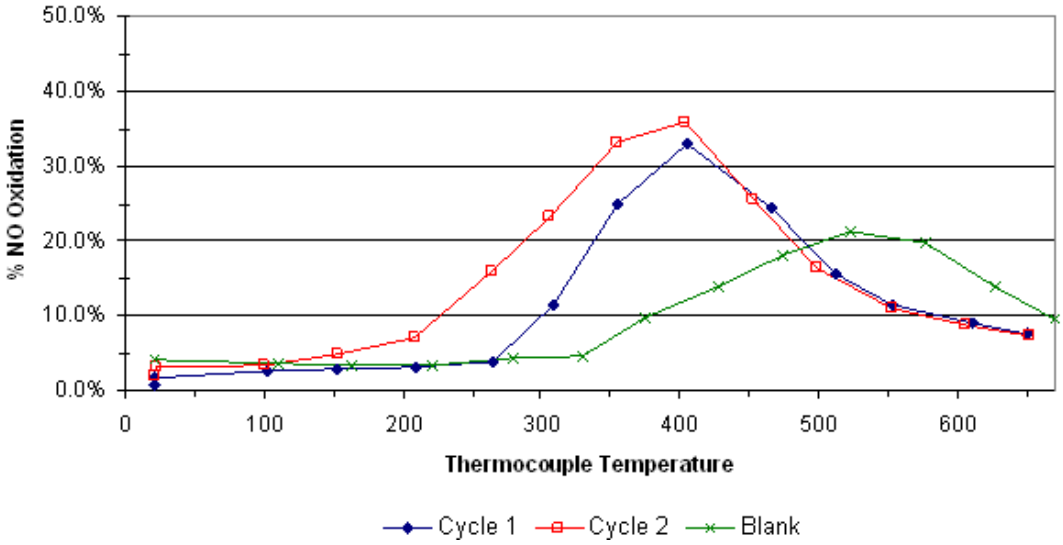

Figure 4: Percentage of NO oxidation as a function of temperature up to 650°C for a 1nm 2%Pt/γ-Al_2O_3 catalyst for 2 cycles and a blank cycle run without a catalyst sample.

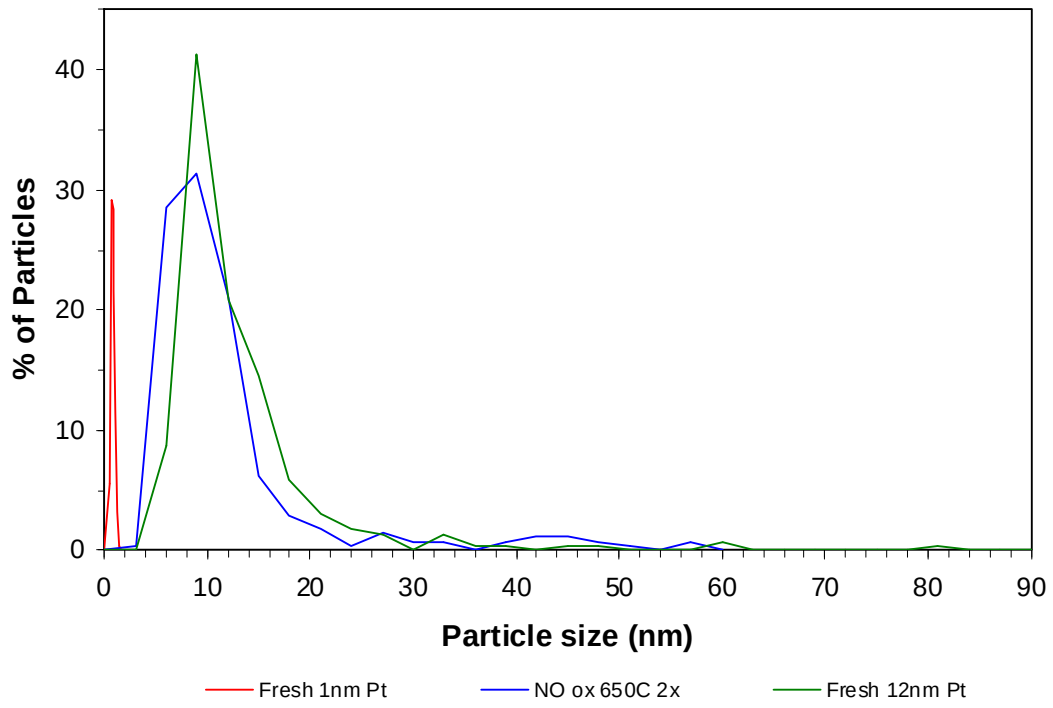

Figure 5: Particle size distribution of fresh 1nm 2%Pt/γ-Al_2O_3, after 2 cycles of NO oxidation up to 650°C and fresh 12nm 2%Pt/γ-Al_2O_3 catalyst.

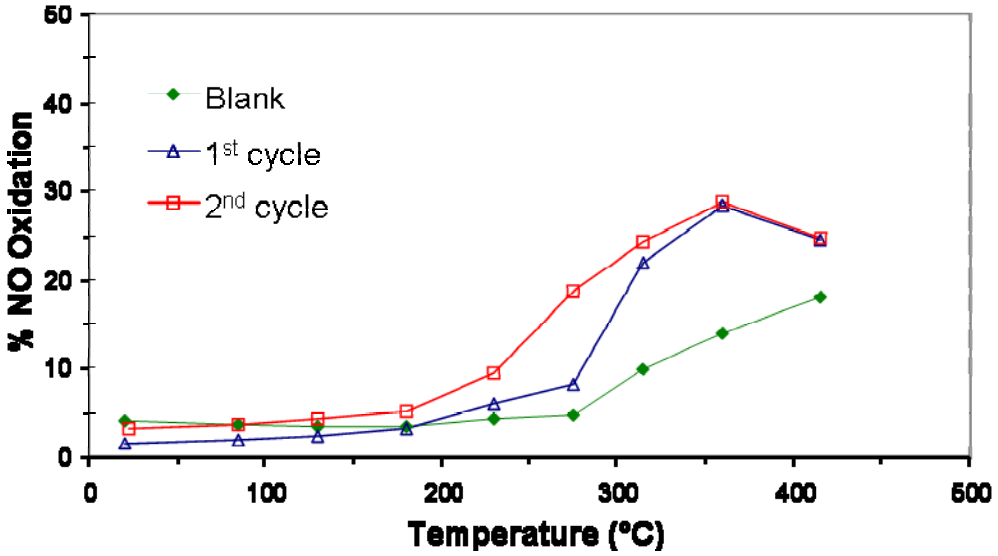

Figure 6: Percentage of NO oxidation as a function of temperature up to 450°C for a 1nm 2%Pt/γ-Al_2O_3 catalyst for 2 cycles and a blank cycle run without a catalyst sample.

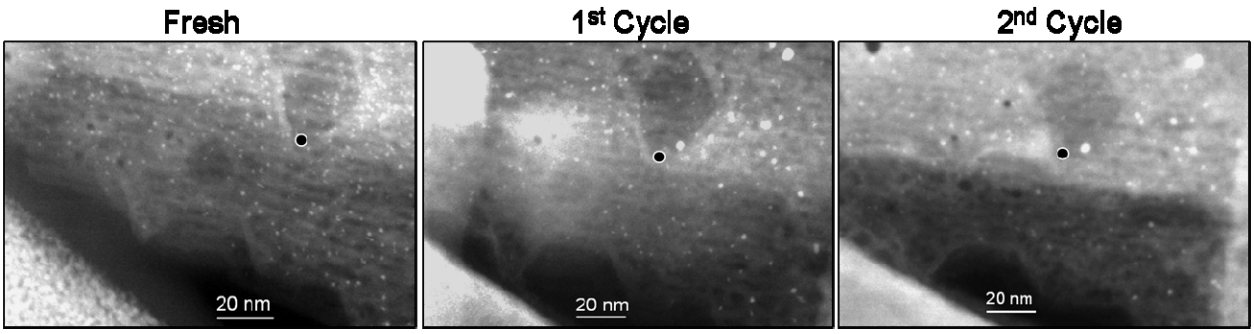

Figure 7: *Ex-situ* STEM images of an area of 1nm 2%Pt/γ-Al_2O_3 fresh, after 1 cycle of NO oxidation up to 450°C and after a 2nd cycle of NO oxidation up to 450°C (left to right, respectively). The dark black circle with a white rim near the center of each image is located in the same spot on each image.

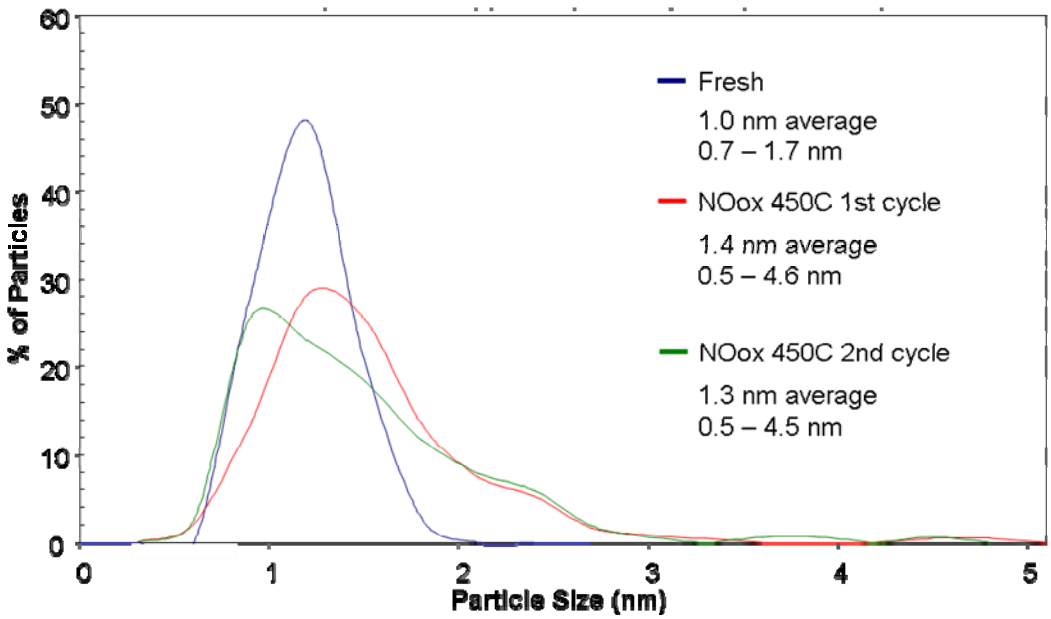

Figure 8: Particle size distribution during an *ex-situ* study that monitored the exact same sample areas of fresh 1nm 2%Pt/γ-Al_2O_3 and after a 1st and 2nd cycle of NO oxidation up to 450°C.

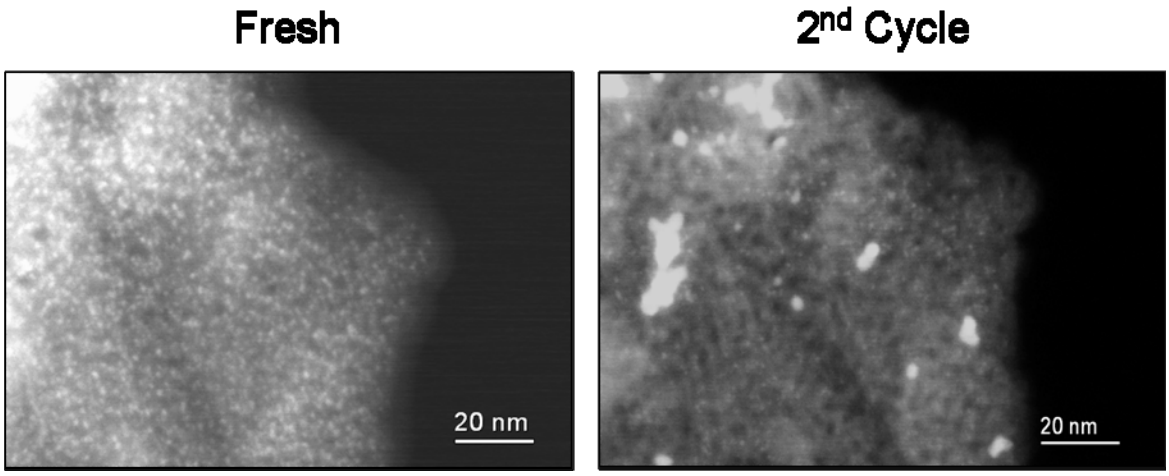

Figure 9: *Ex-situ* STEM images of an area of 1nm 2%Pt/γ-Al_2O_3 fresh and the same area after 2 cycles of NO oxidation up to 450°C (left to right, respectively).

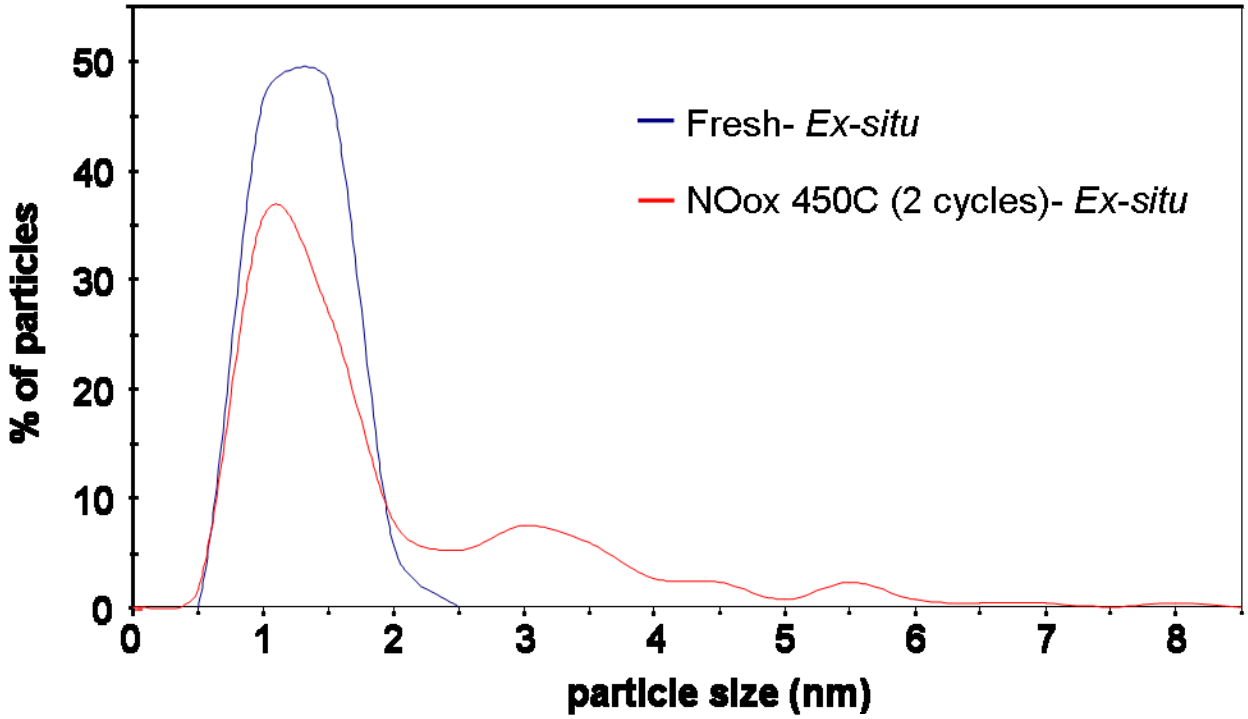

Figure 10. Particle size distribution during an *ex-situ* study that monitored the exact same sample areas of fresh 1nm 2%Pt/γ-Al_2O_3 and after 2 cycles of NO oxidation up to 450°C.

Project 18865 - Materials by Design

Agreement 13723 - Residual Stresses in Thin Films*

*(This project is jointly funded by Propulsion Materials and Heavy Vehicle Systems Optimization)

Principal Investigators: D. Singh and J. L. Routbort; coworkers: Cinta Lorenzo-Martin
Argonne National Laboratory
9700 S. Cass Avenue, Argonne, IL 60439-4838
630-252-5009 dsingh@anl.gov

DOE Technology Manager: Jerry L. Gibbs
(202) 586-1182; fax: (202) 586-1600; e-mail: jerry.gibbs@ee.doe.gov

---

Contractor: UChicago Argonne LLC
Contract No.: DE AC03 06CH11357

Objective

- Measure residual stresses in thin films and coatings as a function of film thickness and relate stresses to film properties such as hardness, fracture toughness, and adhesion energy to relate to film processing variables and to predict durability
- Use techniques developed for measurements of residual stresses in thin films and coatings to measure residual stresses in layered structures produced by joining by high-temperature deformation and to improve their mechanical properties

Approach

- Develop X-ray technique to measure change of lattice parameter of coating constituents as a function of depth and hence to calculate the lattice strains and stresses
- Develop indentation technique to measure hardness, fracture toughness, and adhesion energy of films and coatings
- Relate stresses, properties, and processing conditions to film durability

Accomplishments

- Advanced Photon Source (APS) used to measure stresses in 3–µm thick thin films of nanocrystalline MoN and MoCuN deposited on silicon and steel substrates as a function of depth
- Stresses were found to be sensitive to deposition conditions and thermal annealing
- Preliminary coating/film adhesion energies measured using indentation
- Demonstrated that by proper selection of materials the fracture strength of a composite is increased

Future Directions

- Develop indentation technique to measure film adhesion
- Investigate stresses in superhard, nanocrystalline MoCuN films as a function of deposition conditions and Cu concentration on steel substrates as well as investigate other coatings systems applicable for engine applications

---

Introduction

Plastic-joining has been applied successfully to various advanced ceramic and intermetallic materials [1-2]. However, some limitations arise when dissimilar materials are joined because of the residual stresses generated upon cooling as a result of the coefficient of thermal expansion (CTE) mismatches.

Mora at al. [3-4] studied the development of residual stresses in zirconia toughened alumina (ZTA) composites. Because zirconia has a higher CTE than alumina, stresses develop upon cooling during the sintering process resulting in compression of the alumina phase. In addition to the stresses in the monolithic materials, additional thermal residual stresses arise when different compositions of ZTA materials are joined by plastic deformation. Gutierrez-Mora et al. [3-4] showed that the tensile stress peak is at a short distance away from the joint interface, and coincided with the fracture location during the flexural tests [4]. In general, the presence of residual tensile stresses may pose a detrimental effect on the mechanical properties of joined components.

The intent of this study is to demonstrate that residual stresses, produced during joining by high-temperature plastic deformation, can be utilized effectively for the enhancement of the mechanical properties. The role of residual stresses generated from high-temperature plastic joining is considered for two different compositions (and CTE) of ZTA composites. These composites were joined by plastic deformation to produce a layered structure. Compressive stresses generated in the low CTE phase material are shown to contribute to a strength enhancement. Magnitudes of the residual stress were experimentally measured and correlated to the increase in strength. It is proposed that such an approach can be used for enhancing strength and reliability of as-fabricated components but as well as of existing structures.

Material Design

In this study, the proposed approach is fabricate layered structure (as shown in Fig. 1) in which a material, A, with a specifc thermal expansion is sandwiched between a different material, B, with a different CTE. Materials A and B can be selected with the appropriate CTE and high-temperature deformation characteristics. To generate compressive residual stresses in the outer layers (A), CTE of material B needs to be higher than that of material A.

For a perfectly joined interface, the average residual stresses generated in the layers A and B can be given as [5]:

$$\sigma_A = \frac{-E_A E_B d_B \Delta\varepsilon_o}{(1-\nu)(2E_B d_A + E_A d_B)} \qquad (1)$$

$$\sigma_B = \frac{2E_A E_B d_A \Delta\varepsilon_o}{(1-\nu)(2E_A d_A + E_B d_B)} \qquad (2)$$

E_A, E_B are Young's modulus for materials A and B, respectively, u is the Poisson's ratio, and $\Delta\varepsilon_o$ is the difference in the strain between the two layers and can be given in terms of the CTE of the two materials and the cool down temperature range (ΔT) over which the stresses are generated:

$$\Delta\varepsilon_o = \Delta\alpha\Delta T = (\alpha_A - \alpha_B)\Delta T \qquad (3)$$

It should be noted that from simple force balance,

$$\sigma_B(d_B) + \sigma_A(2d_A) = 0 \qquad (4)$$

From (1), assuming $E_A = E_B$, surface compressive stress in outer layer A can be given as:

$$\sigma_c = -\frac{d_B E \Delta\varepsilon_o}{(1-\nu)(2d_A + d_B)} \qquad (5)$$

where, $(2d_A+d_B)$ the total thickness of the layered composite.

Assuming that the failure occurs at the outer surface A, fracture stress can be given simply as [5]:

$$\sigma_f = \sigma_{f\,A}^{o} - \sigma_c \qquad (6)$$

where, s_{fA}^{o} is the fracture stress for monolithic material A, and s_c is the compressive stress in material A given by (5). Upon substitution,

$$\sigma_f = \sigma_{f\,A}^{o} + \frac{d_B E(\alpha_A - \alpha_B)\Delta T}{(1-\nu)(2d_A + d_B)} \qquad (7)$$

To demonstrate the facture strength enhancement from residual stresses/strains generated from joining by high-temperature plastic deformation, layered composite system of ZTA is considered in which outer layers have 60 vol % alumina and middle layer has 40 vol % alumina. The material properties for these materials are taken from Gutierrez-Mora et al. [4] and are listed in Table 1.

Based on the material properties for ZT60A and ZTA40A as listed in Table 1 and a cooling temperature, ΔT, of 1350°C, the residual stresses generated in the surface layers, obtained from eqn. 2, as a function of the outer layer (A) thickness is plotted in Fig. 2. In these calculations, the inner layer thickness was kept constant at a value of 3.5 mm, and the thickness of outer layer varied from 0.1 mm to 0.4 mm. As shown in the plot, residual compressive stresses increase with decreasing outer layer thickness. By changing the relative thicknesses, d_A and d_B, and the CTE's of material A and B, it is envisioned that the residual stresses can be manipulated and consequently the fracture behavior of the layered composite structure.

The predicted fracture strength (eqn. 7) for failure at the surface is shown in Fig. 3 as a function of outer layer thickness. As one would expect, the strength values decrease with increasing surface layer. Nevertheless, the increase in strengths achieved can be >830 MPa or >20% by introducing surface compressive stresses.

Based on the analysis presented, it is possible to enhance the fracture strength of ZTA composites by surface compressive stresses introduced during joining by high-temperature plastic deformation. Strength enhancements of 20% can be expected for the composite ZT60A/ZT40A/ZT60A used in the analysis and is experimentally demonstrated in this paper.

Experimental Procedures

Sample fabrication

Zirconia toughened alumina with compositions of 40 vol.% and 60% alumina (ZT40A and ZT60A respectively), were made from commercial powders: Al_2O_3 from Malakoff Industries, Malakoff, TX, (average particle size 0.7 µm) and 3 mol % Y_2O_3-stabilized ZrO_2 from Tosoh Corporation Ceramics, Bound Brook, NY, (average particle size 0.3 µm). Powders were ball-mixed in a solution of isopropanol alcohol with 2 ml of Witco Emphos PS-21A and 2% wt. of an organic binder for 12 hours. The resultant mixture was dried and then milled with pestle and mortar and subsequently sieved through a 60 mesh. Rectangular pellets were cold pressed at 250 MPa, and sintered in air at 1450°C for 4 hours. The heating rate was 40°C/hour up to 400°C and 120°C/hour until sintering temperature was reached. Samples were cooled down at 120°C/hour to room temperature. Dense (~95%) pellets of approximately 26 mm x 5 mm x 5 mm were obtained. In order to reveal the microstructure, samples of each composition were polished up to 1 µm diamond paste and thermally etched for 30 minutes at 1200°C for microstructural evaluation.

Joining

Joining experiments were carried out on as-sintered samples in a constant crosshead speed on a universal testing system (Instron Model 1125 Canton MA) equipped with a high-temperature furnace. Two ZT60A bar samples were placed in the furnace chamber such that they sandwiched the ZT40A bar.

Joining tests were performed in argon atmosphere at 1350°C and at a strain rate of $5x10^{-6}$ s^{-1} up to a final strain of 4-5%. Typical stresses reached during joining process were 30-40 MPa. Test conditions were chosen to guarantee plastic flow without grain growth. After joining, layered samples were ground and polished such that the outer layers (ZT60A) had a nominal thickness of 0.4 mm, whereas inner layer (ZT40A) was 3.5 mm.

Microstructural and phase evaluations

Post flexural tests, sample sections taken far away from failure location were cross-sectioned and polished up to 1 µm diamond paste, followed by thermal etching for 30 minutes at 1200°C. Finally the sample was coated with carbon for microstructural observation by Electron Scanning Microscopy (SEM) using a Hitachi Model S-4700-II (Tokyo, Japan).

X-ray Diffraction scans, using an analytical X-ray diffractometer model Philips X'Pert MPD System (The Netherlands) were carried out on each composite sample in order to ensure that no phase changes occurred in the composite constituents, particularly, zirconia, as a result of sample preparation. As-sintered, ground, and thermally-etched samples of each type were analyzed. Cu_{ka} radiation was used for analysis and samples were scanned over 20-90° range at an interval of 0.001°.

Flexural test

Fracture tests using a 4-point-bend method was performed at room temperature on the ZT40A, ZT60A, and layered composites, at a constant crosshead speed on an Instron universal testing system (Model 4505, Canton, MA) using a hardened steel fixtures. The inner and outer loading spans were 10 mm and 20 mm, respectively. The imposed loading rate was 0.5 mm/min. A total of 3-4 samples were tested for each material type and the fracture strength was calculated using the maximum load at failure. To identify the flaws that nucleated failure in the layered structure, fractographic analysis was conducted using a SEM.

Residual stresses measurement

X-ray micro-diffraction was performed on beamline 20-ID of the Advanced Photon Source, Argonne National Laboratory. A 10 keV X-ray beam was selected by a double-crystal Si (111) monochromator and then focused by a Kirkpatrick-Baez mirror. The focused X-ray beam (1×1 μm^2) was incident on the cross-section plane of the layered sample. The X-ray beam was parallel to the interface between the layered sample. The angle between the sample cross-section plane and the incident X-ray beam was 12°. The sample was scanned in the vertical direction with a line-scan step size of 20 µm. The diffracted X-rays at different locations along the cross section were collected by a two-dimensional charge-coupled device (CCD) X-ray detector, which was placed 150 mm away from the sample. An X-ray fluorescence detector was also used to examine the chemical elements in the layered sample. Fluorescence signal from trace Cu impurities in the sample was used to locate the boundary between two adjacent layers.

Results

Microstructural and X-ray analysis

Microstructures of the as-fabricated ZT40A and ZT60A samples are shown in Fig. 4. Average grain sizes for zirconia (lighter phase) and alumina (darker phase) were 0.3 and 0.7 µm respectively. As shown in these micrographs, the samples are close to being fully dense.

Fig. 5 shows the interface of the sample after joining. Arrows indicate the interface. The joint is dense and has no visible residual porosity. Closer examination reveals that the grains on the joining surfaces interpenetrate to accomplish the joining process.

A typical XRD pattern for as-fabricated ZT40A sample is shown in Fig. 6. Peaks for

both zirconia and alumina are present. Further, for zirconia phase, both tetragonal and cubic phases are present. Ratio of tetragonal to cubic zirconia phases was estimated to be 3:1 [6]. However, as a result of sample preparation (grinding and polishing) there was emergence of monoclinic zirconia phase and it's content was estimated as approximately 8%. It should be noted that similar XRD patterns are obtained for ZT60A with stronger alumina peaks.

Flexural test

Four-point-bend tests were carried out on the ZT40A, ZT60A and joined ZT60A/ZT40A/ZT60A samples at ambient temperatures. Outer layers of the joined material were ground down to the chosen layer thicknesses (0.45 mm) with a constant (3.5 mm) inner layer prior to the flexural testing. The average fracture strengths for layered ZT60A/ZT40A/ZT60A samples were 707 ± 81 MPa versus 480 ± 45 MPa for ZT40A and 410 ± 120 MPa for ZT60A and are shown in Fig. 7.

Fractographic analysis of the layered samples post flexure tests showed no evidence of failure initiation at the interface in any of the samples. Figure 8 shows a fractured layered structure with a fracture initiation from the outer (ZT60A) surface. In addition, location of the ZT40A/ZT60A interface can also be seen.

Residual Stress

Fig. 9 shows a typical 2-D micro-diffraction pattern of the layered sample collected by the CCD detector. Partial rings shown in the image were formed by X-rays diffracted from different crystal planes of tetragonal zirconia. The (103) diffraction ring was selected for analysis due to its more uniform intensity distribution. To calculate the residual strain on the sample, two segments of the ring (around f = 0° and 50°) were selected as shown in Fig. 8, where ϕ is the azimuth angle. Integration of the ring segments gives diffraction peaks from which the lattice spacings (d) for specific f can be obtained. The d-versus-$\sin^2\psi$ method was used to calculate the deviatoric strain, where ψ is the angle between the specimen and the crystal coordinate systems [7]. The azimuth angle f is related to ψ according to the simple geometric relationship between the incident X-rays, sample, and X-ray detector. In the d-versus-$\sin^2\psi$ plot, d values obtained at ψ = 0° and 90° give the out-of-plane and in-plane lattice spacings, respectively. The strain-free lattice spacing can be obtained by taking the d value at ψ = 63°, assuming a Poisson's ratio of 0.26 for the sample. These three d values were used to calculate the deviatoric in-plane and out-of-plane strains.

Fig. 10 shows the distribution of in-plane residual strain at different locations along the cross section of the layered sample. An interesting feature can be observed near the joint of the top and the middle layers. In the top layer (ZT60A) near the joint, the strain is compressive, while in the middle layer (ZT40A) near the joint the strain is tensile. There is a sharp transition from compressive to tensile strain at the interface. The magnitude of the maximum strain in both cases was about 0.1%, and the estimated error in strain was ±0.05%. In both the top and the middle layer, the magnitude of strain decreases as the location moves away from the joint, and it becomes a constant at about 100 μm away from the joint interface.

Discussion

Flexural strength tests on the ZT60A/ZT40A/ZT60A layered structure fabricated by plastic joining shows higher strengths over the bend strengths of ZT60A and ZT40A composites individually. The strength enhancement (707 MPa) is close to 47% over the higher strength ZT40A phase (480 MPa) and 70% over than the ZT60A composite (410 MPa). As discussed in the Materials Design section, the strength enhancement is attributed to the compressive residual stresses generated in the outer layer. Fig. 11 shows the strength

prediction based on the eqn. 7 as a function of outer layer thickness and the measured bend strength of the layered structure. This prediction uses the actual thicknesses of the layers in the samples tested and the measured strengths for ZT40A and ZT60A in this study. The predicted value, at an outer layer thickness of 0.0045 m is 615 MPa. The experimentally observed values were 707 MPa, which exceeds the prediction by 15%. It should be noted that the scatter in the measured value of the layered structure is ±81 MPa. Further, there may be errors introduced from the assumptions in material parameters (E, v, CTE) used for the calculations.

Since the failure location is at the surface of the outer layer, compressive residual stresses counteract the applied tensile stresses during the bend test. From the residual strain measurements, it appears strain difference between ZT40A and ZT60A is large (0.0008) near the interface and drops to about 0.0005 at regions away from the interface. It should be noted that these in-plane strains are estimated only from the shift in the diffraction peak of zirconia phase only. Using elastic modulus for ZT60A as 320 GPa (Table 1), compressive stress in the ZT60A layer is estimated as 280 MPa close to the interface and 160 MPa regions away from the interface. These values bound the calculated value (from eqn. 5) of about 213 MPa for a similar geometry of the layered structure.

Gutierrez-Mora et al. [3] estimated residual stresses across the interface in joined ZT20A/ZT80 sample using a micro-indentation technique. They measured residual stresses parallel (in-plane) as well as tensile stresses perpendicular to the interface as a function of distance from the interface. Their values for in-plane residual compressive stresses were as high as 300 MPa near the interface but were reduced to about 200 MPa at 200 μm away from the interface in ZT80A. These higher values are probably result of large CTE mismatch between the joined ZT20A and ZT80A samples and the larger differences in their Young's moduli.

As evidenced by the SEM micrograph of Fig. 8, failure location in the joined layered structures was at the surface. The failure appears to initiate from a surface flaw resulting from sample surface preparation. Thus, for qualitative assessment of fracture strength of ZT60A in the layered structure, residual compressive stress of 160 MPa can be superimposed on the ZT60A strength of 410 MPa. This yields a value of 570 MPa, which is lower than the average strength of 707 MPa observed for the layered structure. Possible reason for discrepancy between predicted and observed strengths for ZT60A could be because of different fracture causing flaw population in the ZT60A composite and the ZT60A outer layer in the joined layered structure.

The fracture strength in ZTA composites increases monotonically with zirconia content. This behavior has been reported in the literature for ZTA composites materials [4]. The fracture strength values obtained through this work are lower than the ones reported by Gutierrez-Mora et al. for the monolithic ZT40A and ZT60A composites. This might be due to lower density (95% of theoretical) observed in this study as compared to density (>99% of theoretical) reported by Gutierrez-Mora et al. [4]. These differences could be introduced during the material fabrication from batch to batch. Nevertheless, it is important to note that the enhancement of >40% for the fracture strength over just ZT40A, the higher strength constituent.

Finally, strength or toughness enhancement in zirconia ceramic systems can result from the tetragonal to monoclinic phase transformation. However, XRD analysis for the phases in ZT60A composite and ZT60A in the layered structure showed similar phases with the presence of small fraction of monoclinic zirconia. Thus, it appears the strength enhancements observed in this study are entirely due to the compressive residual stresses.

Conclusions

We have taken techniques and results from two projects, joining by plasticity, and measurements of residual stresses in superhard, nanocrystalline coatings and applied lessons learned to a graded composite structure. Residual stresses arising from thermal expansion mismatches can be used positively in strength and reliability enhancements of structural ceramics and composites. Zirconia toughened alumina composites with two different compositions (40 vol % alumina and 60 vol %) were joined by a plastic deformation process to produce a layered structure. Residual compressive stresses in the outer 60% vol % alumina layer resulted in strength improvements of 60% over bulk zirconia containing 60 vol % alumina. Results were explained on the basis of a stress analysis and measurement of residual stresses. Experimentally measured strength increase of the layered structure agrees, with the experimental scatter, with the calculations. The strategy for materials design discussed here can be utilized in producing high reliability ceramic components as well as in the repair of existing components.

Future Direction

We will continue to develop the indentation technique to measure surface adhesion energies. We will also explore the applicability of using residual stresses to increase fracture strength at elevated temperatures, but below the stress relaxation temperatures.

References

1. K.C. Goretta, D. Singh, N. Chen, F. Gutierrez-Mora, M. de la Cinta Lorenzo-Martin, A. Dominguez-Rodriguez, J. L. Routbort, Matls. Sci. Eng. **A 498**, 12-18 (2008).
2. T. Nagano, F. Wakai. J. Mater Sci. 28, p5793 (1993)
3. F. Gutierrez-Mora, K.C. Goretta, S. Majumdar, J.L. Routbort, M. Grimdisch, A. Dominguez-Rodriguez, Acta Materialia 50, p3475 (2002)
4. F. Gutierrez-Mora, D. Singh, N. Chen, K.C. Goretta, J.L. Routbort, S.H. Majumdar, A. Dominguez-Rodriguez. J. of European Ceramic Society, 26 961-965 (2006)
5. A. V. Virkar, J. L. Huang, and R. A. Cutler, Journal of the American Ceramic Society, 70 [3], p 164 (1987)
6. C.J. Howard, P.J. Hill. Journal of Materials Science 26, p127, (1991)
7. V. Hauk, *Structure and Residual Stress Analysis by Nondestructive Methods* (Elsevier, Amsterdam, 1997), Chap. 2, pp. 132–215.

Table 1. Material Properties of ZTA Composites [ref. 10]

Material Property	ZT60A	ZTA40A
E (Gpa)	320	320
CTE (10^{-6}/C)	10.22	10.68
s_f^o (Mpa)	580	700
ν	0.26	0.26

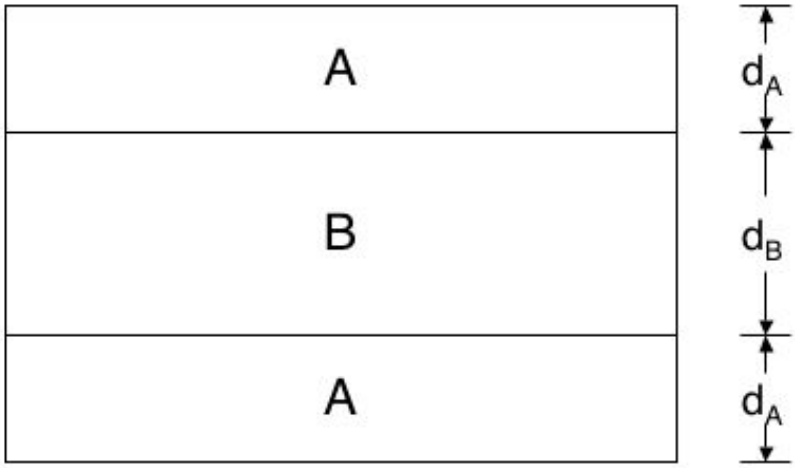

Figure 1. Schematic of the layered structure fabricated by plastic deformation.

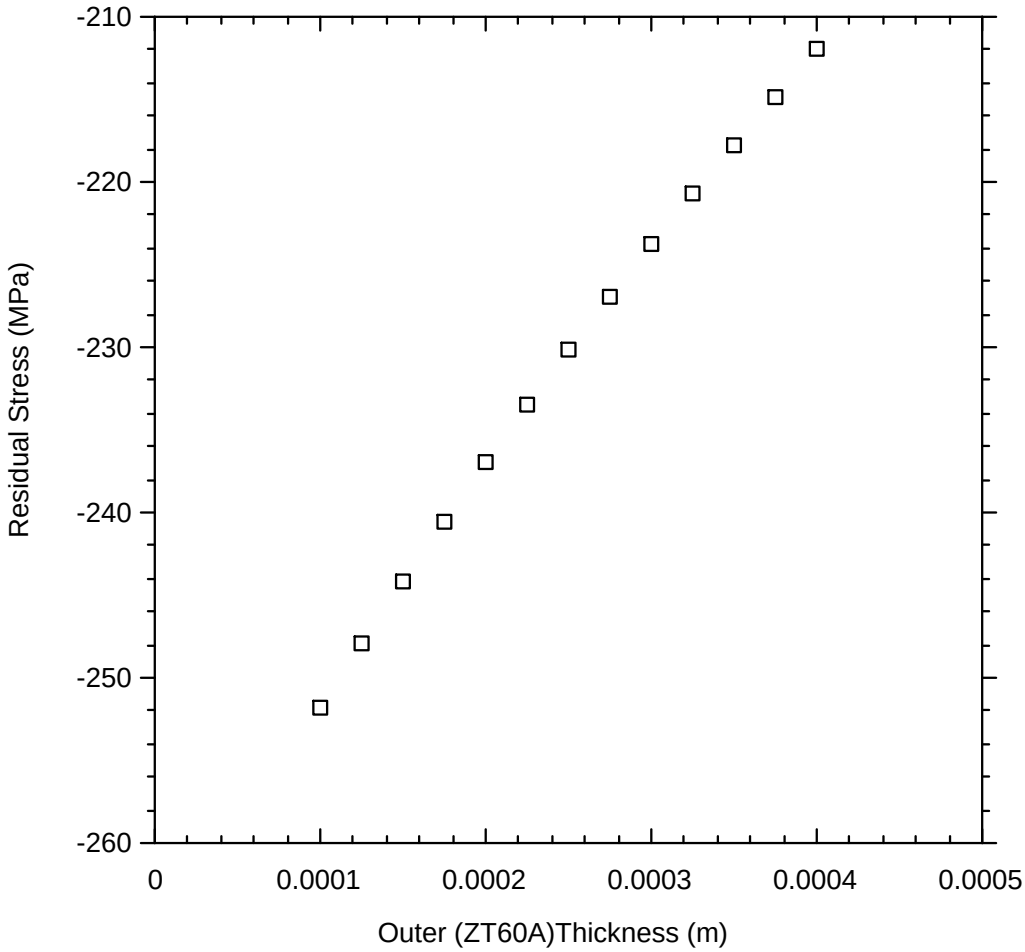

Figure 2. Residual stresses generated as a function of outer layer thickness for ZT60A/ZT40A/ZT60A layered structure

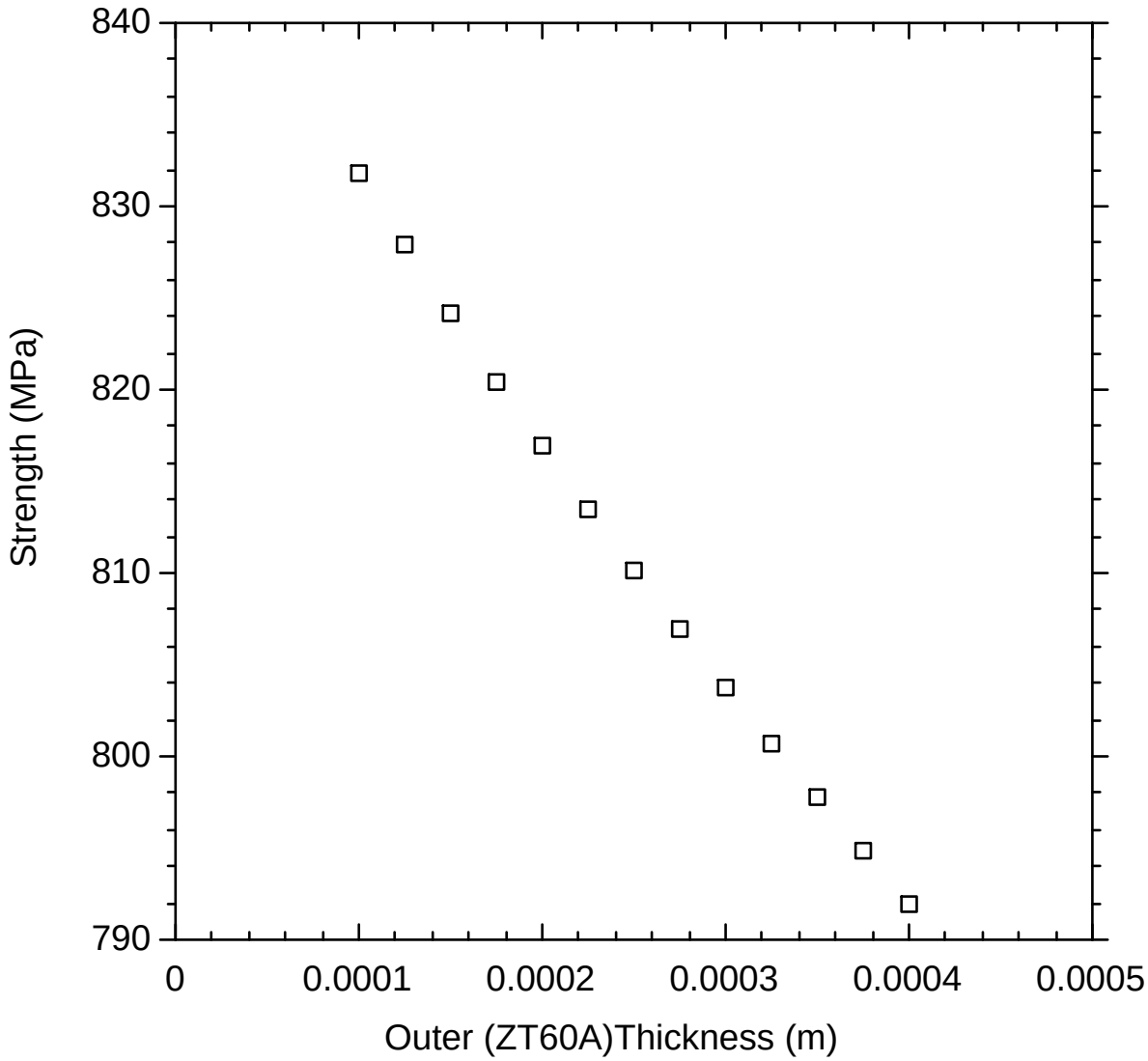

Figure 3. Predicted Strength for ZT60A/ZT40A layered composites as a function of outer layer (ZT60A) thickness for surface failure.

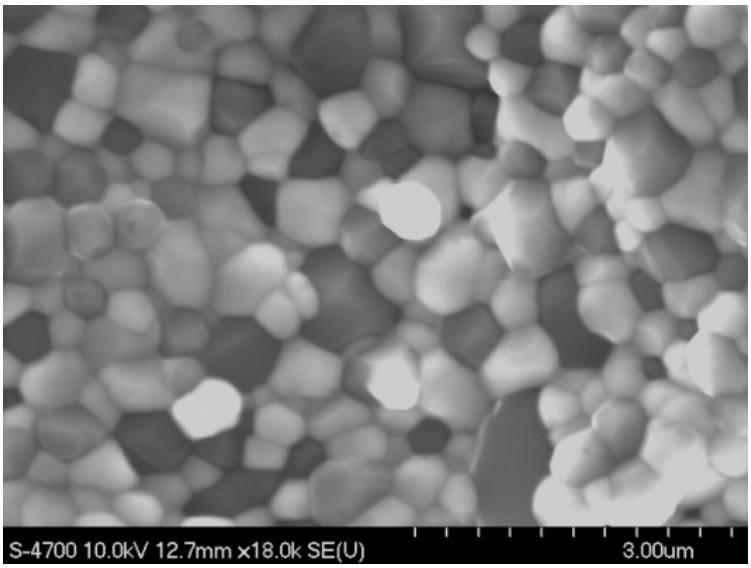

(A)

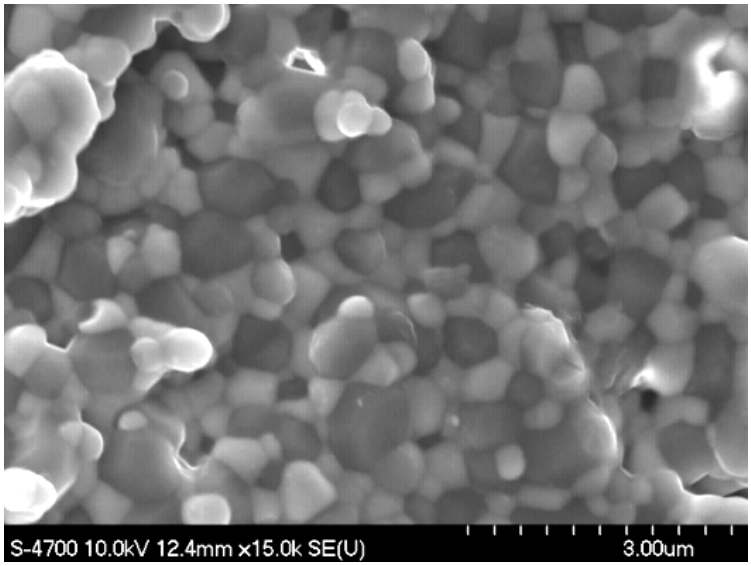

(B)

Figure 4. Microstructures of (A) zirconia toughened 40 vol.% alumina and (B) zirconia toughened 60 vol.% alumina.

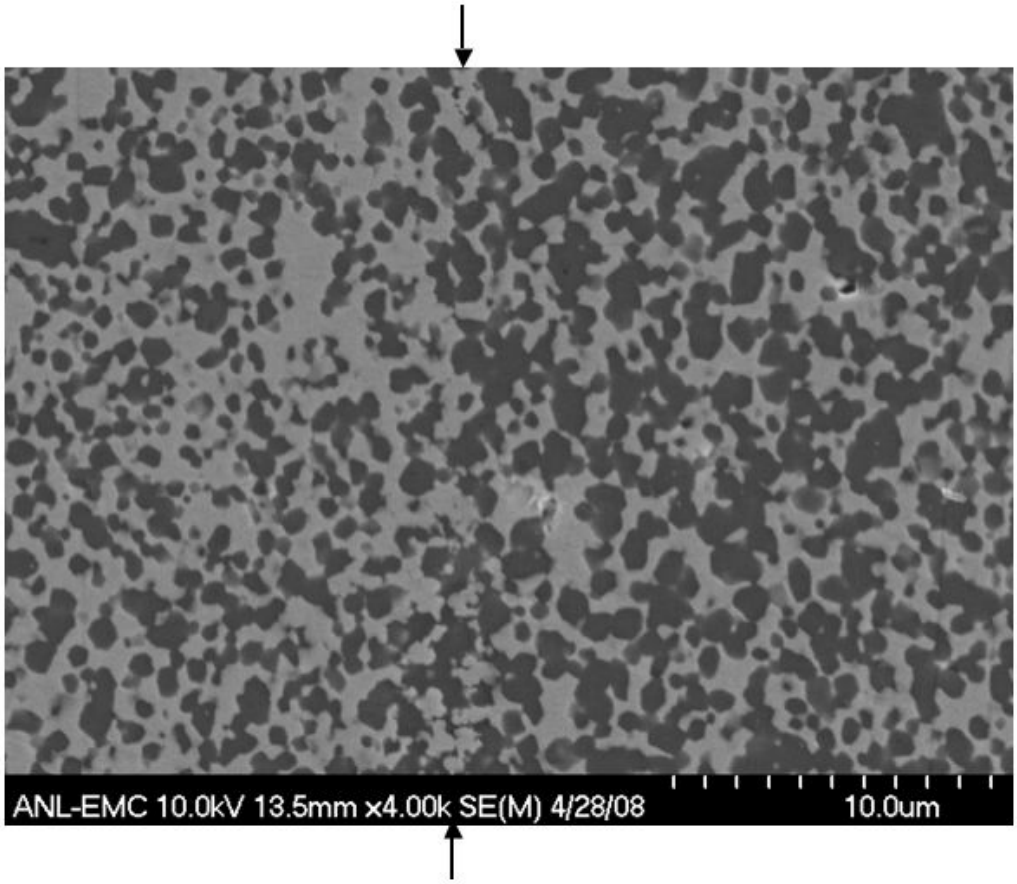

Figure 5. SEM micrograph of the joined interface of ZT40A (left) and ZT60A (right). Arrow indicates the location of the interface. Darker phase is alumina.

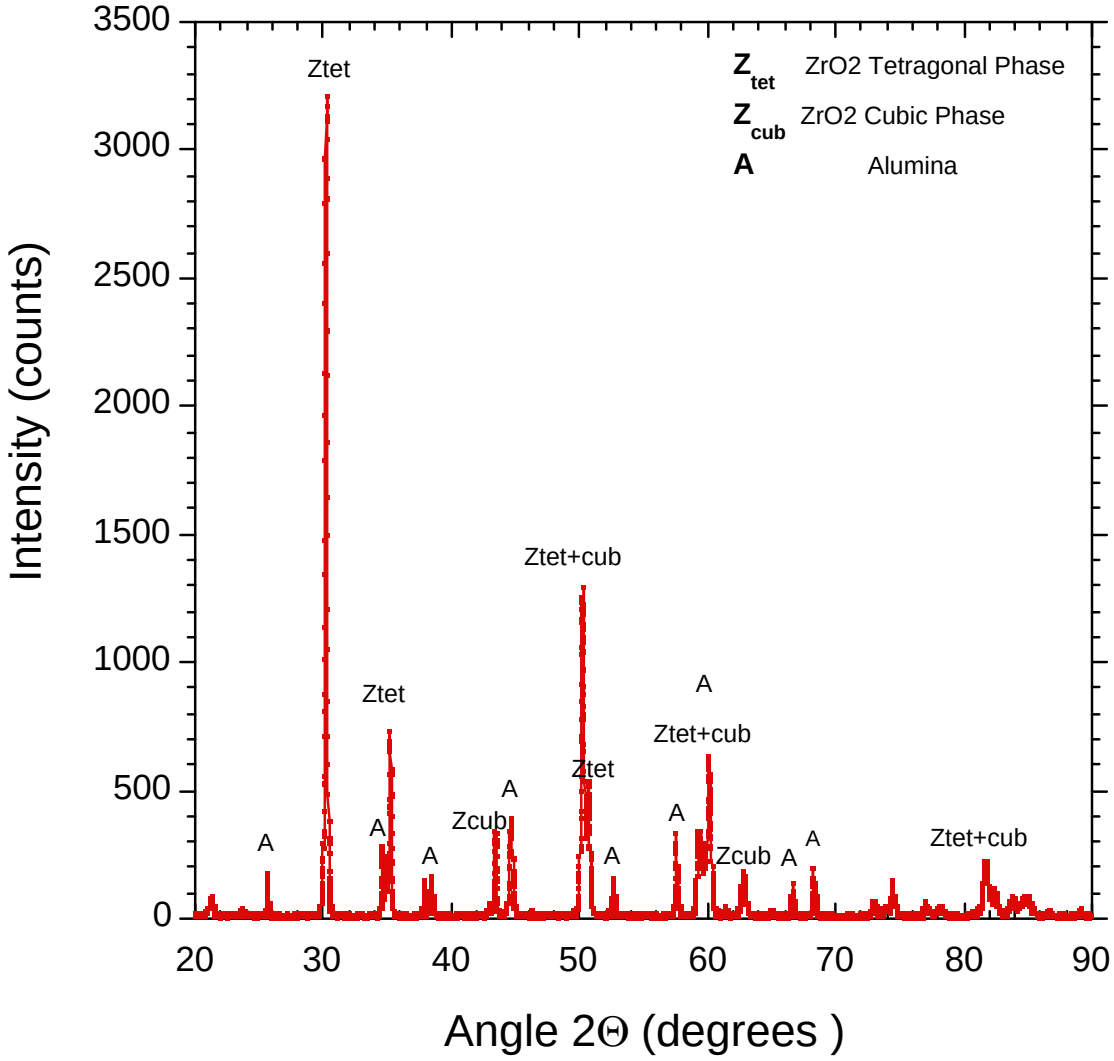

Figure 6. XRD pattern of ZT40A composite sample.

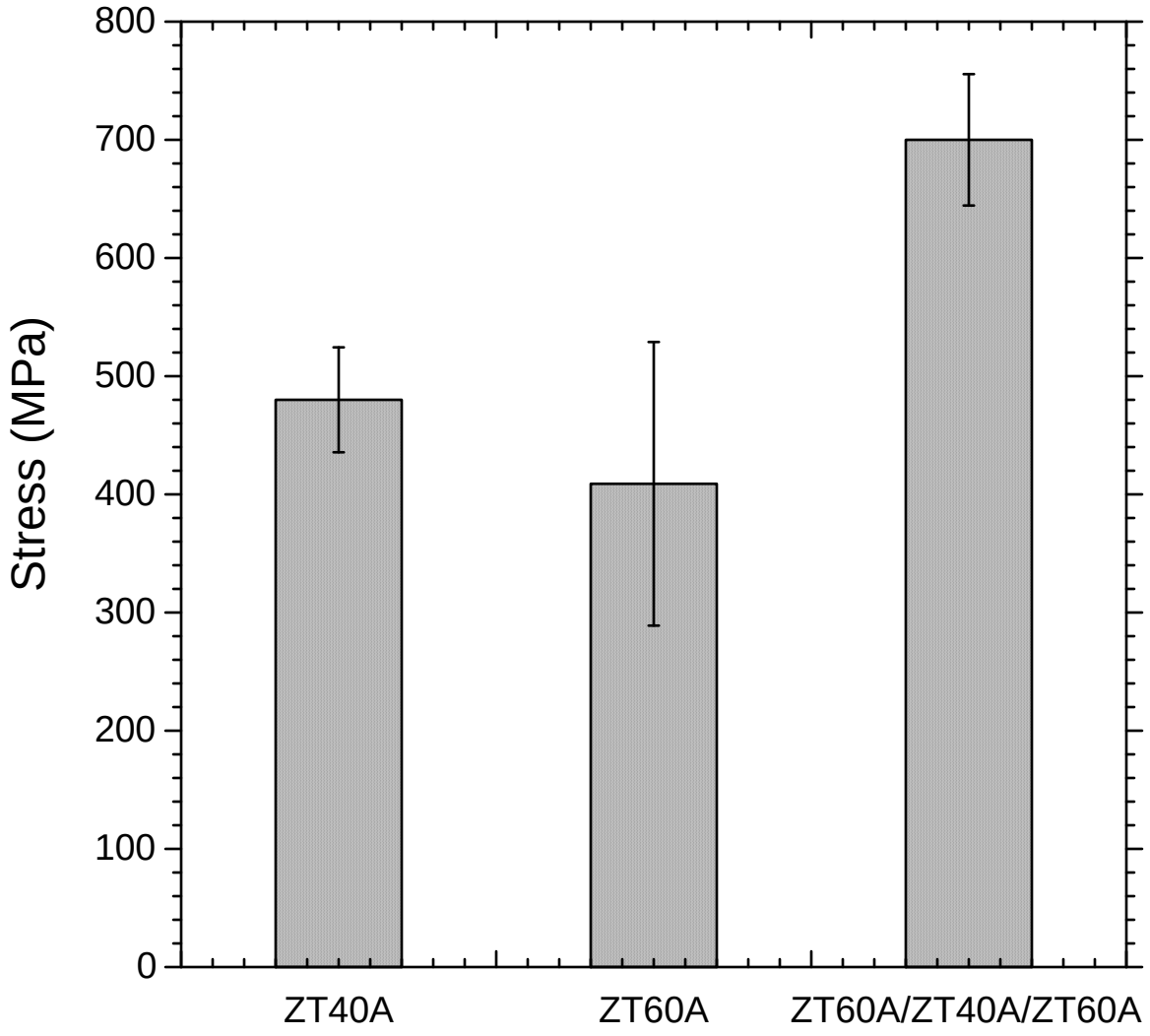

Figure 7. Flexural strength of ZT40A, ZT60A, and layered ZT60A/ZT40A/ZT60A samples.

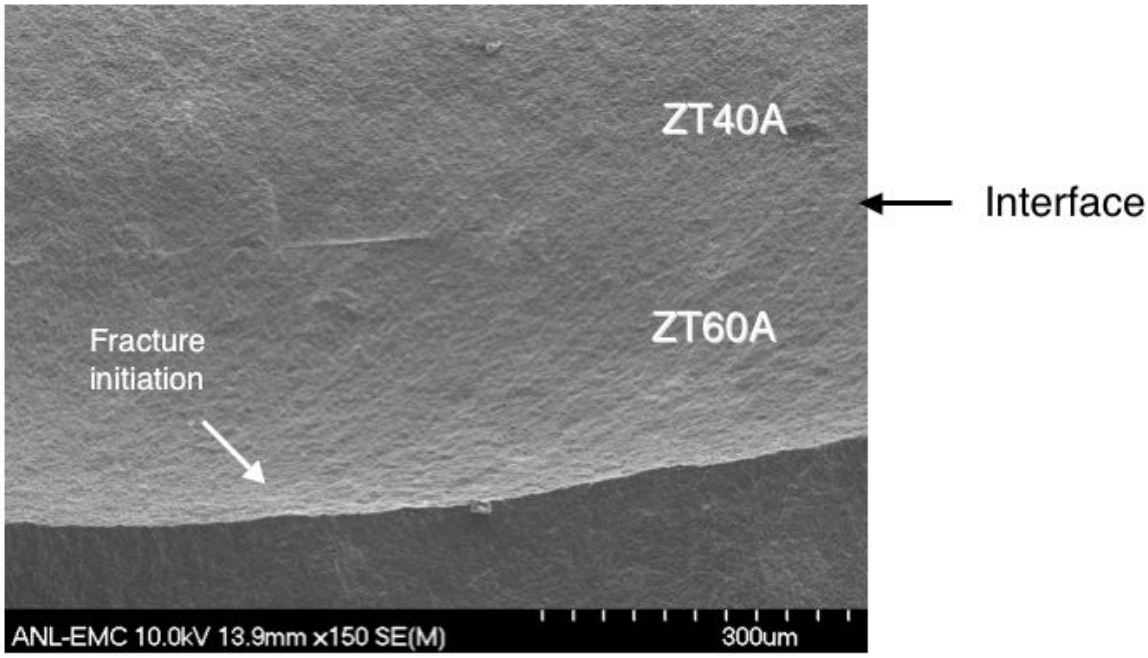

Figure 8. SEM of ZT60A/ZT40A/ZT60A layered structure tested in flexure showing fracture initiation from the surface of ZT60A outer layer.

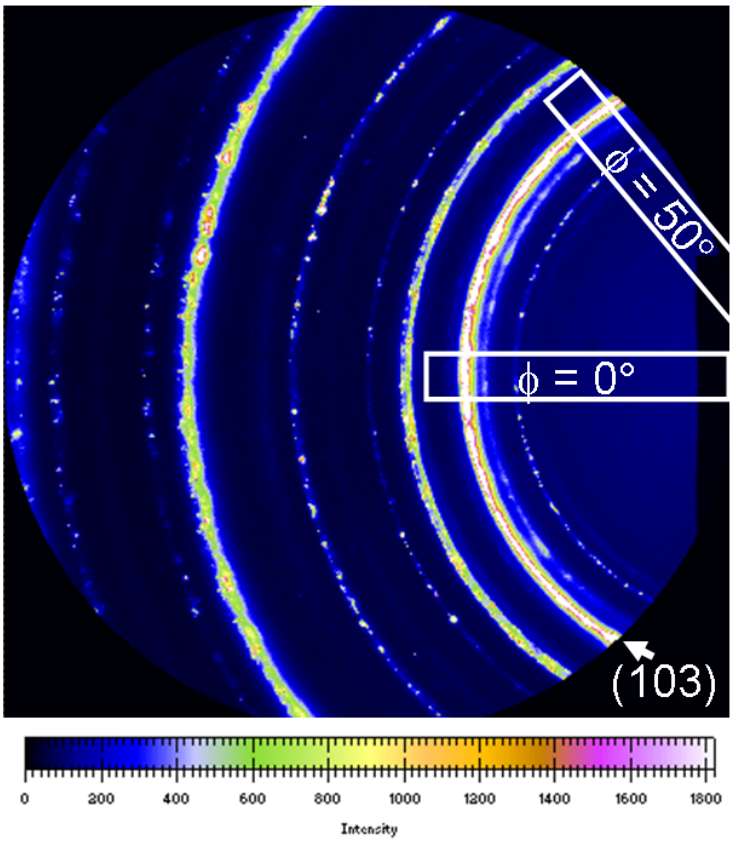

Figure 9. A typical x-ray microdiffraction pattern of the layered sample.

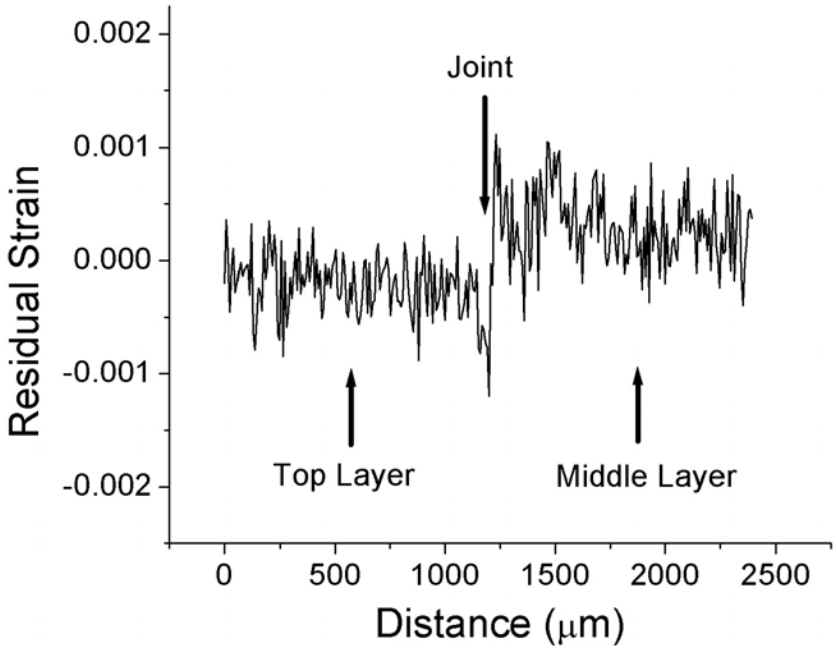

Figure 10. Distribution of deviatoric in-plane strain along the cross section of the layered sample.

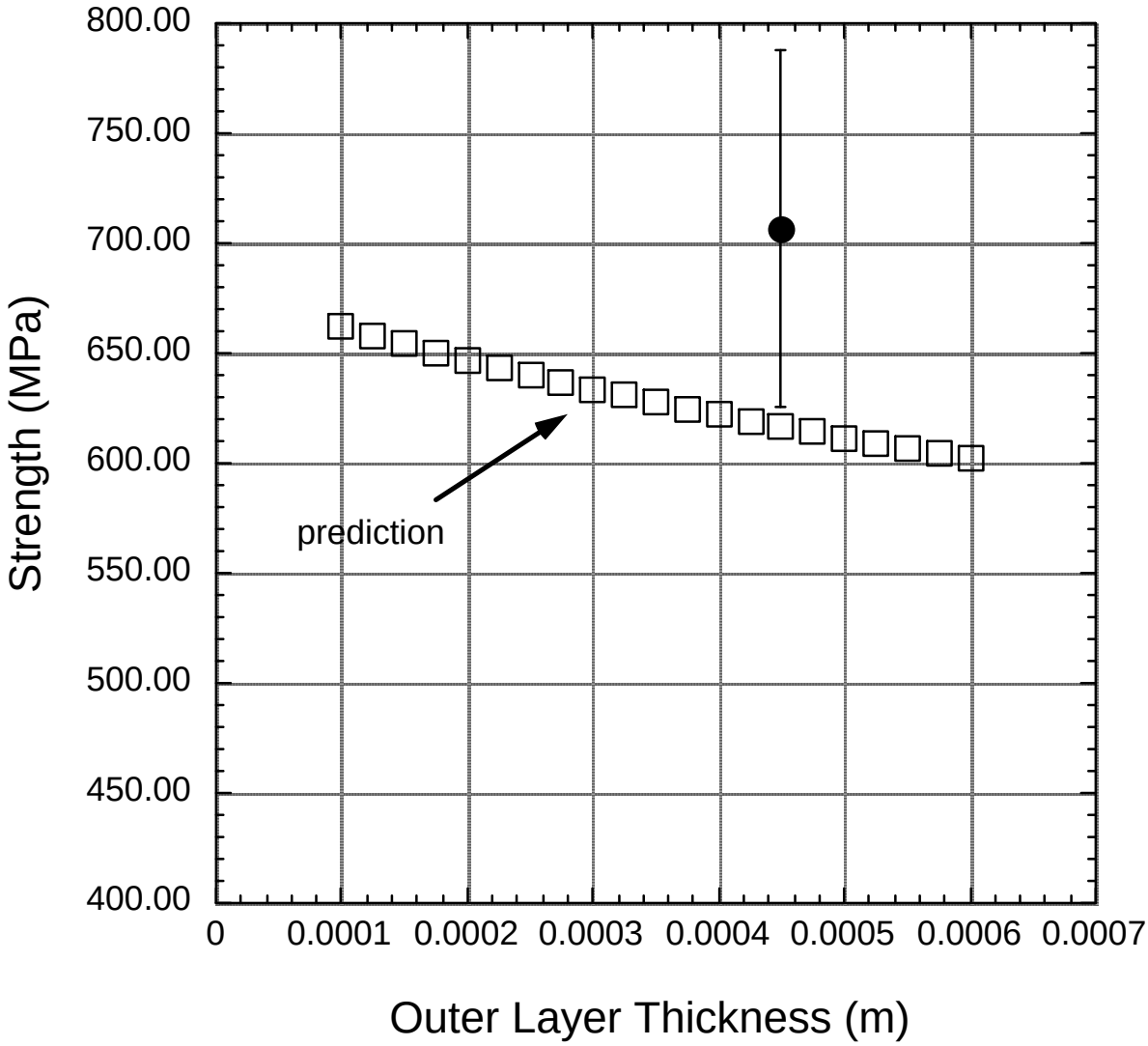

Figure 11. Comparison of experimentally measured flexural strength with the prediction for the layered structure as a function of the outer layer thickness.

Agreement 9105: Ultra-High Resolution Electron Microscopy for Characterization of Catalyst Microstructures and Deactivation Mechanisms

*L. F. Allard, C. K. Narula, J-H. Kwak, * C.H.F. Peden* and M. Jose-Yacaman***
Oak Ridge National Laboratory
P.O. Box 2008, MS-6064
Oak Ridge, TN 37831-6064

** PNNL, Richland, WA*
*** University of Texas-Austin, Austin, TX 78712*

DOE Technology Manager: Jerry L. Gibbs
(202) 586-1182; fax: (202) 586-1600; e-mail: jerry.gibbs@ee.doe.gov
ORNL Technical Advisor: D. Ray Johnson
(865) 576-6832; fax: (865) 574-6098; e-mail: johnsondr@ornl.gov
(865) 576-6832; fax: (865) 574-6098; e-mail: johnsondr@ornl.gov

Contractor: Oak Ridge National Laboratory, Oak Ridge, Tennessee
Contract No.: DE-AC05-00OR22725

Objectives

- Develop and utilize new capabilities and techniques for ultra-high resolution transmission electron microscopy (UHR-TEM) to characterize the microstructures of catalytic materials of interest for reduction of NO_X emissions in diesel and automotive exhaust systems.
- Relate the effects of reaction conditions on the changes in morphology of heavy metal species on "real" catalyst support materials (typically oxides).
- Continue project with Protochips Co. (Raleigh, NC) to demonstrate the utility of a robust MEMS-based heating holder for the ACEM, which allows the behavior of catalytic materials to be studied *in situ* as a function of temperature and time, with stability sufficient not to compromise the full sub-Ångström imaging capability of the instrument.
- Begin development of an environmental cell (E-cell) holder with Protochips Co., utilizing innovative cell structures comprising MEMS-based heater elements and ultra-thin windows.

Approach

- Utilize Oak Ridge National Laboratory ACEM to characterize the atomic morphology and behavior of heavy-metal species such as platinum and rhenium on oxide (and other) support materials (alumina, silica, titania, carbon) as a function of *in situ* heating procedures.
- Utilize ACEM high-angle annular dark-field (HA-ADF) imaging to characterize the structure and chemistry of a series of model bimetallic nanoparticle comprising controlled compositions in the gold/palladium, platinum/zinc, and platinum/rhenium systems.
- Utilize density functional theory for modeling bimetallic catalyst structures and computing the resultant ADF images for comparison to and support of experimental observations.

Accomplishments

- Developed and tested a variety of procedures of *in situ* heating using HTML's special heating holder with Protochips Co. MEMS-based heating devices.
- Utilized heating holder for characterization of a series of Pt/alumina/baria catalysts used for NO_x trap technology.
- Designed and fabricated a new gas-handling system, and used it for testing the first environmental cell specimen holder from Protochips Co.

Future Directions

- In a cooperative project with Protochips Co., continue to develop techniques for *in situ* heating experiments, especially the development of a reliable environmental cell capability for gas reaction experiments.
- Perform precisely controlled *in situ* thermal experiments using *in situ* heating capabilities to understanding the interaction of Pt atoms with catalyst supports, and the development of catalyst nanoparticles and subsequent coarsening kinetics.

Technical Progress

Our development of a new research thrust into in situ microscopy studies of catalytic materials continued this year. We are working in collaboration with Protochips Co. (Raleigh, NC) who provides novel heater elements fabricated utilizing semiconductor micro-fabrication techniques that have proven to have outstanding properties and behavior ideal for *in-situ* electron microscopy studies at the sub-Ångström level. A variety of methods for conducting heating experiments have been developed and tested, and used in several studies that have resulted in publications and presentations as listed at the end of this report. Work on an environmental cell (E-cell) capability was also initiated, resulting in the development and testing of a gas-handling system that was designed to permit accurate control of both composition and pressure of reaction gases inside the cell.

Work also continued in collaboration with colleagues at PNNL studying Pt/alumina and baria/alumina NO_x -trap catalysts. Our studies of bimetallic catalysts continued, in collaboration with Prof. M. Jose-Yacaman of UT-Austin (now of UT-San Antonio), with heating experiments on novel three-shell (i.e. core, inner shell, outer shell) Au-Pd catalysts. These projects have also resulted in significant publications. Examples of the results obtained in these studies are given in the sections that follow.

Development of In Situ Methods

Heating Holder Experiments: The novel MEMS-based (i.e. micro-electro-mechanical systems) heating devices provided by Protochips Co. (Raleigh, NC) are being used in a specimen holder for the aberration-corrected electron microscope (ACEM) designed and fabricated by Prof. Emeritus W.C. Bigelow (U of Michigan). Figure 1a shows the first experimental version of the holder, with a 3mm diameter heater "chip" in place, clamped with the electrical leads. This holder for the ACEM has a tip geometry that will work only in the JEOL microscopes, e.g. the tip width with leads coming in from either side of the long axis of the specimen rod is not compatible with the specimen holder geometry of any other manufacturer. Work with this holder has led to the development by Protochips of the first commercial version of the heating holder, shown in **Fig. 1b**. This holder has a narrower tip profile, but maintains a very thin geometry that can be used not only in the narrow (2mm) objective lens pole piece of the JEOL ACEM, but also in any other current manufacturer's microscope. Our

original design of heating holder also would not permit the holder to be used in conjunction with an energy-dispersive x-ray spectrometer system on the microscope, because x-rays from the sample would be impeded by the heater lead on the detector side of the specimen rod. The new commercial heater rod uses a new design of MEMS chip, which has leads positioned on one end, and the connection is made by a unique clamping mechanism that allows the rod tip to be reduced in width. This geometry completely clears the tip of the rod so that x-rays can be detected appropriately. In expectation of the near-term delivery of an x-ray spectrometer system for the ACEM, the HTML heater rod was recently re-machined to permit the leads to be clamped onto the new design of heater chip, as shown in **Fig. 1c**. For review, **Fig. 2** shows an SEM image of the original heater chip design, with the ceramic film that heats to ≥ 1000°C in 1 millisecond indicated. A carbon film having 1-micron holes in it is supported over the heated ceramic, and in turn supports deposited catalyst powders.

A major concern with the use of **any** heating holder in the electron microscope is the question of "what is the temperature of the sample as it is being observed under elevated temperature operation?" This question has two components; the first is how a sample (e.g. catalyst powder) behaves when deposited onto the holey carbon film, and the second is the question of how the electron beam heating affects the sample, both at a nominal room temperature, and while the imaged area is at elevated temperature. Since these issues are critical to the ultimate understanding of the behavior of ultra-fine catalytic species on support materials, and thereby to the understanding of the catalytic processes being studied, an element of our work is to first systematically calibrate heater chip temperatures over the entire range from RT to >1000°C, and then (and with much greater difficulty!) determine the additional effects of the incident 200kV electron beam on the actual sample both at RT and at elevated temperatures. The latter work is being initiated in collaboration with Prof. A. Datye of the U of New Mexico and students, and will be reported in subsequent quarterlies. Initial measurements of heater chips to calibrate the low temperature regime of operation have been started at the HTML, using infra-red camera technology available in the Physical Properties user center (Dr. Ralph Dinwiddie). Chips are supplied by Protochips along with a table of temperature vs. current, measured using an optical pyrometer that is useful only in the range of 600-1200°C. Their measurements are made while the chips are heated under vacuum, to mimic the use while inside the vacuum of the electron microscope. Our initial 'proof-of-principal' infra-red camera measurements have been made in air; a special vacuum chamber design that permits the chips to be heated under vacuum and also allow the infra-red camera to be positioned close to the chip as required will be described also in a subsequent quarterly. **Figure 3** shows a plot of temperature vs. current, with both the Protochips measurements and the HTML measurements plotted. It is apparent that the air measurements do not match appropriately with the higher temperature vacuum measurements, with the air measurements apparently lower vs. current as might be expected by the fact that air provides an additional method (convection) of heat transfer relative to vacuum (radiation).

As mentioned earlier, we have utilized several heating scenarios over the past year of use of the Protochips heating technology that have all been successful to one extent or another, depending on the requirements of the heating experiment. Two such methods are as follows. First, and most obvious, the (catalyst) sample area of interest is imaged at room temperature, and then heated (instantly!) to a chosen temperature. The major result of heating is a change in the Z position of the sample (i.e. sample height) resulting from simple expansion of the ceramic membrane with temperature. The change in position of the sample area is typically on the order of nanometers, so there is no problem with locating the original area.

After refocusing, the same sample area is re-imaged, with as little as possible exposure of the area to the electron beam (especially at very high magnification). A series of images can be recorded at the initial temperature, to obtain information on the effects of time at temperature on the sample morphology. Alternatively, the temperature can be further increased, and the imaging experiment repeated at the new temperature, again after simply re-focusing the image.

A second heating procedure involves using the essentially instantaneous capability of the heater chip to reach temperature or return to RT. This allows us to image at RT, blank the electron beam, heat the sample to a desired temperature for a chosen time, then return the chip (sample) to RT (instantaneously), and begin imaging the same sample area again. This method has the advantage of not requiring a re-focusing step after the heating cycle, since there is virtually no drift either in X-Y or in the Z direction, because of the outstanding stability of the heater chip. We believe this second method also offers the best resistance to changes in the sample as a result of electron beam exposure, but sequential imaging while at elevated temperature is certainly the best method to obtain information on reaction kinetics. We have to date only used the heating holder for experiments while in STEM mode, in which scanning HA-ADF and BF images are recorded simultaneously, for frame times typically of 17s. We expect to use our TEM capability with a 2K x 2K pixel CCD camera to do experiments in the future, with image times of 1s or less, in the case we need to record rapid sample changes. Having both capabilities in the same instrument is an obvious advantage for our catalyst research work.

Environmental Cell Holder Development: The next phase of development in our in situ thrust has been to extend the use of Protochips MEMS devices to use in a holder that would provide a sealed volume into which gas could be circulated at a controlled pressure (probably in the range of 1-20microns), with an element of the sealed volume being a heater chip onto which catalyst material could be deposited prior to sealing the cell. Figure 5 shows our first prototype E-cell. In this device, the cell was created by upper and lower chips, which had, thin (~30nm) windows of amorphous silicon nitride fabricated on the silicon chip support. These windows were sandwiched around a heater chip, compressing thin wire leads onto the electrode pads of the heater. We had to be able to test our E-cell designs in an external chamber, so we adapted an existing pumping system (a turbo-pumped ion sputter deposition system) to accommodate the airlock entry flange previously used on the HTML's *ex situ* reactor system. The external test chamber allowed the confirmation of the ability of the E-cell to seal atmospheric pressure against a vacuum equivalent to that in the specimen chamber of the ACEM. The E-cell was then inserted into the microscope (with a dummy heater chip having no heater membrane in place), and tested the ability to transmit the electron beam through the sandwich of films. It was clear in the first test that the beam was largely attenuated, probably by the air at 1atm inside the cell. The electron beam path through the gas in the cell is about 700 microns, and a reduction from 760mm Hg to 20microns Hg would significantly reduce the scattering. Because of a concern that developed regarding the thickness of the prototype E-cell (1.7mm) in the 2-mm gap of the microscope's pole piece, we did not continue the *in situ* tests in favor of a new E-cell design in which only two chips, a top special design of heater element and a bottom thin window element, would be used. The fabrication and testing of the 'Beta-2' version of the E-cell holder will be described in the next quarterly report.

<u>Bimetallic Catalyst Heating Experiments</u>

In our early experiments, we were most interested in characterizing the behavior of the MEMS heaters with regard to the ability to record ultra-high-resolution images in STEM ADF mode. As

shown in our 2007 annual report, we could record structure images of Pt nanoparticles (from our NO_x-trap catalyst study with PNNL collaborators) while the particles were held at a nominal temperature of 1000°C. We applied this capability to study the behavior of nanoparticles of AuPd which, as we showed in a recent publication [] have a core-shell structure in the as-prepared condition, with a central core rich in Pd, an inner shell rich in Au, and an outer shell rich in Pd. This system offered an excellent model system to observe changes in behavior with temperature, because of the easily discernible microstructural features in the HA-ADF images. Particles of a nominal Au1-Pd1 composition were dispersed in isopropyl alcohol, and a droplet deposited onto the holey carbon film over the heater surface. Several series of HA-ADF and BF image pairs were recorded at magnifications from 500kx to 8Mx, as temperatures were gradually increased from 350°C to 900°C, in steps of 50°C. **Figures 4a and 4b** show the beginning and end morphologies of a cluster of AuPd particles after this heating sequence. The core-shell structure which is clearly seen in **Fig. 4a** at 350°C was observed to disappear after a few minutes at a temperature of 550°C, as the particles homogenized by diffusion. Two small clusters of AuPd atoms appeared at the arrowed positions 1 and 2 at 550°C, probably as a result of migration of atomically dispersed species not seen at this magnification. Interestingly, only the cluster 1 grew during the rest of the run, as is seen in **Fig. 4b**. Remarkably also, the center particle A seen at 350°C simply diminished greatly in size, with the growth of a new grain on the adjacent surface of the larger particle B. The two particles did not sinter together, even though they were apparently in contact at the temperature of 700°C during the run. New particle 1 grew also, but new particle 2 did not change appreciably after its initial formation at the lower temperature.

In this application example, the clear homogenization of the 3-layer Au-Pd particles was an expected result, explained by a diffusion mechanism. *To our knowledge this is the first time that direct diffusive reconstruction of an alloy particle has been directly observed.* The reasons for the unexpected failure of two primary particles to sinter, but instead to show growth of one particle at the expense of the other, are not immediately clear. One possibility is that particles acquire some charge during the observations, affecting the surface energy. The overall growth behavior is reminiscent of Ostwald ripening effects, although our system involves particle behavior on a uniform surface (thin carbon film), whereas Ostwald ripening generally involves particle coarsening in solid or liquid solutions. The behavior of the particles in this example was not uniformly consistent with Oswald ripening, however, as not all smaller particles diminished in size with respect to adjacent larger particles. We have established collaborations with a number of research groups having an interest in these issues, and the thrust of the work in the near future will be to understand these effects, both on nanoparticles and on highly dispersed species on both model and "real" supports.

NO_x Trap Catalyst Experiments

We have been collaborating with Drs. Ja Hun Kwak and Chuck Peden of PNNL, in studies of new BaO/alumina catalysts. Atomic-resolution electron microscopy with HTML's ACEM is being combined with various spectroscopic tools such as NMR, to fully understand the relationship between structure and performance. Recently, the PNNL group reported the importance of a strong interaction between the BaO and penta-coordinated Al^{3+} sites formed on alumina surfaces [Kwak et al. *J. Catal*. **251** 189(2007)] using high-resolution ^{27}Al solid-state NMR studies. This result strongly suggests that the BaO is dispersed mono-molecularly and preferentially concentrated on the (100) facets of the alumina support, and that penta-coordinated aluminum sites are formed on (100) facets. HA-ADF images recorded in the ACEM also completely confirmed these results, as shown **Fig. 6**. The image of Fig. 6a shows a 2 wt % BaO/γ-Al_2O_3 sample in which single BaO

molecules (bright spots; the oxygen is not imaged in ADF mode) are clearly seen dispersed on the surface of γ-Al_2O_3. This image allows us to differentiate regions on the γ-Al_2O_3 support that have significantly different BaO populations. In region A no BaO units are seen, in accord with the prediction of density functional theory (DFT) calculations that suggest the complete absence of penta-coordinate Al^{3+} sites on other facets that would serve as anchoring points for BaO. In regions B and C of the TEM image the BaO units are fairly uniformly dispersed; the intensity profiles shown in Figs. 6b and 6c are consistent single BaO units. The decoration of facet boundaries by BaO monomers seems to be also evident, for example in regions D of the HR-TEM image. These observations are all consistent with the results of our recent high-resolution ^{27}Al solid state NMR study. These results combined with DFT simulations can explain the unique behavior of NO_2 interaction with BaO. A paper on these results is in preparation for J. Catalysis.

Concluding Remarks:

Our research activities on the forefront studies of the behavior of catalyst clusters and nanoparticles with reaction treatments, imaged at ultra-high resolution with the aberration-corrected electron microscope, are building a foundation towards a better understanding of the phenomena, which control performance in real systems. The implementation of novel methods for conducting these studies on specimens heated inside the electron microscope is the next major step for our research. Major progress has been made in the development of a stable heating holder system that allows full sub-Ångström resolution imaging in HTML's ACEM, and this capability has been used in a number of studies, not only the present project work, but also in support of a variety of catalyst materials studies supported by DOE and the HTML national user program. Extension of the heating capability to development of an environmental cell (E-cell) holder for *in situ* gas reaction studies has been initiated.

References:

1. S. Mejia-Rosales, J C. Fernandez-Navarro, E. Perez-Tijerina, D. A. Blom, L. F. Allard and M. Jose-Yacaman, "On the Structure of Au/Pd Bimetallic Nanoparticles," *J. Phys. Chem. C,* **111**(3), 2007.

Publications and Presentations:

1. "Understanding the nature of surface nitrates in BaO/γ -Al2O3 NO_x storage materials: A combined experimental and theoretical study;"
Ja Hun Kwak, D. Me, C.-W. Yi, D. H. Kim, C.H.F. Peden, L.F. Allard and János Szanyi, J Catalysis (in press).

2. "A New MEMS-Based System for Ultra-High-Resolution Imaging at Elevated Temperatures"
L.F. Allard, W.C. Bigelow, M. Jose-Yacaman, D.P. Nackashi, J. Damiano and S.E. Mick; Micros. Res & Tech, 72(3), March 2009 (in press)

3. **Plenary Lecture** L. F. Allard presented a plenary lecture at the Texas Society for Microscopy, entitled "In-Situ Observation of Catalytic Materials at High Temperatures with the Aberration-Corrected Electron Microscope;" March 2008.

4. D. Ferrer, D.A. Blom, L.F. Allard, S. Mejia, E Periz-Tijerina and M.J. Yacaman, "Atomic Structure of Three-Layer Au/Pd Nanoparticles Revealed by Aberration-Corrected Scanning Transmission Electron Microscopy," *J. Mater. Chem.*, 2008, **18**, 2442. (This article was chosen as a "Hot Paper" and highlighted on the JMC web site at:
http://www.rsc.org/Publishing/Journals/jm/JMCHot_nanotech.asp
Note: The editors state: "*Journal of Materials Chemistry hot papers featured in this nanotechnology section have been rated as "outstanding" by expert reviewers in the field* **.** *"*

5. "A New Paradigm for Ultra-High Resolution Imaging at Elevated Temperatures," L.F. Allard, W.C. Bigelow, D.P. Nackashi, J. Damiano and S.E. Mick; Micros & Microanalysis **14**(Suppl2) August 2008, p. 792-793

Communications and Visits

1. L.F. Allard and E. Lara-Curzio (HTML director) visited PNNL, Oct. 2007. Allard presented a seminar **"Looking at Atoms with the Aberration-Corrected Electron Microscope."** Also reported on status of microscopy work on Pt/alumina-baria NO_x -trap catalysts.

2. L.F. Allard visited BASF Co., Woodbridge, NJ. Dec. 2007 to present seminar **"Characterization of Catalysts via Aberration-Corrected Electron Microscopy**. Discussed possible collaborations on catalyst research with BASF scientists.

3. L. F. Allard presented an invited seminar at Eastman Chemical Co., Kingsport, TN, entitled **"Looking at Atoms with the Aberration-Corrected Electron Microscope: Applications to Catalyst Characterization."** This visit has resulted in a Work for Others funded project entitled **"Atomic Scale Imaging of Gas-Metal Cluster Interactions."**

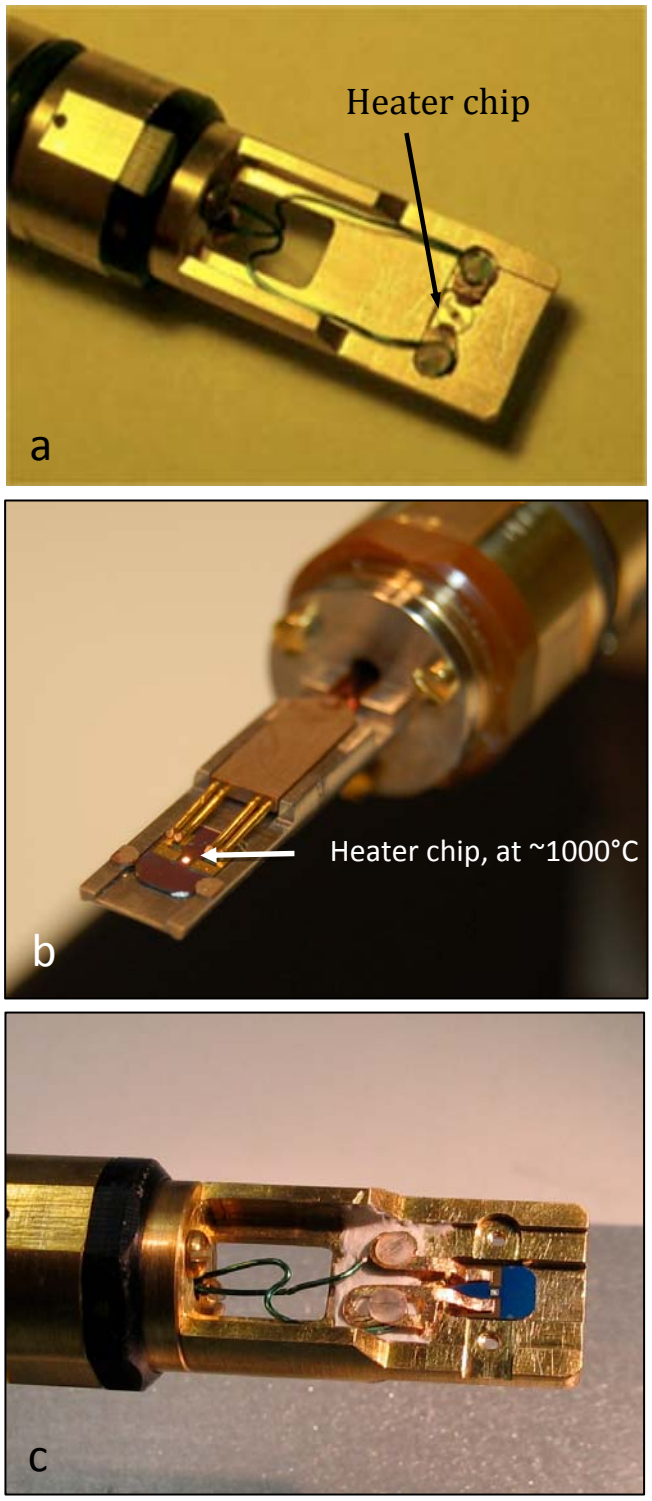

Fig. 1. a) Prototype heater specimen rod for JEOL ACEM, configured to retain original design 3-mm MEMS-based heater devices, as shown; b) Tip of first commercial Protochips heating holder, which utilizes new design of heater chip having electrode pads on one end. A simple clamping mechanisms makes the electrical contacts, and securely retains the heater chip (shown here heated to ~1000°C); c) HTML prototype holder re-machined to retain either original heater chip or new design of chip, as shown here.

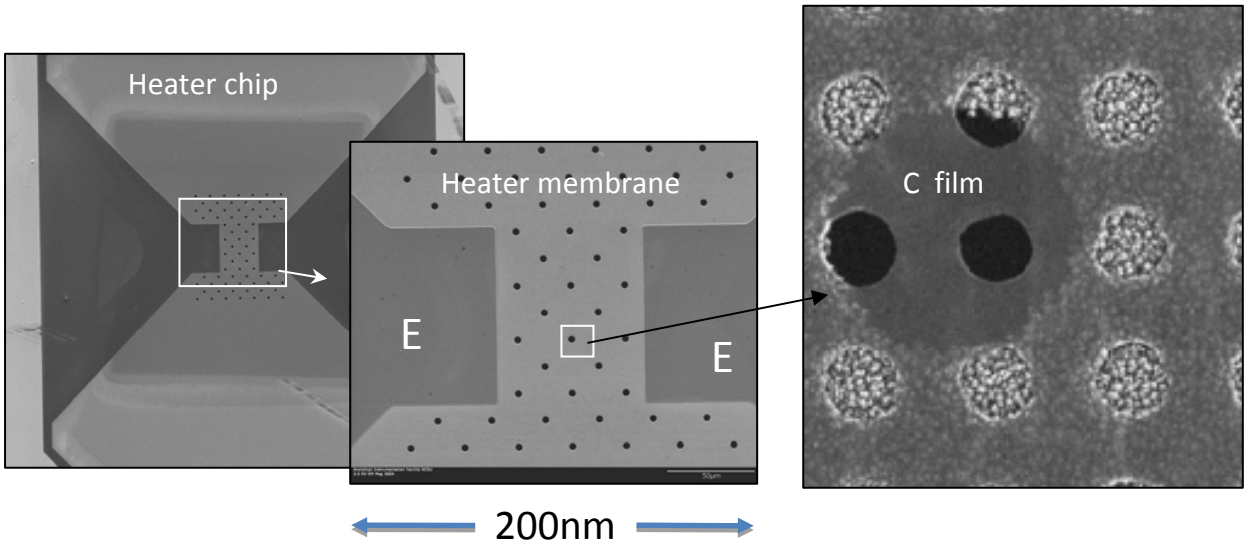

Fig. 2. SEM secondary electron images showing typical MEMS heater geometry. The low-conductivity membrane ceramic is patterned with 3-micron hole, seen in the center image. At higher magnification in the right image the overlying carbon film which supports e.g. catalyst powders is seen.

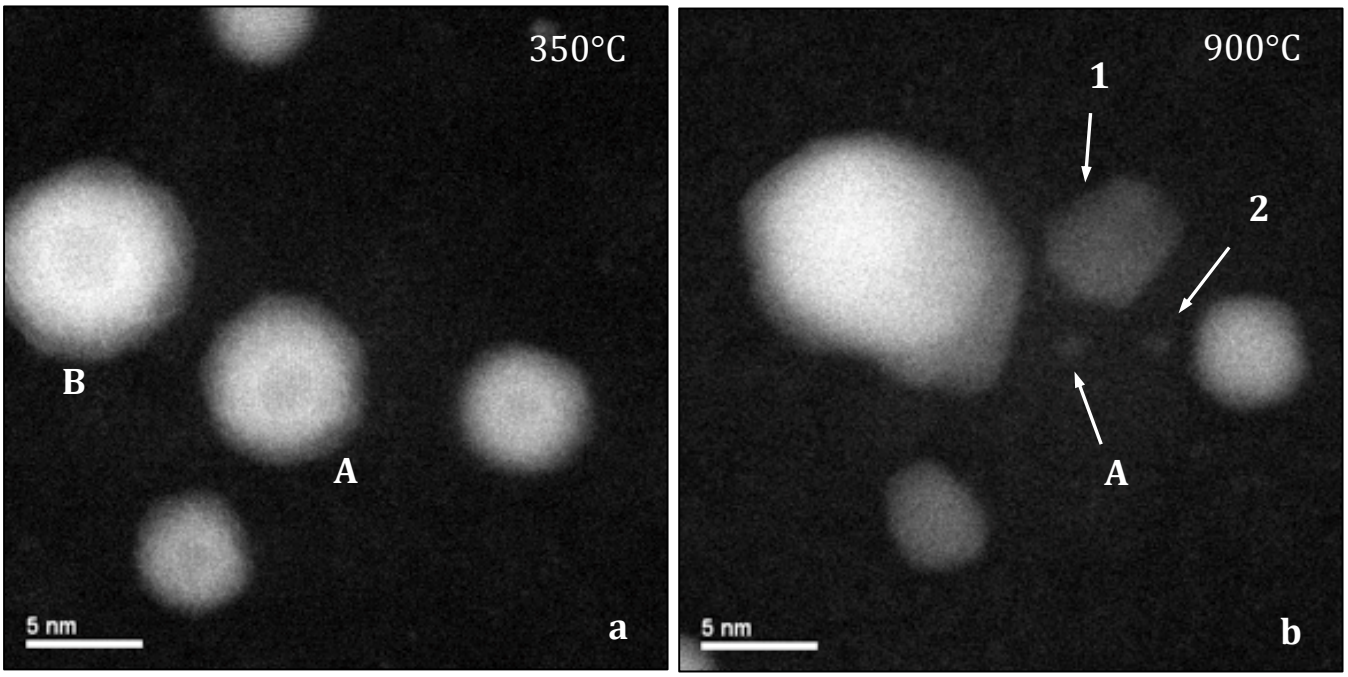

Fig. 3. Initial and final images of 3-layer Au-Pd particles taken from in situ heating experiment. The core/inner-layer/outer-layer structure of the particles remained unchanged at a temperature of 350°C, but the structure homogenized at 550°C, and significant changes were observed during the heating steps up to 900°C as seen in the final image. See text for discussion of details.

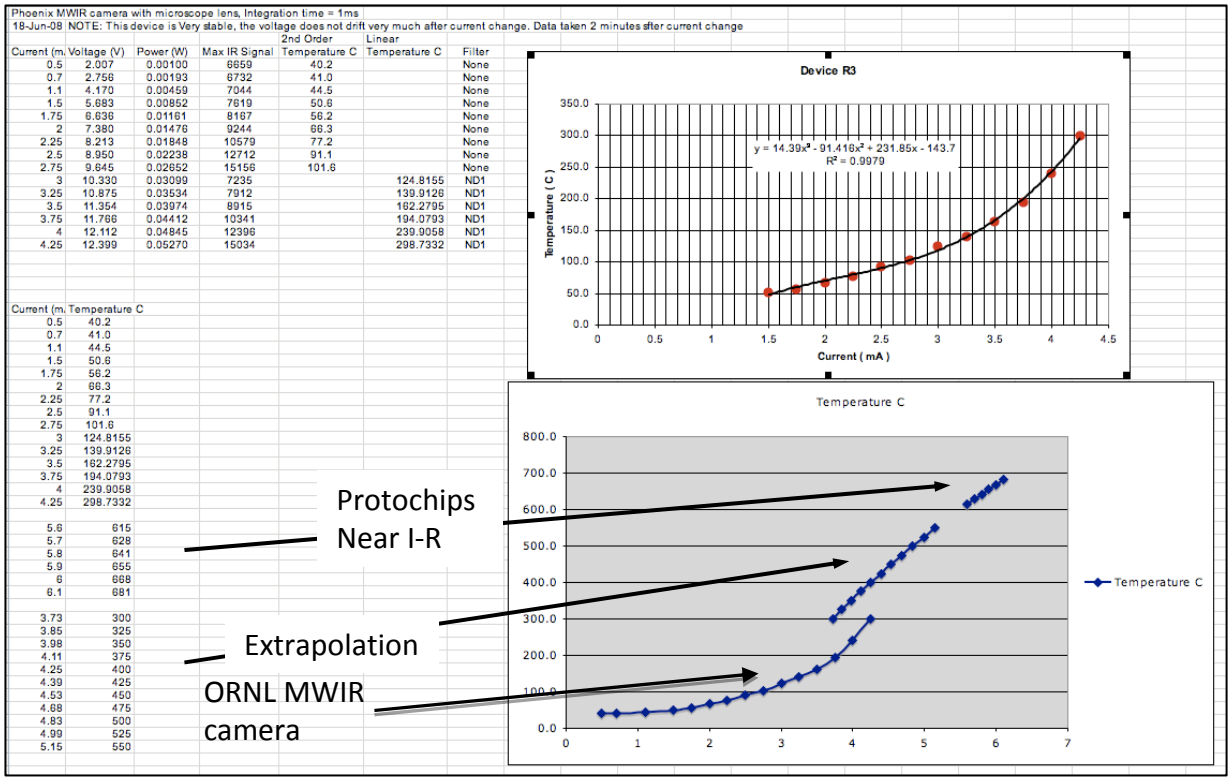

Fig. 4. Example of heater chip temperature calibration from RT to 300°C (upper curve) using ORNL's medium-wavelength I-R camera, which is superimposed on the experimental measurement from 600°C to 700°C (and extrapolated as shown) in the lower plot, made using Protochips near I-R camera. This suggests that the calibration in air vs that in vacuum is not appropriate to give a reliable measure of the chip temperature in the microscope.

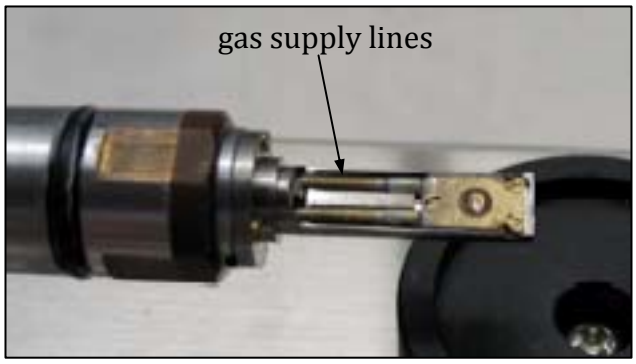

Fig. 5. First prototype E-cell holder, with windows installed. Gas supply lines are show, but electrical leads are internal and not seen.

Fig. 6. Schematic of the gas handling system we have fabricated for the E-cell holder. This system permits accurate control of the gas pressure in the tiny volume of the cell, by supplying gas from a large holding cylinder in which the pressure can be directly measured using a capacitance manometer (Baratron gage).

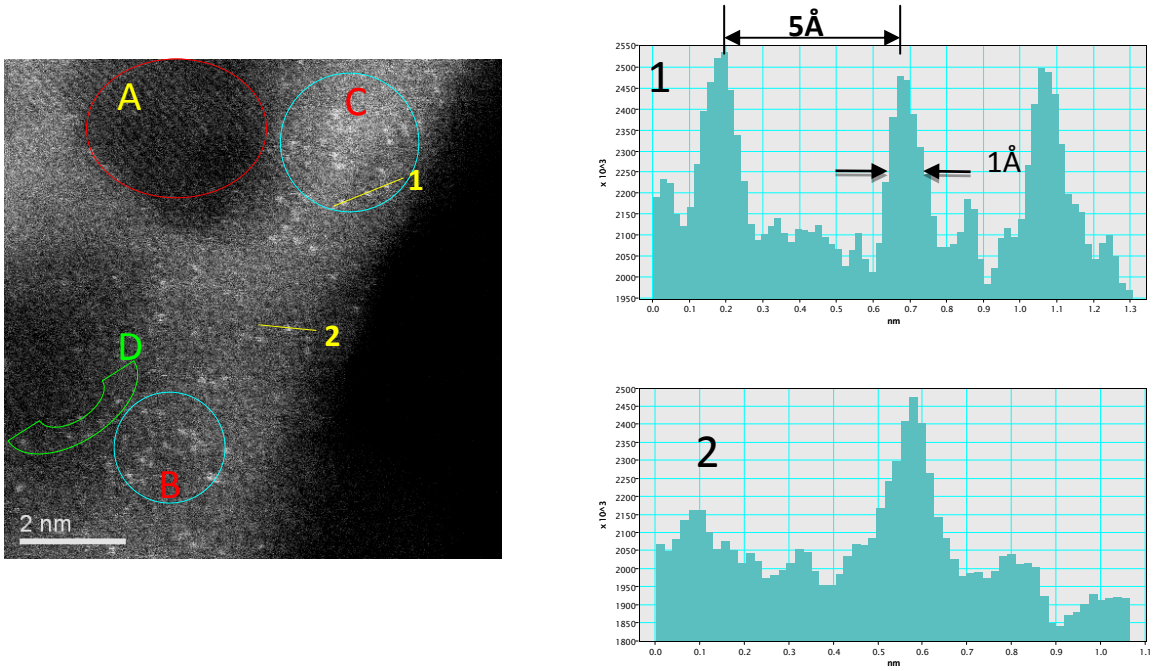

Fig. 7. BaO monomeric species shown in HA-ADF image, supported by γ-alumina. Intensity profile over individual species along lines 1 and 2 as shown, indicate the presence of individual BaO units (note full-width half-max measurement indicates 1Å resolution). See text for details.

Agreement 9110 - Life Prediction of Diesel Engine Components

H. T. Lin, T. P. Kirkland, and A. A. Wereszczak
Oak Ridge National Laboratory
P.O. Box 2008, MS-6068
Oak Ridge, TN 37831-6068
(865) 576-8857; fax: (865) 475-6098; e-mail: linh@ornl.gov

Nate Phillips and Jeff Jenson
Caterpillar, Inc.
Peoria, IL 61656-1875
(309) 578-2969; fax: (309) 578-2953; e-mail: Jensen_Jeff_A@cat.com

DOE Technology Manager: Jerry L. Gibbs
(202) 586-1182; fax: (202) 586-1600; e-mail: jerry.gibbs@ee.doe.gov
ORNL Technical Advisor: D. Ray Johnson
(865) 576-6832; fax: (865) 574-6098; e-mail: johnsondr@ornl.gov

---

Contractor: Oak Ridge National Laboratory, Oak Ridge, Tennessee
Contract No.: DE-AC05-00OR22725
Subcontractor: Caterpillar, Inc., Peoria, Illinois

Objective

- Generate a database and characterize damage mechanisms of candidate advanced ceramics and intermetallic alloys.
- Apply and verify probabilistic life prediction and component design and verification methods for advanced diesel engine components.

Approach

- Evaluate the dynamic fatigue, rotary bending fatigue, and high-temperature fatigue and creep performance of candidate silicon nitride ceramics and TiAl alloys at elevated temperatures in air before and after long-term exposure to simulated engine environments, as well as engine field tests.
- Characterize the evolution and role of damage mechanisms, and changes in microstructure and chemistry, linked to the long-term mechanical performance and reliability of ceramics and intermetallic alloys.
- Predict the failure probability and reliability of complex-shaped diesel engine components subjected to application conditions via the use of life prediction codes.

Accomplishments

- Completed post characterization of microstructure and chemistry and retained mechanical properties of 555-h engine tested silicon nitride valves. The results generated were provided to end user for verification of probabilistic component design and life prediction.
- Completed the failure analysis of vale keepers and determined the cause that resulted in the unexpected stop of engine testing.
- Completed generation of long-term tensile creep database for Daido and Howmet TiAl alloys at different applied stress levels and temperature conditions. The database was provided to end users to confirm the probabilistic life prediction of TiAl components.

Future Direction

- Characterize the mechanical properties and microstructure of candidate materials aiming to improve the thermal management as well as waste heat recovery of high efficiency and clean HD diesel engine.
- Develop mechanical database for candidate materials to meet the challenge of increased high pressure and temperature combustion condition in high efficiency and clean HD diesel engine.

Introduction

There has been considerable interest in the potential for extensive use of advanced ceramics and intermetallic alloys in advanced diesel engine systems because of their superior thermomechanical properties at elevated temperatures. The implementation of components fabricated from these advanced materials would lead to significant improvement in engine efficiency and long-term durability and reduced nitrogen oxides (NO_x) and CO exhaust emissions as required in the 21st Century Truck Program. Interest has focused primarily on research into characterization and design methodology development (life prediction) for advanced silicon nitride ceramics and TiAl alloys to enable the manufacture of consistent, reliable complex-shaped components for diesel engine. The valid prediction of mechanical reliability and service life is a prerequisite for successful use of these materials in internal combustion engine components.

This research project has three primary goals: the generation of a mechanical engineering database, from ambient to high temperatures, of candidate advanced materials before and after exposure to simulated engine environments; the microstructural characterization of failure phenomena in these advanced materials and in components fabricated from them; and the application and verification of probabilistic life prediction methods using diesel engine components as test cases. For all three stages, results will be provided to both material suppliers and component end-users for use in refining and optimizing processing parameters to achieve consistent mechanical reliability, and in validating the probabilistic design and life prediction of engine components made from these advanced materials.

Approach

The retained mechanical strength of both silicon nitride valve stems after 555-h testing in natural gas engine was measured using a four-point bending fixture with 30/60 mm spans. Each valve stems were machined into four half cylindrical type stems for post strength evaluation. In addition, the silicon nitride valve-heads were also evaluated using a customer design fixture under a compressive load via a bench type universal testing machine. These mechanical tests would allow one to evaluate the effect of engine environment on the microstructure and chemical stability and thus mechanical performance and reliability of materials. The mechanical data generated would also allow the end users to verify their probabilistic component design and life prediction results of valve components. Fractography analysis was carried out to characterize the surface morphology and microstructure of fracture surfaces for selected valve stems and valve heads after mechanical test and to determine the strength limiting flaws.

Studies of long-term creep behavior in air of TiAl alloys manufactured by Daido and Howmet were continued in FY2008. Two types of TiAl creep specimens different in final densification process (i.e., one is HIP and the other one is Non-HIP) manufactured by Daido, Tokyo, Japan and designated as RNT650 were received from end user. Also, TiAl tensile specimens manufactured by Howmet, Michigan, USA and designated as 45XD were also received for evaluation. The creep specimens are cylindrical buttonhead type. The test conditions specified (temperatures: 600-750°C, stress levels: 120-390 MPa) are importantly relevant to the temperature and first principle tensile stress profiles encountered by TiAl turbo wheel under the application conditions based on the FEA modeling. The database generated will then be used by the end users to verify probabilistic life prediction of turbo wheel under engine operation conditions, and could also provide important feedbacks to material suppliers for process modification to further improve its high-temperature mechanical performances.

Results

Failure Analysis of Si_3N_4 Valve Keepers

After the great success of 500-h engine field test the 2nd 500-h engine test was initiated to achieve an accumulated 1000-h engine test and to evaluate the long-term durability and reliability of both advanced lightweight silicon nitride and TiAl valves using Caterpillar G3406, which is an in-line 6 cylinders natural gas (NG) engine. However, the engine encountered an unexpected shut down after 55-h of continuous operation under full power, and the total accumulated hour was 555-h. Upon the removal of engine head it was found that all of the valves located in cylinder #6 showed catastrophic fracture; the valve heads were completed broken off leaving the valve stems intact in the cylinder head. Observations showed that a huge clearance was found between the rocker arm and tip of #22 intake valve stem, and the stem was pushed into the spring retainer farther than any other valve. Detailed optical analysis showed that the keeper notch for intake valve #22, which was used to hold the valve in place was substantially worn off as can be seen in Figure 1. In this figure, both halves of the valve keeper for intake valve #22 (labeled A) are shown alongside those from a typically as-received keeper (labeled B). This notch fits inside a groove on the valve to hold the valve in place. As shown in the figure, the notch for valve #22 has clearly worn off. In addition, we observed that the valve stem for this particular valve (#22) was highly polished for the section in contact with the keeper. This further indicates that the valve was moving free of the keeper, and thus falling into the cylinder. When the silicon nitride valve-head fractured and shattered the loose fragments shattered the remaining silicon nitride valves as well as caused the damages to piston and cylinder liner. Thus, it could be concluded that the unexpected failure of the engine field test was not due to the mechanical performance and reliability issue of silicon nitride valves, and instead it was caused by the improper use of wrong valve keepers, which had the significantly different notch dimensions as the valves grooves (Fig. 2).

Characterization of 555-h Si_3N_4 Valves

All of the remaining 555-h engine-tested silicon nitride valves were machined into the half cylindrical valve stems for retained strength evaluation. Figure 3 shows the flexural strength results of the SN235P silicon nitride, half-cylindrical stems after 555-h engine test. Results show that these 555-h tested silicon nitride valve stems exhibit strength values that are about 10-15% higher than those in as-received condition (Fig. 3). Note the fracture strength of the as-received SN235P valves ranges between 610 and 670 MPa. The increased fracture strength measured was in general attributed to the significant decrease in surface roughness (i.e., surface flaw size and distribution), resulting from the repeatedly reciprocating frictional movement between the valve guide and stem, consistent with the results reported previously for the 500-h tested valves [1]. Subsequent fractography analysis showed that all of the strength limiting sites were those remnants of original surface machining grooves. On the other hand, results of valve-head strength revealed no further degradation as compared to those measured for the 500-h valve-heads (Fig. 4). So, it could be concluded that the SN235P silicon nitride valves exhibited superior resistance to the oxidation and corrosion environment of NG engine and thus revealed little or no degradation in mechanical performance and reliability under the application environment [2]. The prediction of probability of failure (POF) based on the retained strength data indicated extremely low POF that was equal or less than the valve predicted by the CARE/Life model (10^{-14}). Therefore, the probabilistic component design and life prediction methodology employed for this silicon nitride valve task was valid and successful. However. A much longer-term engine testing with full power condition will still need to be performed in the future to truly validate the probabilistic component design and life prediction methodology.

High temperature creep behavior of TiAl alloys

Studies of long-term creep behavior in air of TiAl alloys manufactured by Daido and Howmet were continued in FY2008. The purpose of this long-term tensile creep studies was to generate the database and to provide insight into the creep response and mechanisms as a function of temperature and stress level for probabilistic component life prediction. Note that the test matrix of temperature and applied stress levels employed in the present study was based on the condition that the TiAl components will experience under the engine operation conditions. Note that all of the tensile

creep tests were discontinued when the specimen fractured or the test time reached more than 6000-h but did not fail. Tensile creep results of Daido TiAl alloy showed that there was a minor effect of processing method (HIP vs. non-HIP) on the high temperature creep behavior at ≤ 700°C (Fig. 5). Also, both TiAl materials exhibited low creep exponent values (n) ranging between 2-4, independent of applied stress level. At temperatures ≥ 750°C both TiAl specimens exhibited a transition to much higher creep exponent (11-13) at applied stress level of ~ 200 MPa, suggestive of a change in creep controlling mechanisms at this higher temperature and applied stress regime. Note that the high creep exponent value of n is in general attributed to enhanced creep deformation process [3].

Much of the efforts were also placed on the generation of long-term creep database of Howmet TiAl alloy. In general, the creep data indicated that the Howmet TiAl exhibited creep rates that were 2-3 orders of magnitude higher than Daido HIP TiAl under similar test conditions, especially under high stress level regime (Fig. 6). The difference in creep response between Diado and Howmet TiAl alloy was probably due to the difference in microstructure (i.e., domain size and lamellar thickness). Also, at 650°C the Howmet TiAl exhibited a higher creep exponent valve (n~ 11-13) than that obtained for the Daido TiAl (n ~ 2-4) under the similarly applied stress range (240-390 MPa). However, the trend and values of creep exponents obtained at temperatures ≥ 700°C for both TiAl alloys were quite similar, and both exhibited a transition to a higher n valve at stress level of > 200 MPa.

References

1. H. T Lin et al, "Life Prediction of Diesel Engine Components," 2007 Annual Report for Heavy Vehicle Propulsion Materials.

2. H. T. Lin, T. P. Kirkland, A. A. Wereszczak, and M. J. Andrews, "Strength Retention of Silicon Nitride After Long-term Oil Immersion Exposure," *J. Mater. Sci.* 41, 8313-8319 (2006).

3. S. M. Wiederhorn, B. J. Hockey, and T. J. Chuang, "Creep and Creep Rupture of Structural Ceramics," pp. 555-575 in Toughening Mechanisms in Quasi-Brittle Materials, Kluwer Academic Publishers, Norwell, MA 1991.

Presentations and Publications

Presentation

1. H.-T. Lin, "Advanced Silicon Nitride Ceramics for Heavy-Duty Diesel Engine Applications," **Invited paper**, presented at the 2nd International Ceramic Congress, June 29-July4, 2008, Verona, Italy.

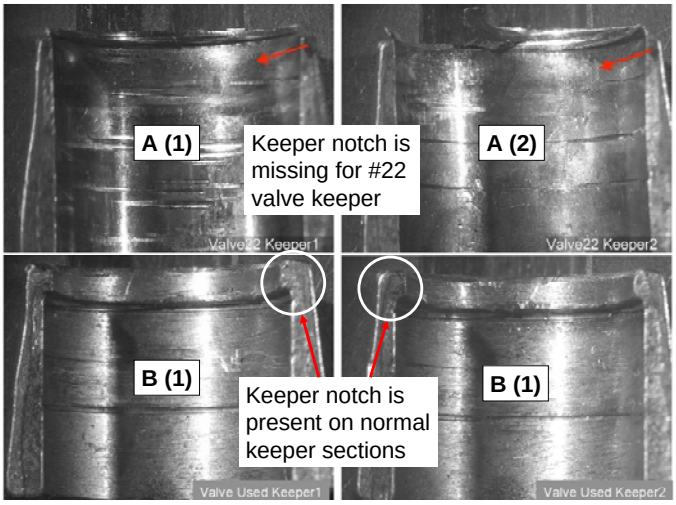

Figure 1. *Photos shows the significant wear occurred in the valve keeper used for silicon nitride valve #22 (A1 and A2). The photos of as-received steel keeper are used for comparison (B1 and B2)*

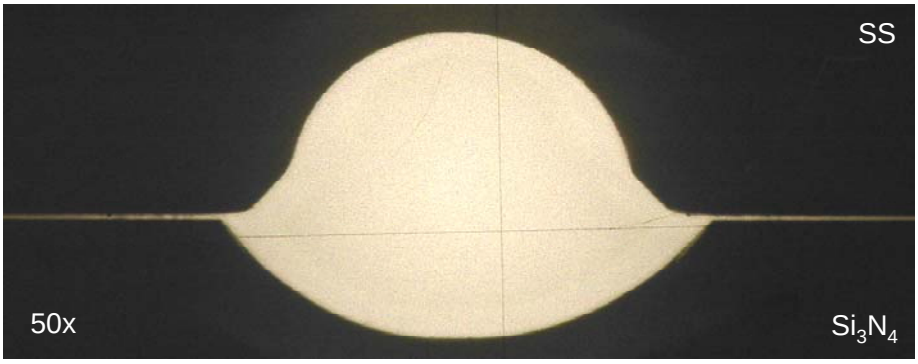

Figure 2. *Comparison of curvature between steel valve keeper and SN235P silicon nitride valve groove. There is an improper match of the curvature.*

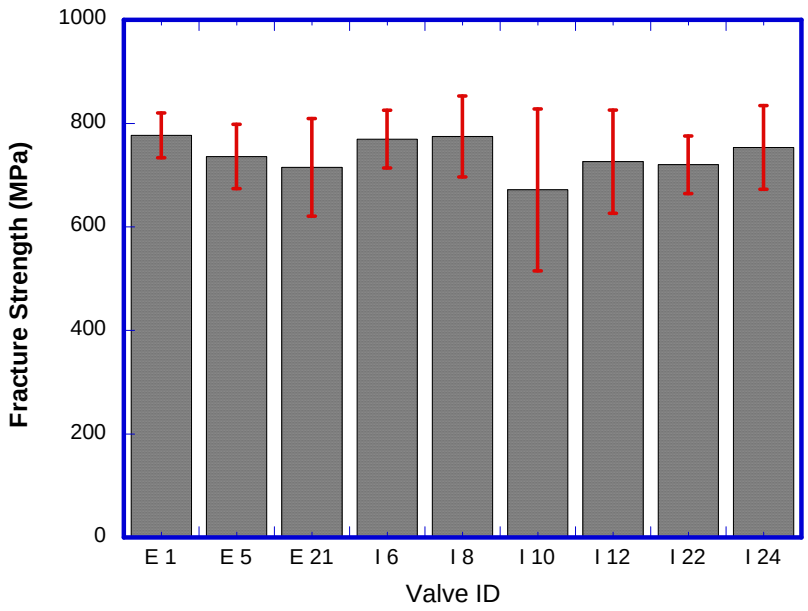

Figure 3. *Fracture strength of half-cylindrical valves of SN235P silicon nitride after 555-h engine test.*

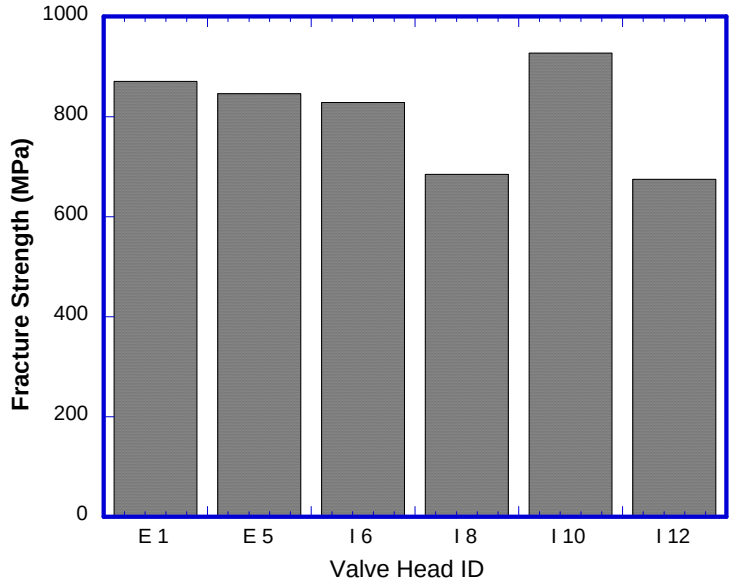

Figure 4. *Fracture strength of valve-heads of SN235P silicon nitride after 555-h engine test*

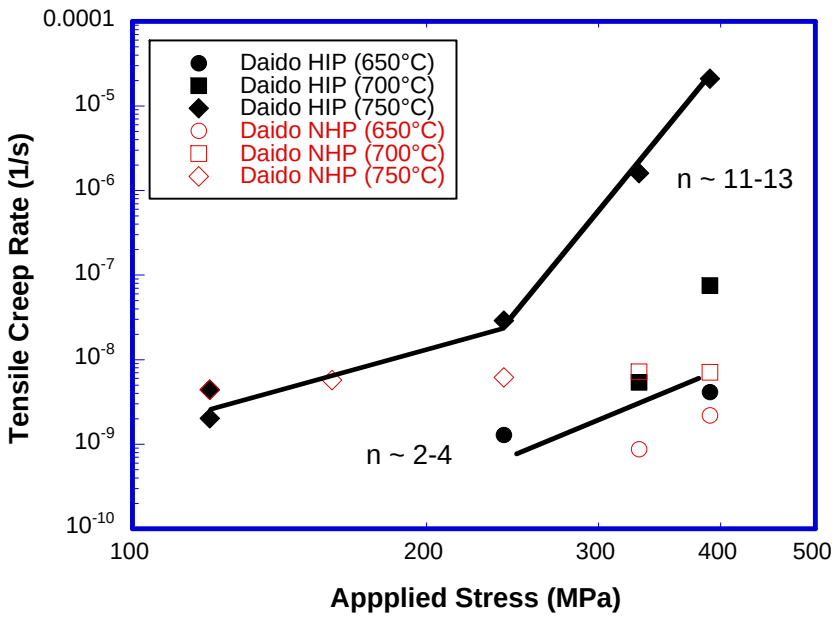

Figure 5. *Tensile creep rates versus applied stress curves of Diado TiAl alloys (HIP vs. non-HIP).*

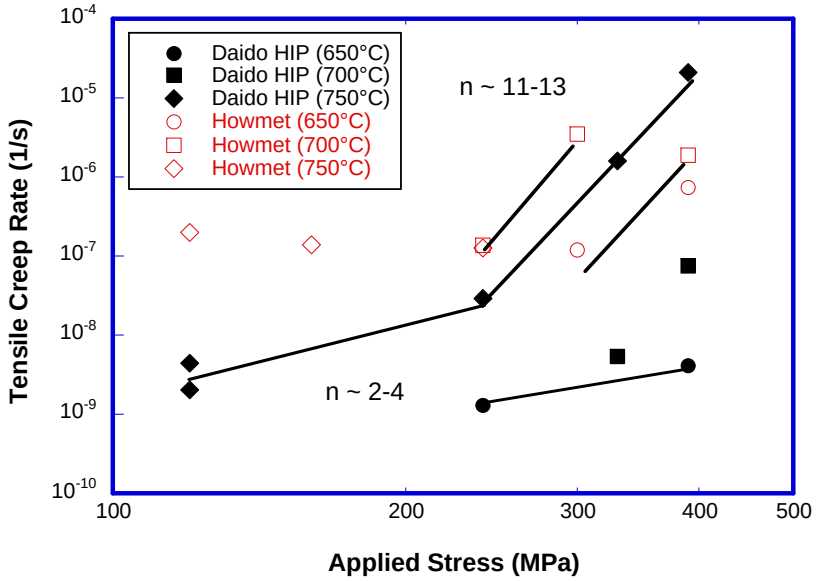

Figure 6. *Comparison of tensile creep rates versus applied stress curves between Diado HIP TiAl alloy and Howmet TiAl alloy.*

Agreement 14957 - Modeling of Thermoelectrics

A. A. Wereszczak, H. Wang,† and O. M. Jadaan§*
* *Ceramic Science and Technology Group*
† *Diffraction and Thermophysical Properties Group*
§ *University of Wisconsin-Platteville, Platteville, WI*
Oak Ridge National Laboratory
P.O. Box 2008, MS 6068, Bldg. 4515
Oak Ridge, TN 37831-6068
(865) 576-1169; fax: (865) 574-6098; e-mail: wereszczakaa@ornl.gov

DOE Technology Manager: Jerry L. Gibbs
(202) 586-1182; fax: (202) 586-1600; e-mail: Jerry.gibbs@ee.doe.gov
ORNL Technical Advisor: D. Ray Johnson
(865) 576-6832; fax: (865) 574-6098; e-mail: johnsondr@ornl.gov

Contractor: Oak Ridge National Laboratory, Oak Ridge, Tennessee
Prime Contract No.: DE-AC05-00OR22725

Objectives

- Measure needed thermomechanical and thermophysical properties of candidate thermoelectric materials (TEMs) under consideration for waste heat recovery and cooling applications in vehicular applications.
- Combine the measured data with established probabilistic reliability and design models to optimally design automotive and heavy vehicle thermoelectric devices (TEDs) for heat recovery and cooling.

Approach

- Measure elastic modulus, Poisson's ratio, strength, coefficient of thermal expansion, heat capacity, thermal conductivity as a function of temperature in candidate TEMs. Compare properties against those of mature TEMs.
- Execute finite element analysis (FEA) to model thermomechanical stresses in TEMs and TEDs.
- Execute probability design sensitivity (PDS) analysis on the TEM within an arbitrary TED, and identify and rank those material properties or dimensions that have the largest effect on reliability.

Accomplishments

- Generated property database on a mature, commercially available TEM (bismuth telluride or Bi_2Te_3)
- Modeled how changes in leg array size, leg aspect ratio, and TED confinement affect reliability.

Future Direction

- Collaborate with a manufacturer of high-temperature-capable TEMs and TEDs and contribute to the reliability improvement of their candidate TEMs.
- Develop a thermomechanical test system that will enable strength measurement of TEM specimens while a thermal gradient is concurrently imposed through the specimen thickness.

Introduction

Potential next generation thermoelectric devices (TEDs) comprised of p- and n-type materials enjoy strong interest for implementation in high temperature and oxidizing environments because their waste heat could be used to generate electricity. However, the intended thermoelectric function of these devices will only be enabled if the TED is designed to overcome the thermomechanical limitations (i.e., brittleness) that are usually inherent to these materials. A thermoelectric material (TEM) with a combination of poor strength and low thermal conductivity can readily fail in the presence of a thermal gradient thereby preventing the exploitation of the desired thermoelectrical function.

This seemingly insurmountable problem can be overcome with the combined use of established probabilistic design methods developed for brittle structural components, good thermoelastic and thermomechanical databases of the candidate TEM comprising the TED, and iteratively applied design sensitivity analysis. This project executes this process to involve TEDs.

There will be several outcomes from this work that will benefit TEM and TED developers and end-users of these potentially high temperature TEDs: mechanical reliability of prototypical TEDS will be evaluated from a structural brittle-material perspective and suggested redesigns will be identified, thermomechanical reliability of developmental TEMs will be assessed, and minimum required thermomechanical properties of hypothetical TEMs would be identified that produce desired reliability in a TED.

Results

Experimental

Several hundred test specimens of p- and n-type bismuth telluride were purchased (Marlow Industries Inc., Dallas, TX) for thermophysical, thermoelastic, and mechanical characterizations. They are shown in Fig. 1. All specimens were fabricated in either a prismatic or a plate geometry as shown in Fig. 2. Additionally, two orientation were examined to study the transverse isotropy habit of the material. The "R-Z" orientation represents a plane parallel to the axisymmetric axis and the "R-R" orientation represents the plane perpendicular to it. This thermoelectric material is mature and its testing provided a reference database that can be used to compare against properties of developmental TEMs.

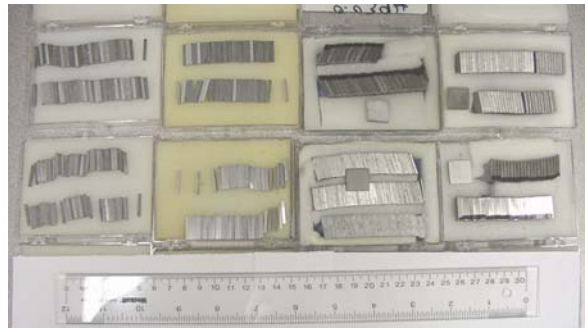

Figure 1. *A large number of Bi_2Te_3 specimens were acquired for property database generation.*

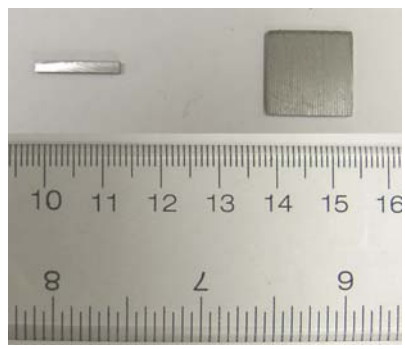

Figure 2. *Prismatic bars and square plates were used for the property measurements.*

Three-point-bending (Fig. 3) was used for the uniaxial flexure strength measurements and the results are shown in Fig. 4. Specimens were cut two different ways, but that did not have an effect on strength. The R-Z orientation was stronger than the R-R orientation for both the p- and n-type materials. The R-Z strengths for both the p- and n-types were equivalent whereas the n-type's R-R orientation was stronger than the p-type's R-R.

Ring-on-ring testing (Fig. 5) was used for the equibiaxial flexure strength measurements and those results are shown in Fig. 6. Only the p-type was measured. Polishing the specimens only had a subtle strengthening effect. Again, the R-Z orientation was stronger than the R-R.

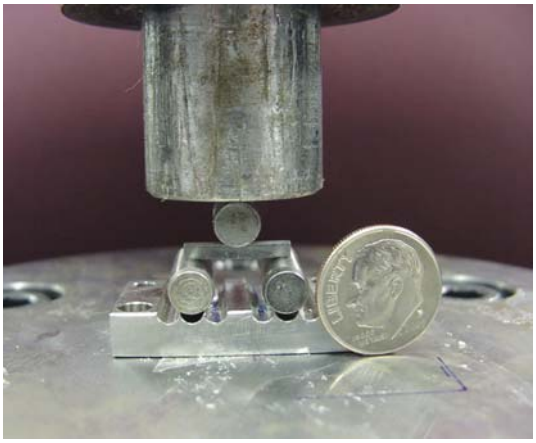

Figure 3. *Uniaxial flexure strength (3-pt-bending) testing fixture. 12.7 mm support span.*

Type	Orientation	Tension Surface	Number of Specimens	Average Max Stress (MPa)	Std Dev (MPa)
P	R - R	As Mach	15	38.2	8.5
P	R - R	Cut	12	38.6	3.1
P	R - Z	As Mach	16	80.9	5.4
P	R - Z	Cut	17	79.4	4.1
N	R - R	As Mach	16	45.7	5.2
N	R - R	Cut	17	45.0	3.8
N	R - Z	As Mach	17	79.5	8.0
N	R - Z	Cut	17	81.1	8.1

Figure 4. *Uniaxial flexure strength results as a function of type, orientation, and surface condition.*

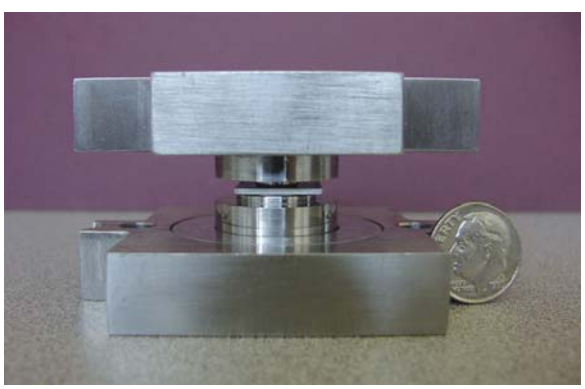

Figure 5. *Biaxial flexure strength (ring-on-ring) testing fixture. 12.7 and 6.35 mm support and loading ring diameters.*

Type	Orientation	Surface Condition	Number of Specimens	Average Failure Stress (MPa)	Std Dev (MPa)
P	R - R	As-Ground	25	29.9	2.2
P	R - Z	As-Ground	25	43.5	3.1
P	R - R	Polished	11	31.9	2.1
P	R - Z	Polished	15	47.6	4.6

Figure 6. *Biaxial flexure strength results as a function of orientation and surface condition for p-type. n-type not evaluated in this matrix.*

Resonant ultrasound spectroscopy was used to measure the elastic properties of the p-type as a function of temperature and orientation using the specimen plate geometry shown in Fig. 2. Their results are shown in Fig. 7. The elastic moduli and Poisson's ratios are similar up to 250°C. The room temperature elastic modulus was measured using the prismatic geometry shown in Fig. 2 for both the p- and n-type materials. Their R-Z elastic properties were equivalent, and the R-R elastic properties too, though the elastic modulus of their R-Z orientation was slightly higher than the R-R orientation for both types (as illustrated in Fig. 7 for the p-type).

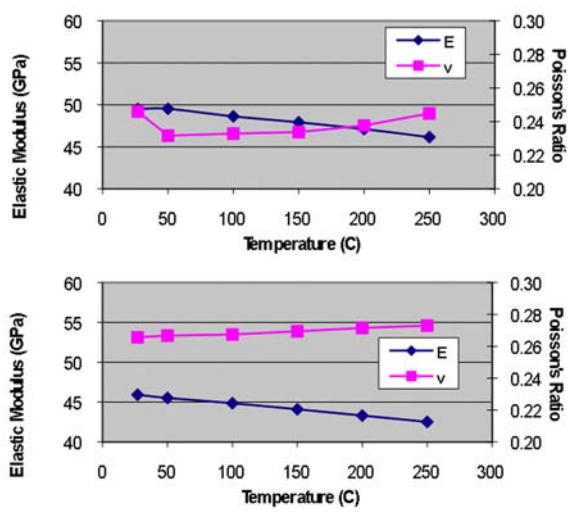

Figure 7. *Elastic properties as a function of temperature for p-type R-Z (top) and R-R (bottom) orientations.*

The coefficient of thermal expansions (CTEs) for both the p- and n-types and R-Z and R-R orientations were measured using a dual-rod dilatometer, and their average values are shown in Fig. 8. The average values were determined up through 240°C. The R-R orientation had a ~25% higher CTE than the R-Z orientation for both types.

The heat capacities and thermal conductivities of both types were measured as a function of temperature and their results are shown in Figs. 9-11. The p-type's values are slightly higher than the n-type.

Type	Orientation	Specimen Number	Average CTE up to 240°C (ppm/°C)
P	R - R	1	18.9
P	R - R	2	18.7
P	R - R	3	18.8
P	R - Z	1	14.3
P	R - Z	2	13.9
P	R - Z	3	13.8
N	R - R	1	17.1
N	R - R	2	17.3
N	R - R	3	17.3
N	R - Z	1	14.7
N	R - Z	2	14.4
N	R - Z	3	14.3

Figure 8. *Coefficient of thermal expansion (CTE) results as a function of type and orientation.*

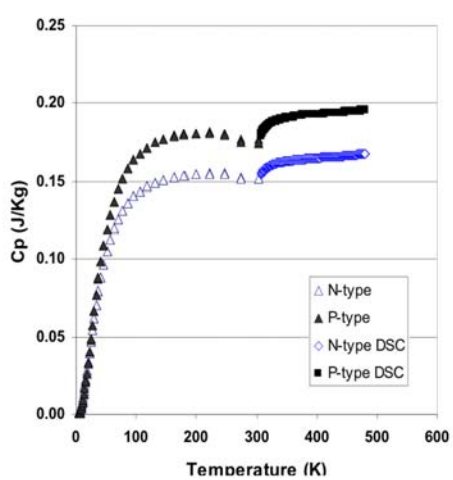

Figure 9. *Heat capacity as a function of type and temperature.*

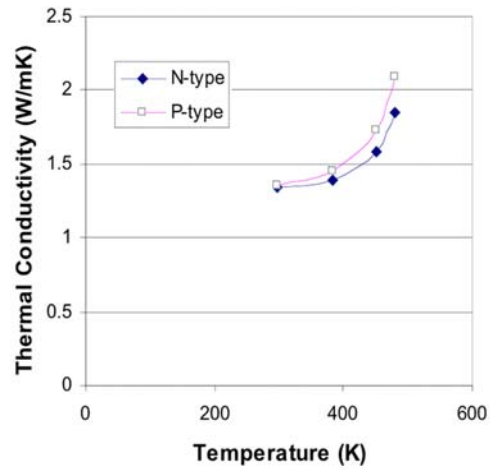

Figure 10. *Thermal conductivity as a function of type and temperature.*

	N-type	P-type
Thermal Diffusivity (cm^2/sec)	0.011	0.011
Thickness (mm)	1.024	1.023
Diameter (mm)	9.530	9.488
Weight (g)	0.561	0.479
Density (g/cm^3)	7.683	6.630
Cp (J/gK)	0.159	0.186
Thermal Conductivity (W/mK)	1.344	1.356

Figure 11. *Room temperature thermophysical properties.*

Modeling

Two primary modeling efforts were conducted, and they involved the consideration of how/if the number of TEM legs in a TED affects reliability, and how confinement of the TED could affect the stress state.

Three leg arrays were analyzed and were 6x6, 8x8, and 10x10, and are shown in Fig. 12. Leg cross-section dimensions were 3x3mm, and 3mm and 6mm heights were considered. An example of their modeling in a TED is shown in Fig. 13, and an imposed thermal gradient is shown in Fig. 14. It was found that reducing the size of the array did not lessen the magnitude of the maximum First Principal stresses in the legs; however, based on purely on the

numbers of legs per array, the probability of survival would higher as the array size decreased.

As was expected, confinement can affect probability of survival. Two situations were considered: an unconfined (Fig. 15) and a confined scenario (Fig. 16). Stiffly bonding the hot-face of a TED will serve to decrease the probability of survival because it ultimately increases the First Principal stresses in the legs.

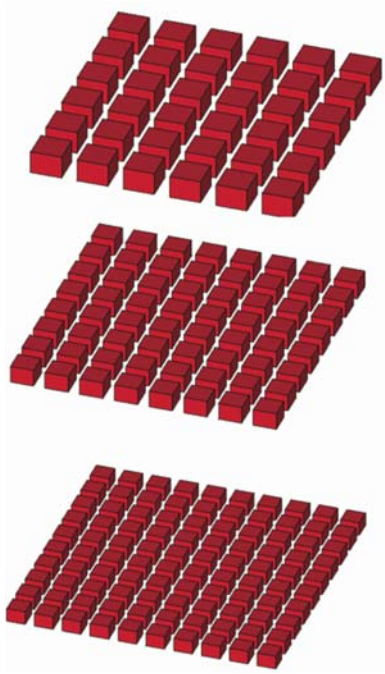

Figure 12. *Three square leg arrays were considered: 6x6, 8x8, and 10x10.*

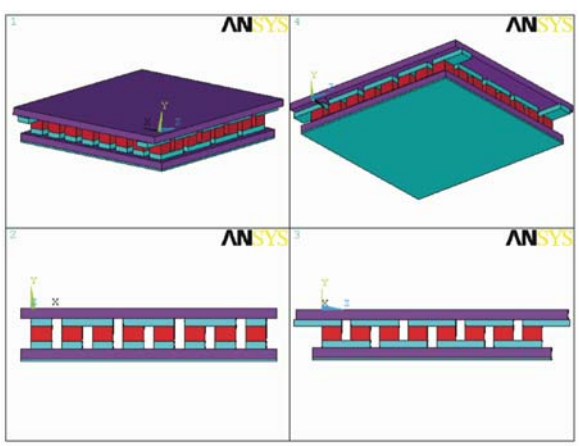

Figure 13. *Example of a modeled TED with an 8x8 leg array.*

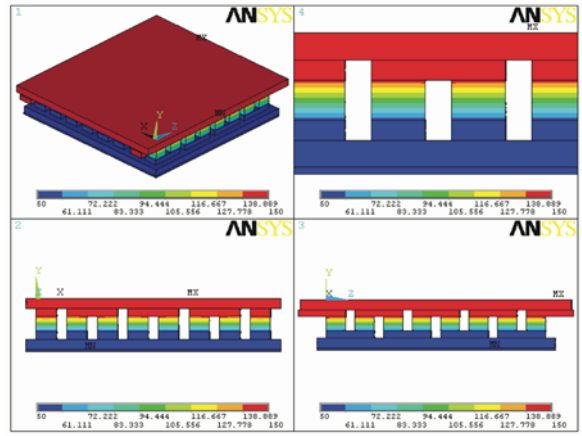

Figure 14. *Thermal gradient across a TED with an 8x8 leg array.*

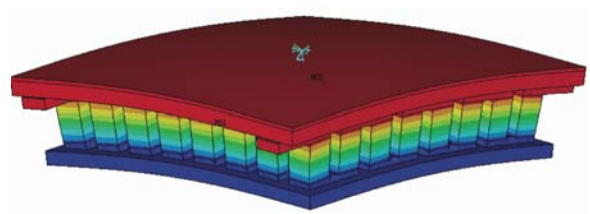

Figure 15. *Unconfined TED showing deformations occurring as a consequence of the Fig. 13 imposed thermal gradient.*

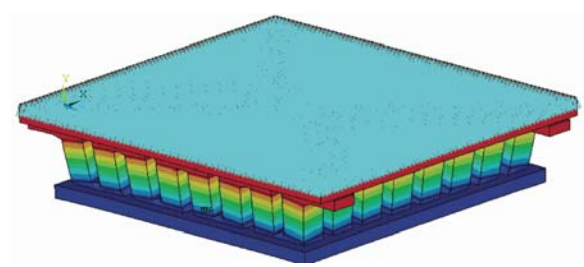

Figure 16. *Hot face-confined (shown at top) TED showing deformations occurring as a consequence of the Fig. 13 imposed thermal gradient.*

Conclusions

Specific material properties and geometrical descriptors can greatly affect tensile stress development in a TE device. These analyses provide guidance on which paths can be pursued to mitigate them.

Agreement 15529 - Erosion of Materials in Nanofluids*

*(*This project is jointly funded by Propulsion Materials and Heavy Vehicle Systems Optimization)*

Principal Investigators: J. L. Routbort and D. Singh,

Argonne National Laboratory

9700 S. Cass Avenue, Argonne, IL 60439-4838

(630) 252-5065; fax: (630) 252-5568; e-mail: routbort@anl.gov

DOE Technology Manager: Jerry L. Gibbs

(202) 586-1182; fax: (202) 586-1600; e-mail: jerry.gibbs@ee.doe.gov

---

Contractor: UChicago Argonne LLC

Contract No.: DE AC03 06CH11357

Objective

- Determine if the use of fluids containing a variety of nanoparticles result in erosive damage to radiator materials and coolant pumps.
- If damage occurs, then develop models to predict the erosive damage.

Approach

- Develop an experimental apparatus to measure erosive loss.
- Conduct experiments to study erosive damage of fluids containing various types and sizes of nanoparticles on typical radiator materials.
- Develop methods to characterize nanofluids and analyze erosion results.

Accomplishments

- Little erosion damage to a typical radiator material, aluminum Al3003, was observed in experiments performed using CuO nanoparticles in ethylene glycol having impact angles of 30 and 90° and velocities up to 10m/s for impact for a total time of 3620 hours. Particle concentration varied between 0.1 and 0.85 vol %.
- Utilized small-angle x-ray scattering technique to measure nanoparticle size, distribution, and shape.
- Determined that polymeric gears are degraded by a SiC/water nanofluid
- Modified erosion apparatus to avoid excessive wear in polymeric gears
- Determined that a SiC/water nanofluid does not degrade aluminum Al3003
- Designed apparatus to measure wear in an automotive water pump

Future Direction

- Erosion of typical radiator materials using fluids containing a variety of well-characterized nanoparticles will be measured, varying the angle, size of the nanoparticles, impact velocity, nanoparticle volume percent, and temperature.
- If erosion occurs, a predictive model will be developed.
- Build apparatus to measure wear in an automotive pump.
- Perform erosion tests using an actual automotive coolant pump
- Measure the pump power of nanofluids and compare to base fluids

---

Forward

Efforts have shifted away from the in-house production of nanofluids, to development of advanced characterization techniques and establishment of working relationships between companies that produce nanofluids. As commercial nanofluids become available, ANL will measure their thermal properties. Fluids that show promise from a heat transfer perspective will then be characterized by measuring the viscosity, thermal conductivity, and heat transfer coefficients while particle sizes will be measured by small-angle X-ray scattering (SAXS) and Dynamic Laser Scattering (DLS). Finally, liquid erosion tests will be performed to determine if the nanofluid will cause deleterious damage to radiator materials.

Introduction

Many industrial technologies face the challenge of thermal management. With ever-increasing thermal loads due to trends toward greater power output for engines and exhaust gas recirculation for diesel engines, cooling is a crucial issue in transportation. The conventional approach for increasing cooling rates is use of extended surfaces such as fins and microchannels. Reducing radiator size will reduce the frontal area and hence the aerodynamic drag. However, current radiator designs have already stretched these approachs to their limits. Therefore, an urgent need exists for new and innovative concepts to achieve ultra-high-performance cooling. Nanofluids seem to show enormous potentials as a coolant for radiators. Literature has many examples of increased thermal conductivity of fluids by the addition of nanoparticles (see review by Yu, et al. [1]. Enhanced thermal conductivity could lead to enhanced heat transfer. A CFD calculation of a Cummins 500 hp diesel engine using an ideal nanofluid as coolant has shown that the radiator size could be reduced 5% [2], reducing weight and size, and hence aerodynamic drag.

In order for the enhanced thermal conductivity to be utilized it must be shown that liquid erosion of typical radiator materials will be tolerable. If nanofluids result in excessive erosive wear, they cannot be used. Hence, the Vehicle Technologies program funds an investigation on liquid erosion of radiator materials using nanofluids.

Results and Discussion of Erosion

It important to understand the fluid flow and model the interaction of the fluid jet/target interactions in the liquid erosion apparatus. This was modeled by Tanju Sofu using a STAR-CD for 90° impacts. The results (Fig. 1) are presented as the near-wall velocity as a function of distance from the center of the target at various velocities. The results agree very well with the actual imprint of the jet impinging the target. The picture shown in Fig. 2 was obtained by painting the surface of the target. One observes the stagnation point and that the maximum damage occurs about 5 mm from the center in accord with the maximum wall velocity, as predicted by the CFD calculation.

SiC is a very promising nanoparticle. It will not oxidize and has a relatively high thermal conductivity, over 5 times greater than CuO. SiC nanoparticles in water were supplied to ANL by Saint-Gobain with 4.0 and 7.3 vol % concentrations. The SiC particles were not a uniform size and contained two peaks in the DLS: one centered at 31 nm and the other at 179 nm. The DLS results are shown in Fig. 3. The results are in very good agreement with the SAXS results.

Damage is likely to be more severe as the kinetic energy of the impacting particle is increased. Hence one would expect that at the same velocity and mean diameters, the SiC (density ≈ 3.2 g/cc) nanofluid would result in more erosion than resulted from the CuO (density ≈ 2.7 g/cc) [3]. Additionally SiC is considerably harder than CuO and the concentration of SiC (2 vol %) was higher than that of the CuO in ethylene

glycol/water (≈1 vol %). Hence all of these factors would indicate that the water containing SiC nanoparticles would be a severe test of damage caused by the nanofluid and would expected to result in more erosion.

Recall that the CuO/ethylene glycol nanofluid did not cause any damage to the target for velocities between 8 and 10.5 m/s at 30, 50, and 90° impact angles for tests lasting between 200-300 h. Damage to the polymeric gears was restricted to ≤ 0.5% weight loss at 10 m/s for 500 h [3].

By comparison the 2 vol % SiC nanoparticles in water resulted in ≈ 4% weight loss to the polymeric gears after 700 h of testing at 5 m/s. A photograph of the erosion damage is shown in Fig. 4. The fact that the polymeric gears were eroded resulted in an impact velocity that continually decreased over time as the pump gears became worn. Hence a peristaltic pump was used to replace the gear pump. Some problems were encountered with fatigue of the rubber tubing resulting in cracks that required moving the rubber hose 10-15 cm each day.

However, after 750 h of testing the 2 vol % SiC/water nanofluid at 8 m/s and at an impact angle of 30°, there was no erosion damage to the aluminum 3003 target. This is most encouraging from an engineering viewpoint, but disappointing from a modeling point of view.

The above observation was obtained at one condition and does not represent the most severe conditions. Hence, it would be premature to conclude that nanofluids will cause no damage in cooling systems.

Issues & Future Direction

It is recognized that the erosion tests conducted so far were designed to accurately and reproducibly control the important erosion parameters, namely velocities, impact angles, and particle size, material, concentration and the fluid. However, conditions in an actual pump are quite different. Hence we have redesigned the erosion apparatus to serve not only to supply fluid under controlled conditions, but to determine if nanofluids will damage an actual automotive radiator pump. The new system will be calibrated during the first quarter of FY09. It consists of the same chamber with the target as used before, and the same motor, controller, a magnetic-type flow meter, and a 5-liter reservoir, but instead of a gear pump, we have obtained a water pump used in automotive applications. The aluminum impellar of the pump can be removed periodically to measure its weight loss and to inspect the damage. Hence we will accumulate not only engineering data on the erosion of the pump, but also more controlled data on the effect of nanofluids on the erosion of the target that is vital to developing predictive models. Additionally, we will obtain data on clogging of piping and pumps resulting from heavily loaded nanofluids.

The new apparatus will be used to investigate ethylene glycol fluids containing different nanoparticles and different vol % nanoparticle loadings. We intend to test a 4 vol % SiC nanofluid and as well as EG/water containing intermetallic nanoparticles. This setup will allow comparison of the pump power required for the nanofluids compared to the base fluid.

Conclusions

No severe erosion damage of aluminum 3003 has been observed to date. However, the nanofluids tested thus far were not the extremes. We have designed and are building an apparatus that will allow not only continuation of the well-controlled tests designed to develop the data required to model erosive damage, but will closely replicate "real world" conditions in an automotive water pump.

References

1. W. Yu, D. M. France, J. Routbort, S.U.S. Choi, "Review and Comparison of Nanofluid thermal Conductivity and Heat Transfer Enhancements, Heat Transfer Engineering, **29**, 432-460 (2008).

2. S. K. Saripella, W. Yu, J. L. Routbort, D. M. France, and Rizwan-uddin, " Effects of Nanofluid Coolant in a Class 8 Truck Engine, SAE Technical Paper 2007-01-21413.

3. Annual Report (FY07), Propulsion Materials, pgs. 152-157.

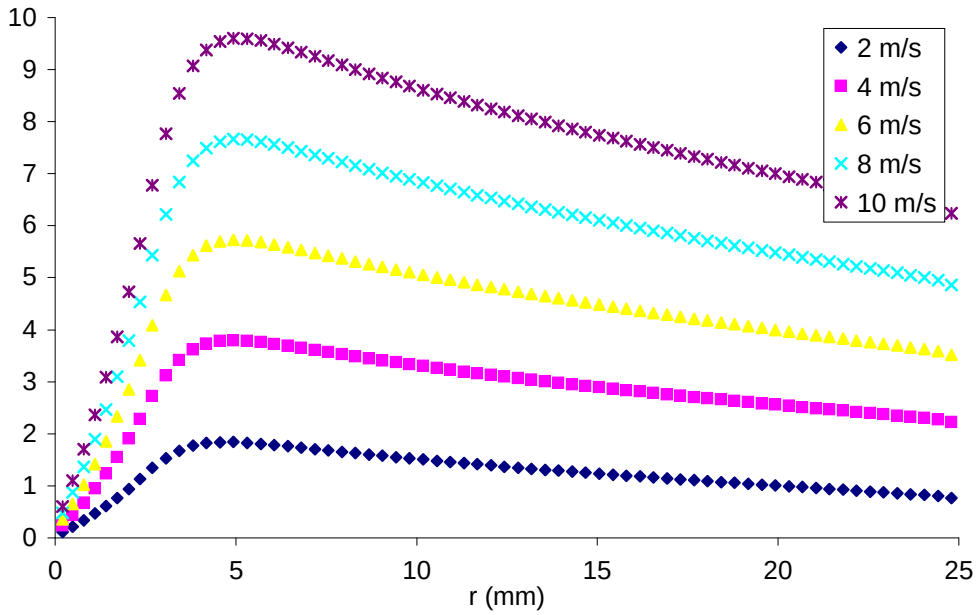

Figure 1. Result of a STAR-CD calculation showing the near-wall speed as a function of position from the center of the target for various velocities.

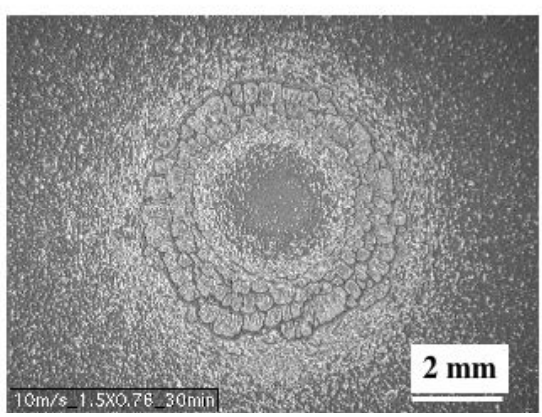

Figure 2. Imprint pattern of water jet impacting a painted aluminum 3003 target.

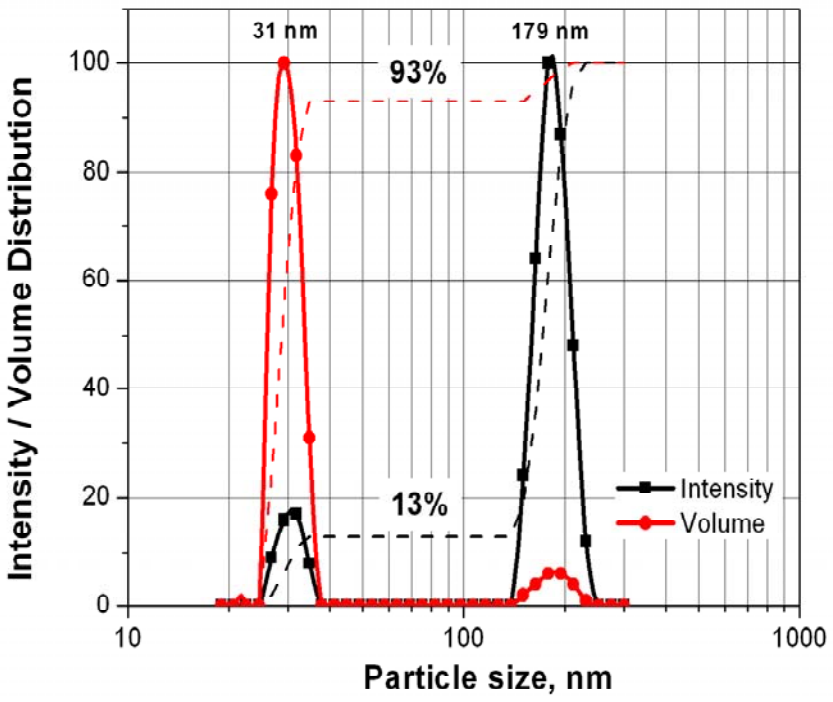

Figure 3. Dynamic Laser Scattering results on SiC/water nanofluid.

Figure 4. Photograph of the erosion of the polymeric gears after 700 hrs of testing with water containing 2 vol. % SiC nanoparticles.

Agreement 16308 – Science Based Approach to Thermoelectric Materials

D.J. Singh
Materials Theory Group
Oak Ridge National Laboratory
P.O. Box 2008, MS 6114, Bldg. 4500S
Oak Ridge, TN 37831-6114
(865) 241-1944; fax: (865) 574-7659; e-mail: singhdj@ornl.gov

DOE Technology Manager: Jerry L. Gibbs
(202) 586-1182; fax: (202) 586-1600; e-mail: Jerry.gibbs@ee.doe.gov
ORNL Technical Advisor: D. Ray Johnson
(865) 576-6832; fax: (865) 574-6098; e-mail: johnsondr@ornl.gov

Contractor: Oak Ridge National Laboratory, Oak Ridge, Tennessee
Prime Contract No.: DE-AC05-00OR22725

Objectives

- Find ways to optimize existing thermoelectric materials and discover new families of high performance thermoelectrics for waste heat recovery applications using modern science based materials design strategies.
- Find low cost materials suitable for application in vehicles with high thermoelectric figures of merit.

Approach

- First principles calculations based on quantum mechanics are used to calculate electronic structure and thermoelectric properties of materials.
- Boltzmann transport equations are solved to obtain electrical transport properties.
- Vibrational properties are obtained using linear response and mechanisms for thermal conductivity reduction are assessed.

Accomplishments

- Performed first principles calculations of transport and other properties of potential thermoelectric materials.
- Predicted thermoelectric properties of moderately hole doped $YCuO_2$, which we find to be a potentially low cost thermoelectric with good performance.
- Found strong coupling between optical and acoustic phonon branches in PbTe providing a mechanism for low thermal conductivity in that material.

Future Direction

- Identify new oxide and chalcogenide thermoelectric compositions suitable for vehicle applications.
- Calculate doping level dependence of thermoelectric properties to guide optimization.

Introduction

The use of thermoelectric devices to convert waste heat in vehicle exhaust to electricity offers potentially significant energy savings. Among the requirements for the effective use of such devices is the availability of high performance thermoelectric materials, with low cost and other properties needed for application in vehicles. The dual requirement for both high performance and low cost has constrained thermoelectric applications in the automotive industry, although thermoelectrics have been effectively inserted in the context of seat cooling.

We are therefore developing improved materials using a science-based approach. In particular, we are using materials design strategies based on first principles calculations of electronic, vibrational and transport properties to identify potentially low cost, high performance thermoelectric materials suitable for application in vehicles. We are also calculating properties of existing materials as a function of doping and other parameters to obtain information needed for optimization of these materials. The emphasis is on the thermoelectric figure of merit, ZT at temperatures relevant to waste heat recovery, as well as materials properties of importance in engineering thermoelectric modules, for example anisotropy and mechanical properties. High $ZT=\sigma S^2T/\kappa$ requires a combination of high thermopower (S), good electrical conductivity (σ), and low thermal conductivity (κ). Our calculations are being done using state-of-the-art computational tools such as the linearized augmented planewave method [1] and the BoltzTraP code [2].

Results

(1) Oxide Thermoelectrics:

We completed work on the origin of the magnetic field dependence of the thermopower in Na_xCoO_2. This allowed us to explain the reduction in the Seebeck coefficient which was associated with spin-entropy and to establish that the thermopower can be quantitatively predicted based only results from first principles calculations, specifically the band structure and Boltzmann transport theory [3]. The understanding of the properties of Na_xCoO_2 from these results is that its thermoelectric performance is determined by the narrow d band electronic structure and the fact that it can be doped with a high density of carriers. Practical difficulties with its application are the high cost and the strong anisotropy of its thermoelectric and mechanical properties. However, based on the fact that the properties of Na_xCoO_2 can be quantitatively determined, we can use the lessons learned from these results to find other more favorable compositions. Accordingly, we started looking for alternate materials that would also have narrow d bands but with potentially lower cost and less anisotropy. Since the O-Co-O bond angles are found to play a key role in Na_xCoO_2 we focused on crystal structures with a similar topology [4-6].

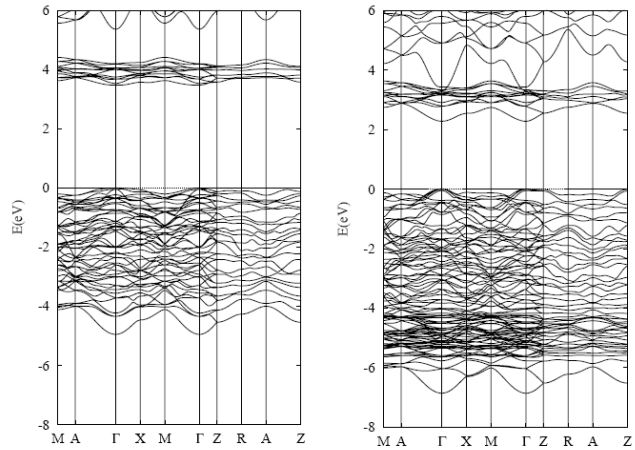

Figure 1: *Calculated band structure of ordered Mg_2TiO_4 (left) and Zn_2TiO_4 (right). Note the narrow d-bands at +2 to +4 eV.*

Based on these considerations and the fact that the mixed valence of Ti often leads to conductivity in titanates, we selected some spinel-based titanates as candidates. These are Mg_2TiO_4 and Zn_2TiO_4, which according to literature order in a tetragonal structure when appropriately annealed. Furthermore, while the Ti has valence IV in these compounds, Ti III is also a common valence, and so it seems reasonable to suppose that these compounds could be effectively doped either by excess Ti or by O vacancies to produce an n-type oxide thermoelectric. We did electronic structure calculations for those materials, and find that indeed they have narrow d bands with charge transfer type band gaps. This is favorable for high thermopower, but the conductivity that may be obtained needs to be established.

As mentioned, our focus is to identify oxide materials that offer a combination of high thermoelectric performance and applicability to vehicular applications. A key consideration that is special for vehicles is that the materials must be at least potentially inexpensive. This constrains the elements that can be used in the thermoelectric materials. In particular, the high cobalt concentration in thermoelectric Na_xCoO_2 is undesirable. We have therefore been screening other oxides with compositions based on lower cost elements using bonding topology as a screen since this was identified in our prior work as underlying the narrow bands of Na_xCoO_2. Based on this, delafossite $YCuO_2$ was identified as a promising candidate material and calculations were done to screen it for thermoelectric performance. This composition is particularly favorable based on our results.

We calculated the band structure and thermopower of $YCuO_2$ as a function of doping and temperature as

well as various transport functions related to conductivity. The band structure as obtained with the linearized augmented planewave method and thermopower are shown in the figure. These show that not only is $YCuO_2$ a potentially low cost material, but that it also has a very high thermopower and is much more isotropic than Na_xCoO_2. In fact, the calculated thermopowers as obtained from the electronic structure using Boltzmann transport theory are clearly superior to those of Na_xCoO_2 at temperatures of relevance for vehicular applications. Furthermore, the more isotropic transport properties of $YCuO_2$ relative to Na_xCoO_2 are important because this result implies that inexpensive ceramic, and possibly sol-gel processing could be used for this material, while much more expensive single crystal and textured ceramic processing is thought to be needed for Na_xCoO_2.

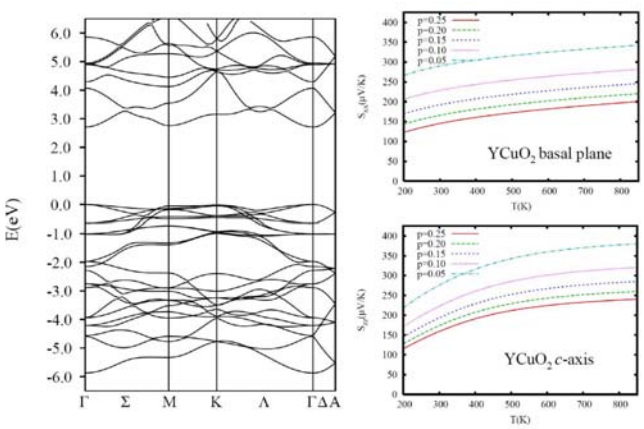

Figure 2: *Calculated band structure (left) and thermopower (right) for delafossite structure $YCuO_2$. Note the very high thermopowers found in the temperature range of relevance for vehicle waste heart recovery. Note also that the basal plane and c-axis thermopowers are both high.*

We are currently studying ways of controlling doping in $YCuO_2$. The electronic structure suggests a number of doping strategies, perhaps the most likely of which is to use excess Cu. In any case, the structure of the valence bands, which are primarily derived from copper states, implies that high conductivity and high power factors are likely.

It will be very desirable to find an electron doped material that can be used in conjunction with hole doped $YCuO_2$ assuming that this delafossite phase is successfully synthesized in a form that shows high figure of merit. One approach will be to continue investigations of narrow band oxides searching for high thermopower systems.

(2) Non-Oxide Materials:

La_3Te_4 is a known high *ZT* thermoelectric that is under investigation for power generation. However, little is known about its electronic structure or the origin of its high power factor or the doping dependence. It is known, however, that the material can be synthesized over a wide stoichiometry range from La_3Te_4 to La_2Te_3 while retaining the same structure.

We performed a series of electronic structure and Boltzmann transport calculations to assess whether this material can have high *ZT* at temperatures important for waste heat recovery. One interesting feature of this system is that similar phases can be made with a variety of rare earths, which suggests that there is room for further optimization via rare earth alloying.

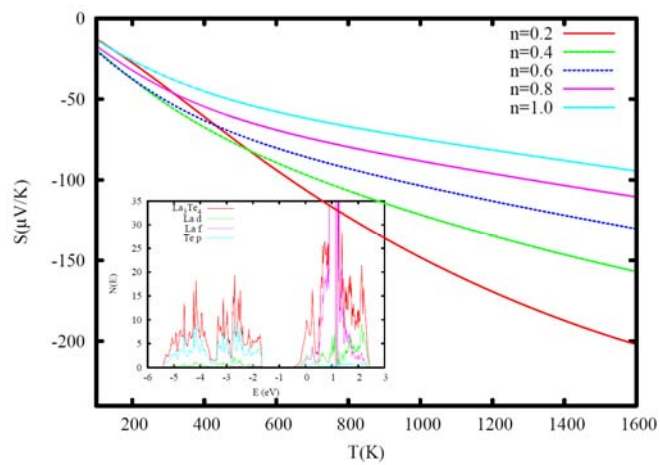

Figure 3: *Calculated thermopower as a function of temperature for La-Te at various doping levels.*

One material of practical interest for vehicular waste heat recovery is PbTe. This material has been used in prototype generators on vehicles. However, little is known about the vibrational properties of PbTe, and in particular there have been no reported first principles calculations of its phonon dispersions. Based on this, we performed detailed first principles calculations of its vibrational properties. Understanding the very low thermal conductivity of materials related to PbTe is a long-standing challenge. In particular, this material has only two atoms per unit cell, no obvious rattling ion, and a highly symmetric structure. Nonetheless, when nanostructured, it can display exceedingly low thermal conductivity. We found that there is a zone center polar soft mode (see figure), indicative of nearness to ferroelectricity. Significantly, we find that the soft mode is very anharmonic and is strongly coupled to strain and to the heat carrying longitudinal acoustic vibrational modes.

This partly explains why nanostructured PbTe based materials, such as the "LAST" phases are such effective thermoelectrics. Besides providing a framework for understanding the properties of PbTe, this result shows that the vibrational properties are strongly dependent on strain. This suggests that besides nanostructuring, materials modifications that induce local strains can also be used to control the properties of PbTe based materials.

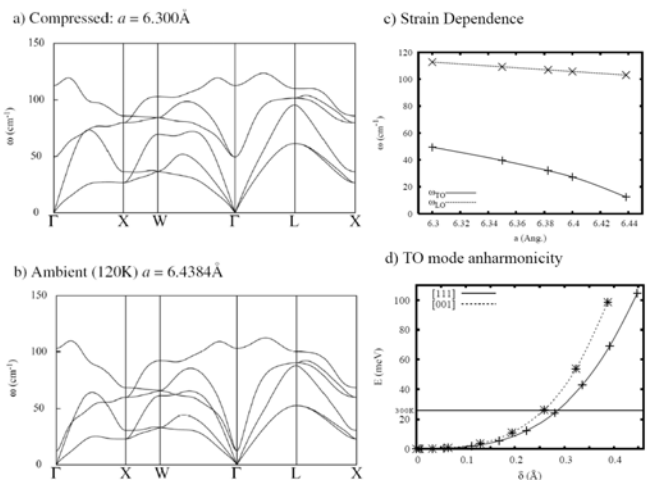

Figure 4: *Calculated phonon dispersions of PbTe (this is the momentum dependent vibrational spectrum of a solid) at two lattice parameters (a,b), dependence of the zone center optic mode frequencies on compressive strain (c) and transverse optic mode anharmonicity (d). The results show strong anharmonic coupling between the soft optic mode and the heat carrying longitudinal acoustic modes*.

Considering our results for the volume dependence of the transverse optic modes, it may be expected that local strain variations, e.g. due to variations in chemical composition or internal interfaces at the level of +/- 1% would be sufficient to shift the minimum of the transverse branch over a large part of the acoustic frequency range and may therefore lead to a substantial change in thermal conductivity. This level of strain variation may be quite realizable in nanostructured materials, since it is within the range than can normally be obtained via epitaxial stabilization in e.g. thin films.

Conclusions

New insights into thermoelectric materials performance have emerged from density functional calculations in conjunction with transport theory. Promising new potentially low cost thermoelectrics, especially $YCuO_2$ have been identified, and a mechanism for thermal conductivity reduction in PbTe has been elucidated.

References

[1] D.J. Singh, "Planewaves, Pseudopotentials and the LAPW Method, 2nd Edition", Springer, Berlin (2006).
[2]G.K.H. Madsen and D.J. Singh, "BoltzTraP: A code for calculating band-structure dependent quantities", Computer Physics Communications **175**, 67 (2006).
[3] H.J. Xiang and D.J. Singh, "Suppression of thermopower of Na_xCoO_2 by an external magnetic field", Physical Review B **76**, 195111 (2007).
[4] D.J. Singh and I. Terasaki, "Nanostructuring and more", Nature Materials **7**, 616 (2008).
[5] D.J. Singh, "Oxide thermoelectrics", Materials Research Society Symposium Proceedings, **1044**, U02-05 (2008).
[6] D.J. Singh, "Band structure and thermopower of doped $YCuO_2$", Physical Review B **77**, 205126 (2008).
[7] J. An, A. Subedi and D.J. Singh, "Ab initio phonon dispersions for PbTe", Solid State Communications **148**, 417 (2008).

Agreement 16309 – Carbon-based Thermoelectrics

Principal Investigators: D.M Gruen, D. Singh, and J. L. Routbort; coworkers: Paola Bruno and Ming Xie

Argonne National Laboratory
9700 S. Cass Avenue, Argonne, IL 60439-4838
(630) 252-5065; fax: (630) 252-5568; e-mail: dmgruen@anl.gov, dsingh@anl.gov, routbort@anl.gov

DOE Technology Manager: Jerry L. Gibbs
(202) 586-1182; fax: (202) 586-1600; e-mail: jerry.gibbs@ee.doe.gov

Contractor: UChicago Argonne LLC
Contract No.: DE AC03 06CH11357

Objective

- Develop a high-temperature, high-ZT thermoelectric

Approach

- Decouple the Seebeck coefficient from the electrical and thermal conductivity to obtain the highest ZT by using nanocrystalline materials based on B-doped diamond, or other forms of carbon (nanocarbon ensembles, NCE) so that by designing the microstructure one can increase the electrical conductivity and Seebeck coefficient while lowering the thermal conductivity

Accomplishments

- Designed and constructed an apparatus to simultaneously measure Seebeck coefficient and the electrical conductivity to 1200°C
- Produced rigid compacts using nano-B_4C-doped and dispersed ultrananocrystalline (UNDC) diamond and measured Seebeck coefficient and electrical conductivity
- Demonstrated that NCEs are stable to 1400°C and that heat treatment and adding B_4C produces a power factor that increases between 30 and 40 times more than the undoped UNDC. Power factor increases with temperature to at least 1000°C

Future Direction

- Measure thermal conductivity of the most promising NCEs
- Continue to concentrate on fabrication, doping, heat treatment to produce higher Seebeck coefficients and electrical conductivities

Introduction

This project has made remarkable progress since it has been fully funded for only one year. The idea to decouple Seebeck coefficient, electrical, and thermal conductivities by using nanocrystalline forms of carbon in bulk materials is unique. It has the potential of producing a high-temperature, high ZT thermoelectric that could replace conventional thermoelectrics made from scarce and expensive materials by a very abundant material, carbon that is environmentally benign, non-toxic, and inexpensive. Thermal efficiencies of 40% are only achievable with ZT=5 at a temperature gradient of 1000°C. This means that the thermoelectric must be stable for long periods to 1400K. No conventional thermoelectric can achieve this.

Experimental

Sample Preparation and Characterization

Nanographite (NG, 30nm particle size) powders either pure UNCD or mechanically mixed with 5 wt % of nano boron carbide (B_4C, 50nm particle size) were placed in 20x10x5mm HOPG graphite crucibles and after an initial compaction step treated with methane gas in a quartz vessel heated in several intervals from ambient temperatures to 1200K in a tube furnace [1]. The contents of the crucibles gained between 70 and 100% in weight with the greatest change occurring between 950 and 1050K. For UNCD, NG and their mixture with B_4C this procedure resulted in the formation of mechanically rigid compacts with densities of 1.5-1.7g/cm^3. Some samples were heat treated at 1400°C in flowing 96% argon/4% hydrogen gas and some of those were further heat treated to 2200°C in flowing argon. Samples were characterized by SEM, Raman, and XRD, but those results are too extensive to report here and will be presented in a paper that is under preparation.

Measurements

The Seebeck coefficient and the dc electrical conductivity were measured using an apparatus based on a well-established design [2]. It consists of a 1500°C, single-zone tube (mullite, 4.4 mm inside diameter) furnace and controller, a Keithley 2700 Multimeter/Data Acquisition System, and a Keithley 6220 Current Source, all controlled by a PC using Labview. The ends of the tube were water cooled and sealed with end caps that allowed fittings for thermocouples and gas inlet/outlets.

A schematic of the alumina sample holder made from a closed-end tube that fit into the larger outer tube is shown in Fig. 1. One half of the outer wall was removed from about 10 cm from the closed end for access. A spring-loaded alumina push rod is used to hold the sample (25 x 8 x 3 mm) against Pt foils (shown in red) placed at each end of the sample. Pt/Pt+10% Rh thermocouples (labeled 1 and 4) are spot welded to the foils. These thermocouples are used to measure temperature and to supply 10 ma of current for the dc electrical conductivity measurements. Two small notches are cut in the sample by a thin (0.175 mm) diamond saw blade at positions about 1/3 and 2/3 from the sample ends. A thin (0.075 mm) Pt wire is tightly wound around these notches and cemented to the sample using Pt ink. These wires are used to secure two additional Pt/Pt+10% Rh thermocouples (2 and 3) and measure the voltage generated by the 10 milli-amp current. The data acquisition system records the six voltages generated by the temperature gradient (adjustable by moving the sample holder's position within the furnace) and six temperatures as well as the dc electrical conductivity. Seebeck coefficient $Q = -\lim_{\Delta T \to 0}(\Delta V / \Delta T)$ calculated from the slope of a plot of ΔV versus ΔT in the limit of ΔT=0, as shown in Fig. 2 for a sample tested at 600°C. At high temperatures, there was larger scatter in the data. However, Q values were considered only if the regression fit parameter, R^2 >

0.85. Correction for the voltage arising from the differences in the length of Pt was included. All measurements were performed in flowing argon gas.

Results

Only nanographite results will be discussed in detail. Monolithic nanographite and their compositions doped with 5 wt % B_4C were evaluated. Effects of boron addition and annealing condition (temperature & time) in Ar-H_2 atmosphere were investigated. Seebeck coefficient (S) and dc electrical conductivity (s) were measured for as-fabricated samples and at various annealing temperatures and hold times. Nanographite and their doped samples were evaluated post annealing at 1400°C in a flowing Ar/4% H_2 atmosphere. Measurements were made at intervals of 4 hours up to a cumulative of 12 hours of anneal time. Further, 5% B_4C doped samples were annealed for 4 hours at 2200°C and 1800°C, respectively, for evaluation. Thermo-power measurements were obtained up to temperatures as high as 1200 K.

Fig. 3 shows the Seebeck coefficients measured as a function of temperature for the 5%-B_4C-nanographite sample for various annealing temperatures and times. Seebeck coefficient was found to increase monotonically with test temperature in both sets of samples. There is a clear increase in the magnitude of the Seebeck coefficient for the annealed samples as compared to the as-fabricated sample.

For the 5% B_4C-nanographite sample, behavior of Seebeck coefficient for the three annealing times explored appears to be quite similar. However, sample after 4 h annealing shows somewhat higher values at elevated temperatures. Sample annealed at 2200°C for 4 h showed similar behavior as the 1400°C annealed samples. It should be noted that data for as-fabricated and 1400°C anneal was from the sample, whereas, the 2200°C annealing was conducted on different sample fabricated under identical conditions.

Fig. 4 shows the dc-electrical conductivity for 5%B_4C-nanographite sample. As-fabricated nanographite sample exhibited 2X conductivity of that of nanodiamond sample. The magnitudes for both nanographite and nanodiamond samples were similar with values of approximately 150 S/cm. After >1800°C annealing treatment, both compositions showed significant increases in room temperature electrical conductivity with values of 350 S/cm and 280 S/cm for the nanographite and nanodiamond samples, respectively. As a function of test temperature, nanographite sample showed a somewhat decreasing trend, however, for the nanographite sample the conductivity appears to increase slightly and saturate at 300 S/cm.

Power factors ($S^2\sigma$) for 5% B_4C doped nanographite was calculated and plotted in Fig. 5. Two key points can be garnered from Figure 5: (a) annealing of the sample dramatically increases the power factor, by as much as an order of magnitude; 2200°C anneal showed the highest power factor largely as a result in the increase in electrical conductivity and (b) power factor increases with the test temperature. Based on the current measuring system, we are limited to reliable Seebeck and electrical conductivity measurements up to 1200 K.

Conclusions

The results for the first year are encouraging. A functioning, reliable Seebeck/electrical conductivity apparatus has been build and robust samples of both undoped and doped with B_4C nanographite and nanodiamond were prepared. Experiments on some NCEs have been completed. Composition, processing, and heat treatments have a large effect on the thermoelectric properties of these materials.

Issues & Future Direction

Considering that thermoelectrics have been under development for 50 years, we have made excellent progress in one year. However, we have to achieve at least another factor 100 increase in the power factor. Additionally, thermal conductivity will be measured to calculate the ZT. We believe that a combination of doping and processing will continue to show significant improvements.

References

1. D. M. Gruen, P. Bruno, and M. Xie, Applied Physics Letters, **92** 143118 (2008).
2. B.-S. Hong, S.J. Ford, and T.O. Mason, Key Engr. Mater., **125-126** (1997) 163-186

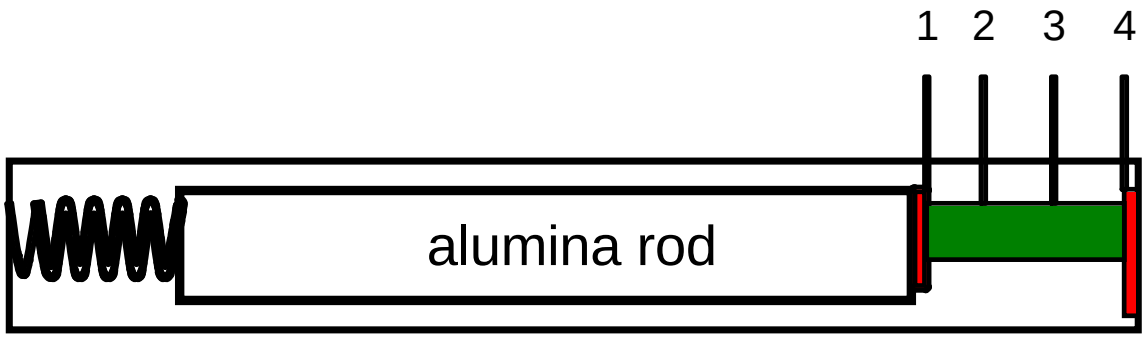

Figure 1. Cut away schematic of alumina sample holder.

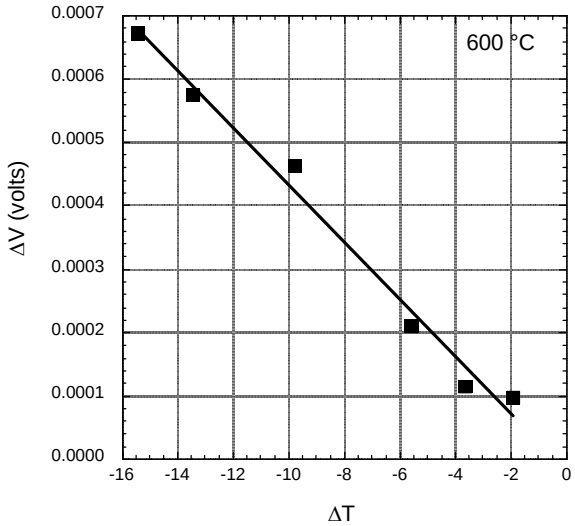

Fig. 2. Plot of ΔV vs. ΔT for 5% B_4C doped nano graphite sample at a test temperature of 600°C. The plot yields a Q= 29.1 μV/K.

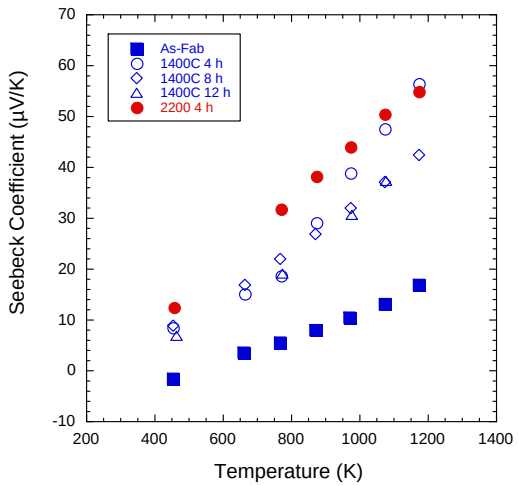

Figure 3. Seebeck coefficients of 5% B_4C-nanographite as a function of temperature and annealing times.

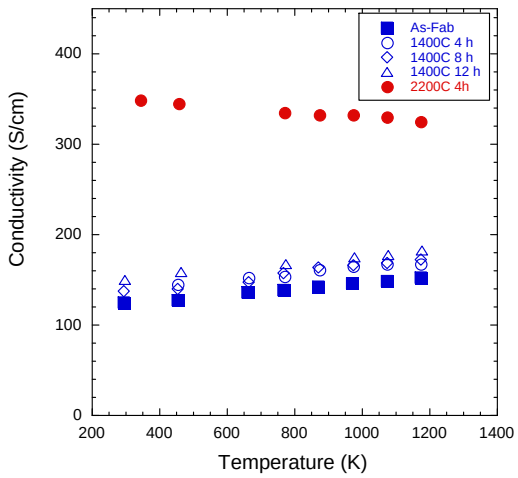

Figure 4. DC electrical conductivity 5% B_4C-nanographite as a function of temperature and annealing times.

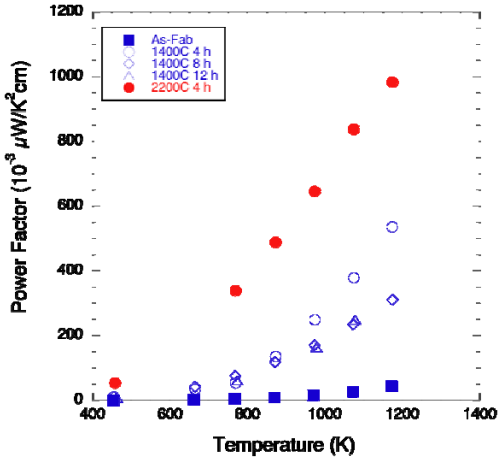

Figure 5. Power factors of 5% B_4C-nanographite as a function of annealing temperature and times.

A Strong Energy Portfolio for a Strong America

Energy efficiency and clean, renewable energy will mean a stronger economy, a cleaner environment, and greater energy independence for America. Working with a wide array of state, community, industry, and university partners, the U.S. Department of Energy's Office of Energy Efficiency and Renewable Energy invests in a diverse portfolio of energy technologies.

For more information contact:
EERE Information Center
1-877-EERE-INF (1-877-337-3463)
www.eere.energy.gov